Experimental and numerical modeling of the impregnation of fibrous media by suspensions in LCM processes

Nihad Abdelhadi Ahmed Siddig

THESE

Pour obtenir le diplôme de doctorat

en Mécanique spécialité Matériaux

Préparée au sein de l'« Université Le Havre Normandie »

Experimental and numerical modeling of the impregnation of fibrous media by suspensions in LCM processes

Présentée et soutenue par
Nihad ABDELHADI AHMED SIDDIG

Thèse soutenue publiquement le 10 Septembre 2021 devant le jury composé de		
Sébastien COMAS-CARDONA	Professeur des Universités, Ecole Centrale de Nantes	Président du jury
Christophe BINETRUY	Professeur des Universités, Ecole Centrale de Nantes	Rapporteur
Chung Hae PARK	Professeur des Universités, IMT Lille-Douai	Rapporteur
Alex SKORDOS	Professeur des Universités, Université de Cranfield	Examinateur
Hatice SINEM SAS	Maître assistant , Université de Sabanci	Examinatrice
Laurent BIZET	Maitre de Conférences, Université Le Havre Normandie	Co-encadrant
Abdelghani SAOUAB	Professeur des Universités, Université Le Havre Normandie	Directeur de thèse

Thèse dirigée par Abdelghani SAOUAB, Laboratoire Ondes et Milieux Complexes

UNIVERSITÉ LE HAVRE NORMANDIE

ED PSIME

LABORATOIRE ONDES et MILIEUX COMPLEXES

Contents

Introduction

Composite materials undergo continuous development in many industrial domains, such as aeronautic, automotive, sports and leisure, and marine applications. The most remarkable features of composite materials lay in their high specific strength and specific modulus compared to the other materials. Their lightweight permits the reduction of fuel consumption in aeronautic and automotive structures. These numerous features can be further extended by adding a solid phase in the form of powders or particles with particular functionalities; the new materials are then called functional composites. These composites can achieve a wide range of new properties, such as thermal and electrical conductivity/insulation, magnetic or optical functionalities. Their advantages also include the enhancement of existing properties like weight saving and the amelioration of mechanical properties. A crucial issue in manufacturing functional composites could come from the complexity of particle addition to their fibrous structures. The challenges of composite processing in the presence of particles arise from the interdependency of variables that govern the particle distribution. Hence, the exploration of the different particle addition techniques is necessary for the advancement of functional composites research.

Several particle addition methods to composite materials have been presented in the literature, such as the deposition of inclusions on the preform surface or adding particles to the liquid resin and the injection of suspensions into the fibrous medium. In the former method, the particle content and distribution can be controlled. In the latter method, particle content varies in time and space. Hence, introducing particles by resin functionalization becomes more challenging as it affects the impregnation process and induces three main issues: an increase in resin viscosity and a decrease in the fibrous preform permeability as a function of particle deposit, resulting in a non-homogeneous particle distribution within the finished part. The filtration of particles is a complex phenomenon that depends on material-related parameters e.g. fabric content and architecture, resin viscosity, particle size, concentration and process-related parameters such as the injection flow rate or pressure.

This work examines the influence of particle addition on composite fabricated by liquid composite molding (LCM) processes. The presented chapters aim to contribute to the comprehension of the physics of particle addition to composites and filtration through fibrous preforms. The study highlights the key parameters that govern the addition of particles to composites, particularly those that intervene in controlling the particle distribution within the fibrous medium at different scales. The presented thesis seeks to address the experimental and numerical modeling of suspension flow through fibrous media and the influence of selected variables on the impregnation process and the particle distribution within the finished part.

Research program

Several researchers tackled the subject of composite functionalization, however, there is still a gap concerning the understanding of the particle addition techniques and their influence on the processing of composites. The study focuses on one of the most used composite manufacturing techniques, i.e., liquid composite molding (LCM) processes. Extensive experimental tests have been conducted, followed by a series of numerical simulations. To understand the different phenomena of particle addition, an extensive literature review is conducted I, followed by material characterization for the identification of the main material parameters II. The investigations carried out are addressed in three experimental chapters II, III, IV and V. The last chapter VI includes the numerical modeling and simulation of the flow and filtration process of suspensions through fibrous media. A short description of each chapter is presented hereafter.

Chapter I: Literature review

In this chapter, a comprehensive literature review is established to present the main notions and terminology in this domain. The previous experimental and numerical studies of particle addition and filtration are presented. The findings concerning the influence of some parameters are summarized. This chapter aims to highlight the main ideas discussed throughout previous research and underline the aspects that were not sufficiently covered.

Chapter II: Material characterization

To understand the complex phenomena induced by particle addition and filtration, extensive characterization of the used materials and constituents is conducted. This second chapter presents all the materials used in the experimental investigations of this thesis. The chapter presents the used preform, fluids, particles and suspensions separately. The characterization of each material is presented, along with a detailed description of the

testing facilities. This chapter holds the first introduction to the influence of some material variables and identifies physical parameters, such as the evolution of permeability with fiber content and the viscosity change with particle content.

Chapter III: Impregnation of particle-loaded fibrous preforms in LCM processes

For the manufacturing of functional composites by LCM processes, the biggest challenge is controlling particle content through the part length. A first experimental investigation of the influence of particle addition is carried out in this chapter, assuming homogeneous particle distribution. The direct deposition of particles on the preform surface was used as the particle addition method to master their distribution throughout the part length. The objective was to eliminate variables connected to the non-even particle spreading to focus on flow kinetics and compaction behavior for particle-loaded preforms at different inclusion volume fractions. Tests compared the influence of two types of micron-scale inclusions: plain and compressible particles.

Chapter IV: Filtration of particle-loaded resin through fibrous media

After the study of particle deposition by direct sieving in chapter III, a second addition method is examined in this chapter. The method constitutes of the preparation of particle-resin dispersions and the impregnation of the neat fibrous structure with these suspensions at different concentrations. Once the effect of a given particle volume fraction on flow kinetics has been identified, the experimental characterization was extended to include the filtration behavior of suspensions through fibrous media. Several experiments have been performed to contribute to the understanding of the fabrication of functional composites and to identify the influence of selected parameters that govern the final particle distribution. The evolution of particle size is extensively studied through a granulometry analysis of suspensions from the inlet to the outlet of the fibrous medium and the particle filtration mechanisms are investigated.

Chapter V: Filtration of micro-scale particle-loaded flow through unidirectional fibers

The experiment presented in chapter IV delivers macro-scale information on the flow and filtration in dual-scale media during suspension injection. After identifying the global filtration trends and mechanisms at the given process and material parameters at the preform scale, a new experimental methodology has been proposed in chapter V to the study of flow and filtration at the tow scale. This chapter aims to observe the filtration and the distribution of the particles through unidirectional fibers during axial injection

of suspensions in down-scaled fibrous media comparative to the tow scale. Single-scale fibrous media constituted of parallel fibers are injected by unidirectional suspension flow parallel to the direction of fibers. The used methods aim to characterize the spatial evolution of particle content and count through the sample length and the influence of particle addition on the evolution of pressure and flow kinetics.

Chapter VI: Numerical modeling of flow and filtration

After the experimental investigations are performed, a numerical tool is developed to simulate the flow and filtration process. The chapter is dedicated to the modeling and simulation of the particle-filled RTM injections. A simulation tool is developed using two of the most widely used filtration models for describing the suspension flow and particle capture through the fibrous medium. The process is implemented in the software COMSOL Multiphysics through solid coupling between flow and filtration models. This simulation tool is used to investigate the influence of physical and numerical parameters on filtration through a parametric study. The parameters of filtration models are identified with the help of the experimental results. The simulation tool is validated by comparison to our various experimental results from chapter IV.

Chapter I

Literature review

I.1 Introduction

Particulate-fillers can be added to composites in many industrial applications, such as aeronautic, automotive, sports and leisure, marine, and structural applications. The addition of particles allows providing new functionalities such as electrical, magnetic, thermal insulation or conduction, and fire resistance; they can also enhance existing properties such as mechanical properties and weight saving. However, the manufacturing of functional composites with LCM processes raises the challenge of flow and filtration of these particles, which further complicates the impregnation process. First, fillers in resin increase the viscosity as a function of particle size and concentration. Second, the deposition of particles in the fibrous bed reduces its permeability. These effects induce non-homogeneous particle distribution and hence variable properties along the part. Therefore, a comprehensive characterization is needed to understand the different parameters that govern particle capture and distribution within the fibrous medium.

This chapter presents a general overview of the literature on the fabrication of particle-loaded composites in liquid composite molding (LCM) processes. It aims to:

- review the primary process physics and challenges in processing particle-loaded composites to help identify the optimal conditions for successful fabrication of these composites,
- explain the key terminology of the topic and plot the general advantages and applications of this type of composites,
- identify some of the gaps in experimental and numerical studies of particle-loaded composites.

The previous research on the processing challenges of particle-loaded composites is detailed. Main particle addition and characterization methods are presented, from which two methods are used in the experimental parts of this work. The chapter also presents previous modeling and numerical studies on single and dual-scale media. Finally, conclusions are drawn to explain the choice of experimental and numerical methods used throughout this work.

I.2 Generalities about composite materials

A composite material is a combination of two or more constituents with distinct properties. The properties of the final material are superior to those of each of the constituting materials [1]. This section presents a brief introduction to constituents of composite materials and their manufacturing processes.

I.2.1 Composite constituents

The main constituents of composite materials are the fibers (or reinforcements) responsible for mechanical properties and the matrix, which ensures the cohesion and orientation of the fibers and the distribution of the stress applied to the parts. In addition, fillers or particles can be incorporated into composites in the form of fragments or powders. They modify the properties of the material to which they are added according to their type and morphology.

Fibrous materials

Different types of fibers are used as composite reinforcements according to the application. Besides the mechanical properties of the final part, such as strength and stiffness, they control other properties such as temperature and creep resistance [2]. Fibers are classified according to their length into short and continuous fibers, and according to their nature into natural and synthetic fibers. Natural existing fibers include flax, kenaf, jute, hemp and cotton. Synthetic fibers are fabricated from raw materials; they provide broad spectra of properties that make them interesting for structural and industrial applications such as aerospace and automotive applications [1]. Glass fibers are the most used type of fibers as a reinforcement [3]. They are fabricated from silica or quartz and mineral additives which are melt and rapidly cooled through the fibertization process. Glass fibers are used for their several qualities, such as insulation, resistance to corrosion, inertness and their mechanical properties such as hardness, strength, flexibility and stiffness [1, 4]. Carbon fibers are used for high-performance applications. Their high cost emerges from its expensive fabrication process, which is mostly the carbonization

of PAN fibers (Polyacrylonitrile) [4]. Aramid fibers are made of aromatic polyamides; they come into two main types: low modulus fibers and high modulus fibers. The first type is used to fabricate cables and bulletproof vests, while the latter is used to fabricate high-performance composites. Other types of fibers include ceramic fibers, boron fibers, polymeric fibers (e, g. high modulus polyethylene fibers), and ceramic fibers [4]. For protecting fibers from their abrasive behavior towards each other, a thin ply of chemical coating named sizing is applied to each fiber right after their fabrication. Fibers are then grouped to form strands or tows, which constitute reinforcements. Sizing provides not only lubrication or protection for fibers, but it could also play the role of a coupling agent between fibers and resin for the subsequent process [1, 3].

Fibrous reinforcements

The type of fibrous reinforcement is selected according to the application and the properties it brings to the final part. Reinforcements are classified according to the fiber orientation in the structure into: (1) Random mats, which are constituted of randomly oriented fibers. Their relatively low fiber volume fraction (and hence high permeability) is generally linked with their low mechanical properties. (2) Woven fabrics, which are constituted of weft and warp threads perpendicular to each other, with tow inter-weaving that defines their architectures. (3) Non-crimp fabrics (NCF), which are constituted of tows stitched parallel to each other in one or multiple layers at given directions; this type of fabric has very interesting mechanical properties.

Curing resin

The matrices used in the fabrication of composites are classified into polymeric, mineral (e.g., silicon carbide) and metallic (e.g., aluminum alloys) [5]. They are added to ensure fiber protection and bonding, load distribution and surface finish. They also determine the final shape of composites. Polymer matrices are the most used among the mentioned types; they are commonly classified into two types: thermosets and thermoplastics. Thermosets like polyester, vinyl ester, epoxy, polyurethane and phenolic exist in a liquid state before processing. Solvents are sometimes added to decrease their viscosity. The reaction is activated thermally or chemically through the addition of hardeners that accelerate the cross-linking. Thermoplastics such as PA, PET, PEEK, and PEKK are commercially available in a solid-state as pellets. They are molten by heat before or during the process, then cooled after the processing to solidify. Researchers use model fluids for the experimental testing of composites during the impregnation processes. They are preferred to curing resins because most of them exhibit a Newtonian behavior at room temperature. Another reason is to avoid the limitations of resin gel time and solidification of resin before the completion of impregnation. Some of the most used

test fluids are silicone oil, glycerol, Carboxymethyl Cellulose (CMC) and DOP (Dioctyl phthalate) [6, 7, 8].

Fillers

Fillers are solid and inert materials in nano or micron-scale sizes which can be added to neat polymers and reinforcements to provide certain properties. They come into wide range of forms and materials. The type of particles is chosen according to the targeted functionality in the finished part. Production techniques and particle properties differ from one type to another. They are classified according to their occurrence to mineral/natural and synthetic particles [9].

One of the most influencing factors in the processing of particle-filled composite is particle morphology, i.e., particle shape and size. Particles can be grouped into aggregates (with strong bonds) or agglomerates (with weaker bonds) depending on the strength of interaction between single particles. The measurement of particle size distribution requires an effective characterization method. Usually, Scanning Electron Microscopy (SEM), optical microscopy and X-ray tomography are used for particle shape and size characterization. Laser diffraction and Dynamic Light Scattering (DLS) are used to determine particle size distribution uniquely. The particle size can be represented by the specific surface area, the surface and volume-weighted mean, the average and the median particle sizes. Particles can be classified according to the order of magnitude of their size into nanoparticles (from 1 to 100 nm) and microparticles (from 1 to 100 μm) [6]. Particles have a wide variety of shapes according to their nature or processing method. Particle shape highly affects the rheology of their suspensions during the process and the mechanical properties of the finished part. Most of the particles come into spherical, blocky, platy, acicular (fibrous), or irregular shapes. Figure I.1 shows some of the encountered shapes of particles in composites processing [10]. Irregular particles increase the viscosity of resin more than spherical ones. Platy and acicular particles increase composite strength. The particle morphology and ability to bond with the polymer resin determine filler performance within the composite. Modifications on the filler surface are sometimes applied to protect them from environmental conditions and interaction with polymers, provide improved flow properties or better dispersion. They can also enhance several properties in the finished part, such as stiffness, strength and hardness. Surface modification techniques are categorized into three main groups; chemical modification, mechanical activation and physical treatment [2, 9].

I.2.2 Composites manufacturing processes

The process selection depends on the properties of the finished part (shape and dimensions) and the application (High diffusion or high performance). Advani and Sozer [3]

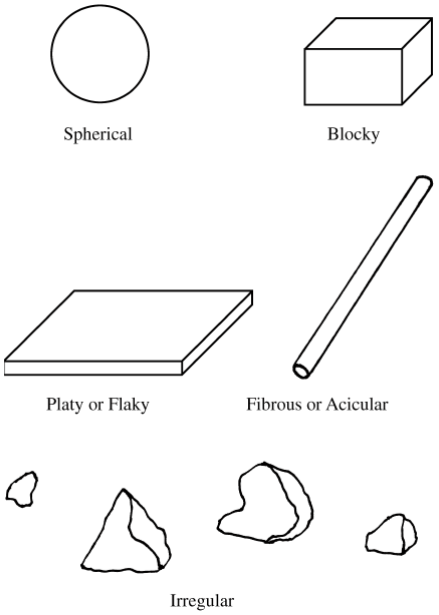

FIGURE I.1: Illustration of typical shapes of particles [11]

classified the fabrication processes into three key groups presented in Table I.1. Another classification of composite manufacturing processes depends on part placement during the process to (a) open mold processes like pultrusion and filament winding and (b) closed mold processes such as Resin transfer molding process (RTM). Closed mold LCM processes will be the focus of the current study. Table I.1 summarizes the main composite fabrication processes according to [3].

TABLE I.1: Classification of composites manufacturing processes [3]

Group No	Transport mechanism	Materials	Physics and challenges	Process examples
1	Suspension flow	-Short fibers + TP/TS resin -Raw material in form of pellets	-Flow of suspensions -Transport, distribution, and orientation of fibers	Extrusion, Injection molding, Compression molding
2	Advanced thermoplastic flow	-Continuous and long discontinuous fibers + TP resin -Fibers are pre-impregnated partially or completely by resin	-Squeeze flow -Heat transfer (Heat and pressure for part consolidation) -Simultaneous deformation of fiber and resin under applied stress and hence anisotropic response	TP sheet forming, TP pultrusion, tape placement process
3	Flow through fibrous media	-Continuous fibers + TS resin	-Flow of resin through fibrous media -Heat transfer	LCM, TS pultrusion, TS filament winding, Autoclave processing

LCM processes

LCM processes are categorized under the 3^{rd} group of porous media manufacturing methods in Table I.1. The main driving mechanism in LCM processes is the flow of the low viscosity resin through the dry fibrous structure to fill pores between fibers. The overall impregnation cycle should be lower than resin gel time. All the LCM processes

share the same flow mechanism, slight differences distinct processes from one another. The main LCM processes include:

- Resin Transfer Molding (RTM), RTM light, Compression Resin Transfer Molding (CTRM), Vacuum Assisted Resin Transfer Molding (VARTM) and Co-Injection Resin Transfer Molding (CIRTM);
- Structural Reaction Injection Molding (SRIM);
- Seemann Composite Resin Infusion Molding Process (SCRIMP);
- Liquid Resin Infusion (LRI);
- Vacuum Assisted Resin Infusion (VARI);
- Vacuum Induced Preform Relaxation (VIPR);
- Resin Infusion between Double Flexible Tooling (RIDFT).

RTM process

RTM is one of the most widely used flow processes for its several advantages. It gives the possibility of producing large parts with complex shapes and inserts because of the flexibility in mold design. The finished RTM parts are near-net-shape and have an excellent surface finish and good mechanical properties [3]. The main RTM process steps as illustrated by Figure I.2 are: (1) reinforcement cutting or preform preparation (2) fiber placement in the mold cavity and mold closing (3) injection of resin through the mold at constant pressure or flow rate and (4) curing, part curing and demolding. A successful RTM part requires a void-free or low void content part with good resin distribution. Nonetheless, the transport of resin in a fibrous medium of high heterogeneity with a complicated pore distribution could leave dry zones, especially in dual-scale media. In addition to the preform architecture, the process robustness is influenced by the fiber content, mold geometry, injection pressure or flow rate. Mathematical modeling and numerical simulation help defining the optimal injection and vent locations. Which reduces time and cost induced by the experimental trial and error [12, 95]. Modeling the RTM process requires a good understanding of the flow of resin through the fibrous bed and the heat transfer during the process, along with the resin curing kinetics. However, resin reaction is out of the scope of this study. The focus will be only on the resin flow through fibrous media.

I.3 Use of fillers in the fabrication of composite materials

Functional composite materials are fabricated by adding fillers that possess the targeted property, such as fire retardancy, thermal conductivity, heat conductivity, magnetic

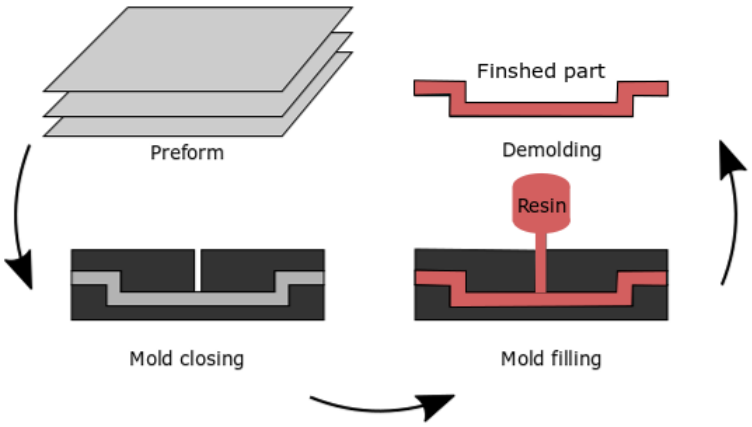

FIGURE I.2: Steps of the RTM process

properties, and optical characteristics. Functional composites are increasingly used in aerospace, automotive, marine, wind energy, electronics, transportation, building and construction, storage and piping, as well as sports and consumer Goods applications [1, 13]. In addition, there is a possibility of combining two functionalities, e.g., the magneto-electric effect in composites. Composite materials loaded with nanoparticles are called nanocomposites. Nanofillers, such as carbon nanotube, silica and clay have at least one of their dimensions in the order of nanometers. They have gained a great interest in the last decades because of their growing use in superconductors and sensing magnetic applications [9].

I.3.1 Advantages and applications

There is an increased interest in the use of fillers for different composites applications. Some of the properties that fillers or particles can provide to composite materials (or enhance) are:

- cost reduction,
- abrasion resistance,
- fire retardancy,
- self-healing,
- electrical/thermal conductivity or isolation,
- sensor effect,
- improving mechanical properties such as modulus, tensile and tear strength, surface hardness and abrasion resistance,

- other purposes for using fillers include: reduction the thermal expansion coefficient, dimension stability, antibacterial effect and electromagnetic shielding.

The influence of particles on the mechanical properties of composite parts has been widely investigated [8, 10, 14, 15]. The mechanical properties are affected mainly by particle size, volume fraction and particle-matrix adhesion [16]. Both rubber and rigid particles lead to increased toughness [11, 17]. Rigid particles increase modulus as the particle volume fraction increases, adjusting the combination of particle size-volume fraction tailor the tensile strength [18]. The strength of particulate-filled composites depends strongly on particles-matrix adhesion; thus, adding coupling agents can help improve the strength [19]. The axial stress transfer between the matrix and ellipsoidal inclusions increases with aspect ratio and decreases with their volume fraction [20]. Nevertheless, particles may favor crack propagation in thermosetting resins in case of particle breakage [21, 22].

I.3.2 Challenges and drawbacks

The addition of a second solid phase alters the structure of the fibrous medium, which will affect the flow process, leading to high interdependencies of process and material variables induced by these changes.

I.3.2.1 Preform permeability

The permeability of the fibrous medium decreases with the increase in particle content within the filter. According to the particle addition method, either to the preform or resin, the influence on permeability is presented hereafter.

Particle-loaded reinforcement The influence of fillers on the permeability of reinforcements depends highly on the particle type and size and the fabric type. For woven fabric, fillers tend to fall in the interstices and reduce their porosity; this leads to a reduction in permeability as a function of filler volume fraction. Like the case with 40-400 μm sized particles in work presented by Caglar et al. [23, 24], in which authors investigated the saturated permeability for twill weave glass fabrics with glass beads. Large inclusions (400-800 μm) caused an increase of permeability as they enlarged the existing pores I.3.

Manfredi and Michaud [13] investigated the influence of self-healing micro-capsules on glass woven fabric impregnated by PEG/water solutions. The study revealed that the unsaturated permeability has increased up to a factor 6 with 125-250 μm capsules. Whereas the fabric functionalization only slightly influenced the saturated transverse permeability. Figure I.4 reports the findings of this study.

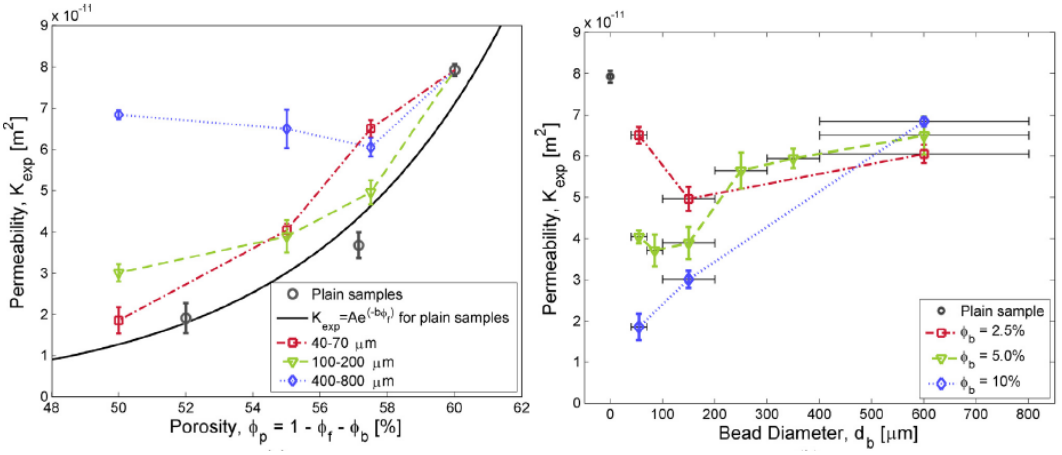

(A) (B)

FIGURE I.3: Permeability of functionalized preform measured along the weft direction as a function of (A) porosity and (B) bead size [23]

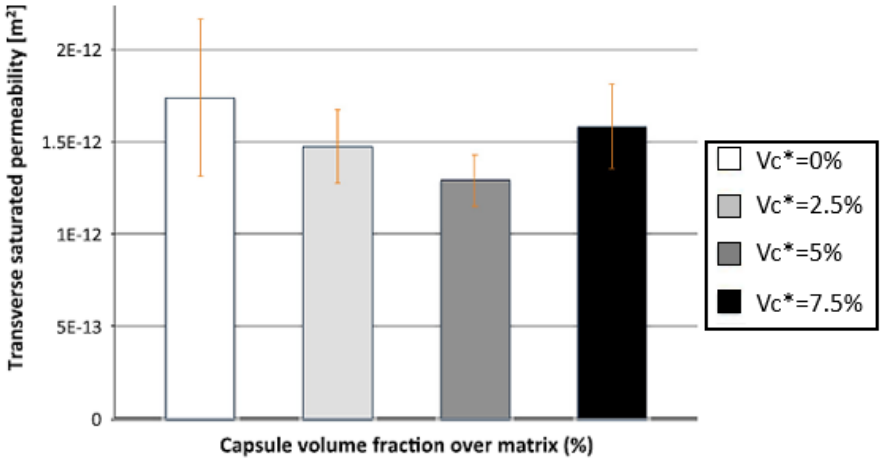

FIGURE I.4: Transverse saturated permeability as a function of the particle volume fraction [13]

These studies show that the influence of filler addition on the permeability of the preform is highly dependent on nature, size and volume fraction. However, most of the presented researches on fabric functionalization introduced solid particles. The influence of different types of particles, such as microballoons, has not been sufficiently addressed.

Particle-loaded resin Particle retention increases the solid volume and hence reduces the volume of the existing pores. Therefore, the evolution of permeability is highly dependent on the amount of particles present at a given instant of time and position. Fernberg et al. [25] explored the spatial evolution of permeability of a plain weave glass fabric with two grades of Alumina Trihydrate (ATH) particles. Pure fluid injections exhibited a constant permeability trend. In contrast, all the other types of suspension impregnations have marked a drop in permeability, especially at the preform inlet (Figure I.5).

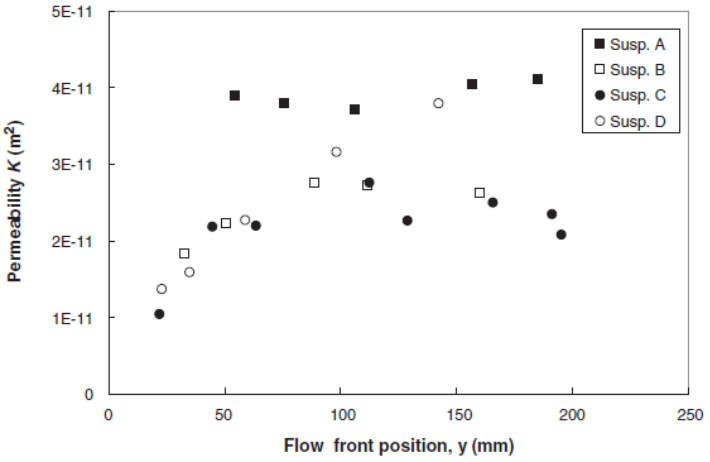

FIGURE I.5: Unsaturated permeability versus flow front position [25]

I.3.2.2 Resin viscosity

It has been shown in the literature that the addition of fillers to any fluid increases its viscosity. The fluid nature, the particle shape, size and concentration control the suspension viscosity. According to particle size, the smaller the particles, the higher the suspension viscosity [26]. Regarding particle morphology, viscosity increases with the irregularity of the particles [6, 16]. Furthermore, the viscosity increases proportionally to the particle concentration.

Even if the carrying fluid is Newtonian (independent of shear rate), suspensions of the same liquid may exhibit different behavior. For example, measurements carried out by Fernberg et al. [25] for a suspension of polyester resin and ATH particles yielded a Bingham type behavior. Lefevre et al. [6] found that the viscosity of suspensions is independent of time for concentrations up to 30% at any shear rate. Higher than 40%, the viscosity increases significantly over time for low rates of shear (0.1 s^{-1}) but remains approximately constant at higher shear rates.

Viscosity models Several models were proposed to describe the evolution of viscosity of suspensions as a function of particle concentration, independently of their size or shape. Relative viscosity η_r is defined as the ratio between the suspension viscosity η and the neat fluid viscosity η_0.

$$\eta_r = \frac{\eta}{\eta_0} \tag{I.1}$$

Einstein and Barnes [27] have shown that the relative viscosity of a suspension is a function of its particles phase volume, assuming that particles are rigid with no force acting on them [28]. The effective viscosity is given by:

$$\eta_r = 1 + 2.5C \tag{I.2}$$

where C is the particle phase volume or concentration. **Batchelor** [29] modified the equation to consider the hydrodynamic interactions due to Brownian movements between particles, Einstein's equation becomes:

$$\eta_r = 1 + 2.5C + 6.2C^2 \tag{I.3}$$

Batchelor's equation can be used with particle concentrations less than or equal to 0.1. **Ball and Richmond** [30] proposed another equation as follows:

$$\eta_r = e^{2.5C} \tag{I.4}$$

They soon replaced this equation with a new one to consider the maximum particle packing at which the viscosity is infinite.

$$\eta_r = \left(1 - \frac{C}{C_{max}})\right)^{-2.5C_{max}} \tag{I.5}$$

From this equation, **Krieger and Dougherty** [28, 31] replaced the 2.5 factor by the intrinsic viscosity, the new equation becomes valid for any particle volume fraction:

$$\eta_r = \left(1 - \frac{C}{C_{max}})\right)^{[\eta]C_{max}} \tag{I.6}$$

C_{max} the maximum packing volume is equal to the inverse of the self-crowding factor. It depends on the particle shape and size distribution. $[\eta]$ is the intrinsic viscosity, the value of $[\eta]$ ranges between 2.5 and 5 for a suspension of spherical particles [14, 27, 32]. In all previously mentioned models, the relative viscosity is independent of particle diameter. However, **Selvakumar et al.** [28] recently modified Krieger and Dougherty's model to account for particle clustering and interfacial layer formation for nanofluids.

For suspensions with a Newtonian behavior, **Eilers** [33] suggested the following model:

$$\eta_r = \left(1 + \frac{[\eta]C}{2(1 - \frac{C}{C_{max}})}\right)^2 \tag{I.7}$$

Mooney [34] extended Einstein's equation to a wider range of particle sizes and concentrations up to 50%. A partially empirical equation is used for suspensions of monodisperse and rigid spherical particles:

$$\eta_r = exp\left(\frac{2.5C}{1-\frac{C}{C_{max}}}\right) \tag{I.8}$$

Where 2.5 is the same factor introduced by Einstein for dilute suspensions. The value of ϕ_m is in the range $0.52<\phi_m<0.74$. **Erdal** [35] proposed an empirical equation for viscosity, where A1 is an empirical constant.

$$\eta_r = \left(1-\frac{C}{A1}\right)^{-2} \tag{I.9}$$

Most of these presented models agree with Einstein's equation at low concentrations. The behavior of suspensions with changing shear rates remains complex. Thus, concentration-dependent models are sometimes preferred to shear-dependent ones [14]. However, when suspensions exhibit non-Newtonian behavior, their viscosity depends on shear rate, time and particle concentration C.

I.3.2.3 Particle distribution

A common problem in particle-filled LCM processing is the final particle distribution along the part length due to particle filtration by the preform during impregnation. The properties of the finished part are directly related to the particle distribution; non-even distribution results in non-homogeneous composite properties along the part. In the study carried out by Lefevre et al. [6], the particle distribution at the end of impregnation exhibited two different profiles for a series of experiments with different injection parameters. Figure I.6 shows the filtration trends for two experiments: a U-shaped profile (test 39) and a decreasing trend profile (test 85). In this figure, d_p and V_f denote respectively the particle diameter and the fiber volume fraction.

Louis et al. [36] have studied the evolution of concentration for nanoalumina and nanosilica particle suspensions against variable process parameters. Authors found that the sensitivity of particles to filtration depends mainly on their sizes and their agglomeration behavior. The fiber content of the preform was the parameter that influenced the final particle distribution the most. Whereas, filtration trend was less affected by the change in resin viscosity, initial particle concentration, and resin overflow volume. No agglomeration behavior is observed with nanosilica particles; thus, they did not influence the filtration trend. The nanoalumina, which formed micron-scale agglomerates, exhibited both surface and deep bed filtration behaviors (Figure I.7 A). Micron-sized particulates could have a similar effect as the nano-sized agglomerates that act as effective particle size. In addition, retained particles could act as a filter themselves and increase the particle-particle interactions that quicken clogging. The viscosity of fluid did not seem to influence the particle filtration trend (Figure I.7 B).

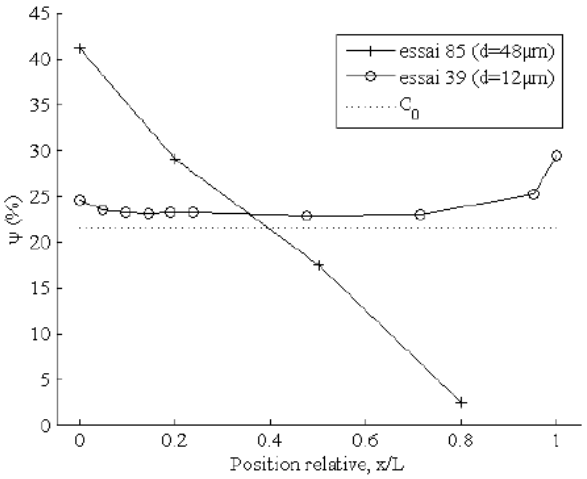

FIGURE I.6: Final particle distribution in the part. Results of filtration experiment No. 39, with d_p=12 μm and V_f=18.8 % and experiment No. 85, with d_p=48 μm and V_f =13% (at L=20cm, and C_0=21.5%vol) [6]

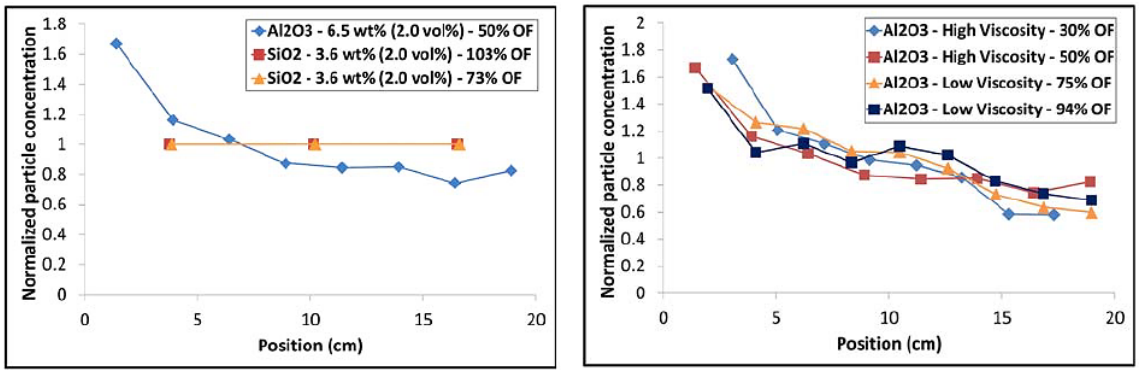

(A) (B)

FIGURE I.7: The evolution of particle concentration with the preform length at variable (A) particle agglomeration behavior and (B) fluid viscosity [36]

Abliz et al. [37] studied the filtration of two types of nanoparticles (silica and boehmite) suspended in epoxy resin using Thermogravimetric analysis (TGA). The filtration curves have shown a high dependency on the fiber volume fraction with both types of particles. Figure I.8 plots the particle concentration throughout the part length. It was found that the filtration of nanoparticles is mainly related to the particle size distribution and the dual-scale of the preform. Moreover, the study identified a fiber content threshold after which the fibrous medium is clogged even by a low concentrated suspension.

The evidence from these studies highlights the necessity for experimental evaluation of variable interdependencies for micron-scale particles, which was not sufficiently dealt with.

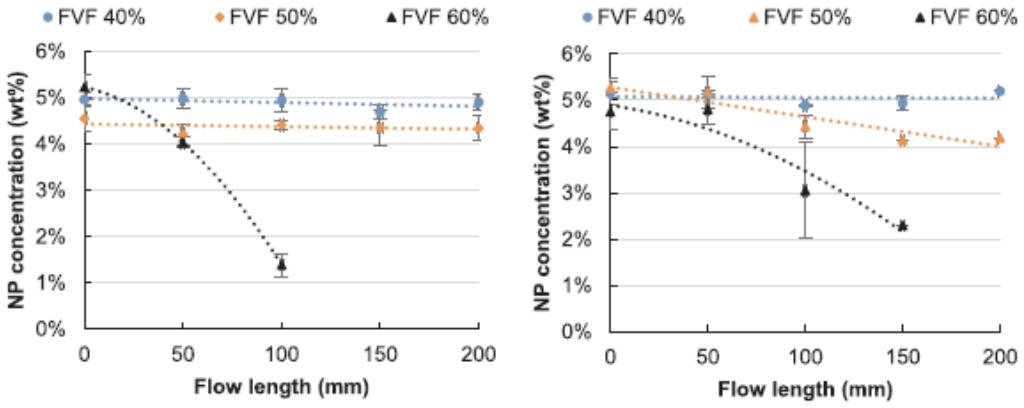

FIGURE I.8: The evolution of the concentration of Boehmite nanoparticles along flow length at different fiber content values parallel (left) and transverse (right) to fiber direction. [37]

I.4 Measurement of particle content

The characterization of particle content depends on the carrying fluid. When the polymeric resin is used, the measurement is performed after the resin solidification. Two characterization methods fall under this category; burn-off and imaging methods. In addition, other characterization methods can be applied using model fluids, such as particle tracing using μPIV (microparticle imaging velocimetry) and light scattering.

Burn-off technique

In the thermal decomposition technique, samples of composites are cut after resin cure and heated to a temperature above the resin and fiber decomposition temperature and below the particle degradation temperature. The remaining particles are weighed and the percentage of particles present in the sample is determined as the sum of the retained particles and the particles in movement. Lefevre et al. [6] used calcination method for composites of synthetic fibers and ATH particles. Samples were prepared and cut at different locations then heated up to 600°C to decompose fibers and resin. Louis et al. [36] have used the same technique for quantifying the particle retention within composite parts of aramid fibers and epoxy resin loaded with silica and alumina nanoparticles.

Imaging and optical techniques

In these techniques, samples of composites are cut after solidification, polished, and observed using an imaging method. Estimations for particle retention areas were presented by Fernberg et al. [25] for cured samples of ATH and polyester resin using optical microscopy. Qualitative microscopy analysis was performed for the inter-tow and intra-tow regions to detect the factors influencing the particle capture. The study concluded

that the part length has a tangible effect on particle filtration and distribution. High flow front irregularities were reported. Nordlund et al. [39] investigated the deposition mechanisms using microscopic imaging and micro-particle image velocimetry (μ-PIV) through a series of meso-scale and macro-scale experiments. The study has shown that large particles are captured at the tow interface, whereas small particles penetrated the fiber bundles. Yum et al. presented in [40] and [38, 41] a methodology to observe the distribution of titanium dioxide particles and carbon nanotubes (CNT), coupling electron probe micro-analyzer (EPMA) and SEM analysis. Abliz et al. [37] have used SEM analysis along with optical microscopy for studying the influence of particle size and fiber distance distribution on the filtration of two types of nanoparticles (silica and boehmite). Results revealed that filtration is highly dependent on the particle size distribution and the preform structure.

Suspension sampling and characterization

This method is based on extracting samples of suspensions at different locations to track the evolution of concentrations. It can be applied to resin or model fluid samples. For example, Herzig investigated particle concentration's spatial and time evolution through granular media for water treatment applications through a vertical column. Samples are then examined under light scattering to determine the particle concentration [42]. In their study, Chohra et al. [43] called into question the filtration of Aluminum Oxide (Al_2O_3) particles in the through-thickness direction using Corn syrup as a test fluid. The porous medium constituted of six layers of E-glass woven fabric. At the end of the impregnation, layers of fabric are rinsed, and the particles are sieved and weighed.

I.5 Particle addition methods

Several particle addition techniques were adopted depending on the type of particles, reinforcement and the carrying liquid. These techniques are classified according to the medium that incorporates the fillers into particle-loaded resin or particle-loaded preform methods. Other researchers used the dip-coating technique that combines the two mentioned methods.

Addition of particles to the resin

Dispersion of particles in the liquid resin is one of the most used particle addition techniques for LCM applications. This method consists of the preparation of homogeneous suspensions of pure resin and fillers and the impregnation of the reinforcement with the dispersion [6]. Many authors have used this technique for the fabrication of functional composites and the study of filtration and flow of particles in porous media

[6, 8, 35, 44, 45, 46]. The main challenges are the increase of resin viscosity, the decrease in reinforcement permeability and the potential filtration of particles by the medium leading to a non-homogeneous filler distribution.

Pre-deposition on the dry reinforcement surface

In this method, particles are spread on the fiber surface by manual or automated sieving. Using this technique ensures a relatively good particle distribution through the part length. However, particles are not embedded in the intra-tow regions when their sizes are larger than the micro-pores sizes. Indeed, particle deposition influences the preform permeability and compaction behavior depending on the type and architecture of the preform, as well as the particle size [13, 23].

Dip-coating

In textile technology, dip-coating consists of dipping individual fibers, strands or reinforcements in a particle-loaded fluid to allow their functionalization. This method has been used for loading single glass fibers with self-healing micro-capsules [47, 48]. The liquid evaporates after the coating process leaving only the deposited particles at the fiber surface. This method was also successfully used for particle deposition at a carbon fiber reinforcement. The strands were first dipped in a particle-loaded resin, then partially cured and finally impregnated by neat resin [49].
However, this study is limited to the first and second particle addition methods.

I.6 Pre-deposition of particles on the fabric surface

Recent studies have questioned experimentally the addition of micron-scale particles to fibrous structures to identify the key effects of the inclusion incorporation. Three examples of the studied applications are presented in the coming sections.

I.6.1 Permeability enhancement

Researchers have introduced a second solid phase to composite structures for contributing to permeability enhancement and the reduction in impregnation time in the past years. The main objective of this process is to modify the shape or size of the meso-channels, which increases the local meso-porosity along with keeping the same macro-V_f. Salvatori et al. [50] incorporated spacers fabricated by 3D printing to plies of a G-weave reinforcement. A stack of five plies was placed in the mold; then, a spacer was deposed on the surface and covered with the other five reinforcement plies. Two types of spacers

were used with two different scenarios: (1) a spacer with a melting point (T_m) higher than the resin processing temperature that withstands the pressure and temperature and contributes to mechanical properties amelioration. (2) a spacer with a T_m lower than the process temperature that collapses and gives a more homogeneous fiber distribution in the mold cavity; it is thus called sacrificial spacers. Figure I.9 A details the spacer design in a 3D form for (a) the unit cell, and (b) the spacer structure. Figure I.9 B shows a cross-section of the fabric-spacer-fabric structure. This study has shown that when a two-step injection strategy is applied (in-plane and through-thickness flow), the addition of sacrificial spacers reduces the impregnation time by 75%. At the same time, the intact spacer resulted in a 20% increase in the bending modulus. The presence of spacers also increased saturated permeability by almost two orders of magnitude compared to the plain fabric. However, the permeability decreased with the increase in the spacer mesh size because of the enhanced fiber nesting. Further investigations should include adding functionalities to the spacers or studying the influence of adding a different solid phase, e. g. micron-scale particles with a homogeneous distribution to avoid fiber nesting.

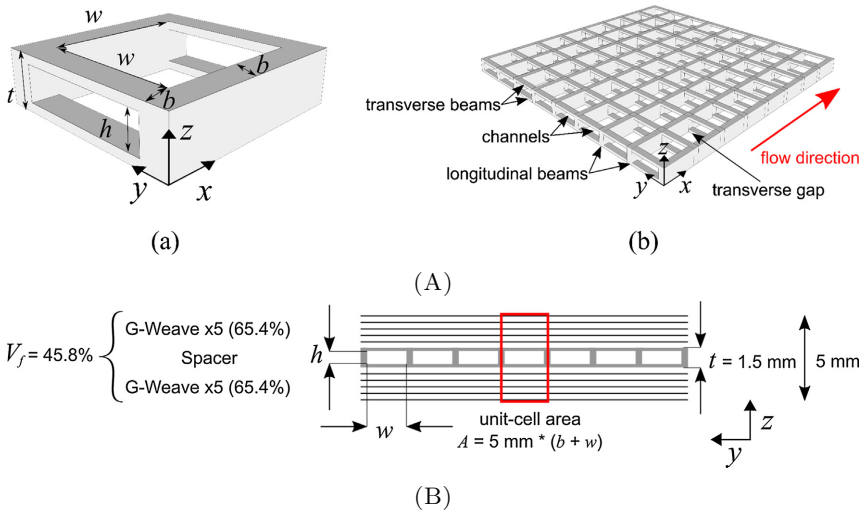

FIGURE I.9: The use of 3D spacers for permeability enhancement, with (A) three-dimensional design of (A.a) unit cell and (A.b) entire spacer with t=1.5 mm, b=1 mm, h=1 mm, and a variable w and (B) Scheme of a cross-section perpendicular to flow of a sandwich-like preform with core spacer, showing local and global fiber volume fraction [51]

I.6.2 Self-healing applications

Manfredi and Michaud [13] investigated the functionalization of plain woven fabric with self-healing microparticles of 125 to 250 μm. The inclusions were sieved manually at the top surface of the fabric. Authors have studied the influence of these inclusions on fabric compaction, flow front advancement and permeability at different particle percentages. Figure I.10 shows the particle deposition on a 2x2 twill weave fabric. These figures illustrate the tendency of inclusions to fall in the interstices of the woven fabric.

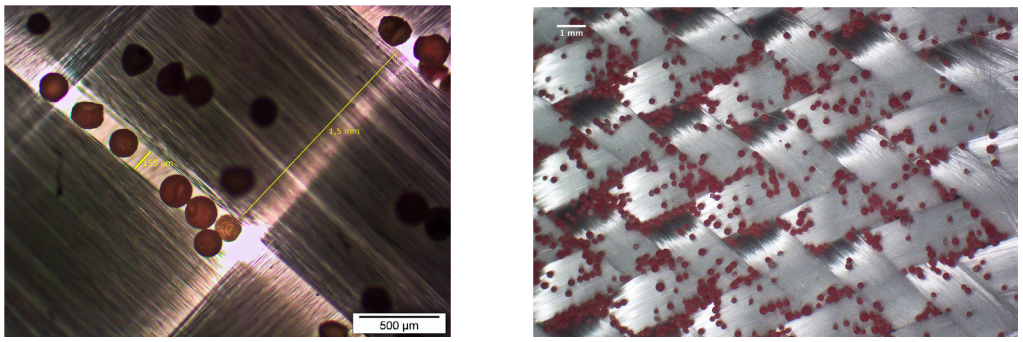

FIGURE I.10: Optical images with the sieved self-healing micro-inclusions, with (a) capsules in the inter-bundle region and (b) deposition of inclusions on the top of fabric [13]

I.6.3 Model particulate inclusions

Caglar et al. [24] conducted a comprehensive experimental study of particle-filled woven fabric. The study contained model glass microspheres of sizes in the range 40-800 μm and volume fractions of 2.5 to 10% (Figure I.11). The authors addressed the effect on fabric permeability and compaction behavior. First, the specific surface area of the porous structure was reconstructed with x-ray microtomography and implemented in Kozeny-Carman's model to estimate permeability. The authors have identified a threshold curve that is related to particle size and fiber content. Two scenarios are observed when particles are added to woven fabric: (i) below the critical particle content; beads tend to fill the existing spaces without much changing the preform behavior and (ii) above the critical particle content, out-of-plane fiber bending and consolidation of fiber bundles may take place with high particles sizes or high particle volume fractions. The study has also shown that the fabric type has a tangible effect on the particle behavior within composites.

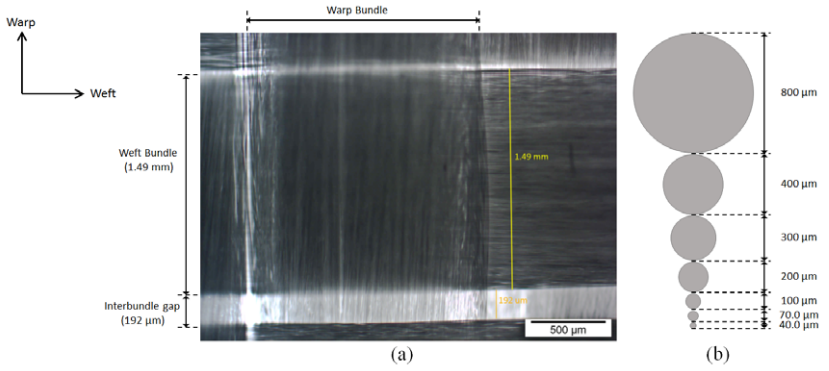

FIGURE I.11: (a) Optical microscopy image showing the typical bundle dimension in weft direction and inter-bundle gap, (b) representative inclusions scaled to the optical microscopy image [24]

I.7 Filtration of particle-filled resin through fibrous media

Filtration is the capture of particles suspended in fluids by the porous medium throughout the flow path. The phenomenon of filtration is studied for a wide range of technological applications that contains separation processes such as water treatment [52, 53], oil and gas field [54], and paper industry. For composite applications, the distribution of particles is a crucial factor that governs the properties of the finished part. Some of the parts are designed to be functionally graded, while others are aimed to acquire homogeneous properties throughout the whole part. Mechanisms that control the filtration and distribution of particles are classified into surface and deep bed filtration. The particle size governs the former type, while the latter is influenced by the interactions induced by particle type.

I.7.1 Filtration types

Figure I.12 shows some of the filtration types explained in this section; cake filtration and deep bed filtration.

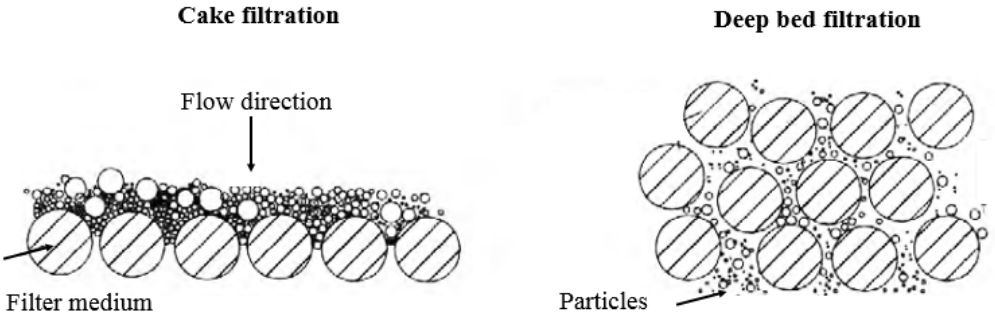

FIGURE I.12: Types of filtration [55]

Cake filtration

The build-up of a particle layer at the external preform inlet or surface is known as cake filtration. It is encountered when the particles have sizes comparable to or greater than the average pore size or when a highly concentrated suspension accumulates on a porous surface. It takes place in two steps; first, the deposition of particles on pores on the filter surface, then the accumulation of suspended particles on the deposited ones. The high deposition of particles accelerates the clogging of the medium.

Deep bed filtration

It takes place when the particle size is smaller than the average inter-pore spacing. In this case, suspensions enter the pores medium and travel through the medium before. Particles are captured inside the fibrous filter due to multiple forces acting on the suspended particles at different depths of the porous medium. It is caused either by mechanical or Physico-chemical filtration. In **mechanical filtration**, the inter-fiber distances are smaller than the particles of the suspension to be filtered. This leads to a fast plugging of the filter due to increased particle deposit. **Physico-chemical filtration** is the deposition of particles under the effect of the particle-particle or the particle-fiber interactions. As a result, particles are prone to stick to the surface of the filter surface. Particles could also form agglomerates on the surface of the previously deposited particles by particle-particle interactions. This could be followed by mechanical blockage of suspended particles in the constrictions.

I.7.2 Forces acting on suspended particles

A suspension is a mixture of insoluble solid particles dispersed in a liquid. Dispersions of particles with at least one dimension of a size ranging from 1 nm to 1 μm are called colloids, with particle sizes starting from 1μm mixtures are called suspensions. During the phase of suspension preparation, prior to the fabrication of functional composites, two main difficulties are encountered: keeping a homogeneous dispersion throughout the process and strong interfacial bonding between particulate fillers and matrix [56]. In addition, different interactions take place in a suspension; they depend on particle and fluid types and particles' relative position and size. The forces acting on particles in a suspension include hydrodynamic forces, Brownian forces, gravity forces, and physico-chemical forces. **Brownian diffusion** is the random motion of particles immersed in the fluid under the effect of shocks with the molecules of the surrounding fluid. Brownian diffusion is present when the particle diameter is less than 1 μm.

Hydrodynamic forces, such as drag and inertia forces, represent the forces exerted by the fluid on particles. They are directly linked to the kinetics of particles and the forces they undergo. The stokes number characterizes the behavior of particles in front of an obstacle. This number is used to predict whether the particle will follow the fluid's motion or collide with the obstacle. Most suspended particles are prone to sedimentation induced by **gravitational forces**. These forces result in phase separation of the particles. Gravitational stability is enhanced by the decrease in the relative density of particles and the suspending fluid, the decrease in the particle size to enhance their Brownian motion or the increase of viscosity of the suspending fluid.

Physico-chemical forces include Van der Walls forces, which are short-range attractive forces between the particles and the surface of the grains constituting the porous

medium and Electrostatic forces, which are the electrostatic charge developed by most of the micron-scale particles. These forces can lead to forming particle agglomerates or separation by repulsion. They depend on the types of fluid, particles and filter material.

According to the force applied on particles, four retention sites are distinguished by Herzig [52]: surface, crevice, constriction and cavern sites. Figure I.13 illustrates some of the encountered filtration mechanisms in granular media [55], these mechanisms can apply to fibrous media.

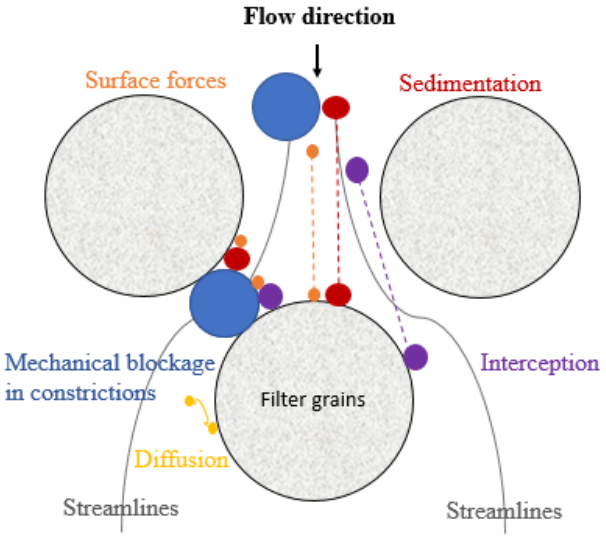

FIGURE I.13: Filtration mechanisms [55]

I.7.3 Dispersion techniques

These methods are applied to obtain a homogeneous dispersion of particles in the suspension. Techniques of dispersion are classified into physical and chemical techniques. Figure I.14 shows a schematic of the two classes of dispersion techniques.

Physical techniques are constituted of direct mixing of suspensions using mechanical force, either with mechanical stir, high shear mixing (HSM) or extruder and ultrasonic agitation. However, mechanical stir has shown a poor dispersion quality for some studies, while the extruder is the most used mechanical dispersion technique. It was proven that the dispersion technique has a strong influence on the sample quality [58].

Chemical Techniques could be classified into three categories: surfactant assistance, polymer wrapping and surface functionalization. Surfactant facilitates the link between particles and liquid. Polymer wrapping envelopes the surface of particles by a specific layer to be compatible with the fluid. Surface functionalization consists of modifying the particle surface to graft chemical groups; it could make particles soluble or link them

with the polymer or liquid. Dispersing agents are added to the suspension in order to limit the sedimentation of the charges.

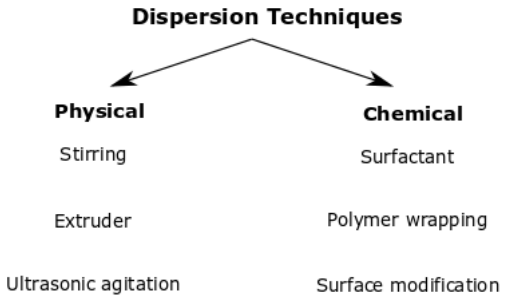

FIGURE I.14: Different dispersion techniques

I.7.4 Effect of particle characteristics on filtration

The particle fabrication process is responsible for its shape and size. The particle type plays a significant role in the determination of the filtration trend.

Particle size

Herzig and Le Goff defined three different classes of particle sizes; particles of a size greater than 30 μm are prone to mechanical filtration, whereas those of size lower than 1 μm are subjected to Physico-chemical filtration. Between these two classes, both mechanisms can take place [59]. However, the particle size does not determine the filtration trend alone; the average pore size of the filter should be considered for a complete conclusion on the subject, as smaller pore sizes enhance the mechanical blockage of the filter at the same particle size. This is demonstrated by Chohra et al. [43] in their analysis of the through-thickness filtration of aluminum oxide and corn syrup suspensions in a woven E-glass fabric. All experiments were carried out at constant particle and fiber content. Only the particle size varied from one test to another from 20 μm to 80 μm. Figure I.15 shows that the smaller-sized particles resulted in the most homogeneous distribution, while the largest-sized ones caused a highly uneven distribution. The authors proposed a model for predicting particle distribution that has shown a good agreement with experimental results. The study has revealed that retained particle distribution depends on the inlet particle granulometry relative to the preform architecture and pore distribution.

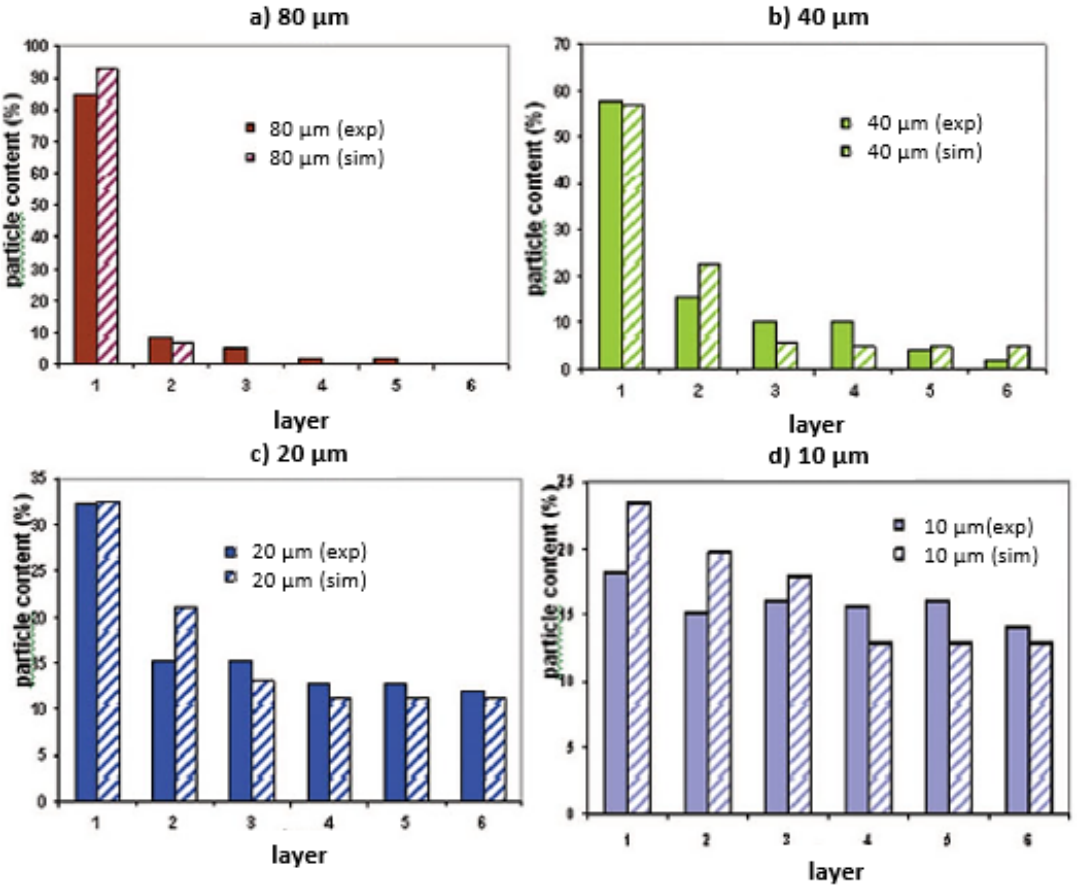

FIGURE I.15: Experimental (plain) and simulation (hatched) results for the influence of particle size on filtration, for particles of sizes: 80, 40, 20 and 10 μm [43]

Particle shape

The particle shape affects their filtration from different aspects. First, the non-uniform shape of particles enhances their capture by the fibrous structure due to mechanical filtration. Second, non-uniform particles increase the carrying fluid viscosity, enhancing their filtration. The shape of particulate fillers also plays a major role in determining the properties of the final part; the increase in the particle aspect ratio improves some of the mechanical properties [11].

Particle concentration

A number of studies have found that the initial concentration of suspensions does not influence the filtration trend, both experimentally [36] and numerically [35]. This quantity determines only the local particle content. When a higher amount of particles is required along the part length, adjusting the injected suspension concentration is recommended. However, future studies should further verify the influence of particle concentration on the filtration behavior with micron-scale particles.

Several recent studies have questioned the addition of micron-scale particles to resin or fabric through porous media experimentally in LCM processes. Some of these studies are presented in Table I.2, which shows the materials used for each study, the particle dispersion and characterization methods.

TABLE I.2: Materials and characterization of particle filled composites in the literature

Research	**Lefevre et al.** [60]	**Shaker et al.** [8]	**Chohra et al.** [43]
Resin/Test fluid	Polyester/DOP	Vinylester	Vinylester/Corn syrup
Particles	ATH, glass, Ceramic	SiO_2	Aluminum Oxide (Al_2O_3)
Reinforcement	Mat and Synthetic felt	Woven	Woven
Dispersion method	Manual dispersion	Mechanical stirring	-
Characterization	Calcination	Dilatometry	Rinsing +particle weighing
Research	**Fernberg et al.**[25]	**Nordlund et al.**[39]	**Manfredi and Michaud** [13]
Resin/Test fluid	Polyester	Polyester/Glycerol solutions	Silicon oil
Particles	ATH	ATH and Fluorescent	Self-healing microcapsules
Reinforcement	Woven	NCF	Woven
Dispersion method	-	-	Manual sieving
Characterization	Optical microscopy	μPIV and Optical microscopy	Optical microscopy and permeability

I.8 Numerical simulations of filtration

The filtration problem is governed by coupling the flow of suspensions through fibrous media and the transport and retention of the suspended particles by the filter. Therefore, numerical simulations help understand the complex phenomena of the filtration process and saving the time spent in experimental investigations. Numerical filtration studies can be classified according to the fibrous medium to macroscopic models that deal with the medium as a homogeneous entity of a macroscopic porosity ϵ and investigations that follows the trajectory of single particles.

I.8.1 Particle trajectory analysis

A numerical simulation was carried out by Haji et al. [61] for the study of flow and filtration of suspensions through dual-scale fibrous media in LCM processes. Three sub-models were presented in this study: a flow sub-model for describing the flow of suspension in the micropores using the Stokes–Darcy coupling, a solid sub-model for modeling the particle dynamics during impregnation using the equations of motion of each particle and particle-fluid mixture. A filtration sub-model based on the model of Lefevre [60] is dedicated to simulating particle capture through the porous medium. The rheological behavior of the suspension is modeled by the Carreau empirical model to consider both Newtonian and non-Newtonian behaviors. The geometry, the injection strategy, the initial and boundary conditions are presented in Figure I.16 A.

Figure I.16 B plots the part of the results of flow and filtration behaviors at the end of impregnation. It was found that the specific deposit σ increases near the inlet then decreases continuously toward the outlet. The accumulation of particles decreases the

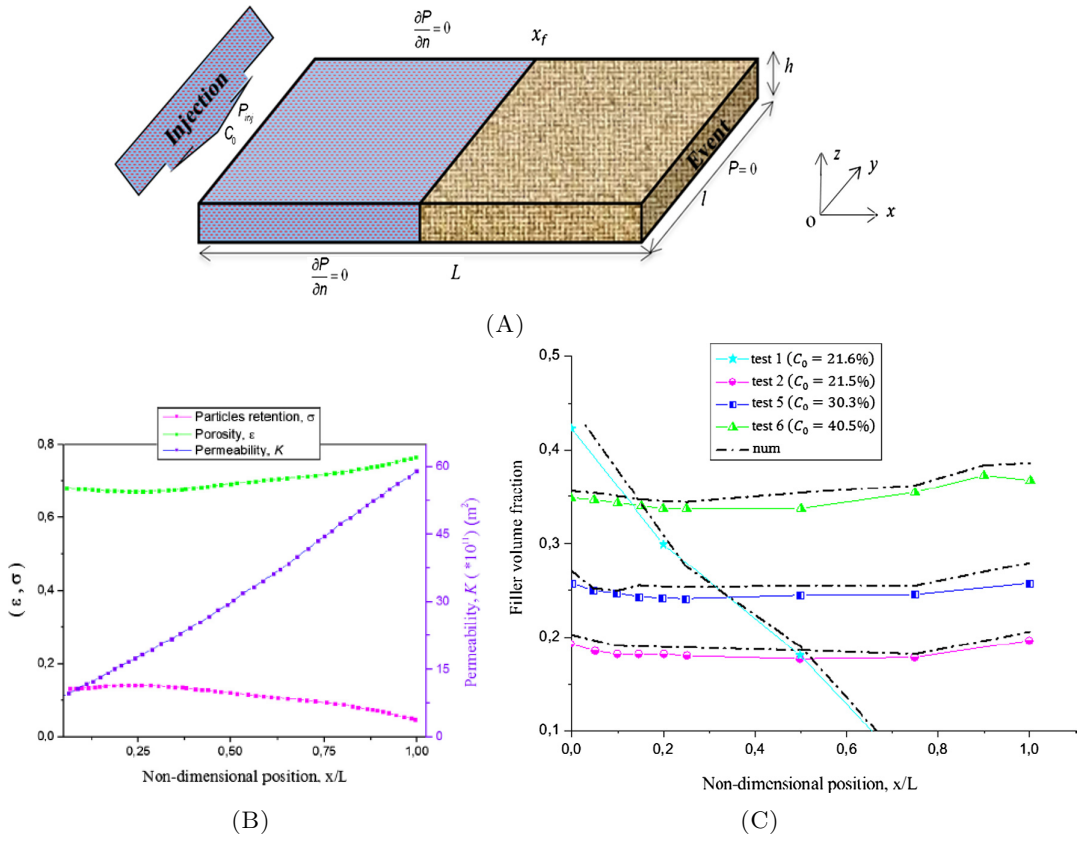

FIGURE I.16: Problem definition and simulation results, with (A) injection and boundary conditions, (B) evolution of particle content and resin viscosity with flow path and (C) Particle content vs flow path, a comparison with experimental results [61]

porosity of the medium; hence it is minimum at the preform inlet and increases toward the end of the preform. A quasi-linear increase of permeability is noticed along the part length proportionally to the evolution of porosity. The numerical results of the proposed model were compared and validated with experimental results from the literature. Comparison to the experimental results has shown a good agreement (Figure I.16 C) for the profiles of the spatial particle distribution carried out with four tests.

The perspectives of this study included defining new experimental methods to quantify the concentration of fillers during the injection, which will help to understand the different physics of the complex filtration process.

The numerical study of Hwang et al. [62] tackled the flow and deposition of particles in dual-scale permeable porous media in LCM processes using the level-set finite-element method. The developed model described a single particle trajectory by taking into account the hydrodynamic particle-fluid interactions near the wall of the porous domain. A Stokes-Brinkman coupling describes the flow, and a fictitious domain approach models the freely suspended particles. Filtration simulations with a single particle are carried out to investigate the effects of permeability, particle size and pressure drop on particle deposition. Through the analysis of velocity fields, the mechanisms of particle deposition were identified. Figure I.17 A illustrates the effect of particle size on its deposition with

the radii 10, 20 and 30 μm starting their movement from the same position. The term decoupled in the figure denotes using the conventional trajectory determined by integrating the unperturbed velocity without particles. It was found that larger particles are deposited earlier than the small-sized ones because they collide to the medium first. Filtration simulations of a suspension with 500 particles are performed to validate the effectiveness of the used approach. Figure I.17 B presents the simulation results for 500 randomly injected particles of a radius of 20 μm in a porous medium constituted of three elliptic tows. Only 17 particles out of 500 were deposited on the middle surface of the central tow, whereas other particles pass through tows to the outlet. Once particles are captured at one tow surface, the transport of particles through the neighboring regions of the same tow increases. This results in the formation of a particle layer at the tow surface. Further analysis should focus on performing a parametric study for exploring the influence of the tow size, permeability and initial particle concentration.

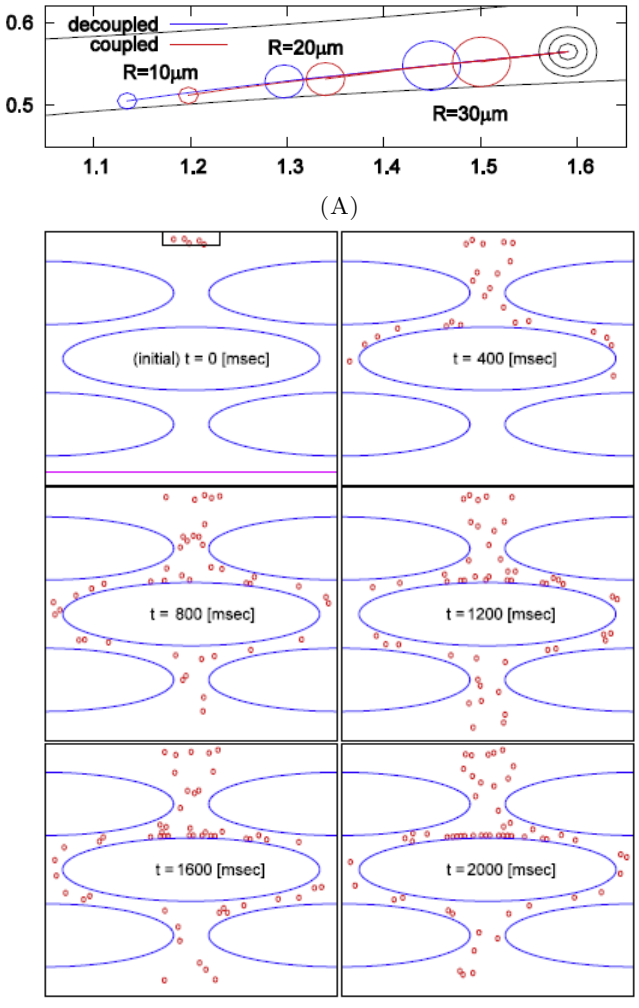

FIGURE I.17: Numerical results on particle distribution in a dual-scale model, with (A) Effects of the particle with a single-particle injection and (B) randomly inserted 500 particles of a fixed size the radius 20 μm for 2 s [62]

I.8.2 Macroscopic simulations

The work presented by Erdal [35] studies the fabrication of ceramic-ceramic composites. A preceramic polymer (PCP) resin filled with SiC type particles is infiltrated through a fibrous preform throughout the process. The macroscopic filtration model developed by Erdal [35] treats the constituents of the problem as three entities: the polymer, the filtered particles and the suspended particles. The flow and filtration models are coupled through the flow velocity, permeability and suspension viscosity. To consider the moving flow problem and the mold shape irregularities, the solution was based on a boundary-fitted coordinate system (BFCS). Governing equations are discretized using the finite difference method (FDM) with dynamic mesh generation. The coupling between flow and filtration is modeled by equations solved at each node of the system and for each time step. The system of equations proposed by Erdal is presented in section VI.4.4.1 of this work.

The model simulates the unidirectional flow of suspensions through the part length and explores the evolution of flow and filtration variables. Figure I.18 shows one of the simulation results for the spatial particle distribution in a 2D part (I.18 A) as a function of the preform permeability (referred to as K_0 in the figure) at the end of impregnation. Results show more homogeneous particle content through the length with higher permeability values. Figure I.18 B illustrates the flow front contour in an irregular shape part impregnated with particle-filled resin.

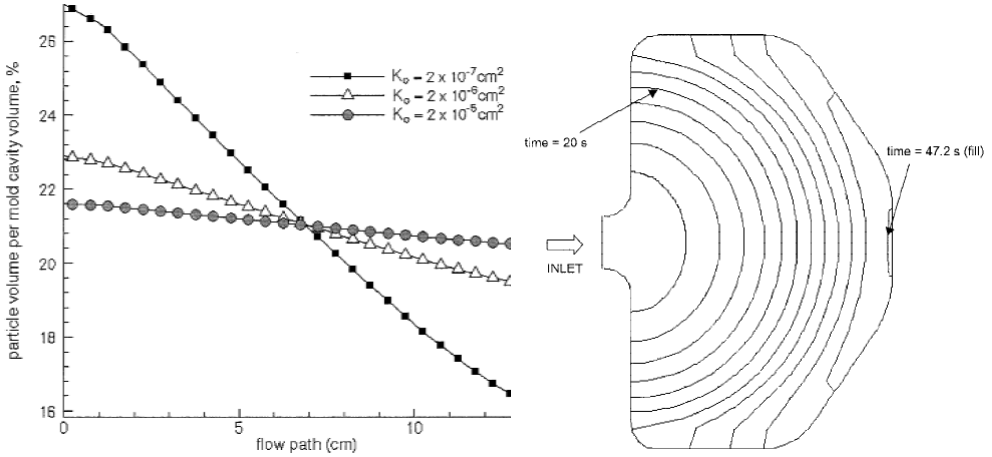

(A) (B)

FIGURE I.18: Numerical simulation results showing (A) Particle content vs flow path and (B) Flow front advancement in an irregular shape part [35]

This work determined the relations between processing conditions to filler distribution numerically. However, for future studies, the authors have recommended the determination of variables interdependencies experimentally and the validation of the model with experimental results.

Sinem Sas and Erdal [63] extended the model developed by Erdal to simulate the CRTM process using a different simulation tool. The process model constituted of two steps: injection and compression (Figure I.19). During the injection stage, suspension flows into the mold, which is partially closed. The modeling of this stage is the same as the RTM simulation. During the second stage, the inlet is closed and the preform porosity changes due to the compression and the subsequent deformation of the flow domain. The simulation is performed in the commercial software Comsol multiphysics through a coupling between flow and filtration models.

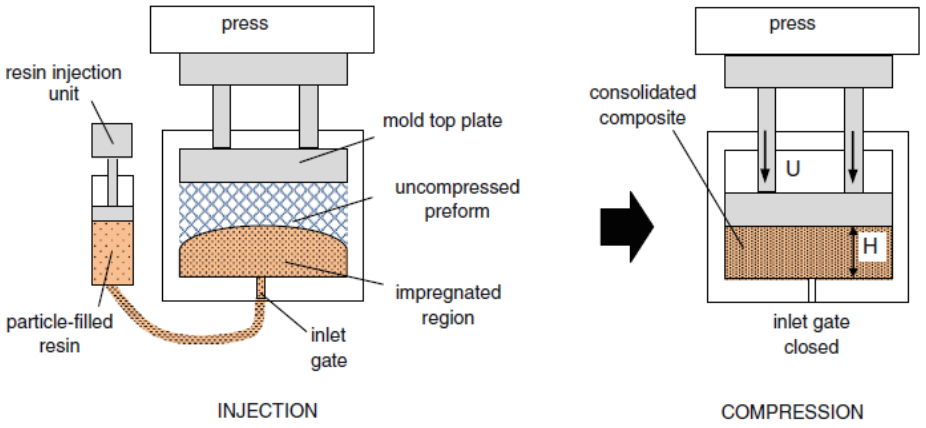

FIGURE I.19: Injection and compression phases of the particle-filled CRTM Process [63]

The authors compared the particle distribution with RTM and CRTM processes. Figure I.20 shows the spatial particle content at the end of impregnation with the two processes injected at different injection flow rates. It was found that better particle distribution was attained with the CRTM process. Lower injection flow rate resulted in a slightly better particle distribution in CRTM process. The numerical results of this study were compared to analytical solutions and experimental results from the literature. Evidence from this study has shown that the CRTM process exhibits a more homogeneous particle distribution. The study highlighted that the anisotropy of the preform did not influence the particle distribution homogeneity. The developed simulation tool can be used to explore other injection scenarios and mold configurations. However, further analysis of the RTM process is needed to help distinguish the most influencing parameters using the same simulation tool.

Based on the model proposed by Erdal, Shaker [8] performed a series of simulations using the Finite element commercial software COMSOL Multiphysics. The authors have modeled the flow and filtration process along with an experimental validation conducted with ceramic micro-particles. Experiments were carried out by injecting suspensions with different initial concentrations into the fibrous medium cavity using line injection under vacuum action. The model has successfully predicted the particle distribution, and the numerical results agreed to the experimentation. The flow is modeled with Darcy's law;

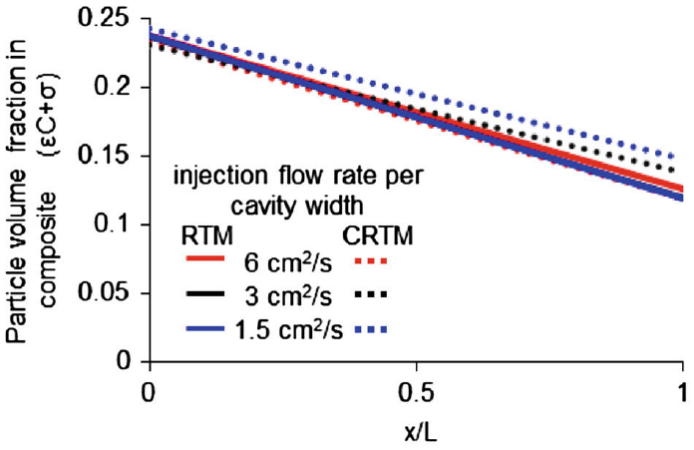

FIGURE I.20: Effect of injection flow rate on particle distributions in the mold at the end of the process with RTM and CRTM processes [63]

the concentration and the filtration kinetics are represented with two differential equations implemented in COMSOL. The level set function tracks the flow front movement. Figure I.21 plots the particle content evolution along the part length at different instants of time for a suspension of 2% of initial filler content in volume. A progressive increase in the particle content is observed at all the positions with time. This study also highlighted the increase of impregnation time with the increase of particle concentration in suspension.

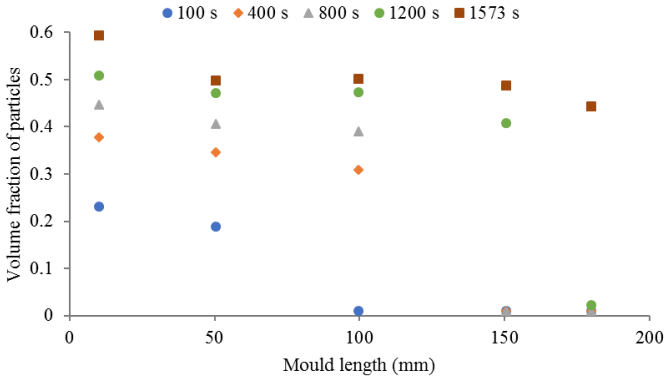

FIGURE I.21: Spatial particle distribution at different instants of time [8]

This work related the ceramic particle distribution to the coefficient of thermal expansion (CTE) of the cured sample. Good accordance was found between numerical and experimental results. However, the implementation of flow and filtration models in COMSOL Multiphysics software is interesting as it offers strong coupling capabilities and a user-friendly interface. Further numerical investigations are needed using the same approach to determine the main filtration parameters using the experimental results.

The experimental investigation of filtration presented by Lefavre et al. [60] was followed by macroscopic modeling and simulation for the suspension flow and retention of particles. The modeling stage was constituted of solid coupling between flow and filtration

sub-models through a continuous update of material properties. Darcy's law was used to model the suspension flow. The filtration model is based on Herzig's model [52] derived for the analysis of filtration in water treatment applications. It is constituted of a filtration kinetic equation and concentration conservation equation, in addition to equations for modeling the change in the medium porosity and the liquid deposit between particles. Suspension viscosity and permeability are evaluated and updated at each time step because of their continuous spatial and timely evolution with particle deposit.

This model was implemented in the commercial software COMSOL Multiphysics along with MATLAB. The model shows good agreement with the experimental results in terms of particle content and successfully predicted the evolution of the other filtration variables. Figure I.22 decomposed the overall particle content ψ to suspended ϵC and retained σ particles at the end of impregnation.

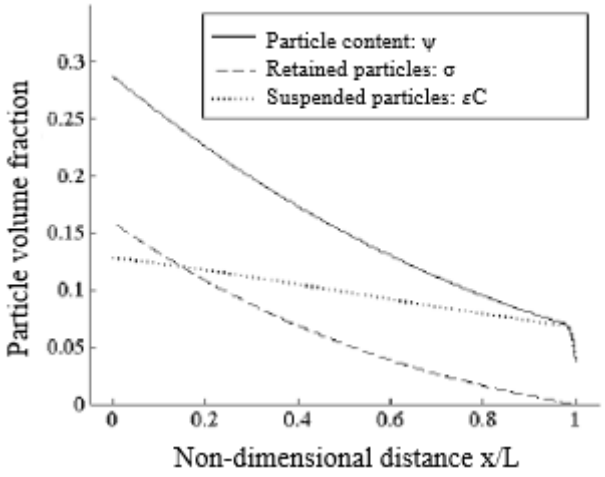

FIGURE I.22: Spatial distribution of particle content at the end of an experiment with C_0=20% [6]

Lefevre has suggested several perspectives for the continuation of this work:

- improving the proposed rheology model,
- extending the model to 2D geometries,
- working on the direct determination of the physical input parameters of the model without having to resort to the experimental identification of the parameters,
- studying the influence of particle size on the parameters of the model,
- taking into account the double-scale porosity.

The presented macroscopic models provide a good estimation of the final particle distribution at the end of the impregnation process, which is one of the biggest challenges in processing functional composites. Furthermore, these models can be easily used for

validation with macroscopic experimental tests. In addition to the perspectives drawn by each work, an intriguing area in this field is the determination of the filtration parameters. Further studies need to be done to help estimate these parameters as at variable process and material variables with the help of numerical methods and experimental results.

I.9 Conclusion

This chapter outlined the fundamental notions and terminology used for the study of the fabrication of particle-loaded composites. It presented a short description of the constituents of composite materials and processing techniques. Attention was drawn to LCM processes which are increasingly used for the fabrication of functional composites. The importance of these composites is highlighted along with the presentation of the functionalization methods and applications throughout previous studies.

The functionalization of the preform and resin were among the most used methods for particle addition to composites. However, particle incorporation adds several challenges during the impregnation process. The drawbacks included a drop in the fabric permeability and an increase in the fluid viscosity. The combination of these effects induces a non-homogeneous distribution of particulate-fillers throughout the flow path for both longitudinal and transverse flow. The evidence from this review implies that controlling particle distribution is one of the most crucial challenges for the manufacturing of functionalized parts, either designed for homogeneous or functionally graded distributions. The chapter also reviewed some of the experimental studies on the filtration of inclusions by fibrous preforms. The main sampling and characterization methods of particle content for both cured composite samples and suspensions are reported and the filtration types and mechanisms are introduced.

Despite its interest, filtration has not been sufficiently covered from an experimental perspective, especially with micron-scale particles. There is still a need to explore the influence of process and material variables on the particle capture, which will help control and tailor the particle content through the part length at the preform and the tow scales. The presented results from the literature recommend using an improved non-destructive technique to extract particle content associated with a trusted measurement method for particle content characterization. Due to the high variable interdependency, it is important to characterize first the effect of particle incorporation on the flow process at homogeneous distribution and fixed size.

The chapter presented some of the numerical studies for single-scale and dual-scale media. The flow and filtration models implemented in most of the numerical simulations will be detailed in chapter VI. However, some filtration models need to be further validated experimentally. These models also include several filtration parameters that can

not be determined directly and need to be estimated from experiments at the different process and material variables. Further analysis should focus on determining the physical input parameters of the filtration model without having to resort to the experiments. Moreover, the determination of variable interdependencies should be covered with the help of experimental characterization and numerical simulations.

Many researchers have tackled the subject; however, there is still a gap concerning the physical understanding of the particle addition techniques and their influence on composite processing. This study focused on the liquid composite molding (LCM) processes, with two distinct particle addition techniques: fabric and resin functionalization. An extensive experimental study will identify the key parameters that influence finished part characteristics for two particle addition methods. First, the particle distribution will be fixed by the pre-deposition of fillers on the preform surface, and the influence on the permeability and fabric compaction will be studied. Second, the particles are dispersed in the liquid resin and the interdependencies of process parameters and variables are analyzed separately. A focus is drawn on the influence of selected quantities on particle distribution at the preform and the tow scale. The experimental characterization will focus on the influence of particle addition on the parameters that control the flow process, e.g., resin permeability, resin viscosity, and their filtration and distribution in the fibrous medium. The experimental study is followed by a series of numerical simulations for the tested filtration cases. After the parameter identification step, the simulation will be tested with new scenarios to validate the method's effectiveness.

Chapter II

Material characterization

II.1 Introduction

The first chapter presented an overview of the researches conducted on particle addition to composite materials using LCM processes. The current chapter seeks to present all the constituents used for the experimental investigation of particle addition. The characterization of particle size, shape, and rheological behavior of suspensions is mandatory for composites processing. Robust characterization of these materials is fundamental to predict their behavior during the process, to achieve the optimum performance and the highest manufacturing quality. The properties of the reinforcement, model fluids, curing resin and particles are detailed hereafter. For each material, the adopted testing method and the used experimental set-ups and devices are presented.

Several materials are used to study the influence of particle addition on flow and filtration in LCM processes throughout this work. The choice of materials used in this study has been made to transport composite applications, where micron-scale inclusions are often added to bring new functionalities to the finished part. A dual-scale fabric was chosen to constitute the fibrous medium. Fillers or particles are generally chosen in line with the functionality needed in the finished part. Model particles of different types and sizes in the order of micrometers are characterized and used following different methodologies. The functionality of particles is not addressed in this research. The carrying fluid is varied between model fluids for testing purposes and curing resin for composite fabrication. The key objectives of this chapter are:

- providing a detailed description of all the materials used in the experimental investigations of this work,
- presenting the testing methods and set-ups of the used materials and identifying the behavior of neat fabrics and pure liquids,

- characterizing suspensions of particles and model fluids at different particle volume fractions.

Throughout the experimental studies presented in the chapters III to V, different materials are used depending on the testing method and objectives. Textile, particles, model fluids and curing resins used for each investigation, as well as their properties and characterization, experimental set-ups are addressed in the coming sections. The ranges of the explored material-related parameters are detailed in each chapter.

II.2 Fabric

The same type of fabric has been used for all the experimental investigations of this study to avoid the variability in results that arise from the type of the reinforcement structure and focus on investigating other variables such as the fiber content. The used fabric is a 96% quasi-UD E-glass fabric from Chomarat. A key advantage of using this type of fabric is the possibility of keeping a dual-scale porous medium, along with obtaining a continuous network of flow channels for fiber volume fractions (V_f) up to 50% [64]. This is extremely important for the study of particle transport through the flow domain. Also, the use of this type of fabric results in robust mechanical properties due to its continuous and aligned fibers. The properties of the fabric are presented in Table II.1. Tows have an average thickness of 0.5 mm in the loose state. Stitches bound tows and keep them aligned in one direction. Figure II.1 illustrates a microscopic observation of the fabric. Properties of textiles are affected by several parameters such as fiber density, areal and lineal weight (see Table II.1). Characterization of the preform requires the determination of their fiber content, compression behavior and permeability. The determination of these quantities is detailed hereafter.

TABLE II.1: Properties of the E-glass fabric

Type	Areal weight (g/m^2)	Lineal weight (Tex)	Fiber mean diameter (μm)	Fiber density (g/cm^3)
Quasi-UD	646	1200	17.4±0.2	2.54

II.2.1 Areal weight A_w

The areal weight of a fabric is the mass of the fabric divided by its area. For the calculation of A_w, ten samples of fabric are cut with the dimensions 10x10 cm^2, each sample is weighed using a precision scale, and the A_w is calculated using the formula:

$$A_w = \frac{m_f}{A_f} \tag{II.1}$$

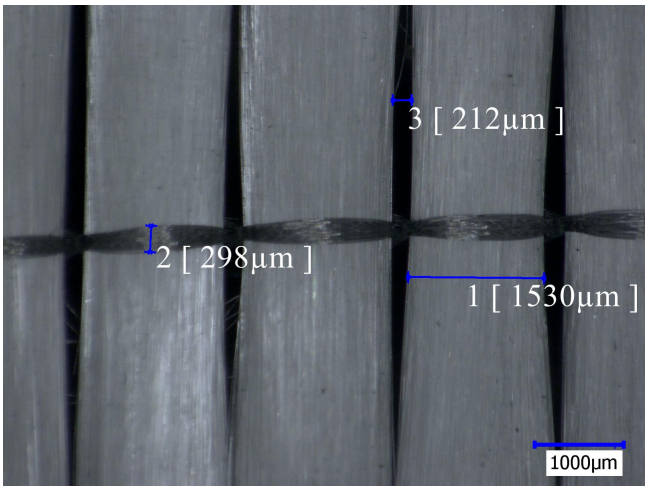

FIGURE II.1: Quasi-unidirectional fabric

Where m_f and A_f are the mass and area of the textile sample respectively. The value of A_w for the used fabric is 646 g/m^2 (from technical data sheet).

II.2.2 Fiber volume fraction V_f

The V_f controls the percentages of micro and macro voids in the inter-tow and intra-tow regions. For the same quasi-UD fabric used in this study, Bizet [64] compared the surface percentages of micropores and macropores for different V_f values. Figure II.2 shows the micrographs taken for cross-sections of composite panels fabricated using the RTM process with fiber volume fractions of (a) 44.1%, (b) 52.7%, (c) 59.7% and (d) 67.7% respectively. Results reported a decrease in the surface rates of micropores and macropores with the increase of fiber content. It was also found that the interconnection between macropores is highly controlled by the V_f. A very low percentage of macropores is noticed for the highest V_f (67%). The fiber content V_f of each configuration is calculated by Equation II.2.

$$V_f = \frac{nA_w}{e_f \rho_f} \tag{II.2}$$

where n is the number of plies, e_f is the mold thickness and ρ_f is the fiber density.

II.2.3 Compression behavior

LCM processes combine the compression of fibrous reinforcements and fluid flow [65]. A proper characterization of the compression behavior helps to understand the deformability of the fibrous structure under pressure. The intra-tow and inter-tow friction ensure their cohesion. Each reinforcement type has a limit after which the tow and fiber

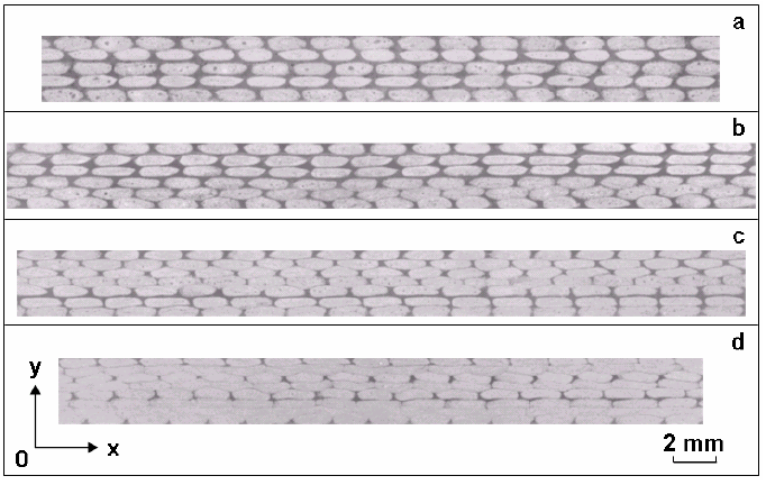

FIGURE II.2: Optical micrographs of composite cross-sections at V_f of (a) 44.1% ; (b) 52.7% ; (c) 59.7% ; (d) 67.7% [64].

displacement takes place and the V_f starts to increase remarkably. Therefore, the compressibility of the dry quasi-UD fabric is investigated to characterize the influence of pressure on the evolution of the fiber content and the total fabric thickness.

Experimental set-up

Instron 5582 universal testing machine with a maximum load capacity of 30 kN is used for compression testing. The set-up is constituted of two flat compression platens mounted on the machine. Bluehill software is connected to the testing unit for data acquisition and analysis. Figure II.3 illustrates the machine and sample placement within the compression platens.

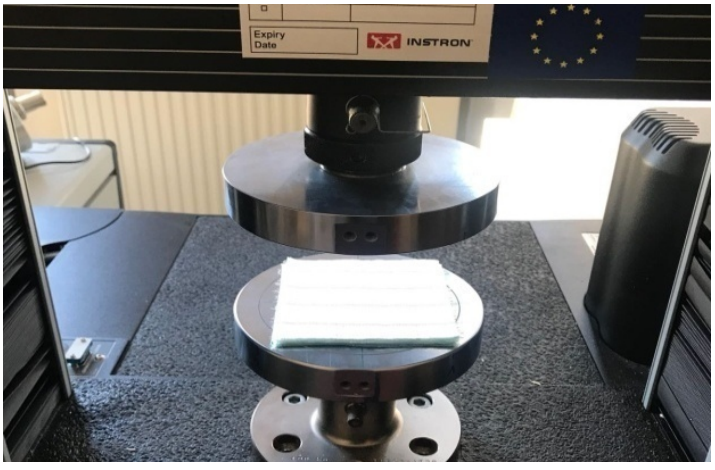

FIGURE II.3: Placement samples of the quasi-UD fabric within the compression plates of the universal testing machine Instron 5582

Six plies of 10 X 10 cm^2 samples of the dry quasi-UD fabric were cut and stacked in the lower plate for testing. The upper platen displacement was set to a speed of

0.24 mm/min. The pressure is applied gradually from 0 to 1 bar. Figure II.4 presents the displacement traveled by the upper platen under the applied force (II.4 A) and the evolution of the fiber content (II.4 B). As a result of platen displacement from -4 to -3.2 mm, the thickness changed from 3.3 mm to 2.1 mm, giving a maximum displacement of 1.2 mm. The experiment revealed that the dry reinforcement has begun to be compressed at around $V_f = 45\%$ to the maximum fiber content (around 59%) at 1 bar. It was found that the fiber content increased with the applied pressure, while the overall stack thickness decreased following a power law. The increase in the fiber volume fraction and the thickness of stacks are caused by the flattening, the displacement and the re-arrangement of fiber-tows relative to each other as a function of the applied pressure [66].

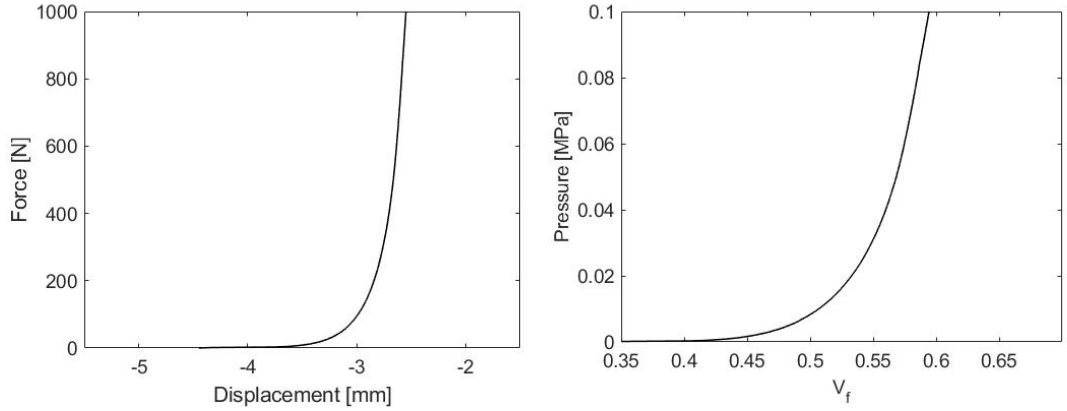

(A) (B)

FIGURE II.4: Compaction behavior of the fibrous reinforcement: (A) displacement under the applied force and (B) evolution of fiber content with pressure

II.2.4 Permeability measurement

An RTM set-up designed for linear injections is used for permeability measurement experiments. For all the tests presented in this section, the neat fibrous medium is impregnated with pure model fluids (without particles).

II.2.4.1 Experimental set-up

The testing facility is constituted of the permeability measurement bench, the acquisition system and the weighing systems.

Mold and injection unit

The experiments were performed in the permeability measurement set-up illustrated by Figure II.5 A. The mold consisted of Pyrex glass top and steel bottom, with cavity

dimensions: 615 mm length, 120 mm width with an adjustable thickness. A silicon joint was placed between the mold and the stack to minimize the risk of race-tracking. Silicone oil was injected into the mold cavity at constant pressure from the injection unit Hypaject (Plastech T.T.), designed for constant pressure injections for values up to 7.0 bar. The outlet fluid is weighed by a Denver Instrument balance with an accuracy of 0.01 g for a maximum mass of 400 g. Plies of the preform were stacked in the mold cavity (Figure II.5 B) along the fiber direction. The preform was of 296 mm length, 100 mm width and 2.85 mm thickness.

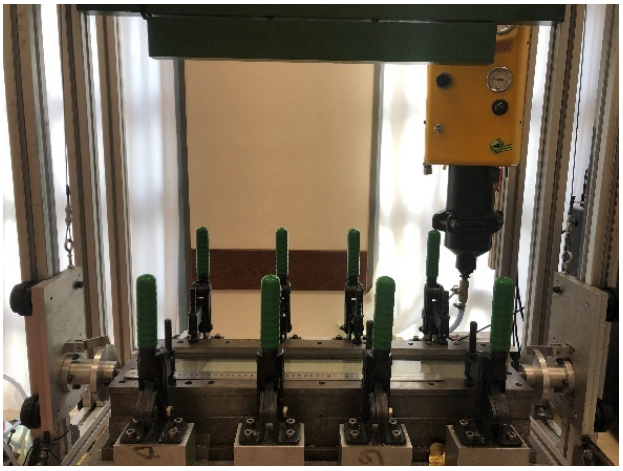

(A)

(B)

FIGURE II.5: The experimental set-up, with (A) the permeability measurement bench and (B) the mold cavity

Monitoring and acquisition systems

Eight pressure sensors are installed at the bottom of the mold at regular distances. The time evolution of pressure at each sensor is visualized with LabView 8.5.1 through an acquisition system. The pressure sensors measure the relative pressure (absolute pressure- atmospheric pressure). The mass readings were acquired by the Pinnacle USB 1.2 software. The flow front advancement is recorded by a camera. Images obtained

from the injection process video are processed in Aphelion software to deduce the flow front positions with time.

II.2.4.2 Unsaturated permeability

Several methods were proposed for the determination of the unsaturated permeability of a fibrous medium in LCM processes. These methods are based on the measurement of flow front advancement throughout the part length with time during the transitory phase.

Squared flow front method (K_{SFF})

It is based on the square of flow front position x_f^2 plotted against time. The slope m of linearity fit (x_f^2 =f(t)) is used in the Equation II.3 for the determination of the unsaturated permeability value [67]. This method is widely used for in-plane unidirectional flow injected at constant pressure [13].

$$K_{SFF} = \frac{m(1 - V_f)\eta}{2P_0} \tag{II.3}$$

where η denotes the viscosity and P_0 is the injection pressure.

Three measurement methods were proposed by Ferland et al. [68] to determine the evolution of the unsaturated permeability with time. These methods are based on Darcy's law adapted to a one-dimensional flow at a constant injection pressure: the elementary method, the interpolation method and the single point method.

Elementary method (K_{ELE})

It consists of calculating the average of the flow front positions as a function of time. By a three-point linear interpolation calculation, the front velocity is determined by Equation II.4.

$$v(t_i) = \frac{1}{2}\left[\frac{x_f(t_{(i+1)}) - x_f(t_i)}{t_{i+1} - t_i} + \frac{x_f(t_i) - x_f(t_{i-1})}{t_i - t_{i-1}}\right] \tag{II.4}$$

The apparent permeability is then deduced for each time step by implementing the velocity $v(t_i)$, the viscosity of the fluid η, the porosity ϵ and the pressure gradient in Darcy's law (Equation II.5).

$$K_{ELE} = \frac{\epsilon\eta v(t_i)}{\frac{dP}{dx}} \tag{II.5}$$

Interpolation method (K_{INT})

It combines Darcy's law with the mass conservation equation as follows:

$$K_{INT} = \frac{\epsilon \eta D^2}{2} \tag{II.6}$$

By applying the least squares method we obtain:

$$D = \frac{\sum x_f(t_i)\sqrt{I(t_i)}}{\sum I(t_i)} \tag{II.7}$$

with the term I(t):

$$I(t) = \int_0^t P_0(t)dt \tag{II.8}$$

P_0 is the pressure at the inlet (x=0 m).

Single point method (K_{SP})

It determines the permeability at each flow front position point with the Equation II.9 from the pairs $(x_f(t_i), I(t_i))$.

$$K_{SP} = \frac{\epsilon \eta x_f^2(t_i)}{2I(t_i)} \tag{II.9}$$

An example with one of the experiments is presented hereafter. Figure II.6 plots the flow front kinetics for the experiment conducted at constant injection pressure of P_0= 1.2 bar. The preform had a fiber content of 53.1%. The mold dimensions are 100 mm width, 296 mm length and 2.63 mm thickness. Silicone oil (Rhodorsil 47V100) with a viscosity of 0.1155 Pa.s (at 20 $°C$) was used as a model fluid. The unsaturated permeability is calculated according to the three presented methods (elementary, interpolation and single point methods). The evolution of x_f, x_f^2 and the flow front velocity are presented respectively in the Figures II.6 A, II.6 B and II.6 C.

The evolution of the unsaturated permeability values K_{ELE}, K_{INT} and K_{SP} with the preform length are presented in Figure II.7.

From Figure II.7, it can be observed that K_{ELE} shows the most variations with the length. The most remarkable fact is that the three permeability values converge near the end of the preform. The interpolated permeability K_{INT} has a unique value along the preform (Equation II.6). Therefore, it will be used for the determination of K_{unsat} throughout this study.

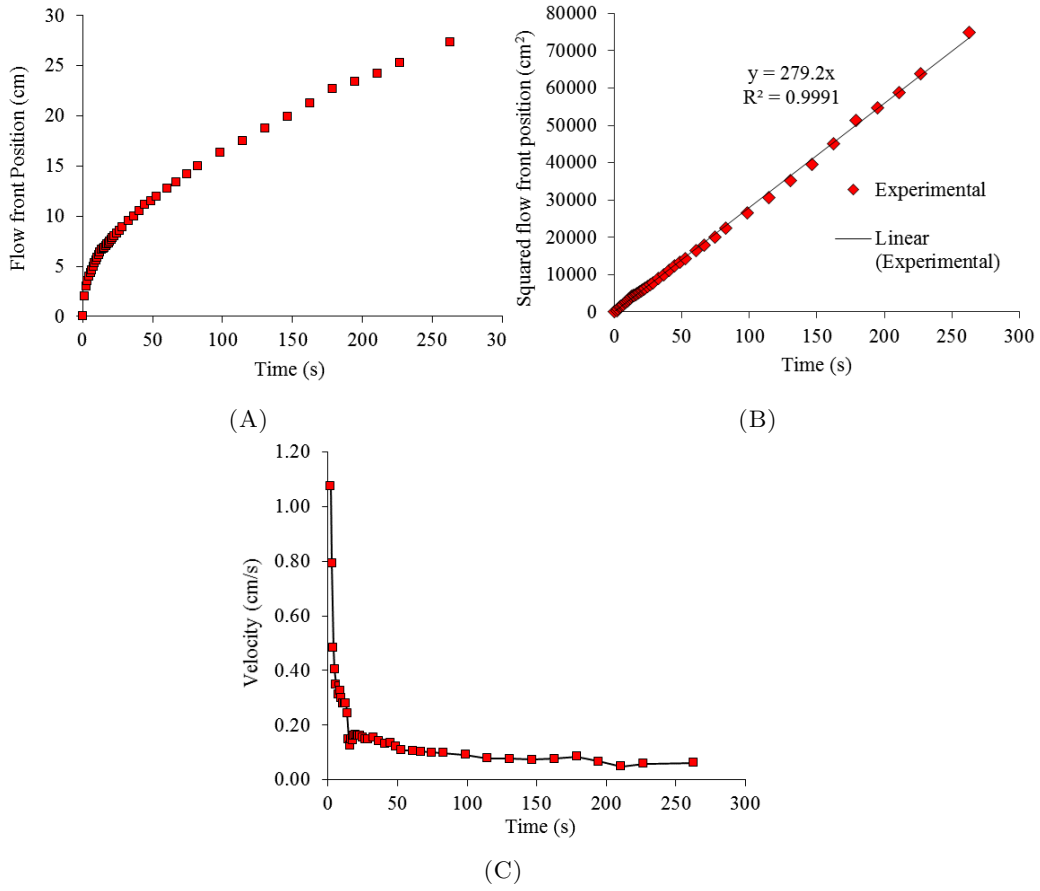

FIGURE II.6: Evolution of flow kinetics with time (A) flow front position, (B) squared flow front position and (C) flow front velocity

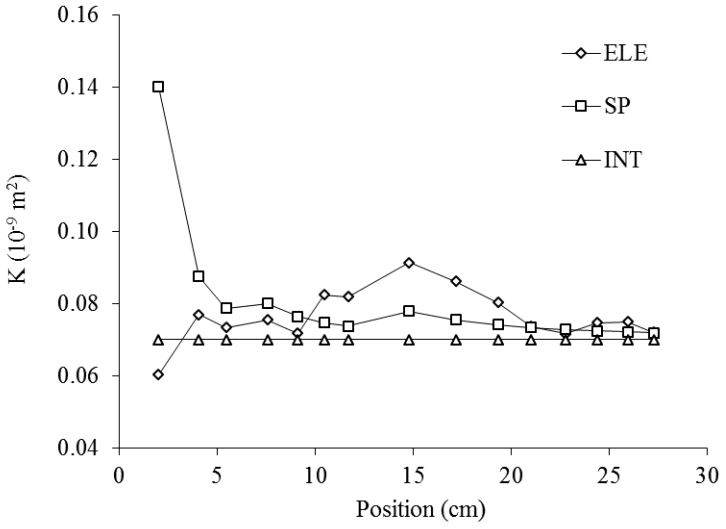

FIGURE II.7: Unsaturated permeability values using the elementary method, the interpolation method and the single point method

II.2.4.3 Saturated permeability

The saturated permeability is measured after the full impregnation of the preform. It is given by Darcy's law as follows:

$$K_{Sat} = -\frac{L\eta}{A}\frac{Q}{\triangle P} \tag{II.10}$$

A is the cross-section area of the flow domain, L, length of the preform, Q, the volumetric flow rate and $\triangle P$, the pressure gradient between the injection point and vent. The volumetric flow rate Q is deducted from weighing the outlet fluid using the scale (Denver Instrument balance) at constant time intervals for several pressure values. Data of mass is registered with the help of Pinnacle USB 1.2 software. The mass flow rates are plotted against the pressure values and the slope of $Q = f(\triangle P)$ gave an average of the ratio $Q/\triangle P$ in Equation II.10. The saturated permeability is calculated for different V_f values

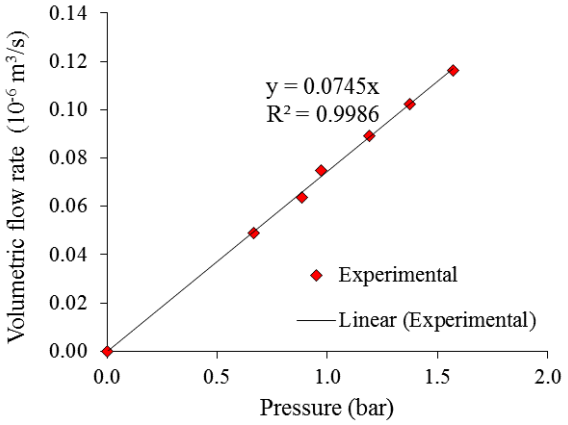

FIGURE II.8: Identification of the slope $Q = f(\triangle P)$

of the Q-UD fabric. The V_f is varied by the adjustment of the mold thickness and the variation of the number of plies. In this part, the steps of the saturated permeability calculation for the same experiment of section II.7 are presented. The volumetric flow rates are calculated at pressure values of 0.7, 0.9, 1, 1.2, 1.4 and 1.6 bar, respectively. Figure II.8 shows the plot Q versus $\triangle P$.

The same methodology is applied for the V_f values 38%, 53% and 62%. Results on unsaturated and saturated are grouped in Figure II.9. Each point of the curve is an average of three experiments. Conforming to literature, K_{unsat} and K_{sat} values (Figures II.9 A and II.9 B respectively) decreased with the increase of V_f following an exponential relation. This is a consequence of the narrowing of flow channels and the reduction in porosity. Permeability values for the same preform, same V_f and with identical process variables may differ. Many variations interfere in the process, such as the relative positions of the plies for each experiment, which may influence the shape and size of flow channels. The saturated permeability was slightly higher than the unsaturated

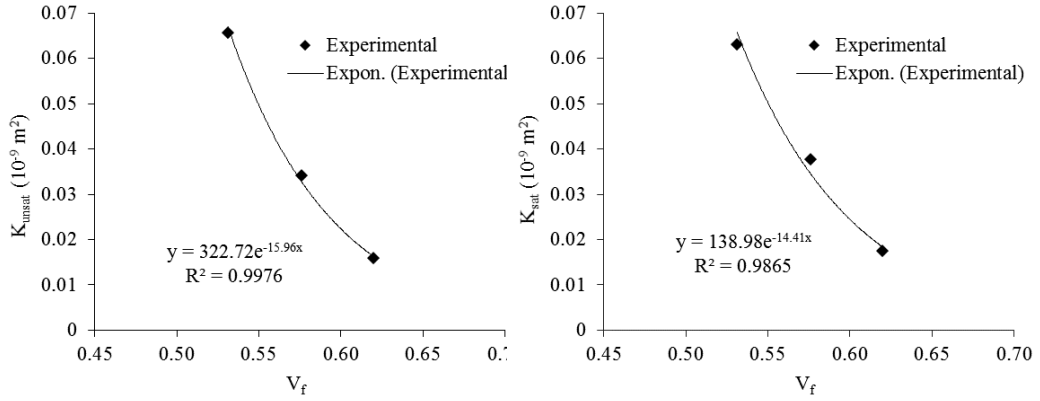

FIGURE II.9: Results on (A) unsaturated and (B) saturated permeability values at V_f= 38%, 53.1% and 62%

permeability at V_f= 53% and 62% and slightly lower for V_f= 38%. The differences between the values of K_{unsat} and K_{sat} comes from the occurrence of transient capillary effects during the unsaturated flow, while the saturated flow is described by geometrical drag [69].

II.3 Model fluids and resin

Two types of test liquids were used for flow experiments: silicone oil and aqueous glycerol solutions. The characterizations of viscosity and density are detailed for each fluid hereafter.

II.3.1 Silicone oil

Rhodorsil 47V100 silicone oil from Silitech SA was used as a model fluid for permeability measurement experiments. According to technical data sheet, it has a viscosity (η) of 0.1 Pa.s and a density (ρ) of 0.965 g/cm^3 at 25 °C. The viscosity of silicone oil is dependent on its temperature. A relation was proposed by the supplier for viscosity determination as a function of temperature:

$$\eta = \frac{(-1.9 * T + 153.5)}{1000} \tag{II.11}$$

with T, the oil temperature in degrees Celsius. Figure II.10 shows the evolution of the silicone oil viscosity with its temperature. The figure shows the evident decrease in viscosity with the increase in temperature. The room temperature was recorded at the beginning of each experiment to enable the determination of the silicone oil viscosity as per Equation II.11.

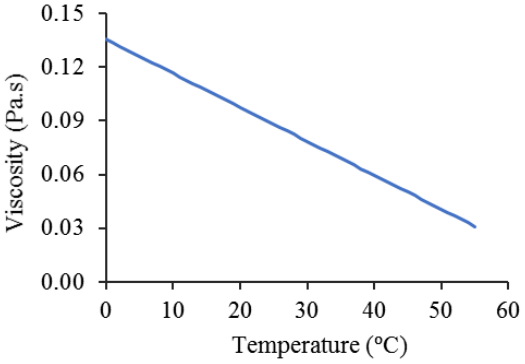

FIGURE II.10: Change of silicon oil viscosity with temperature

II.3.2 Glycerol aqueous solutions

Glycerol S67922 from SONODIS with a density of 1.225 g/cm^3 was mixed with purified water at two different percentages: 75%/25% and 88%/12% (by mass). The density and viscosity of mixtures (without particles) are presented in Table II.2. Mixtures have measured densities of 1.18±0.01 g/cm^3 and 1.19±0.01 g/cm^3 for 75% and 88% glycerol contents respectively at room temperature. The values of the measured density agree with literature [7, 70]. Figure II.11 plots the viscosity of glycerol/water blends as a function of glycerol content.

TABLE II.2: Properties of glycerol/water mixtures

Glycerol percentage (% wt)	Water percentage (% wt)	Density (g/cm^3)	Viscosity (Pa. s)
75	25	1.19	0.035 [7]
88	12	1.22	0.175

II.3.3 Curing resin

Polyester resin (ENYDYNE I 98992 A) with 2% of the catalyst LUPEROX K1S was used for the fabrication of composite panels in chapter III. The resin has a density of 1.11 g/cm^3 at 20 °C. For the study of the micron-scale particle filtration (chapter V), SR GreenPoxy 56 resin with the reference SR 8100 from Sicomin was mixed with the hardener SD 8822 with the percentages: 100g/31g (by mass) or 10 ml/ 39 ml (by volume) respectively. At 20 °C, the densities of resin and hardener are 1.158 ± 0.01 g/cm^3 and 0.937 ± 0.01 g/cm^3 respectively.

II.3.4 Dispersing agent

The wetting and dispersing additive BYK-W-940 is a solution of an unsaturated polycarboxylic acid polymer and a polysiloxane copolymer. The agent has a density of 0.95

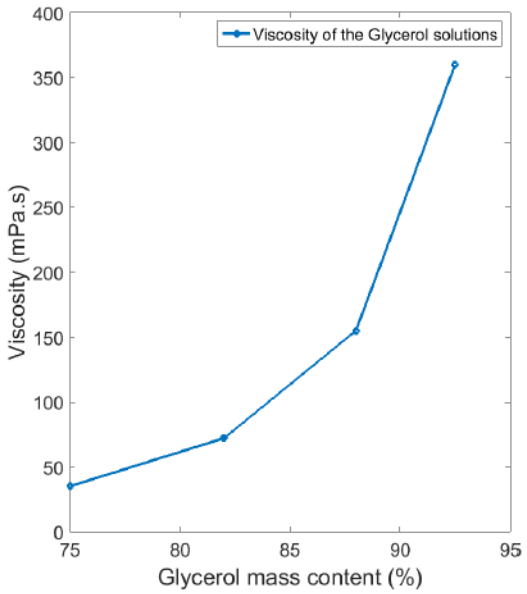

FIGURE II.11: Viscosity of glycerol-water mixtures as a function of glycerol mass content [7]

g/cm^3 at 20 °C. BYK-W-940 is added to stabilize suspensions and to prevent fillers from sedimentation and agglomeration. The dispersing agent is added to the carrying fluid with a percentage in the range of 0.5% to 1.5% of the mass of the added particles, according to the supplier.

Acrylic casting resin from Electron microscopy sciences is used for sample coating. Four drops of hardener are added to each 28.35 g of resin for a 13-26 mm thickness mold.

II.4 Particles

Microparticles of different types are used for the characterization of of particle-loaded composites in LCM processes. Only the effect of particles on the processing is investigated in this work. The functional properties of composites provided by particle addition are out of the scope of this study. Polymeric and ceramic particles are selected with different size distributions and properties. Each type of the chosen particles is added to the process differently depending on its size, either to resin or to the fibrous preform.

II.4.0.1 Polymeric particles

Two types of polymeric particles having a comparable average diameter were used for process characterization. The main distinction between the two types lies in their properties: Expancel microspheres are spherical hollow particles, where the other type consists of fully dense particles. The properties of each type are summarized in Table II.3.

Expancel microspheres

The Expancel microballoons from AkzoNobel consist of polymeric shells containing a gas that expands with heating. This results in increased particle size and a decrease in the shell thickness and particle density. Gas remains inside the particles, making them compressible under applied pressure. When the pressure is released, particles regain their original shape. Figure II.12 illustrates the effect of heat on the particle size and the shell thickness of Expancel particles. The low density of Expancel microspheres makes them interesting for lightweight composite applications. Two different sized hollow microspheres were used for this study: Expancel 920 DU 40 with a mean measured diameter of 39.4 μm and Expancel 920 DU 120 with a mean diameter of 129.6 μm. The distribution of Expancel particles was measured using a KEYENCE optical Microscope by calculating an average of 100 particle diameters. Table II.3 presents the properties of the polymeric particles. Figure II.13 shows microscopic images for the two grades of Expancel. The Figure II.13 A and II.13 B show the Expancel 40 microspheres before and after heating at 150 °C for 1 minute. The Expancel 120 microspheres are shown after expansion in the Figures II.13 C and II.13 D.

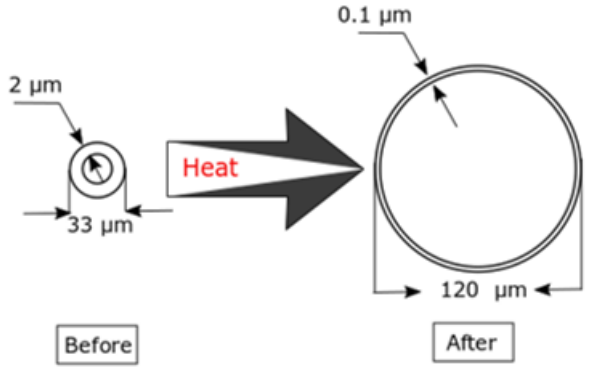

FIGURE II.12: An illustration of the effect of heating on the size of Expancel particles

PVC particles

The used fully dense PVC particles (Figure II.14) have a mean diameter of 133 μm and a density of 1.38 g/cm^3. The shape of the used PVC particles is semi-spherical with a

TABLE II.3: Properties of polymeric particles

Property	**Expancel**		**PVC**
Grade	920-DU-40	920-DU-120	-
Average particle diameter μm (supplier)	40	120	120
Average particle size μm (measured)	39.4	129.6	133
True density (g/cm^3)	0.0745	0.0903	1.3800
Physical form	Spherical		Semi-spherical
color	Transparent		White

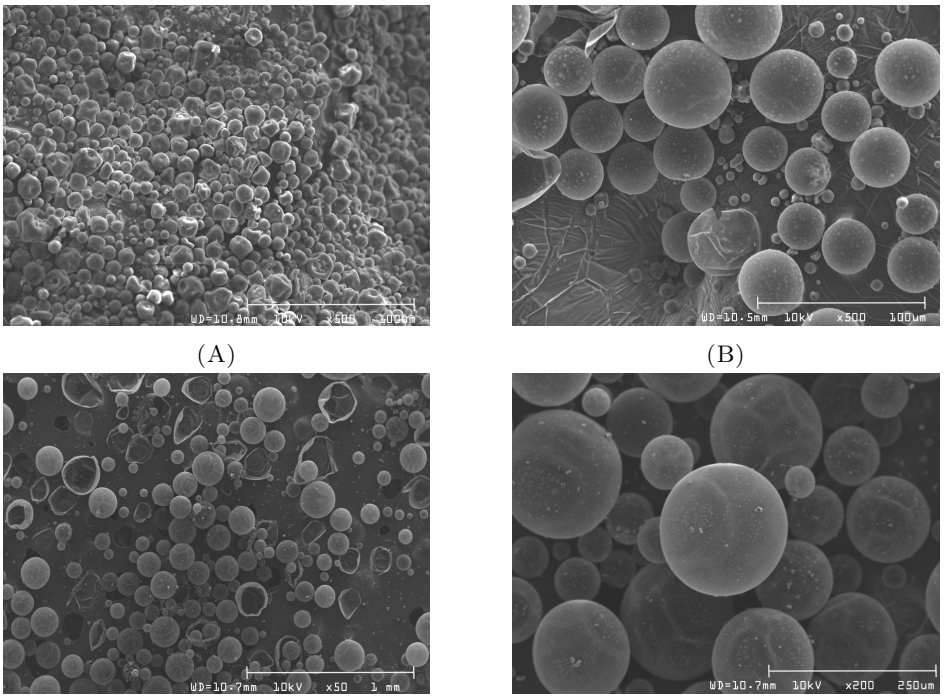

(A) (B)

(C) (D)

FIGURE II.13: SEM observations for Expancel 40 (A) before and (B) after expansion, and Expancel 120 after expansion at magnifications of (C) x50 and (D) x200

relatively rough surface.

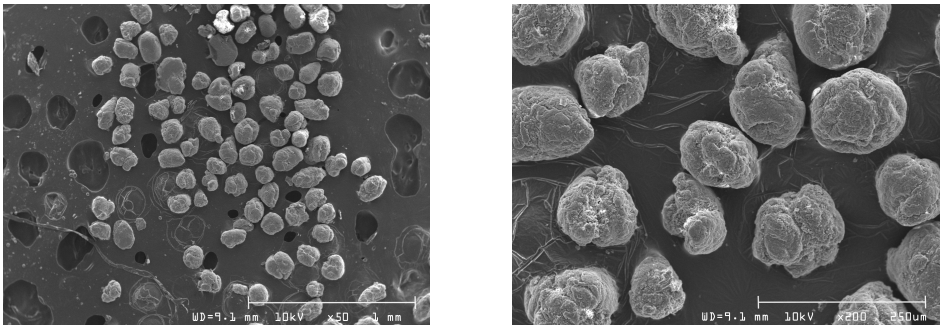

(A) (B)

FIGURE II.14: SEM observations for PVC particles at magnifications of (A) x50 and (B) x200

II.4.0.2 Ceramic particles

3M ceramic microspheres are alkali aluminosilicate ceramic particles. They are used to characterize suspension filtration with three different grades: W-210, W-410 and W-610. Each grade represents a different size distribution range. Particles are observed under the scanning electron microscope (SEM) HITASHI S3000N. Figure II.15 shows the SEM images of the particle grades: W-210 (II.15 A), W-410 (II.15 B) and W-610 (II.15 C) at a magnification of x2500. It was observed that most particles are spherical

with some debris. Each grade presents a wide range of particle sizes. The properties of these particles are detailed in Table II.4.

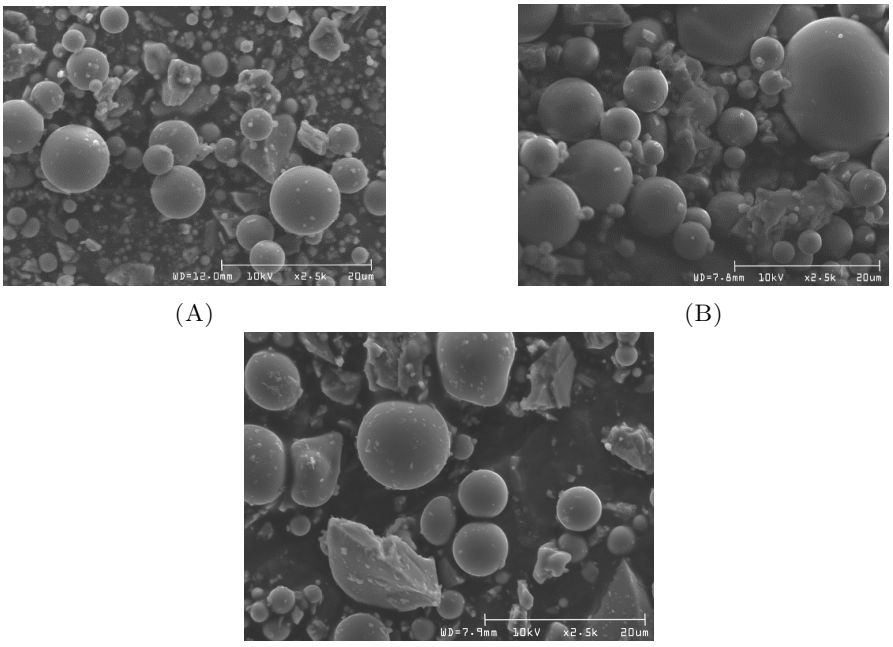

(A) (B)

(C)

FIGURE II.15: SEM images for 3M ceramic particles: (A) W-210, (B) W-410 and (C) W-610

TABLE II.4: Properties of 3M ceramic particles

Property	**Value**		
Grade	W-210	W-410	W-610
Median particle size* (μ**m**)	5.2	7.9	15.2
Effective top size** (μ**m**)	11	17	37
True density (**g**/cm^3)	2.35		
Physical form	Spherical		
Color	White		

*Measured by liquid granulometry **Provided by the manufacturer

Particle size distribution

The laser diffraction granulometer Mastersizer HYDRO 2000 SM from MALVERN Instruments (Figure II.16) was used for the characterization of particle size distribution. The measurement range is from 0.02 to 2000 μm for wet dispersion. Results are post-treated with the software integrated into the device.

A suspension consisted of 3M particles and distilled water purified with VWR Puranity TV 3 UV/UF. The suspension was stirred with the magnetic stirrer FB15001 (from

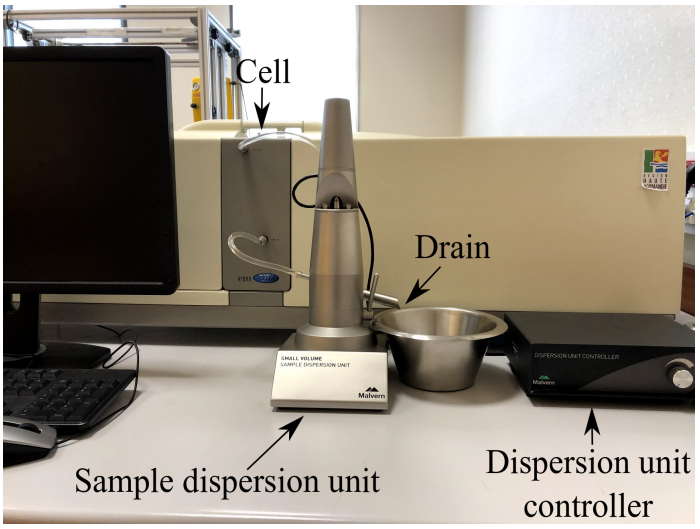

FIGURE II.16: The granulometer Mastersizer HYDRO 2000 SM

Fisher Scientific) for 30 minutes before each measurement to avoid particle agglomeration. Three measurement cycles of 12 seconds were performed for each sample. In each cycle, suspensions are mixed in the dispersion unit at 2400 rpm, then pumped to the flow cell, where it passes through the analyzer beam. Refraction indices for ceramic microspheres and water are respectively 1.53 and 1.33. Figure II.17 presents the granulometry of W-210, W-410 and W-610 grades. Tests revealed the wide polydispersity that each grade has. Particle sizes ranged from less than 1 μm to 100 μm. The median particle sizes d(0.5) are 5.2 μm, 7.9 μm and 15.2 μm for W-210, W-410 and W-610, respectively (Table II.4). It means that 50% of the particles in the sample are larger than that size and 50% below it.

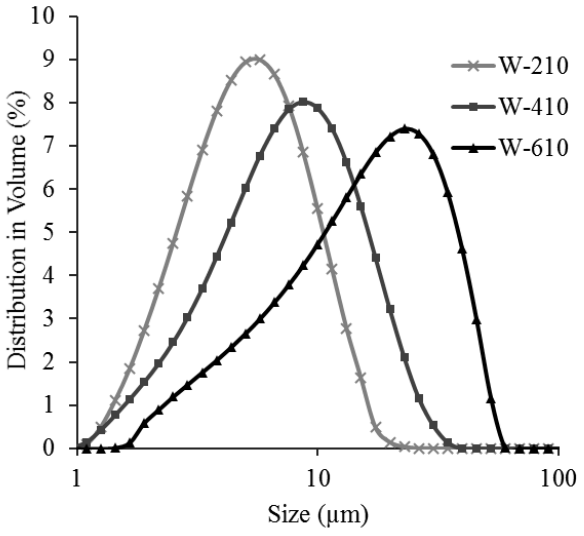

FIGURE II.17: Particle size distribution of ceramic particles measured by laser diffraction

II.5 Suspension characterization

Efficient characterization of any suspension requires the determination of its effective density and viscosity. Both quantities increase with the addition of particles. The rise of their values depends mainly on the particle nature and volume fraction. The viscosity of suspensions is also affected by the shape and the size of particles. In the following sections, the evolutions of density and viscosity are discussed for suspensions of ceramic particles and glycerol/water mixtures.

II.5.1 Density of suspensions

The density of suspensions is determined using the law of mixtures (Equation II.12). It is based on the determination of an effective density ρ_e from the liquid and the solid phase densities ρ_l and ρ_p respectively, and the solid phase concentration C. This method was demonstrated by Richardson and Meikle [71] and confirmed later by E.Barnea and J.Mizrahi [72] and Poletto et al. [73].

$$\rho_e = (1 - C)\rho_l + C\rho_p \tag{II.12}$$

Density measurements were performed for suspensions of 3M ceramic particles and purified water. A pycnometer of 5 ml capacity and precision of ± 0.01 g/cm^3 is used for the tests. Suspensions of 1%, 2%, 3%, 4%, 5% and 10% concentrations were prepared and tested. Each suspension is weighed with a high precision balance (± 0.1 mg). Knowing the volume of the pycnometer, the experimental density is calculated by the relation $\rho = m_e/V_e$, where m_e and V_e are the effective mass and volume of the suspension, respectively. The theoretical density of the suspension is obtained by substituting the concentrations and component densities in Equation II.12. Figure II.18 shows the experimental and theoretical density values. The increase in particle concentration exhibited a linear rise in suspension density. Experimental results have shown good agreement with the theoretical ones. The low error indicates the reliability of this method. Thus, it will be used to characterize particle concentrations in glycerol/water mixtures throughout the study.

II.5.2 Viscosity of suspensions

Six suspensions with different concentrations were prepared with the three ceramic particle grades, in addition to one sample with pure fluid. Table II.5 gives the studied concentrations (in volume) as well as their corresponding mass percentages. The glycerol/water blends are first mixed with the dispersing agent using a magnetic stirrer for 20 minutes at a moderate mixing speed. Next, the mass of dispersant BYK-W-940 is

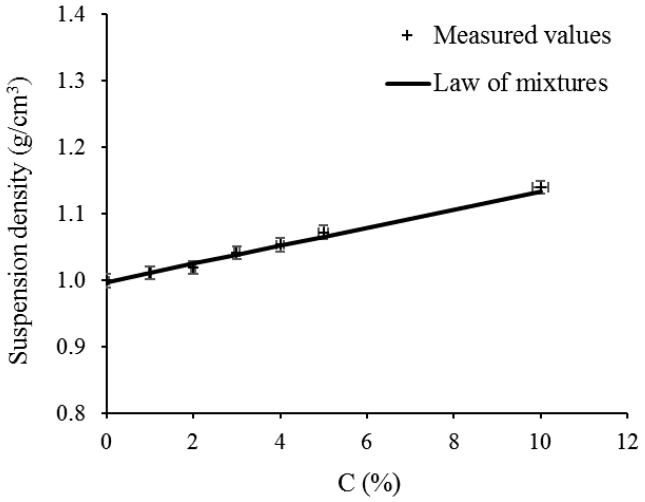

FIGURE II.18: Experimental and theoretical density as a function of particle concentration for suspensions of purified water and ceramic particles

set to 1% of the mass of particles. Then the ceramic particles are weighed and added to the mixture and stirred for 2 hours.

TABLE II.5: Viscosity measurement experiments

Sample No.	1	2	3	4	5	6	7
Concentration (Vol.%)	0	1	2.5	5	10	20	40
Mass percentage (wt.%)	0	2	5	10	20	40	80

II.5.2.1 Experimental set-up

The hybrid rheometer DHR-3 was used for the viscosity measurements. The rheometer is a cone-plate type with a cone angle of 2.006 °, a diameter of 60 μm and a truncation of 53 μm. The device was calibrated and the testing temperature was set to 20 $°C$. A volume of 2.5 ml of suspension was tested at each experiment. The data was acquired and post-processed with the software TRIOS from TA-Instruments. The main objectives are to study the effects of particle size, particle concentration and shear rate on viscosity. The viscosity measurements are performed for the three ceramic particle grades (W-210, W-410 and W-610). The shear rate was varied between 10^{-1} and $10^{3} s^{-1}$.

II.5.2.2 Effect of shear rate

Figure II.19 shows the evolution of viscosity for suspensions of different concentrations and varying shear rates (from 10^{-1} to 10^{3} s^{-1}). Broadly speaking, viscosity was unchanged with the shear rate for particle concentrations up to 20% for the three grades: W-210 (Figure II.19 A), W-410 (Figure II.19 B) and W-610 (Figure II.19 C). The constant viscosity throughout the experiment shows that the suspension remains Newtonian

for concentrations of particles up to 20% vol. (40% wt.). At a concentration of 40% vol., a non-linear rheological behavior is observed for the three grades. Thus, the suspension under study is considered as a non-Newtonian fluid at this concentration. The viscosity follows a plateau from 10^{-1} to 100 s^{-1}, then starts to increase slightly showing a shear thickening behavior, then follows a plateau again just before reaching 10^3 s^{-1} shear rate. The variations of viscosity with shear rate are more pronounced using the lower-size grade (W-210). The shear thickening behavior is generally observed for high concentrated suspensions at elevated shear rates. It is the increase of viscosity with the increase in shear rate [74]. The value of the shear rate at which the curve changes is called the critical shear rate [26]. It is around 1 s^{-1} for the three grades of concentrations of 40%. This shear thickening behavior is due to the movement and the re-arrangement of particles in the suspension that increases with shear rate. It depends on the particle size distribution, particle shape and concentration, as well as the properties of the carrying liquid. The shear rate dependence is a combination of the viscous forces, surface forces, and Brownian motion forces [75].

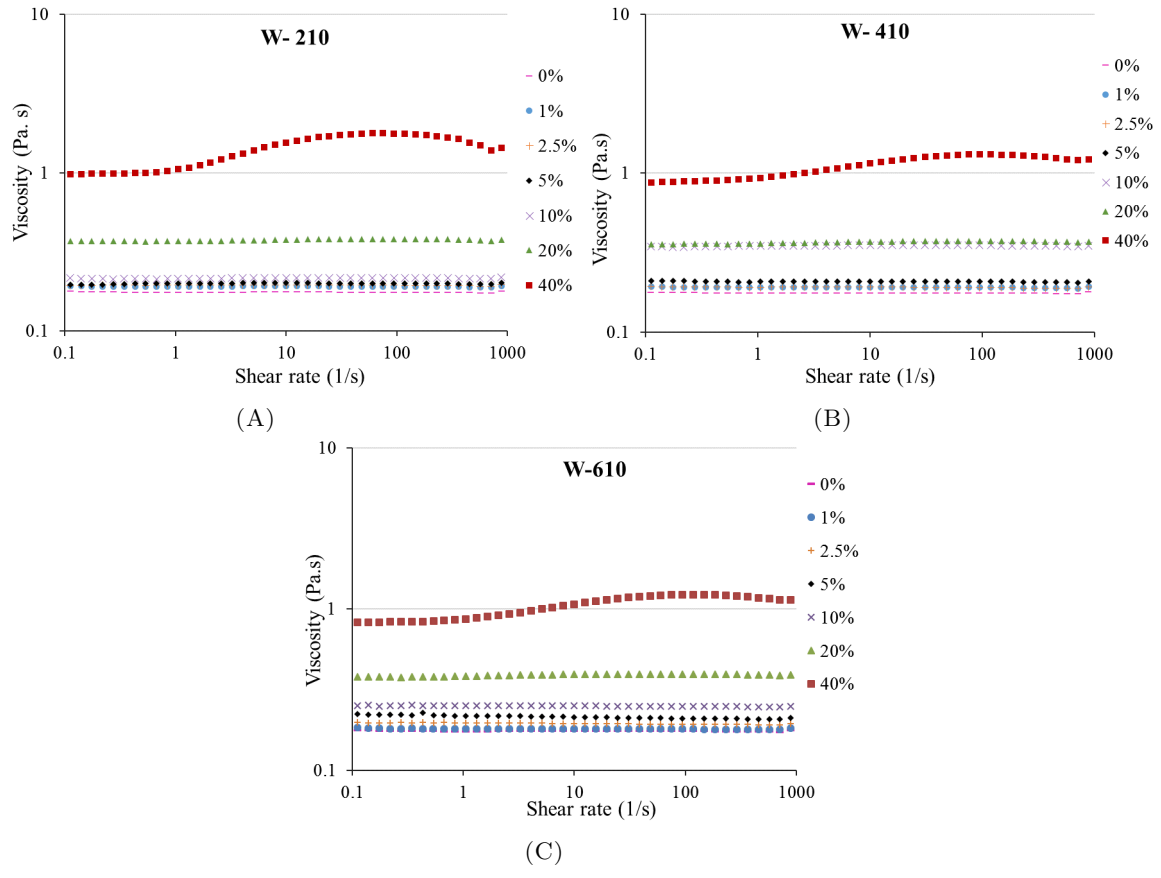

FIGURE II.19: Change of viscosity with the shear rate for the ceramic particle grades (A) W-210, (B) W-410 and (C) W-610

II.5.2.3 Effect of particle concentration

Figure II.20 plots the viscosity against the particle concentration C in the suspension. It is noticed that viscosity increases slightly with increased particle concentration up to C= 10%. A sharp increase in viscosity is noticed right after up to the maximum explored concentration of 40%. These results agree with previous experimental findings [74, 76]. Similar results were found by Fernberg et al. for the evolution of viscosity as a function of the concentration of ATH particles dispersed in a polyester resin [25]. When the particle concentration increases, the particle-particle interactions limit the freedom of particle movement and affect fluid flow, resulting in increased viscosity.

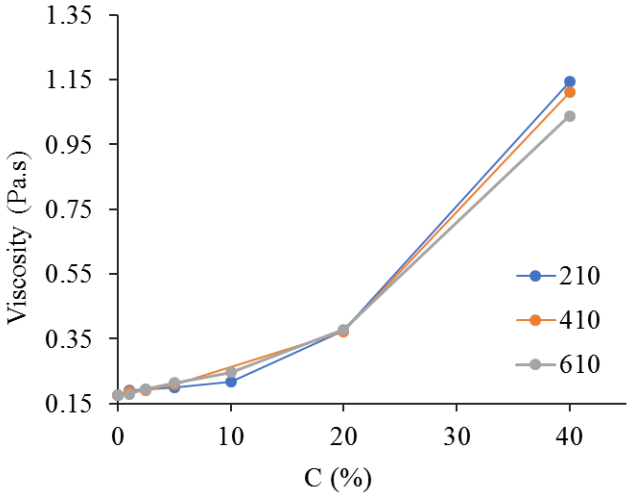

FIGURE II.20: The dependency of viscosity on the suspension concentration. Each measurement represents an average of three values

At C = 20%-40%, the upper viscosity curve represents the lower particle grade W-210, the lowest curve shows the viscosity of the highest particle size W-610 and the curve in between corresponds to the viscosity of the intermediate particle size W-410.

II.5.2.4 Effect of particle size

For monodisperse particles, the general behavior is that viscosity is inversely proportional to particle size; the smaller the particle size, the higher the viscosity. For the explored ceramic microspheres, only slight differences were found between the three particle distributions (Figure II.21). That's due to the high particle polydispersity for each grade and the slight differences in the range of particle sizes from one grade to another. The effect of particle size was more remarkable for suspensions with the highest explored concentration (C = 40%). For polydisperse particles, the viscosity depends on the ratio of fine to coarse particle fractions in the suspension [77]. At a given particle volume fraction, the viscosity decreased as the ratio of the large to small particle size increased. Farris [78] developed a model based on purely geometric arguments for the

viscosity of polydisperse suspensions. In his model, Farris assumed that the fine and coarse particles behave independently of each other in the suspension.

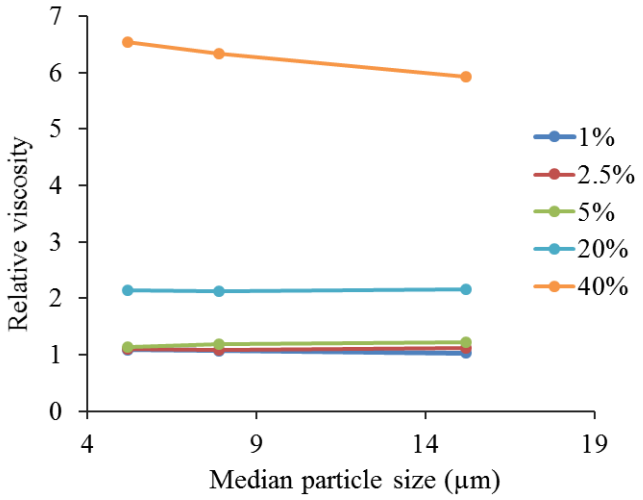

FIGURE II.21: The evolution of viscosity with particle size

II.5.2.5 Viscosity modeling

Several viscosity models were presented in section I.3.2.2, i.e., Einstein, Batchelor, Ball and Richmond, Cheng and Law, Mooney, Erdal, Eilers, and Kreigher and Dougherty models. In this section, these models are evaluated to choose the best representation for the experimental data. The measured viscosity values are fitted to each model. The root mean square error (RMSE) given in Equation II.13 was considered as a base of comparison to the capability of the model to describe these data. N is the number of data points. Theoretical and experimental data are denoted by η_{model} and η_{exp}, respectively.

$$RMSE = \sqrt{\frac{\sum_{i=1}^{N} (\eta_{model} - \eta_{exp})^2}{N}} \tag{II.13}$$

Two main parameters govern most of the models: the maximum packing fraction C_{max} and the intrinsic viscosity $[\eta]$. C_{max} is the inverse of the crowding effect. It depends on the particle shape, size distribution and arrangement in the suspension; its value ranges from 0.52 to 0.74 for monodisperse spheres. The value of $[\eta]$ for spherical particles in an ideal dilute suspension is 2.5. A deviation from these values is possible in the case of polydisperse or non-uniformly shaped particles. For the ceramic particles used in this study, a non-uniform particle shape and wide particle size polydispersity are found from the experimental characterization.

TABLE II.6: Parameters of viscosity models from experimental data fitting

Model	Maximum packing fraction C_{max}			Intrinsinc viscosity $[\eta]$			RMSE
Grade	W-210	W-410	W-610	W-210	W-410	W-610	
Einstein	-	-	-	-	-	-	0.69
Batchelor	-	-	-	-	-	-	0.54
Ball and Richmond	0.45	0.46	0.48	-	-	-	0.11
Kreigher and Dougherty	0.41	0.41	0.41	1.21	1.34	1.27	0.11
Cheng and Law	1.45	1.39	1.27	-	-	-	0.07
Erdal	0.65	0.66	0.67	-	-	-	0.06
Mooney	1.14	2.67	2.26	3.07	3.95	3.68	0.05
Eilers	0.67	0.86	0.84	3.14	4.08	3.78	0.05

Table II.6 reports the values of all parameters as well as the corresponding RMSE between experimental and theoretical values. Intrinsic viscosity $[\eta]$ and packing fraction C_{max} increased with particle size with Ball and Richmond model. For Eilers and Mooney models, $[\eta]$ and C_{max} increase with the grades W-210 and W-410, then decrease for the grade W-610 to a value in between the lower and medium values (W-210 and W-410). Values of parameters remain unchanged with Kreigher and Dougherty model. C_{max} decreases with particle size for Cheng and Law model, while it increases with particle size for Erdal's model. Non-logical packing fraction values were obtained by fitting data to Mooney's model, the values varied between 1.14 and 2.67, while the maximum value should not exceed 1. The lowest error corresponds to the model that fits the experimental

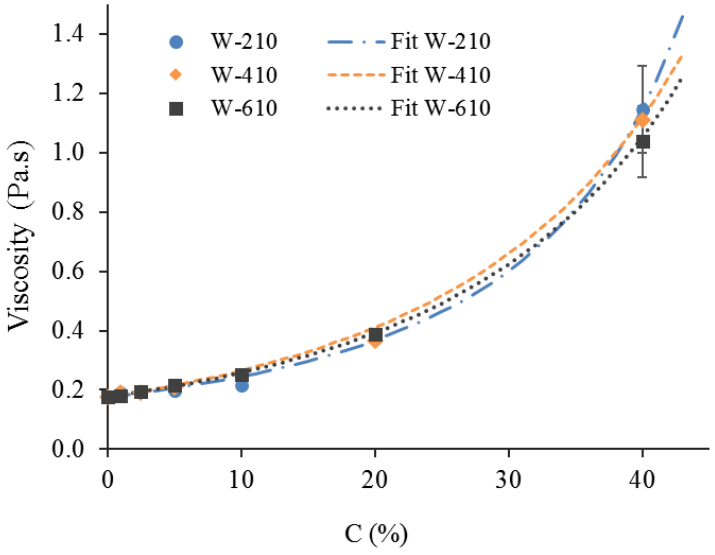

FIGURE II.22: Suspension viscosity as a function of particle concentration and size (each point is an average of three values, error bars represent the standard deviation)

data the best. From Table II.6, it is evident that Eilers and Mooney models are the best to describe the data of the performed experiments for the used materials, with an error of 0.05. Whereas the other models exhibit errors of 0.06 to 0.69. As Mooney's model exhibits unrealistic values for the maximum packing fraction, Eilers model is chosen as the best fit.

Figure II.22 presents the fit of experimental viscosity data to Eilers model for suspensions of the three grades. The model shows a good representation of experimental data. Slight differences are noticed between viscosity curves. This is due to the widespread of particle sizes, which was also translated by the slight differences in the parameter values $[\eta]$ and C_{max}.

II.6 Conclusion

In summary, this chapter presented the main materials used in the experimental studies of this research as well as their testing methods. The quasi-unidirectional fabric and its characterization are presented and discussed. The saturated and unsaturated permeabilities are measured as a function of the fiber content. The compression behavior for the neat and dry quasi-UD preforms has shown a clear decrease in the overall thickness of plies and a rise in the fiber content following a power law with the applied pressure. These tests are addressed in the next chapters in the presence of particles, to investigate the effects of the addition of a second solid phase on the compaction behavior of the dry preform and the flow process.
The types and morphology of the used particles are outlined. Two categories of particulate-fillers are presented; polymeric and ceramic particles. The polymeric particles consisted of solid and hollow types. These microspheres are added to fibrous preforms in chapter III by manual sieving to study the effect of particle nature on flow for homogeneously distributed particles. The three grades of ceramic particles, which were found to have a wide granulometry are added to glycerol solutions to investigate the flow and filtration of suspensions through fibrous media with macroscale (chapter IV) and micron-scale experiments (chapter V).
The chapter also detailed the density and viscosity measurements of neat liquids and suspensions. It was found that the density increases linearly with particle content following the law of mixtures. The evolution of viscosity as a function of concentration followed the Eilers model as the best fit. No correlation was highlighted between viscosity and shear rate for suspensions with concentrations lower than 20%. In the following, the range of the used particle concentrations will not exceed 10%. Thus, suspensions are assumed to have a Newtonian behavior and the variations with shear rate and time will be neglected. Only the dependency on concentration will be considered throughout the study. The Eilers model, which fitted the results the best will be used for the filtration modeling phase in the numerical simulation of chapter VI.

Chapter III

Impregnation of particle-loaded fibrous preforms in LCM processes

III.1 Introduction

As detailed in section I.3.1 of chapter I, particle addition to composite materials enhance or modify specific properties in the finished part. Properties included electrical and thermal conductivity, fire resistance and self-healing applications etc. [61, 79, 80]. Hollow microspheres or microballoons are added to fabricate lightweight parts [81] and reduce the cost of fabrication of composites by replacing part of the resin. They are also used as additives for painting and the fabrication of foams. Composite materials such as syntactic foams are widely used in low-density and high damage tolerance applications [82]. Hollow microspheres are also used in many applications, such as marine, aerospace and civil engineering [83].

Different techniques of particle addition to composite materials are discussed in section I.5. The choice of the incorporation method is dependent upon the particle characteristics and volume fraction. Among these methods, two ways compatible with LCM processes were presented previously in section I, i.e., preform and resin functionalization. The most common particle incorporation method is adding particles to resin and injecting suspension into the fibrous medium. This method combines several variables into the process and complicates the impregnation. Moreover, it results in most of the cases in a heterogeneous distribution of particles. Both methods will be addressed throughout this research: particle-loaded preform and particle-loaded resin. The former method will be addressed in this chapter while the latter is investigated in chapter IV.

One potential application of adding a second solid phase to the fibrous medium is permeability and flow kinetics enhancement. i.e., the use of inclusions to reduce the impregnation time and to increase the permeability. This is ensured by modifying the pores so that the permeability increases at the same fiber content. Tonejc et al. have used 3D printed structures directly printed onto the fabric for in-plane permeability customization [84]. In addition to the change in permeability. These interphases caused a thickness increase and altered the mechanical properties and the compression behavior of the finished parts. Szebényi et al. introduced 3D printed structures to unidirectional carbon fiber reinforcements. The produced part exhibited enhanced ductility in static flexure tests [85]. Salvatori et al. [86] used thermoplastic 3D structures fabricated with 3D printing to enhance the permeability. Two types of spacers were added: solid and degradable spacers. The authors characterized the compaction and flow behavior of the hybrid structure. Spacers increased the in-plane saturated permeability by two orders of magnitude from the plain fabric initial permeability. The spacers with smaller mesh sizes exhibited better compaction behavior. However, the high rise in permeability caused a deteriorated dual-scale impregnation behavior dramatically. At the end of the injection process, the flow reached the mold outlet, leaving behind a large unsaturated zone. A new injection strategy led to complete structure impregnation with 75% shorter filling times than the first method. Better impregnation also includes the amelioration of the capillary number towards its optimal value. The use of an intermedium more permeable than the fabric structure was widely studied in the literature; for example, using flow-mesh and distribution media in VARTM for faster in-plane flow, followed by a through-thickness impregnation. The incorporation of a particulate solid phase was performed for their effect on permeability and mechanical properties. Manfredi and Michaud [13] reported an increase in the in-plane saturated permeability as a result of the addition of self-healing inclusions. No significant variations were found in the transverse permeability values from plain to particle-filled fabrics in this study. The measurement method used, which was fully saturated, is less sensitive to capillary phenomena (enhanced by the presence of particles). An investigation of the change of permeability and compaction behavior with the addition of glass beads with different sizes and volume fractions was carried out by Caglar et al. [87].

Inclusions exist in several forms with different natures. For flow and compaction behaviors, the most influencing parameter is the particle type. According to their nature, inclusions can be classified into plain and hollow particles. The two types are expected to influence the process differently. Although the two types of particles are extensively used for different composite applications, few studies have investigated their influence on the compaction of the dry fibrous preform and the impregnation process. In this chapter, micron-sized particles of considerably large size are deposited on the fabric's surface; then, the fluid is introduced to the system at a constant pressure drop. The functionalization of the preform is studied to eliminate the effect of the uneven distribution of particles and the increase in resin viscosity induced by resin functionalization.

The goal here is to limit the number of parameters that intervene in the processing of functional composites by LCM processes and focus on particle influence on the flow process. The objectives of this chapter are:

- studying the fabrication of particle-loaded composites by fabric functionalization,
- investigating the effect of particles of fixed size and variable volume fractions on the impregnation process,
- testing the effect of particle type and volume fraction on the fabric permeability and compression behavior.

Two types of particles are studied: solid rigid particles and hollow compressible ones. The effects of these particles on the flow front advancement, filling time, capillary number, fabric permeability and compression behavior are explored through a series of tests at fixed material parameters, such as fiber volume fraction, fluid viscosity and particle size, and variable particle volume fractions. Composite panels are fabricated to analyze the distribution of the two types of particles in the microstructure qualitatively and quantitatively.

III.2 Experimental methodology

This study aims to compare the effects of the two types of particles on the impregnation process. Throughout the flow experiments, the only variables are the particle type and the corresponding particle volume fraction V_p. All the other process and material parameters are kept constant.

III.2.1 Materials

The characterization of materials used in this part is detailed in chapter II.

Model fluid

Silicone oil (Rhodorsil 47V100) was used as a model fluid for permeability measurement experiments. The properties of silicone oil are detailed in section II.3.1. As its viscosity is dependent on temperature, the room temperature was recorded at the beginning of each experiment.

Resin and hardener

For the fabrication of composite panels, polyester resin (Enydyne 198992A) was mixed with 2% of the catalyst LUPEROX K1S (refer to section II.3.3).

Particles

Two types of polymeric particles were used (Expancel microspheres and PVC particles). Expancel microspheres are used for their low density, elasticity, compressibility and adhesion properties. They can also contribute to the cost reduction of composites by replacing a part of the resin. PVC inclusions are used as model particles that can represent any of the commonly used functional plain types. The two types have a comparable average particle diameter: Expancel 120 with an average size of 129.6 μm and PVC with an average diameter of 133 μm. A lower grade of Expancel microspheres was used; Expancel 40 with an average size of 39.4 μm and compared to the higher grade. Expancel microspheres are hollow compressible particles, while the PVC particles are plain rigid ones. The properties and characterization of each type are addressed in section II.4.0.1.

III.2.2 Set-up and methods

The induction machine was needed to heat the plies of fabric after functionalization and before the flow experiments. The compression response of the dry functionalized fabric was tested as explained in section II.2.3 of chapter II. To test the particle effect on flow kinetics, flow experiments were carried out using a permeability testing bench.

Induction heat press machine

The induction machine transfers the heat from the mold to the working space by induction (Figure III.1). The Aluminum mold contains two sides: the bottom side is fixed, and the upper part can be translated vertically. First, a ply is placed on the fixed part and the temperature is set to 150°C. Then, the upper part is moved towards the bottom part and fixed at a close distance (around 1 mm) to the functionalized ply surface without touching it.

Particle deposition method

The deposition of particles on the top surface of the fabric plies is performed by manual sieving. Each ply of fabric containing particles is then heated for 2 minutes in the induction machine without compression at $150°C$. Figure III.2 illustrates the heating

FIGURE III.1: An illustration of the induction machine constituted of a hydraulic press and the mold heated by induction

method as well as the positions of the upper and lower mold plates at the heating stage. Figure III.3 shows the evolution of Expancel 120 particles with heating. The first target of the heating step is to enable the expansion of Expancel microballoons. Another objective is the attachment of both types of particles on the top surface of the fabric. This is to avoid their detachment and migration with the flow during the impregnation. As the applied heat ($150°C$) is above the glass transition temperature of polymers, the shell of Expancel and PVC particles softens and gets attached to the fiber surface. This attachment persists even when the fabric and particles cool down.

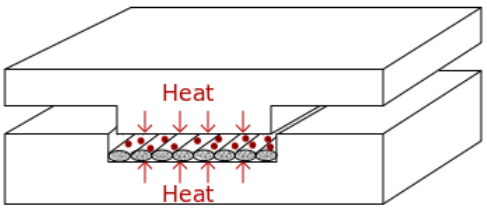

FIGURE III.2: Illustration of the placement of a particle-loaded ply in the induction mold

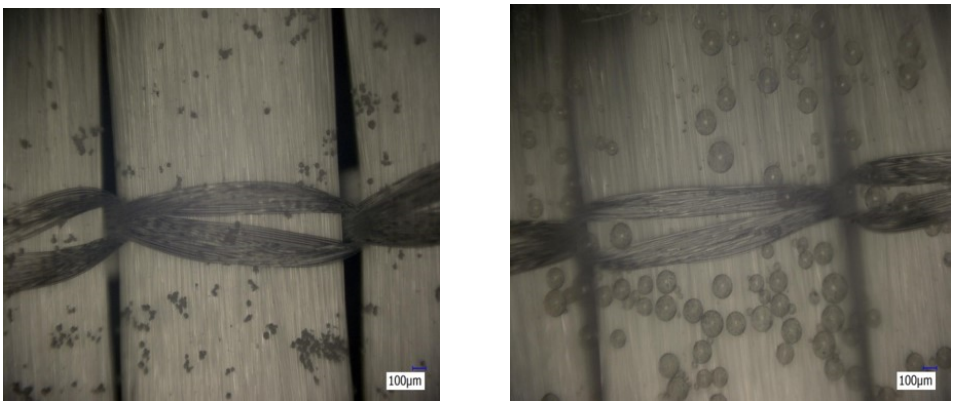

(A) (B)

FIGURE III.3: Optical microscope images of Expancel particles deposited on the preform surface (A) before and (B) after heating

Permeability measurement set-up

For permeability measurement experiments, the bench presented in II.2.4.1 is used. Silicone oil is injected from the pressure pot through the piping to the mold inlet (Figure III.4). For the measurement of the unsaturated permeability (section II.2.4.2), the flow front is registered by a camera installed at the top of the mold through the glass plate. The fluid passes through the mold cavity to the outlet, where a container is placed on a scale to measure the volumetric flow rate of the fluid at different injection pressures. The saturated permeability is determined using Darcy's law as detailed in section II.2.4.3. The Denver Instrument balance used for weighing the outlet fluid has an accuracy of ± 0.01 g at a maximum mass of 400 g. The mass readings were acquired with the help of Pinnacle USB 1.2 software.

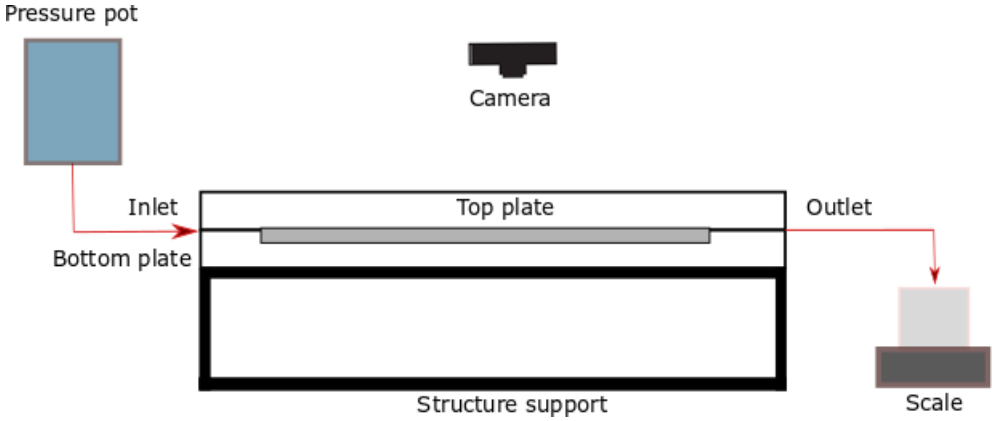

FIGURE III.4: A schematic front view of the permeability measurement bench

III.2.3 Parameters and protocol

Low particle volume fractions V_p of 0.47%, 0.94%, 1.88% and 3.76% were chosen to explore the influence of slight modifications of the porous medium on its permeability, as previous findings reported permeability decrease at higher V_p values [24]. The four V_p were tested for each type of particles: Expancel 120 (referred to as Expancel1, Expancel2, Expancel3 and Expancel4), PVC (referred to as PVC1, PVC2, PVC3 and PVC4). In addition to the same explored V_p (0.47%-3.76%) values with the grade Expancel 40, referred to as Expancel5, Expancel6, Expancel7 and Expancel8 (Table III.1). Knowing the density values for each type of particle, the corresponding particle mass is determined and measured. Particles are then sieved on the fabric surface.

Three permeability experiments were performed for the quasi-UD fabric without particles at different V_f values. Each experiment is performed three times, which gives a total of 45 experiments. The fiber content was varied by adjusting the number of plies and the mold thickness as follows: i) 53.1% (6 plies with a mold thickness 2.63 mm), ii) 57.6% (6 plies with a mold thickness of 2.85 mm) and iii) 62% (7 plies a mold thickness 2.85 mm).

TABLE III.1: Experimental parameters for permeability measurement

Expancel 120	Expancel1	Expancel2	Expancel3	Expancel4	-	-	-
Expancel 40	Expancel5	Expancel6	Expancel7	Expancel8	-	-	-
P VC	PVC1	PVC2	PVC3	PVC4	-	-	-
Particle volume fraction V_p (%)	3.76	1.88	0.94	0.47	0	0	0
Fiber volume fraction V_f (%)	53.1	53.1	53.1	53.1	53.1	57.6	62.0
Porosity ϵ (%)	43.1	45.3	45.9	46.4	46.9	42.4	38.0

The porosity of the fibrous bed is altered as a result of particle addition as a function of their volume fractions V_p [13, 23]. The following set of equations gives the modified porosity.

$$\epsilon_0 = 1 - V_f \tag{III.1}$$

$$\epsilon = \epsilon_0 - V_p \tag{III.2}$$

$$\epsilon = 1 - V_f - V_p \tag{III.3}$$

ϵ_0 and ϵ are the initial and the modified porosity of the medium after particle addition, respectively. The initial porosity is a combination of micropores and macropores in the intra-tow and inter-tow regions, respectively. The used method places the microparticles precisely on the tow surface, which reduces the macropore fraction. No particles are expected to penetrate the intra-tow regions because the size of particles is much larger than the inter-fiber spaces for the used fabric.

Experimental protocol

The protocol presented in Table III.2 is applied for all the particle-filled preform experiments. It is for the range of particle volume fractions and porosity values presented in Table III.1.

Table III.2: Experimental protocol

No.	Step	Details
1	Particle preparation	The corresponding particle mass to reach the required volume fraction is determined and weighed.
2	Fabric preparation	Plies of fabric are cut with the dimensions 100x296 mm^2
3	Particle placement	- Particles are sieved on the top surface of each ply. - Plies are heated in the induction machine without compression for 2 minutes at 150 °C.
4	Fabric placement	Functionalized plies are stacked in the mold cavity.
5	Experiment preparation	The mold is closed, camera is set in position to enable the visualization of the front advancement. The injection unit is filled with the Silicone oil, the pressure in the injection unit is set to the required value. The acquisition system is checked, a container is installed on the weighing scale and the scale is connected to the acquisition system for the measurement of the mass flow rate for the determination of the saturated permeability II.2.4.3.
6	Impregnation	The pressure acquisition and the camera and the impregnation are started. started.
7	Permeability measurement	Unsaturated permeability is measured at an injection pressure of 1.2 bar. The impregnation is then continued and the saturated permeability is measured at variable injection pressure values (from 0.7 to 2.0 bar).

III.3 Compaction behavior of particle-filled fabrics

The influence of particle addition on the compression behavior of the fibrous preform is investigated through a series of compression experiments, with a pressure cycle ranging from 0 to 1 MPa. For each experiment, six stacked plies of dry quasi-UD fabric with the dimensions of 100 X 100 cm^2 samples were tested at a constant cross-head speed of 4 μm/sec (0.24 mm/min). Particle mass content is adjusted to give the same volume fractions used for permeability measurement experiments in section III.4 for the given sample size. Microspheres were weighed and sieved to the top surface of each ply and the functionalized plies are heated. Plies are stacked parallel to each other (in the fiber direction) and placed on the universal testing machine Instron 5582. The compression

tests were carried out as detailed in section II.2.3. The results of compression tests are shown in Figure III.5 for neat and particle-functionalized fabric.

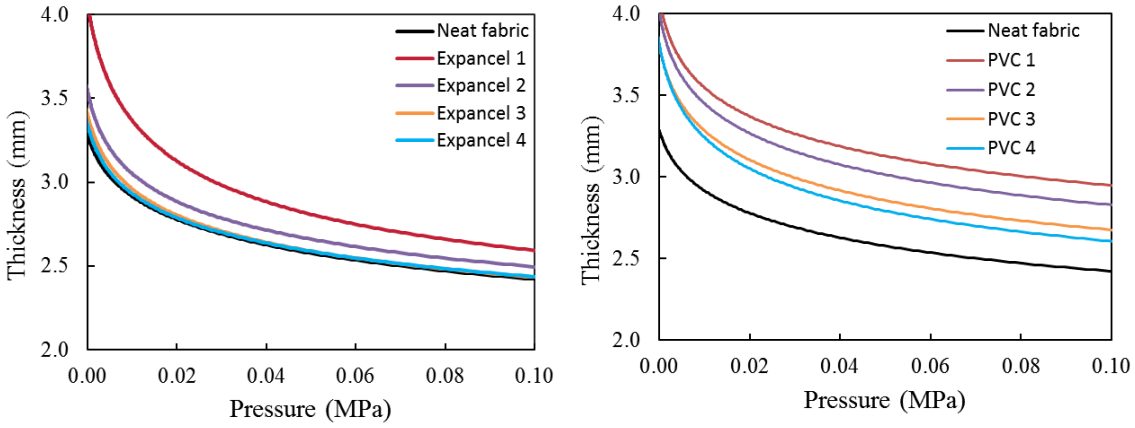

FIGURE III.5: The evolution of thickness with pressure for the quasi-UD fabric functionalized with (A) compressible and (B) rigid particles.The numbers 1, 2, 3 and 4 denote the particle volume fractions V_p: 3.76%, 1.88%, 0.94% and 0.47% respectively

Figure III.5 reports the evolution of the sample thickness with the compaction pressure for the neat and functionalized quasi-UD fabric with compressible (Figure III.5 A) and solid microspheres (Figure III.5 B). Results revealed that the thickness of the stack constituted of fabric and particles continuously decreases as a function of the applied pressure until it reaches a plateau. Moreover, the overall stack thickness increased with fabric functionalization as a function of particle content V_p. This increase is more pronounced for rigid PVC particles than the curves of Expancel particles which were closer to the neat fabric curve. Thickness increase is caused by the particles deposited onto the yarns. These results are in agreement with the findings of Manfredi and Michaud for woven fabrics functionalized with self-healing capsules [13]. The thickness-pressure relation follows a power law as shown by Robitaille et al. [88]:

$$e_{stack} = AP_n^B \tag{III.4}$$

where A and B are respectively the coefficient and the exponent of the power-law. P_n is a dimensionless compaction pressure [89], it is given by:

$$P_n = \frac{P}{1\,MPa} \tag{III.5}$$

where P is the applied pressure. The constant A is the thickness at P_n=1 ($P = 1MPa$).

The thickness-pressure curves were fitted to the power-law (Equation III.4) for all the compression tests, with plain and functionalized fabrics. Curve fitting to power-law was realized after removing the points which correspond to the part where the upper platen was not yet in contact with the stack [89]. Table III.3 lists the values of the constants A and B and the R-squared (R^2) for all the curves. The constant A is related to the stack

thickness, whereas B is the curve shape factor. From Figure III.6, it can be observed that A is increasing continuously with rigid inclusions. A varies only slightly with the compressible type with an average value of 2.056±0.014 mm. The value of A is more influenced by the addition of plain particles, as it reflects the thickness change of the overall stack. B is related to the curve shape; its value is fluctuating as a function of V_p. The power-law exponent B exhibits a value of 0.084 for neat fabric versus an average value of 0.084±0.014 and 0.082±0.005 for compressible and plain microspheres. Higher R^2 is obtained with the solid particles, which reflects more regular curves and a better fit to experimental data. The compression behavior of the hollow microspheres may have induced these variations in results. These findings highlight the need to adapt the power law of neat fabrics to consider the particles present in functionalized preforms by considering the particle nature and volume fraction.

TABLE III.3: Values of constants in the thickness-pressure power-law fit for the compressible (Expancel) and plain particles (PVC)

V_p (%)	**Compressible particles**			**Plain particles**		
	A [mm]	B	R^2	A [mm]	B	R^2
0	1.977	-0.084	0.995	1.977	-0.084	0.995
0.47	2.056	-0.071	0.964	2.106	-0.090	0.993
0.94	2.037	-0.076	0.972	2.192	-0.083	0.986
1.88	2.07	-0.078	0.977	2.317	-0.083	0.988
3.76	2.061	-0.102	0.989	2.442	-0.079	0.992

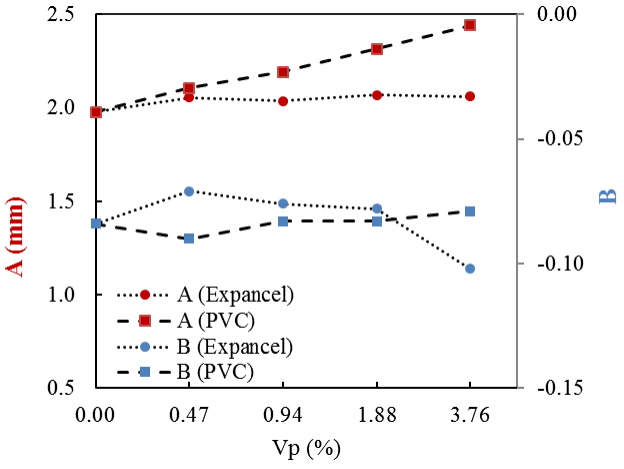

FIGURE III.6: Evolutions of the parameters A and B in the thickness-pressure power law fit for the compressible (Expancel) and plain particles (PVC)

The results on thickness evolution (Figure III.5) are used for the determination of the corresponding V_f. The fiber content is determined by:

$$V_f = \frac{n * A_w}{e_{stack} * \rho_f} \tag{III.6}$$

where e_{stack} is the overall thickness of the stack of fibers and particles from the data on Figure III.5. As a reminder, n is the number of plies and A_w is the areal weight of the fabric.

Figure III.7 reports the increase of V_f with pressure. The general behavior is that the V_f increases with the applied pressure. Comparing the neat and functionalized fabric results, it is observed that higher achievable V_f is attained with neat fabric. At a given V_p, higher V_f can be achieved with compressible inclusions (Figure III.7 A) than with rigid ones (Figure III.7 B). Figure III.7 C highlights the compaction behaviors of the two types of particles at the maximal V_p compared to the plain fabric. The flattening of Expancel particles under applied pressure narrows the inter-yarn spaces and reduces thickness, while the rigid particles constitute a barrier for packing, resulting in an overall thickness increase.

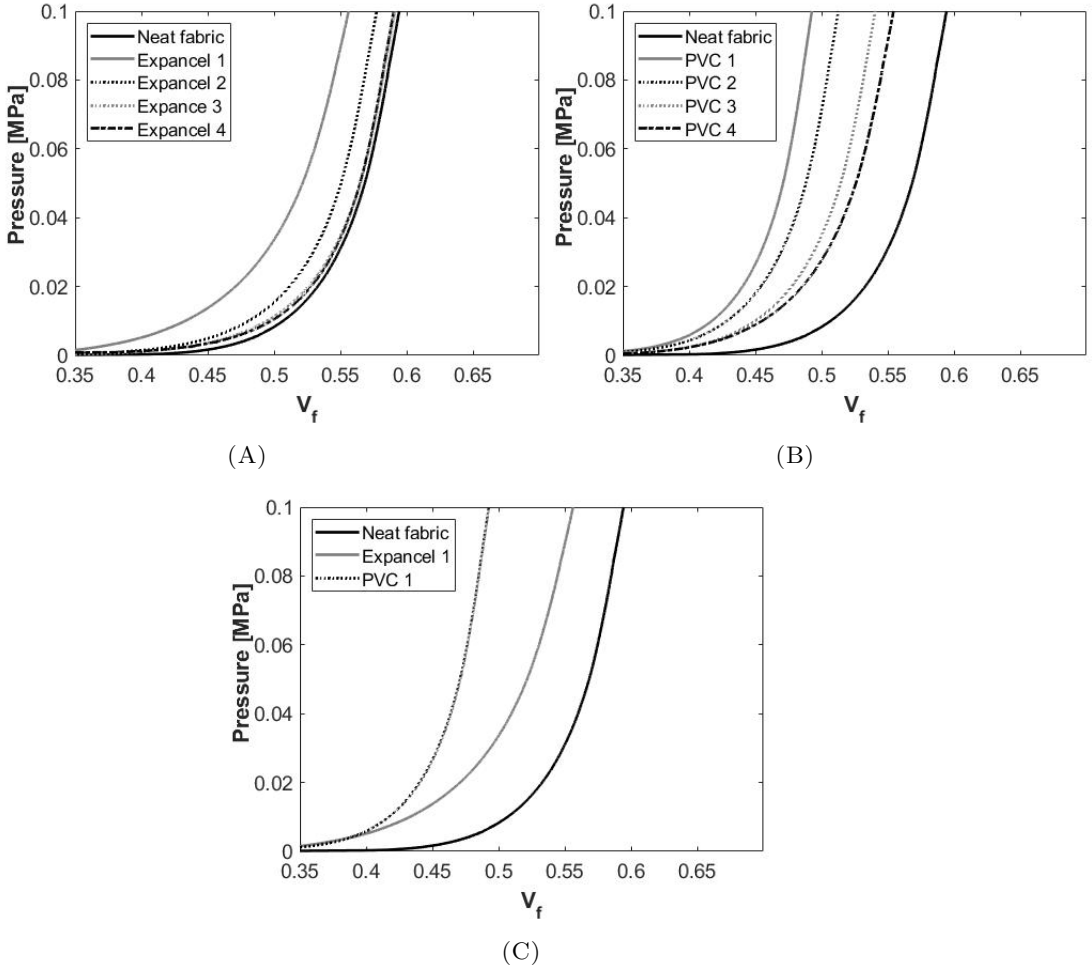

FIGURE III.7: Effect of (A) compressible and (B) rigid particle addition on the fabric compaction behavior in comparison to non-functionalized fabric, with (C) a comparison between the two types. The numbers 1, 2, 3 and 4 denote the particle volume fractions V_p added to the fabric is: 3.76%, 1.88%, 0.94% and 0.47%, respectively

The fiber volume fraction and thickness values were compared at a fixed pressure (0.1 MPa) for a solid understanding of the different compression results. This comparison

was established in Figure III.8 for the two types of particles at the four explored V_p values. A higher thickness increase was achieved by adding the plain particles (2.94 mm at V_p= 3.76%) compared to an overall thickness of 2.59 mm with Expancel. At the same time, higher V_f increase was achieved by the incorporation of compressible microspheres (49.8% at V_p= 0.47%) versus 45.9% with PVC particles incorporation at the same V_p.

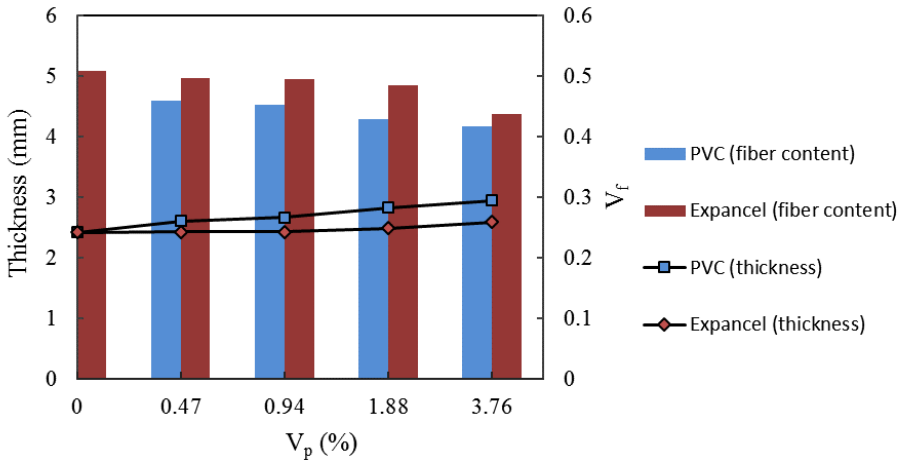

FIGURE III.8: Thickness and fiber content of the stack as a function of particle content at a pressure value of 0.1 MPa

The results of compression tests with PVC are consistent with the previous study of Manfredi and Michaud performed for self-healing inclusions at V_p= 2.5%, 5% and 7.5% [13]. The overall thickness increase is caused by the solid nature of particles in both studies. The unloading phase of functionalized fabrics in the same study exhibited a disordered behavior. Particles were examined under the optical microscope after each compression test. It was observed that PVC particles were not crushed under pressure as no debris was found on the fabric. A small minority of Expancel particles were damaged by plastic deformation. Manfredi and Michaud [13] reported an increase of porosity with the addition of capsules compared to the plain fabric, which indicates that these capsules form a hindrance for fabric packing. However, a decrease in porosity is observed for the highest particle content (7.5%) at high pressures due to particle rupture.

III.4 Results on flow experiments

The in-plane permeability under unsaturated and saturated conditions is measured for all the experiments listed in Table III.1 in the fiber direction. The model fluid is injected at a constant pressure of 1.2 bar. The evolution of flow front positions with time is registered with a camera and extracted using Aphelion's image treatment software. The room temperature is recorded for viscosity calculation. The unsaturated permeability is then determined using the interpolation method, as explained in section II.2.4.2. After the complete impregnation of the preform, the model fluid leaves the mold to the weighing scale. The mass of the outlet fluid is recorded for three minutes at different pressure

values between 0.9 and 1.6 bar and used to calculate the mass flow rate. The saturated permeability is then determined using Darcy's law (Equation II.10) according to the method described in II.2.4.2 (for more details on permeability measurement methods refer to section II.2.4). In the following, the results on the saturated and unsaturated permeability of particle-filled preforms are presented, discussed and compared. The outlet fluid was observed after each experiment; no particle wash-out was noticed for both types. This confirms that particles remain on the fabric till the end of impregnation, thanks to the particle attachment method.

III.4.1 Unsaturated permeability

The effect of particle volume fraction V_p on the unsaturated permeability of the quasi-UD fabric is outlined in Figure III.9. This Figure illustrates the evolution of the unsaturated permeability K_{unsat} for Expancel particles (40 and 120 μm), PVC particles and the neat fabric. The permeability is plotted versus the porosity (Figure III.9 A) and the particle volume fraction V_p (Figure III.9 B). These figures show that the addition of both types of particles decreases the unsaturated permeability as a function of the particle content. As the V_p decreases, the porosity increases, and the permeability tends to converge to the neat fabric permeability value. This trend is observed for all the particle volume fractions except for one point at V_p= 0.47%, where the permeability dropped sharply, to increase again at higher V_p values. This phenomenon could be explained by one of these hypotheses:

1. In the Kozeny-Carman relation (Equation VI.37), the permeability is inversely proportional to the squared specific surface of the porous medium S. The value of S shows complex trends as a function of V_p. At low V_p, the specific surface of the structure increases, leading to a drop in permeability in the order of S^2. With the increase of V_p, S starts to decrease slightly as a result of network formation by fibers and particles, which explains the re-increase of the permeability at V_p= 0.94% [90].

2. According to Caglar et al. [87], the permeability is a result of two competing mechanisms: the opening of new pores and the obstruction of the existing pores by particles or by fiber nesting. Particles of low V_p mainly fill the macropores while higher particle content increases the size of macropores. The drop in permeability at V_p= 0.47% means that the prominent mechanism is the filling of existing macropores by the deposited particles.

The solid particles resulted in the highest permeability values that are close to the clean fiber bed. As for the hollow microspheres, the lower grade (40) resulted in a permeability higher than the one obtained with the addition of the larger size grade (120). This is

explained by the fact that smaller sizes do not obstruct the macropores, it constitutes smaller gaps that could conserve the pore continuity. It is important to note that at a fixed porosity (1-V_f-V_p), the addition of solid particles resulted in higher unsaturated permeability than with the unfilled fibrous bed. In other words, part of the fiber volume can be replaced by solid particles to enhance the permeability of the fabric, along with keeping the same pore percentage.

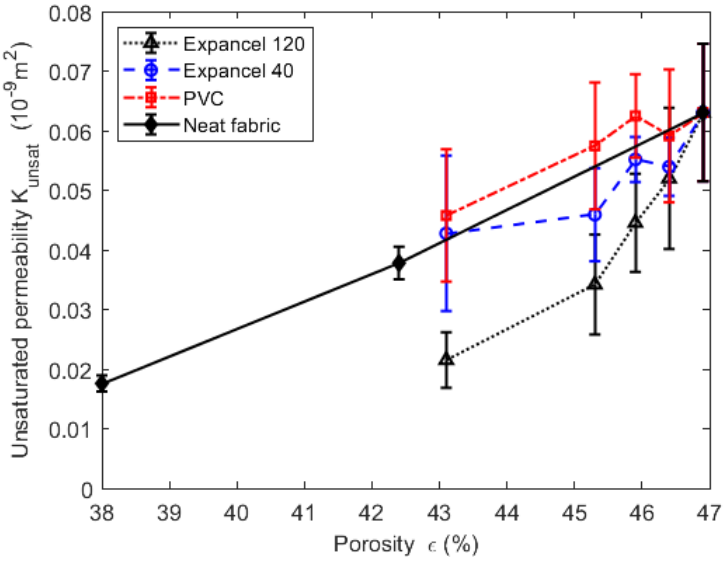

(A)

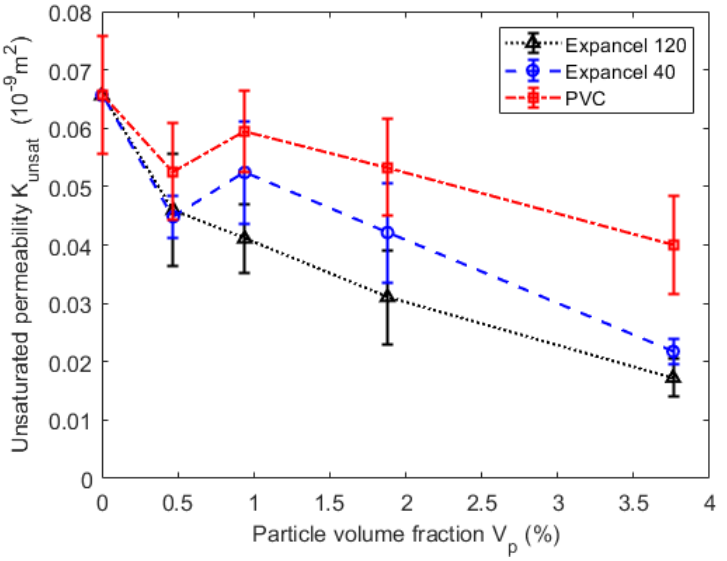

(B)

FIGURE III.9: The evolution of the unsaturated permeability with (A) particle volume fraction V_p and (B) porosity ϵ. Each of the permeability values shown below is an average of three experiments

III.4.2 Saturated permeability

The influence of particle deposition on the saturated permeability K_{sat} is presented in Figure III.10 as a function of porosity (Figure III.10 A) and V_p (Figure III.10 B). A similar permeability trend as K_{unsat} is found for K_{sat}. The saturated permeability dropped with the increase in particle content and increased with porosity. Fabrics functionalized with PVC particles marked higher permeability than with the compressible microballoons. The addition of Expancel 120 exhibited lower permeability than with the lower grade Expancel 40.

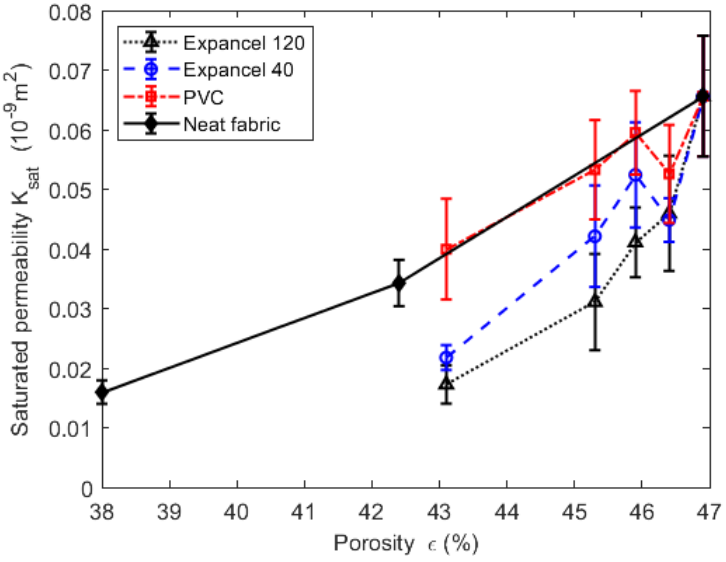

(A)

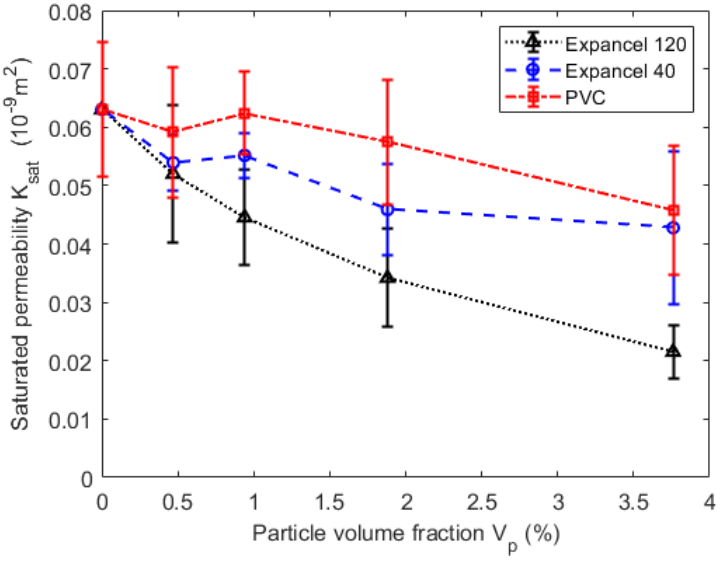

(B)

FIGURE III.10: The evolution of the saturated permeability with (A) particle volume fraction V_f and (B) porosity ϵ. Each of the permeability values shown below is an average of three experiments

These results show that the permeability of functionalized reinforcement is strongly dependent on the particle nature. Results highlight that K_{unsat} and K_{sat} permeabilities for a quasi-UD fabric functionalized with rigid particles are higher than the one filled with hollow compressible microspheres at the same porosity and V_f. The addition of fillers alters the architecture of the porous medium according to their nature. Rigid particles constitute a hindrance between stacks, leading to a local increase of the pore size, translated by the permeability increase. Whereas the compressible particles fit into the existing macropores, adjust their shape accordingly, filling the channels and reducing the permeability values compared to quasi-UD fabric without inclusions.

To quantify the influence of particle addition, K_{unsat} and K_{sat} are normalized to the neat fabric permeability as follows:

$$K^*_{unsat} = \frac{K_{unsat}}{K_{unsat-UD}} \tag{III.7}$$

$$K^*_{sat} = \frac{K_{sat}}{K_{sat-UD}} \tag{III.8}$$

The calculated values of these ratios on Figure III.11 confirm that, at the same V_f (53.1%), both K_{unsat} and K_{sat} decrease by the addition of particles as a function of their volume fraction. However, at a given V_p (or ϵ), this figure highlights two important results:

1. There is a significant decrease in the permeability with compressible inclusions (Expancel 120 and 40) in comparison to rigid ones (PVC) with comparable sizes.
2. K_{unsat} is slightly more affected by the addition of particles than K_{sat}. This is because particles add more resistance to flow during the transitory phase.

The permeability of a given fabric structure is directly related to its compaction behavior. Hollow particles which were more compressed with pressure resulted in a lower permeability. On the other hand, rigid inclusions which increased the overall stack thickness and thus the porosity of the medium have given higher permeability values. This could explain the permeability differences between the two types of particles at the same V_f and V_p. Compression curves have further emphasized the permeability results on the difference between rigid and compressible particles and their effects on particle-filled reinforcements.

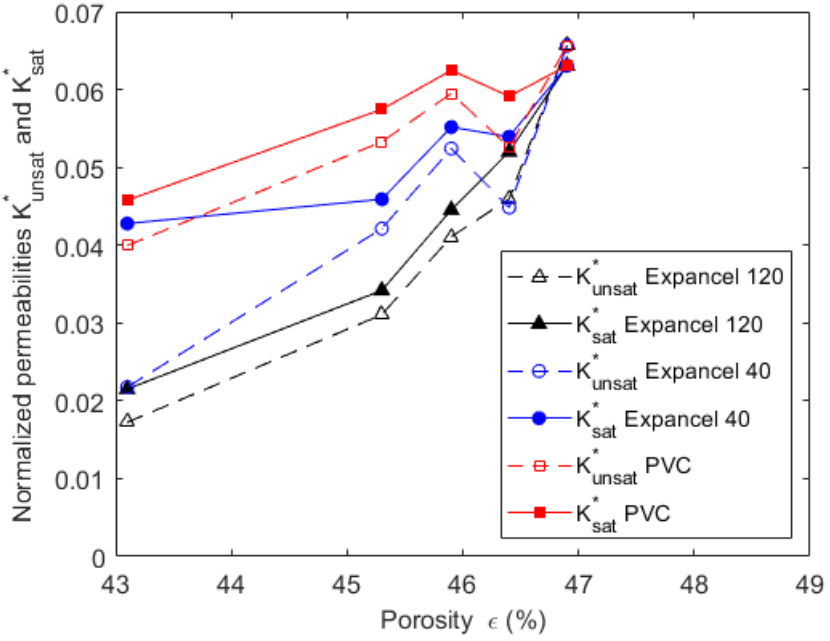

FIGURE III.11: Normalized unsaturated and saturated permeabilities $K_{unsat}{}^*$ and $K_{sat}{}^*$

III.4.3 Permeability ratio

The permeability ratio (R_s) is the ratio between the unsaturated to the saturated permeability. It is given by:

$$R_s = \frac{K_{unsat}}{K_{sat}} \tag{III.9}$$

Figure III.12 presents the evolution of R_s as a function of V_p for the three categories of particles. It can be observed that R_s decreases monotonously with preform functionalization for all particle types, except at V_p= 0.47%, where a sudden drop occurs (corresponding to the permeability behavior at this particle content). Comparing the three particle categories, R_s exhibited similar values at the range of the experimental error up to V_p= 1.94%. After this percentage, the gap between the different R_s values is highly widened at the maximum explored V_p (3.75%). At this point, higher R_s values are found with rigid inclusions than with compressible ones. Moreover, larger compressible particles Expancel 120 exhibited a higher permeability ratio than Expancel 40, which means that there is a limit of V_p after which the effect of particle size and type becomes prominent on the permeability behavior. The R_s was slightly higher than 1 for the neat fabric (1.05), while it dropped to values lower than 1 with particle addition. This means that the addition of particles has altered the fluid behavior from wetting to non-wetting. The findings of this study agree with the results of Caglar et al. [23] for composites with glass inclusions.

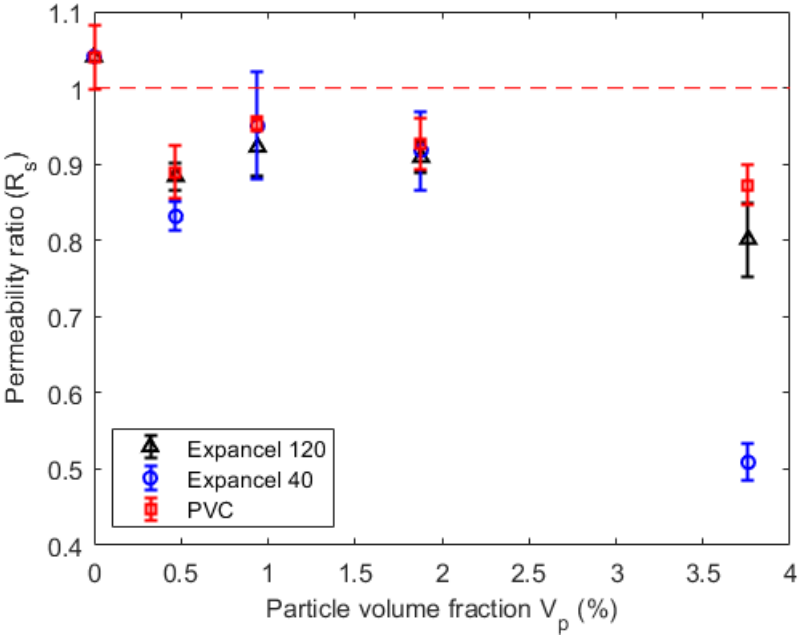

FIGURE III.12: Evolution of the permeability ratio R_s as a function of particle volume fraction V_p

III.4.4 Evolution of pressure

The time evolution of pressure is recorded every 30 seconds with the help of pressure sensors distributed along the mold length. The timely evolution of pressure is plotted in Figure III.13 for all the sensors at their different locations (Expancel 1 case in Table III.1). The pressure profile can be divided into three zones: (1) a first zero pressure zone for which the liquid has not yet reached the sensor, (2) a second zone corresponding to the arrival of the liquid and the progressive filling of the preform adjacent to this sensor and (3) a third zone which begins when the liquid leaves the preform. From this point on, the pressure tends to gradually stabilize towards a constant value that depends on the sensor location from the inlet.

III.4.5 Flow front advancement

Flow front positions were compared in Figure III.14 for PVC and Expancel particles at different particle volume fractions at 3 min from the beginning of impregnation. It was found that the addition of particles delays the flow front as a function of V_p. However, the flow front was more advanced with PVC particles than with Expancel ones at the same instant of time and with the same V_p. Furthermore, it was observed visually that the addition of particles gives a more regular flow front and reduces the fingering effect. This observation needs to be investigated closely.

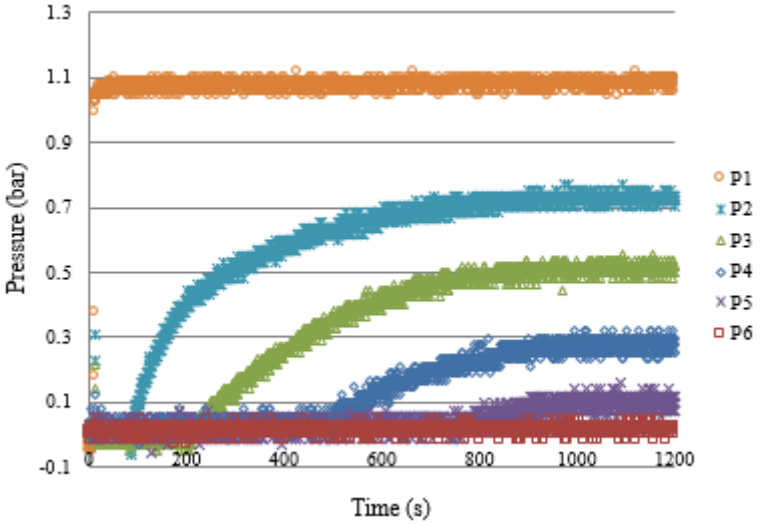

FIGURE III.13: Evolution of pressure with time and position

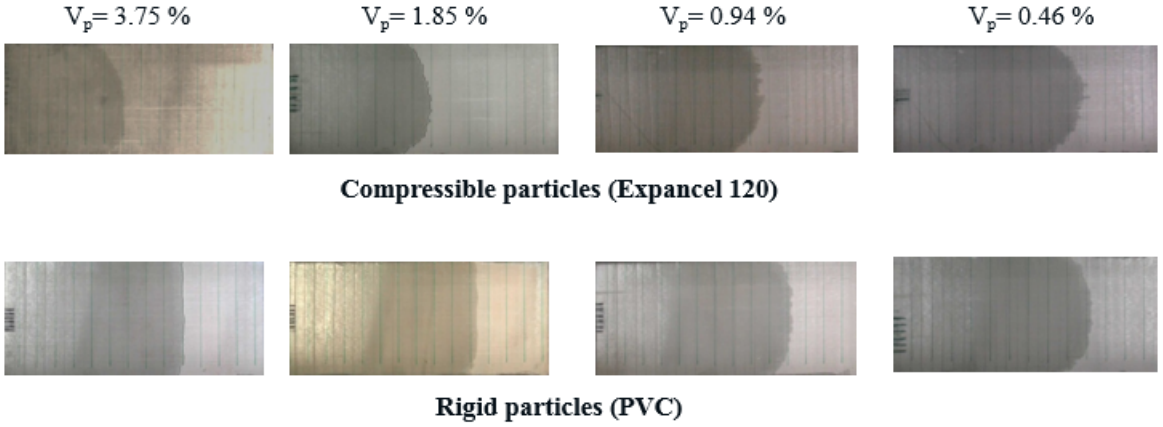

FIGURE III.14: Flow front positions at t=3 min for Expancel 120 and PVC particles at different V_p

III.4.6 Impregnation time

The addition of spherical inclusions induced a delay in flow front advancement, translated by an increase in impregnation time. For each experiment, filling time in the presence of particles t_i was normalized to the one with the neat fabric t having the same fiber content:

$$t^* = \frac{t_i}{t} \tag{III.10}$$

t_i is the filling time of the study case, t is the filling time of the neat fabric.

Figure III.15 compares the normalized values t* of the compressible particles to the rigid ones as a function of V_p. Interestingly, it was found that the filling time increases quasi-linearly with the particle volume fraction for all the categories and sizes of particles.

However, this increase is higher and steeper for Expancel ones at the same V_p and can reach up to 2 times higher than the rigid ones. The larger size of the hollow particles (Expancel 120) imposed longer impregnation cycles in comparison to Expancel 40 for half of the V_p values and similar for the other half.

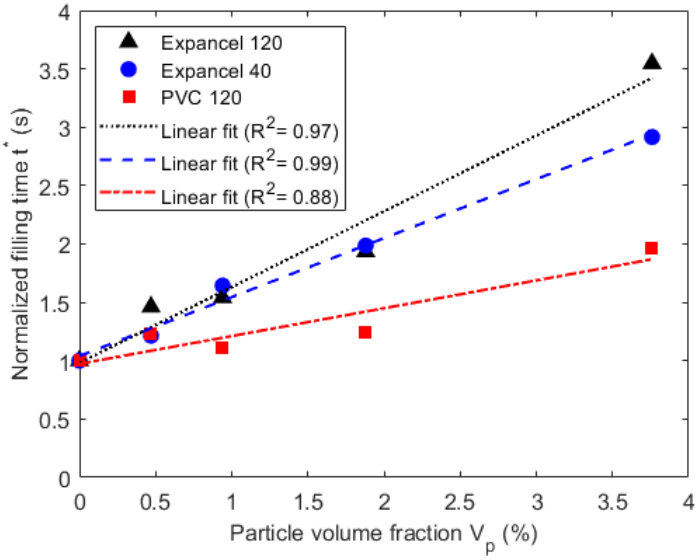

FIGURE III.15: Comparison between the normalized filling times for the compressible and rigid particle-loaded preforms

III.4.7 Capillary number

The capillary number (Ca) characterizes the ratio between viscous to capillary forces. At high Ca, when viscous forces are dominant, fluid flows easily in the macro channels. When capillary forces prevail, fluid flows faster in micropores (low Ca). The capillary number is responsible for the discrepancy between the unsaturated and saturated permeability values. It also determines voids entrapment tendency. It relates the liquid and preform properties with the injection conditions. Ca was determined for all the experiments throughout the impregnation process using:

$$Ca = \frac{\eta v}{\gamma} \tag{III.11}$$

where η is the viscosity of the silicone oil, γ its surface tension at the liquid-vapor interphase and v is the fluid velocity. Figure III.16 gives the capillary number values throughout the experiments versus time normalized to the final filling time of each case. The results are presented for the compressible microballoons (Figure III.16 A) and the solid inclusions (Figure III.16 B). Results revealed that the capillary number with compressible inclusions is lower than that of the neat fabric. While experiments with rigid ones were comparable to the Ca of the non-functionalized fabric. It was found

that the addition of the compressible microspheres reduces the Ca of fabric towards its optimal value. The optimal capillary number Ca_{opt} is defined as the value at which the capillary and hydrodynamic forces compensate and fluid flows at the same velocity in the inter-tow and intra-tow regions leading to a minimum amount of entrapped voids in the final part. It is indicated with a red dashed line in Figure III.16. The Ca_{opt} depends on the type and architecture of the reinforcement [51]. For the same quasi-UD fabric used in this study, Ca_{opt} was found to be in the order of 1.2 10^{-3}, with a minimum void percentage of 2% [91]. At Ca values lower than Ca_{opt}, the fabric tends to entrap macro-voids. Above Ca_{opt}, the fabric tends to entrap micro-voids. According to these outcomes, Expancel particles may ameliorate the impregnation and thus result in a lowering voids entrapment. For the compressible particles, Ca_{opt} is situated between 0.94% and 1.88%. Below these percentages, capillary forces prevail (indicating macro-voids). Higher than this limit, micro-void entrapment is enhanced. This indicates that high V_p creates larger-sized flow channels. For the explored experiments, an optimal percentage of hollow microspheres remarkably improved the capillary number. However, hollow microspheres should be taken as they can themselves be considered voids, with a known percentage. The effect of hollow particles on the mechanical properties should also be investigated extensively.

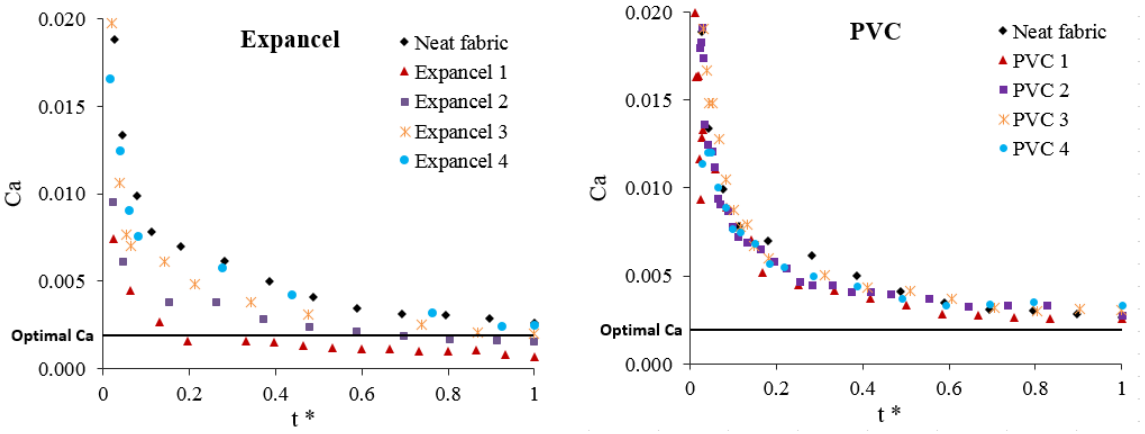

(A) (B)

FIGURE III.16: Time evolution of capillary number Ca for the (A) rigid and (B) compressible particles. The superscripts 1,2,3 and 4 denote the particle volume fractions 3.76%, 1.88%, 0.94% and 0.47% respectively

III.5 Discussion on compression and permeability tests

The influence of the particles on the fibrous structure depends on their nature; the elastic microspheres are compressed with behavior comparable to the fabric response. In contrast, rigid ones keep their original shape between plies of fabric, opening the macropores. It is important to highlight that in the case of the rigid inclusions, the increase in particle size may increase the permeability due to significant pore opening.

Inversely, with compressible microspheres, the increase in particle size at fixed volume fraction decreased the permeability. The influence of the compressible microspheres on permeability herein can be compared to that of the small beads, which filled the existing micropores. Whereas the rigid particles act like the large-sized particles in [87]. Caglar et al. highlighted in their study that when particles are added to fibrous preforms, one of these scenarios may occur according to the critical particle content: they fill the empty pores without significantly influencing the preform consolidation, or they cause an out-of-plane fiber bending. The probability of the second scenario is increased with the increase in particle size and/or volume fraction.

The type of fibrous reinforcement plays an essential role in the general behavior of the stack. In the case of woven fabrics, particles tend to fall in the interstices. Hence, it does not affect much the empty spaces between the superposed plies. Manfredi and Michaud have stated that, on the one hand, Urea-formaldehyde capsules may break at an applied pressure higher than 1 bar if they are not protected in the interstices of the fabric. On the other hand, pores between tows at these zones will be blocked, leading to a permeability drop [13]. For quasi-UD fabric, most particles are placed on the top surface of the ply, where it will be in direct contact with the upper ply. The deviation from previous studies could be explained by the difference in the used materials, such as the nature of the used particles, whether plain or hollow, rigid or elastic and their size and volume fraction, the type and architecture of preforms as well as the fiber volume fraction, i.e., the number of layers and compaction thickness (mold height).

III.6 Microstructure analysis

The fabrication of composite samples followed the flow experiments and the compression tests to investigate other parameters which were not detectable with the first experiments. Such as the actual placement of particles within the preform plies and their spatial distribution.

III.6.1 Fabrication of particle-filled composite panels

Six composite panels with the dimensions of 200x100x3 mm^3 were fabricated. The same quasi-UD fabric was used at a fixed V_f of 53%. The polyester resin Enydyne 198992A is injected into the medium with a vacuum pressure of 0.5 bar by infusion between two plates. The six experiments were carried out with following particle types and percentages: (1) Neat fabric, (2) Expancel 120 of 3.76% and (3) 1.88%, (4) PVC of 3.76% and (5) 1.88% and (6) Expancel 40 of 1.88% V_p. Figure III.17 illustrates the fabrication process of the particle-loaded composite panels.

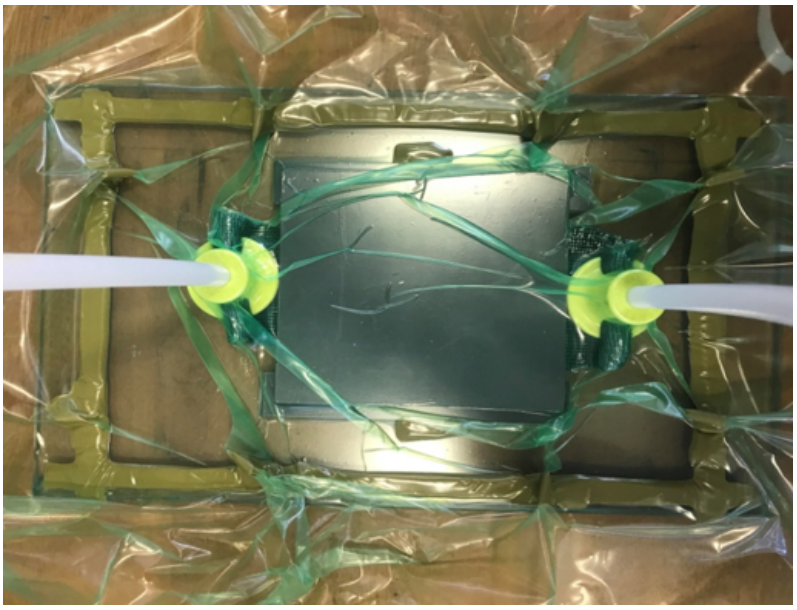

FIGURE III.17: Fabrication of functionalized composite panels using infusion between two plates

After the cure of the composite panels, samples were are cut using water jet cutting to the dimensions (25x10 mm^2). They were then polished and observed under the optical microscope.

III.6.2 Qualitative analysis of microstructure

Microscopic images are post-processed with the help of the image processing software Aphelion. Figure III.18 presents the image treatment process for a composite sample functionalized with 1.64% of PVC particles. The applied steps are as follows:

- the original microscope image is rotated and cropped if needed to keep only the sample area,
- the image is transformed to a binary image by the threshold,
- micropores are suppressed by mathematical morphology threshold,
- particles are cleaned manually and inter-tow regions that contain resin are separated,
- the three phases are grouped in one image that presents clearly: the tows (in black), the inter-tow region (in gray) and the particle (in white).

From Figure III.18 it can be observed that particles remain in the inter-tow regions. Almost no particles penetrate the intra-tow zones. Images show a clear separation between the reinforcement plies as a result of particle presence.

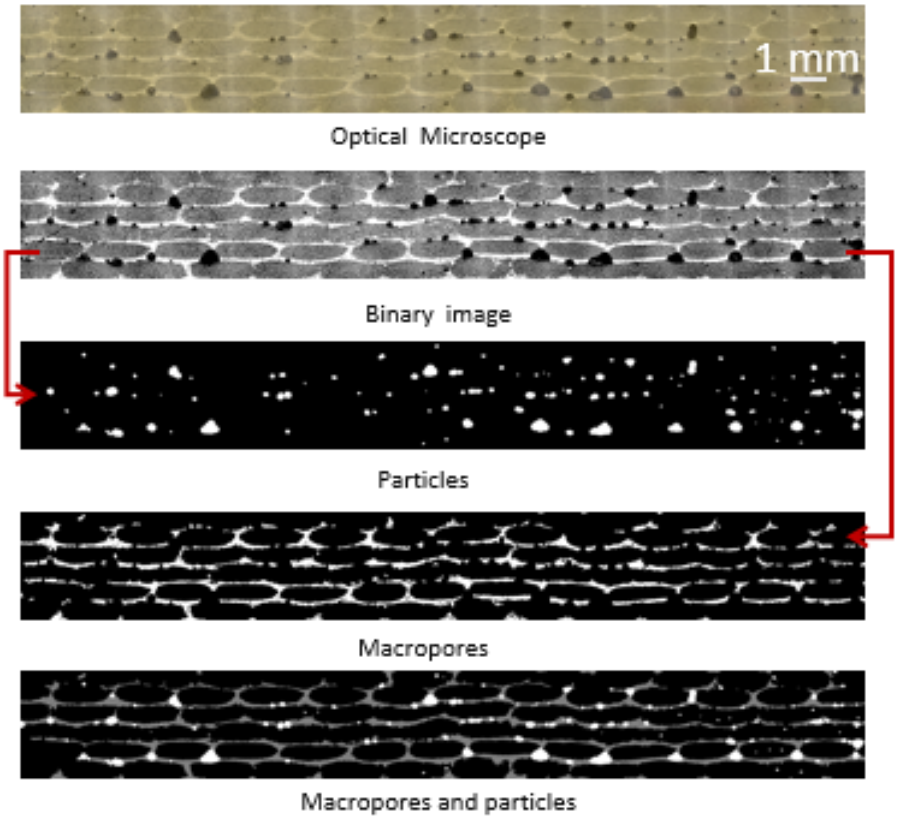

FIGURE III.18: Image processing with Aphelion for a cross-section of a functonalized composite sample constituted of six plies of fabric

The volume and mass of samples are measured, then the density of each sample is determined by dividing its mass by the measured volume. The average density of samples was 1.71 g/cm^3. Results revealed that the Expancel 120 and 40 and PVC particles 120 of 3.76% and 1.88% did not significantly affect the sample density at such low V_p values. The average thickness of the neat fabric samples was 3.31 mm. Expancel 120 and 40 particle grades increased the overall thickness by 1.8%, versus 6.4% with PVC particles at the same V_p (3.74%). With the help of optical microscopy, the thickness of samples was measured at three different locations, at the sample center and two equal distances between the center and the two sample extremities. The standard deviation of the three thickness measurements of each sample has shown that the PVC rigid particles have added higher dimensional stability to the composite panel, with a standard deviation of 0.5-1 μm versus 3.6 μm for neat fabric. The Expancel microballoons registered a standard deviation of 1.5-8.9%μm and 9.5-60.6 μm for Expancel 40 and Expancel 120 respectively.

Figure III.19 presents the microstructures of compressible and solid particle-filled composite panels. The four figures represent receptively the cases of Expancel 120 with theoretical V_p= 3.74% (Figure III.19 A) and 1.88% (Figure III.19 B), and PVC with theoretical V_p= 3.74% (Figure III.19 C) and 1.88% (Figure III.19 D). Cross-sections show that the particles increase the inter-tow spacing, and consequently the overall thickness

of the stack. The compressible microspheres were deformed and tended to fill the existing macropores due to compaction in both inter-plies and inter-yarn spaces. That is why they influenced the thickness only slightly. Hence, these micrographs agree with the permeability findings. It can also be observed that the compressible microspheres are easier to distinguish from resin than the PVC ones.

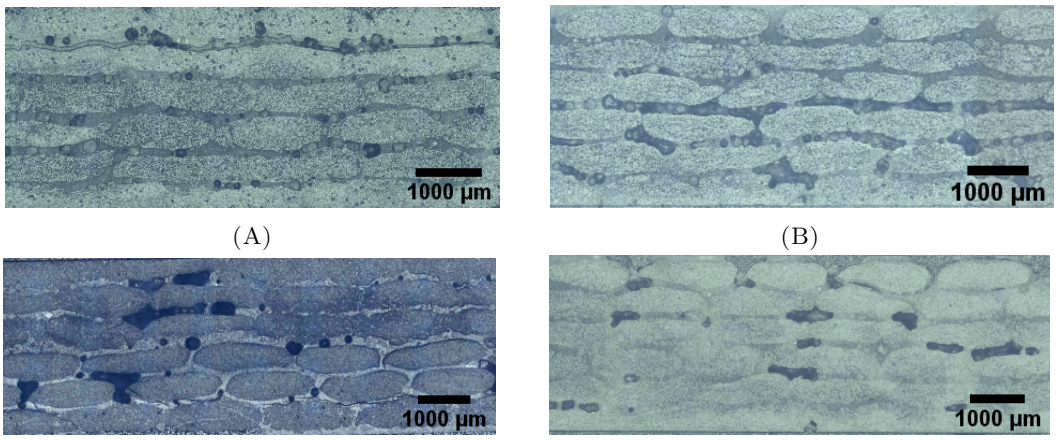

(A) (B)

(C) (D)

FIGURE III.19: Cross-sections of particle-loaded composites with (A) Expancel 120 (3.74%), (B) Expancel 120 (1.88%), (C) PVC (3.74%) and (D) PVC (1.88%)

III.6.3 Particle distribution

Although a uniform particle distribution was assumed, the manual sieving method may result in a disordered particle configuration. The particle and preform characteristics play a major role in the particle distribution within composite laminates. With woven fabric, a quasi-periodic pattern was formed resulting from particle accumulation in the interstices [87]. For the observed samples, the actual V_p was determined using image processing on samples with plain and hollow particles. The experimental V_p herein is assumed to be equivalent to the surface fraction; it is determined by dividing the particle area by the total sample area. For the hollow microspheres (Expancel 120), samples of 3.74% and 1.88% V_p gave values of 3.81% and 1.73% respectively (Error percentage of 1.6% and 7.5%). For PVC particles, V_p of 1.76% and 0.41% are found by image analysis versus theoretical V_p of 3.74% and 1.88%, which gives error percentages of 53.1% and 77.9%. The image processing reproduces acceptably the theoretical fraction of the hollow microspheres because the spherical/oval shape helps to differentiate between a particle and a pore in the characterization stage. For the PVC particles, the foremost cause of the discrepancy is the challenging particle separation from resin. In addition, some of the particles may probably have detached from the sample in the polishing stage. Hence, these errors can be attributed to the lack of proper particle isolation during image processing. From these results, the sieving method gave acceptable particle distribution along the sample length. However, using an automated particle deposition method for

fabric functionalization for more homogeneous distributions is recommended whenever applicable.

III.7 Conclusion

This chapter investigated the influence of fabric functionalization by manual sieving on flow kinetics and compaction behavior of the fibrous structure. Two types of particles with comparable sizes were added to quasi-UD preforms; hollow compressible and plain microspheres. The study examined the influence of fabric functionalization in LCM process on permeability, impregnation time, compression behavior and capillary number. It was found that both unsaturated and saturated permeabilities decreased with the addition of inclusions. However, the unsaturated permeability was more influenced than the saturated one, as particles added more resistance to flow at the transitory injection phase. On the one hand, the compressible microballoons registered steeper permeability reduction than the solid ones at the same V_p and V_f. On the other hand, they contributed to decreasing the capillary number towards the optimal value, and thus their addition could have led to lower void content. It was assumed that Expancel particles are compacted between the preform plies lowering their porosity, while PVC ones formed a hindrance that slightly widened existing pores.

Compression tests were performed to investigate the permeability findings. Expectedly, results revealed that Expancel particles were compressed under applied pressure and slightly increased overall stack thickness. The rigid PVC particles caused a tangible thickness increase. That confirmed the permeability results and explained the behavior of each type of particle. The qualitative analysis of the microstructure of the fabricated panels confirmed that the compressible particles fit the existing pores while solid inclusions increase thickness by creating a barrier between plies. There were significant differences between the theoretical V_p and the one characterized by optical imaging with the PVC particles. However, the analysis has shown a good agreement between theoretical and experimental V_p with the compressible microspheres.

The improvement of the capillary number resulting from the addition of hollow compressible microspheres raises an important question: Does encased voids with known percentage and distribution improve void entrapment behavior? However, due care must be paid to the evolution of mechanical properties with hollow microspheres. Therefore, developing an analytical model is vital for predicting the bulk permeability of the functionalized fabric. The model should consider the particle nature (solid or compressible), size, and particle volume fraction. For simplification, the model could assume a homogeneous and constant porosity of the medium, considered as the $1 - V_f$-V_p.

After studying the influence of particle addition on the preform, the next chapter will address the resin functionalization. For the coming part, the assumption of homogeneous particle distribution will no longer be valid. The influence of the used method on the flow process will be studied in detail. Chapter IV sheds new light on the effect of multiple process and material variables on the flow and filtration kinetics. The focus will be drawn on the filtration of suspensions of polydisperse particles through fibrous media and the evolution of their spatial distribution. Now that the effect of particle addition V_p at fixed size is studied, the next chapter will characterize the effect of size and percentage of solid particles on their distribution along the part length.

Chapter IV

Filtration of particle-loaded resin through fibrous media

IV.1 Introduction

The previous chapter (III) addressed one of the composite functionalization methods, i.e., the addition of particles to fibrous preforms by direct sieving. This chapter deals with one of the most familiar particle addition methods: the incorporation of particles into the liquid resin and the injection of suspension into fibrous media. However, this method adds several challenges to the impregnation process: the increase of resin viscosity, the decrease in the preform permeability and the particle capture by the medium with different mechanisms leading to their non-homogeneous distribution within the part. Consequently, the presence of particles can lead to additional issues, such as the increase of process time and the entrapment of air bubbles. In this chapter, and the impregnation process becomes more complex as it groups high variable interdependencies. Herein, the problem of resin infiltration becomes a problem of particle filtration [43, 52, 63] and the final particle distribution is the key question.

Throughout literature, particle distribution has been investigated using different characterization methods, as presented in section I.4. Thermal decomposition was used for measuring the total particle content in cured samples [8, 36, 40, 60]. Although proven efficiency, the burn-off method exhibits several drawbacks, such as being a destructive, expensive and time-consuming test technique. Particle content was also characterized using optical methods such as microscopy [25], micro-particle image velocimetry (μ-PIV) [39] and SEM analysis [37, 40]. However, using the imaging techniques, the estimation of particle concentration is limited to the viewing window and does not always provide a representative estimation for the whole sample. Other techniques included the use of test fluids for the measurement of particle content (non-cured composites) [43]. Herzig

[42] presented a testing methodology for the study of filtration in granular media for water treatment purposes. In this method, the extracted suspensions are examined under light scattering to determine the particle concentration. The methodology used by Herzig is an effective way for the extraction of samples. According to the author, the light scattering technique for concentration measurement could be inaccurate and not representative of the concentration in the whole suspension sample. Therefore, there is a need for an improved non-destructive method to extract suspensions samples along with a trusted and precise characterization method for particle content.

This part investigates the spatial evolution of particle concentration throughout the fibrous medium. An experimental study at the preform-scale is carried out to address the flow and filtration behaviors of suspensions. Micron-scale plain particles of polydisperse distributions dispersed in glycerol aqueous mixtures are used for the flow experiments. The sampling method presented in this study is inspired by the work of Herzig for water treatment purposes applied herein to the RTM process. Concentration is characterized using a simple and accurate method with proven efficiency, which is the measurement of the suspension effective density [92]. The influence of five main process and material variables was investigated. In addition to the characterization method, the study novelty lies in the polydispersity of particles, as it raises new questions such as: will the size distribution remain constant throughout the part length? what is the evolution of the median size? what are the retention mechanisms and capture sites for the different size categories?

The objectives of this chapter are summarized as follows:

- studying the general behavior of flow and filtration of polydisperse particles through fibrous media,
- analyzing the influence of process and material parameters on particle deposit,
- exploring the evolution of particle size distribution throughout the part length between the inlet and outlet of the preform,
- extracting the particle distribution of retained particles,
- identifying the main mechanisms of particle filtration.

IV.2 Experimental methodology

The plies of fabric are stacked in the mold cavity, the mold is closed, the inlet pressure is set, and the suspension is injected into the fibrous medium at a known initial concentration. The concentration value varies with the traveled distance because the fibrous medium retains part of the suspended particles. The experimental method used

in this study measures the particle concentration along the preform length at the end of impregnation. The developed technique is inspired by the study of Herzig [59] in his analysis of the filtration of aqueous suspensions in granular media for water treatment applications in vertical columns.

IV.2.1 Materials

The present section summarizes the parameter values of materials used in this chapter. The characterization of each material is detailed in chapter II.

Preform

The quasi-unidirectional fabric described in II.2 is used for this experimental investigation. For a mold thickness of 2.63 mm, three fiber volume fractions were explored for the filtration experiments: 38%, 48% and 58%, with of 4, 5 and 6 plies respectively. The plies had a width of 100 mm and a length of 420 mm. Throughout this chapter, only one type of textile is explored to eliminate the variations induced by fabric architecture and highlight the influence of other variables such as fiber volume fraction. The characterization of the used fabric is detailed in section II.2.

Model fluid

Glycerol aqueous solutions are used as the model fluid. Glycerol S67922 from Sonodis with a density of 1.225 g/cm^3 is mixed with purified water with the percentages of 75%/25% and 88%/12% (by mass). The mixtures have respective density values of 1.19 and 1.20 g/cm^3, and viscosity values of the without particles η_0 of 0.035 $\pm$0.002 Pa.s and 0.175 $\pm$0.003 Pa.s. Starting from η_0, the addition of particles increases the viscosity as a function of their concentrations. The evolution of viscosity with particle concentration is addressed in section II.5.2. To avoid particle sedimentation and agglomeration, the dispersing agent BYK-w-940 is added to the fluid with a percentage of 1% from the mass of the added particles. The specifications of these mixtures are presented in II.3.2.

Particles

Ceramic particles from 3M are used with three different grades (W-210, W-410 and W-610). Each grade represents a specific size distribution, with median particle sizes of 5.2 μm, 7.9 μm and 15.2 μm respectively. The properties of each grade are detailed in Table II.4 of section II.4.0.2. From the SEM and granulometry analysis, particles exhibited a wide polydispersity, with particle sizes ranging from less than 1 μm to 100 μm.

IV.2.2 Experimental set-up

The permeability measurement bench used in chapter III and described in II.2.4.1 was adjusted to meet the experiment requirements. Four hollow screws were installed at the bottom of the mold (Figure IV.4). Each screw was connected to a tube to allow the collection of the suspension at specific locations. The sampling tube has an internal diameter of 6 mm. The sampling hole that connects the tube to the mold has an internal diameter of 2 mm. The end of each sampling tube is attached to a valve, which is kept closed during the impregnation. After the completion of the experiment, valves are opened to collect the suspension samples. The plies are stacked in the fiber direction at the center of the mold giving symmetric distances from the middle of the preform to the inlet and the outlet of the mold. A silicon joint was placed between the reinforcement and the mold to avoid edge effects. The same injection unit Hypaject and acquisition system described in II.2.4.1 is used for the suspension injection during filtration experiments. The pressure is set to 1.0 or 1.4 bar for all the filtration experiments. The flow front advancement is recorded by a camera. Figure IV.4 presents a schematic of the testing facility.

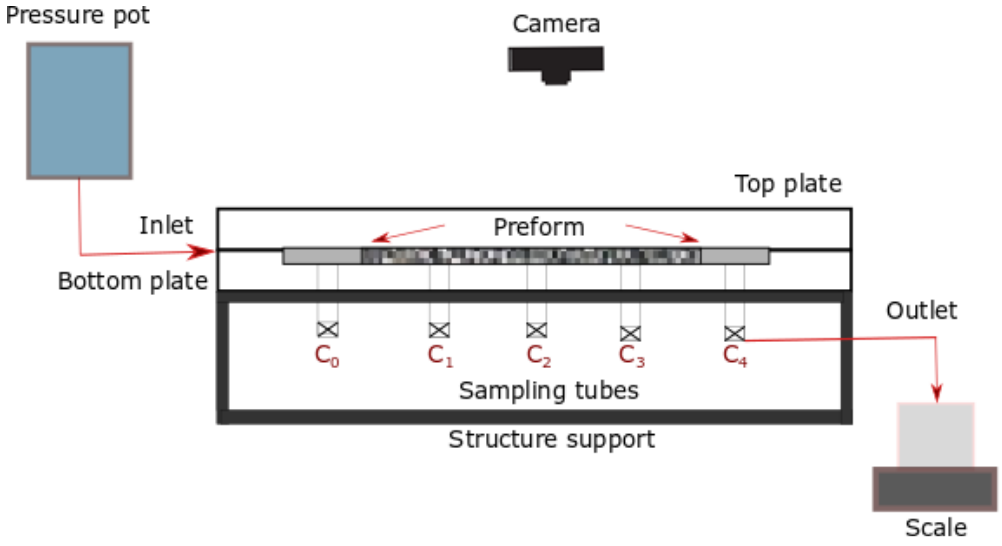

FIGURE IV.1: Scheme of the experimental set-up (front view)

Sampling tubes

Five sampling tubes are distributed throughout the bottom surface of the mold as follows: C_0 located at the mold inlet, C_1, C_2, C_3 are located at equal distances of 12.5 cm from each other throughout the reinforcement and C_4 is the outlet of the mold (Figure IV.5). The numbers 0, 1, 2, 3 and 4 refer to the location of the sampling point from the inlet, whereas C stands for concentration. The sampling tube has an internal diameter of 6 mm. The sampling hole that connects the tube to the mold has an internal diameter

of 2 mm. The sampling tubes, as well as the pressure sensors, are illustrated by Figure IV.6.

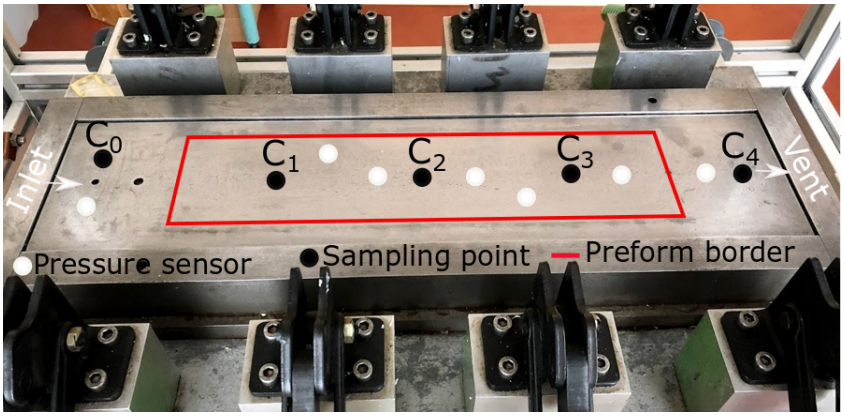

FIGURE IV.2: Positions of the sampling points in the mold

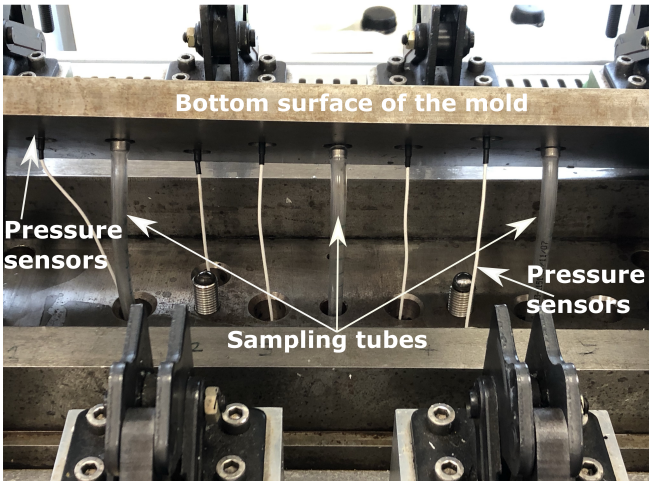

FIGURE IV.3: Installation of sampling tubes at the bottom surface of the mold

IV.2.3 Parameters and protocol

Five series of experiments were carried out. For each series, one variable was changed while the others were kept constant. Table IV.4 presents all the studied ranges of variables: initial concentration C_0, injection pressure P_0, initial viscosity η_0, fiber volume fraction V_f and particle size d_p. The fibrous bed had volume fractions of 38%, 48% and 58%. Neat fluid had initial viscosities (without particles) of 0.035 and 0.175 Pa.s. The injection was realized at a constant pressure of 1.0 or 1.4 bar. Particle size distributions in suspensions had median diameters of 5.2 μm, 7.9 μm and 15.2 μm. Low particle concentrations are chosen to avoid clogging that could arise from high particle content and the particle-particle interactions that significantly increase the viscosity. Each line of Table IV.4 presents a series of experiments with only one variable per experiment.

TABLE IV.1: Experimental conditions

Figure No.	Examined variable	C_0 (%)	P_0 (bar)	η_0 (Pa.s)	V_f (%)	$d_p(\mu m)$
Fig. IV.8 and Fig. IV.10	Initial concentration C_0 (%)	1 3.7 6.8	1.0	0.035	48	15
Fig. IV.11 and Fig. IV.12	Initial Injection Pressure P_0 (bar)	3.7	1.0 1.4	0.035	48	15
Fig. IV.13 and Fig. IV.14	Initial viscosity η_0 (Pa. s)	3.7	1.0	0.035 0.175	48	8
Fig. IV.15 and Fig. IV.16	Fiber volume fraction V_f (%)	3.7	1.0	0.035	38 48 58	15
Fig. IV.17 and Fig. IV.18	Median diameter of particles $d_p(\mu m)$	5	1.0	0.035	38 48	5 8

Each viscosity value corresponds to a specific glycerol/water percentage, η_0= 0.035 Pa.s (75%/25%) and 0.175 Pa.s (88%/12%).

Experimental protocol

All the filtration experiments are performed following the protocol detailed in Table IV.5 according to the parameters presented in Table IV.6.

IV.2.4 Suspension preparation

Three main concentrations were prepared and explored through the series of experiments: 1%, 5% and 10%. Flow experiments without particles were carried out for comparison. The required particle mass for each concentration is determined using Equation IV.2. Where w_p is the particle mass, ρ_p is the true density of particles and V_l is the volume of liquid.

$$w_p = \frac{\rho_p C}{1 - C} V_l \tag{IV.1}$$

The dispersing agent BYK-w-940 is added to the mixture with a percentage of 1% from the mass of the added particles to ensure a homogeneous suspension and to avoid the agglomeration and the settling of particles (as mentioned in II.3.4). Table IV.6 presents the particle content in volume and mass, as well as the required mass of the dispersing agent.

IV.2.5 Concentration and density measurement

At the end of each experiment, sampling tubes are emptied into separate containers. The suspension is then dispersed with the magnetic stirrer FB15001 for 30 minutes. Then the density of the suspension is measured using a 5 ml capacity pycnometer. Knowing the mixture density ρ_e, the neat liquid density ρ_l and the particle density ρ_p, the concentration is deduced using the mixture Equation II.12. This method was chosen

TABLE IV.2: Protocol of filtration experiments

No.	Step	Details
1	Fiber placement	Plies of fabric are cut with the dimensions 100x420 mm^2 and placed in the mold cavity. The mold is closed.
2	Suspension preparation	- The glycerol/water are mixed with the required percentages. - The dispersing agent is added to the fluid. - The particle mass is determined as detailed in IV.4.4 weighed and added to the mixture. - The suspension is dispersed with a magnetic stirrer for a minimum duration of 2 hours till the start of injection.
3	Experiment preparation	The camera is fixed at the top level of the mold to enable the visualization of the flow front advancement. The sampling tubes are closed. The pressure in the injection unit is set to the required value. The acquisition system is checked. A container is installed on the weighing scale.
4	Impregnation	The injection unit is filled with the suspension. The pressure acquisition, the camera and the impregnation are started simultaneously.
5	Sampling	The samples of suspensions are collected at the end of each experiment in separate containers.
6	Concentration measurement	Each container is dispersed with the magnetic stirrer for at least 30 minutes. The density of each sample is measured using a pycnometer, then the concentration is determined.

because it was found a practical, reliable and rapid way for concentration measurement throughout fibrous media for the range of experiments carried out in this study.

IV.3 Introduction

The previous chapter (III) addressed one of the composite functionalization methods, i.e., the addition of particles to fibrous preforms by direct sieving. This chapter deals with one of the most familiar particle addition methods: the incorporation of particles into the liquid resin and the injection of suspension into fibrous media. However, this method adds several challenges to the impregnation process: the increase of resin viscosity, the decrease in the preform permeability and the particle capture by the medium

TABLE IV.3: Volume and mass percentages of particles in suspension samples

Concentration (% vol.)	Particle percentage (%wt.)	Mass of dispersing agent (g)
0	-	-
1	2	0.24
5	10	1.24
10	20	2.62

with different mechanisms leading to their non-homogeneous distribution within the part. Consequently, the presence of particles can lead to additional issues, such as the increase of process time and the entrapment of air bubbles. In this chapter, and the impregnation process becomes more complex as it groups high variable interdependencies. Herein, the problem of resin infiltration becomes a problem of particle filtration [43, 52, 63] and the final particle distribution holds a fundamental question.

Throughout literature, particle distribution has been investigated using different characterization methods, as presented in section I.4. Thermal decomposition was used for measuring the total particle content in cured samples [8, 36, 40, 60]. Although proven efficiency, the burn-off method exhibits several drawbacks, such as being a destructive, expensive and time-consuming test technique. Particle content was also characterized using optical methods such as microscopy [25], micro-particle image velocimetry (μ-PIV) [39] and SEM analysis [37, 40]. However, using the imaging techniques, the estimation of particle concentration is limited to the viewing window and does not always provide a representative estimation for the whole sample. Other techniques included the use of test fluids for the measurement of particle content (non-cured composites) [43]. Herzig [42] presented a testing methodology for the study of filtration in granular media for water treatment purposes. In this method, the extracted suspensions are examined under light scattering to determine the particle concentration. The methodology used by Herzig is an effective way for the extraction of samples. According to the author, the light scattering technique for concentration measurement could be inaccurate and not representative of the concentration in the whole suspension sample. Therefore, there is a need for an improved non-destructive method to extract suspensions samples and a trusted and precise characterization method for particle content.

This part investigates the spatial evolution of particle concentration throughout the fibrous medium. An experimental study at the preform-scale is carried out to address the flow and filtration behaviors of suspensions. Micron-scale plain particles of polydisperse distributions dispersed in glycerol aqueous mixtures are used for the flow experiments. The sampling method presented in this study is inspired by the work of Herzig for water treatment purposes applied herein to the RTM process. Concentration is characterized using a simple and accurate method with proven efficiency, which is the measurement of the suspension effective density [92]. The influence of five main process and material variables was investigated. In addition to the characterization method, the study novelty lies in the polydispersity of particles, as it raises new questions such as: will the size

distribution remain constant throughout the part length? what is the evolution of the median size? what are the retention mechanisms and capture sites for the different size categories?

The objectives of this chapter are summarized as follows:

- studying the general behavior of flow and filtration of polydisperse particles through fibrous media,
- analyzing the influence of process and material parameters on particle deposit,
- exploring the evolution of particle size distribution throughout the part length between the inlet and outlet of the preform,
- extracting the particle distribution of retained particles,
- identifying the main mechanisms of particle filtration.

IV.4 Experimental methodology

The fabric plies are stacked in the mold cavity, the mold is closed, the inlet pressure is set, and the suspension is injected into the fibrous medium at a known initial concentration. The concentration value varies with the traveled distance because the fibrous medium retains part of the suspended particles. The experimental method used in this study measures the particle concentration along the preform length at the end of impregnation. The developed technique is inspired by the study of Herzig [59] in his analysis of the filtration of aqueous suspensions in granular media for water treatment applications in vertical columns.

IV.4.1 Materials

The present section summarizes the parameter values of materials used in this chapter. The characterization of each material is detailed in chapter II.

Preform

The quasi-unidirectional fabric described in II.2 is used for this experimental investigation. For a mold thickness of 2.63 mm, three fiber volume fractions were explored for the filtration experiments: 38%, 48% and 58%, with of 4, 5 and 6 plies respectively. The plies had a width of 100 mm and a length of 420 mm. Throughout this chapter, only one type of textile is explored to eliminate the variations induced by fabric architecture and highlight the influence of other variables such as fiber volume fraction. The characterization of the used fabric is detailed in section II.2.

Model fluid

Glycerol aqueous solutions are used as the model fluid. Glycerol S67922 from Sonodis with a density of 1.225 g/cm^3 is mixed with purified water with the percentages of 75%/25% and 88%/12% (by mass). The mixtures have respective density values of 1.19 and 1.20 g/cm^3, and viscosity values of the without particles η_0 of 0.035 $\pm$0.002 Pa.s and 0.175 $\pm$0.003 Pa.s. Starting from η_0, the addition of particles increases the viscosity as a function of their concentrations. The evolution of viscosity with particle concentration is addressed in section II.5.2. The dispersing agent BYK-w-940 is added to the fluid with a percentage of 1% from the particle mass particles to avoid particle sedimentation and agglomeration. The specifications of these mixtures are presented in II.3.2.

Particles

Ceramic particles from 3M are used with three different grades (W-210, W-410 and W-610). Each grade represents a specific size distribution, with median particle sizes of 5.2 μm, 7.9 μm and 15.2 μm respectively. The properties of each grade are detailed in Table II.4 of section II.4.0.2. From the SEM and granulometry analysis, particles exhibited a wide polydispersity, with particle sizes ranging from less than 1 μm to 100 μm.

IV.4.2 Experimental set-up

The permeability measurement bench used in chapter III and described in II.2.4.1 was adjusted to meet the experiment requirements. Four hollow screws were installed at the bottom of the mold (Figure IV.4). Each screw was connected to a tube to allow the collection of the suspension at specific locations. The sampling tube has an internal diameter of 6 mm. The sampling hole that connects the tube to the mold has an internal diameter of 2 mm. The end of each sampling tube is attached to a valve, which is kept closed during the impregnation. After the completion of the experiment, valves are opened to collect the suspension samples. The plies are stacked in the fiber direction at the center of the mold giving symmetric distances from the middle of the preform to the inlet and the outlet of the mold. A silicon joint was placed between the reinforcement and the mold to avoid edge effects. The same injection unit Hypaject and acquisition system described in II.2.4.1 is used for the suspension injection during filtration experiments. The pressure is set to 1.0 or 1.4 bar for all the filtration experiments. A camera installed at the top of the mold records the flow front advancement. Figure IV.4 presents a schematic of the testing facility.

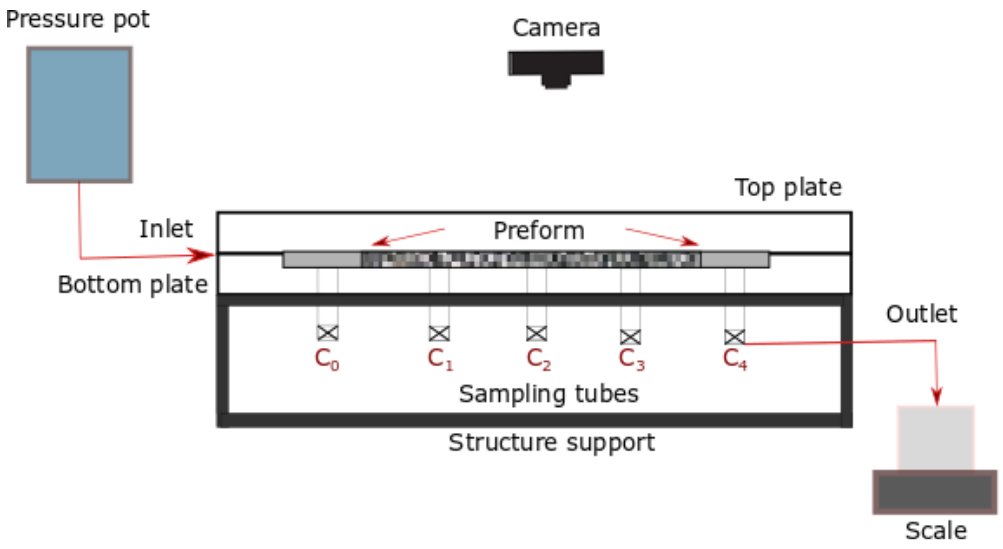

FIGURE IV.4: Scheme of the experimental set-up (front view)

Sampling tubes

Five sampling tubes are distributed throughout the bottom surface of the mold as follows: C_0 located at the mold inlet, C_1, C_2, C_3 are located at equal distances of 12.5 cm from each other throughout the reinforcement and C_4 is the outlet of the mold (Figure IV.5). The numbers 0, 1, 2, 3 and 4 refer to the location of the sampling point from the inlet, whereas C stands for concentration. The sampling tube has an internal diameter of 6 mm. The sampling hole that connects the tube to the mold has an internal diameter of 2 mm. The sampling tubes, as well as the pressure sensors, are illustrated by Figure IV.6.

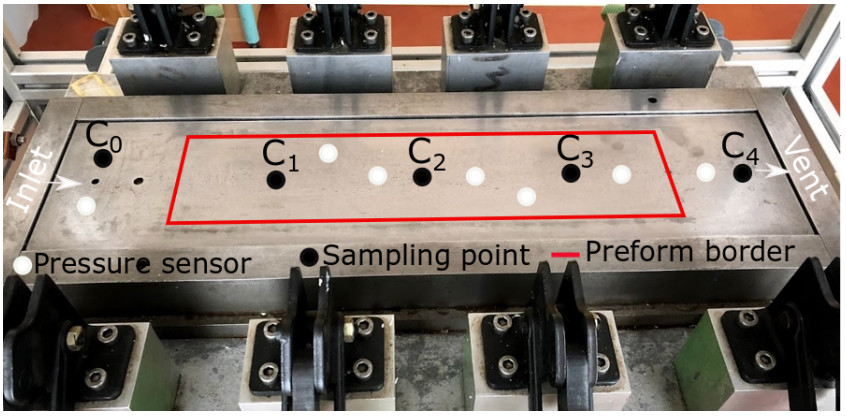

FIGURE IV.5: Positions of the sampling points in the mold

IV.4.3 Parameters and protocol

Five series of experiments were carried out. For each series, one variable was changed while the others were kept constant. Table IV.4 presents all the studied ranges of

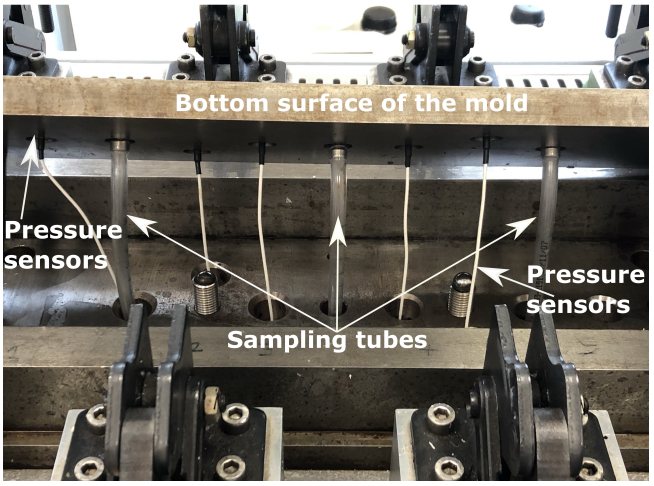

FIGURE IV.6: Installation of sampling tubes at the bottom surface of the mold

variables: initial concentration C_0, injection pressure P_0, initial viscosity η_0, fiber volume fraction V_f and particle size d_p. The fibrous bed had volume fractions of 38%, 48% and 58%. Neat fluid had initial viscosities (without particles) of 0.035 and 0.175 Pa.s. The injection was realized at a constant pressure of 1.0 or 1.4 bar. Particle size distributions in suspensions had median diameters of 5.2 μm, 7.9 μm and 15.2 μm. Low particle concentrations are chosen to avoid clogging that could arise from high particle content and the particle-particle interactions that significantly increase the viscosity. Each line of Table IV.4 presents a series of experiments with only one variable per experiment.

TABLE IV.4: Experimental conditions

Figure No.	Examined variable	C_0 (%)	P_0 (bar)	η_0 (Pa.s)	V_f (%)	$d_p(\mu m)$
Fig. IV.8 and Fig. IV.10	Initial concentration C_0 (%)	1 3.7 6.8	1.0	0.035	48	15
Fig. IV.11 and Fig. IV.12	Initial Injection Pressure P_0 (bar)	3.7	1.0 1.4	0.035	48	15
Fig. IV.13 and Fig. IV.14	Initial viscosity η_0 (Pa. s)	3.7	1.0	0.035 0.175	48	8
Fig. IV.15 and Fig. IV.16	Fiber volume fraction V_f (%)	3.7	1.0	0.035	38 48 58	15
Fig. IV.17 and Fig. IV.18	Median diameter of particles $d_p(\mu m)$	5	1.0	0.035	38 48	5 8

Each viscosity value corresponds to a specific glycerol/water percentage, η_0= 0.035 Pa.s (75%/25%) and 0.175 Pa.s (88%/12%).

Experimental protocol

All the filtration experiments are performed following the protocol detailed in Table IV.5 according to the parameters presented in Table IV.6.

TABLE IV.5: Protocol of filtration experiments

No.	Step	Details
1	Fiber placement	Plies of fabric are cut with the dimensions 100x420 mm^2 and placed in the mold cavity. The mold is closed.
2	Suspension preparation	- The glycerol/water are mixed with the required percentages. - The dispersing agent is added to the fluid. - The particle mass is determined as detailed in IV.4.4 weighed and added to the mixture. - The suspension is dispersed with a magnetic stirrer for a minimum duration of 2 hours till the start of injection.
3	Experiment preparation	The camera is fixed at the top level of the mold to enable the visualization of the flow front advancement. The sampling tubes are closed. The pressure in the injection unit is set to the required value. The acquisition system is checked. A container is installed on the weighing scale.
4	Impregnation	The injection unit is filled with the suspension. The pressure acquisition, the camera and the impregnation are started simultaneously.
5	Sampling	The samples of suspensions are collected at the end of each experiment in separate containers.
6	Concentration measurement	Each container is dispersed with the magnetic stirrer for at least 30 minutes. The density of each sample is measured using a pycnometer, then the concentration is determined.

IV.4.4 Suspension preparation

Three main concentrations were prepared and explored through the series of experiments: 1%, 5% and 10%. Flow experiments without particles were carried out for comparison. The required particle mass for each concentration is determined using Equation IV.2. Where w_p is the particle mass, ρ_p is the true density of particles and V_l is the volume of liquid.

$$w_p = \frac{\rho_p C}{1 - C} V_l \tag{IV.2}$$

The dispersing agent BYK-w-940 is added to the mixture with a percentage of 1% from the mass of the added particles to ensure a homogeneous suspension and to avoid the agglomeration and the settling of particles (as mentioned in II.3.4). Table IV.6 presents

the particle content in volume and mass, as well as the required mass of the dispersing agent.

TABLE IV.6: Volume and mass percentages of particles in suspension samples

Concentration (% vol.)	Particle percentage (%wt.)	Mass of dispersing agent (g)
0	-	-
1	2	0.24
5	10	1.24
10	20	2.62

IV.4.5 Concentration and density measurement

At the end of each experiment, sampling tubes are emptied into separate containers. The suspension is then dispersed with the magnetic stirrer FB15001 for 30 minutes. Then the density of the suspension is measured using a 5 ml capacity pycnometer. Knowing the mixture density ρ_e, the neat liquid density ρ_l and the particle density ρ_p, the concentration is deduced using the mixture Equation II.12. This method was chosen because it was found a practical, reliable and rapid way for concentration measurement throughout fibrous media for the range of experiments carried out in this study.

IV.5 Effect of material and process variables on the evolution of particle concentration

Suspensions are injected with known initial concentrations. During impregnation, retention of particles changes the concentration locally throughout the part length. The profile of concentration is a function of several interdependent process and material parameters. An intriguing area in filtration study is determining the most influencing variables at a given impregnation process. Hence, the influence of each one of the selected variables was tested through comprehensive series of experiments. Figures IV.7 a and b illustrate the concept of the experiment, the placement of sampling tubes and the concentration curve plotting. The sampling is indicated from the mold inlet to the outlet (from left to right). The concentration profiles are plotted against the non-dimensional positions $\frac{x}{L}$= 0, 0.27, 0.5, 0.73 and 1, where L is the distance between C_0 and C_4 (55 cm). The influence of each variable is tested separately. All the concentration profiles will be plotted as the example shown in figure IV.7.

In the following, the effects of the selected parameters on flow kinetics and particle concentration are analyzed separately.

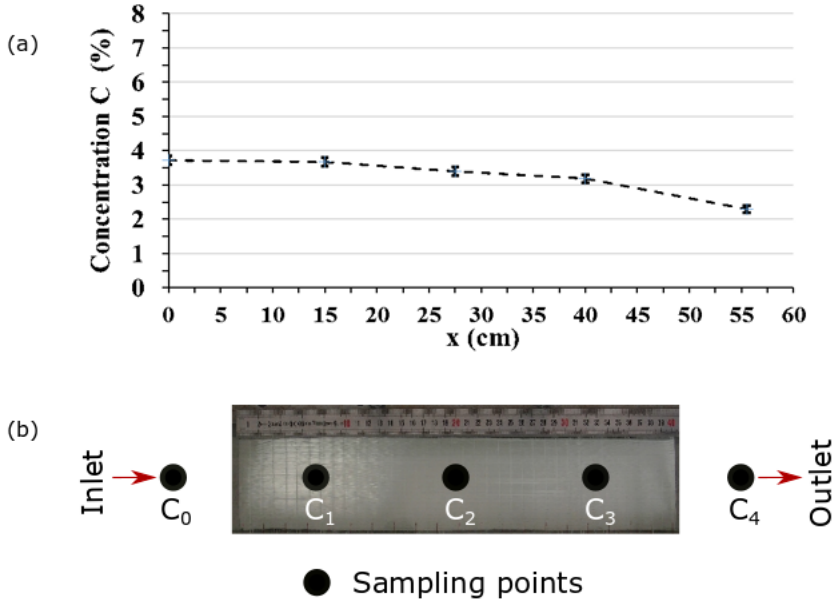

FIGURE IV.7: An illustration of (a) the evolution of particle concentration (grade W-610) for C_0= 3.7% at P_0= 1.4 bar and (b) the corresponding sampling points along the mold

IV.5.1 Initial particle concentration

A clear increase in filling time is recorded as a function of initial particle concentration. The flow front is delayed as a function of C_0. This can be clearly observed from Figure IV.8, which presents the squared flow front positions plotted against time. A decrease in the slope of $x_f^2 = f(t)$ is registered with C_0.

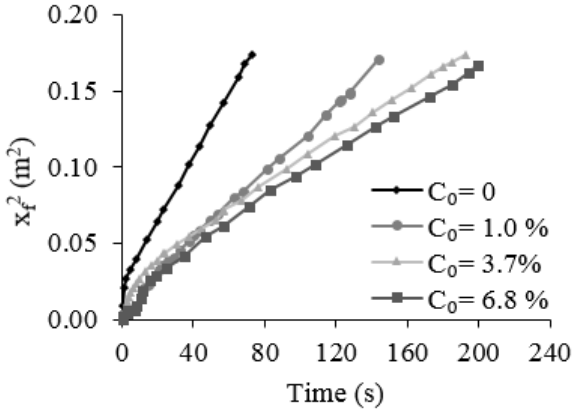

FIGURE IV.8: Evolution of squared flow front with time at variable initial concentrations

Figure IV.9 illustrates the difference in flow front positions for the series of experiments presented in Figure IV.8, which are executed at a constant pressure of 1 bar. The figure allows the visualization of the exact positions of the flow front at t = 30 s, 1 min, and 2 min, for respective initial concentrations of 0%, 1%, 3.7%, and 6.8%. It can be observed

that the flow front is ahead for the case of pure fluid and the lag distance rises as the particle content increases. These images confirm that the addition of particles induces an increase in filling time that depends on the particle concentration.

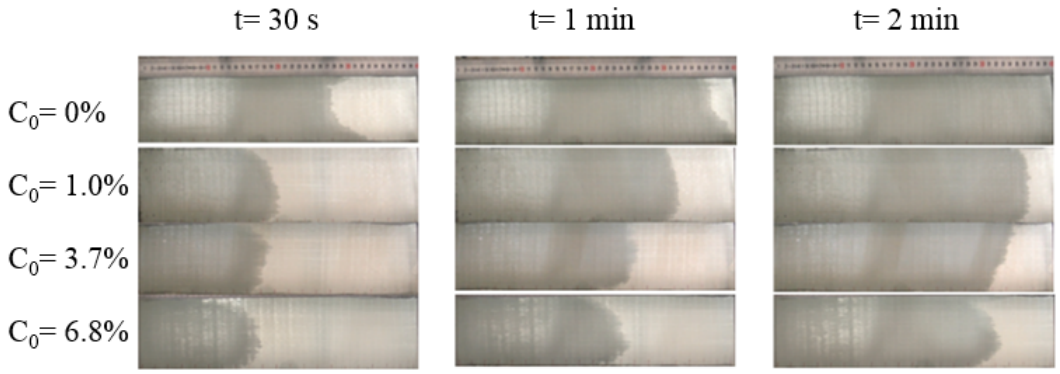

FIGURE IV.9: The time evolution of flow front at P_0= 1.0 bar for different initial particle concentrations

Figure IV.10 A shows the evolution of particle concentration with initial values C_0= 1.3%, 3.7% and 6.8%. From this figure, it can be noticed that the particle content in suspensions decreased with the flow distance for most of the experiments, with similar trends for all the tested initial concentrations. Figure IV.10 B shows the concentration normalized to its initial values (C/C_0). We can see from this graph that the higher the initial value, the lower the variations of (C/C_0) along the part length. C values depend on the initial one, i.e., if a high particle content is required in the final part, a higher C_0 should be injected. The concentration alone does not seem to determine the filtration behavior. This substantiates previous findings in the literature, which stated that the retention probability is independent of the suspension concentration [6, 36, 52].

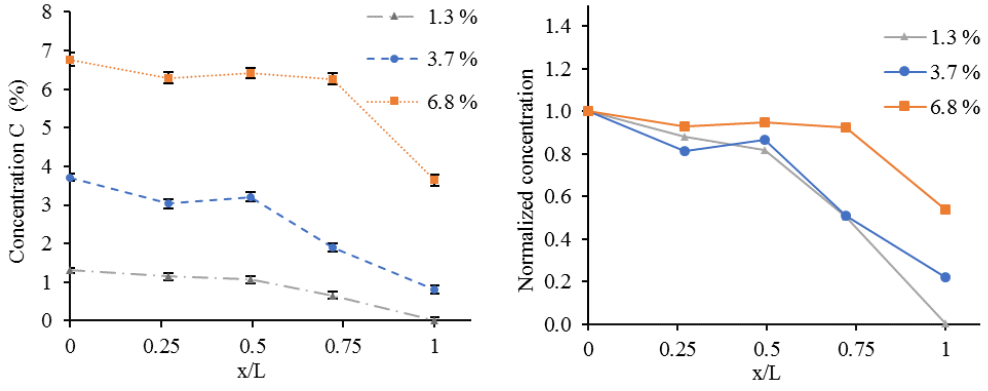

(A) (B)

FIGURE IV.10: Particle concentration with different initial value as shown by (A) Measured experimental values $(Cvsx/L)$, and (B) experimental concentration values normalized to C_0 $(C/C_0$ vs $x/L)$

IV.5.2 Injection pressure

Two tests were performed at the same experimental conditions; only the injection pressure was varied. Figure IV.11 which compares the flow front positions with time at P_0= 1 bar and 1.4 bar shows clearly that the injection pressure has a direct influence on flow kinetics. The experiment of the lower pressure value resulted in a reduced flow velocity and hence a longer filling time.

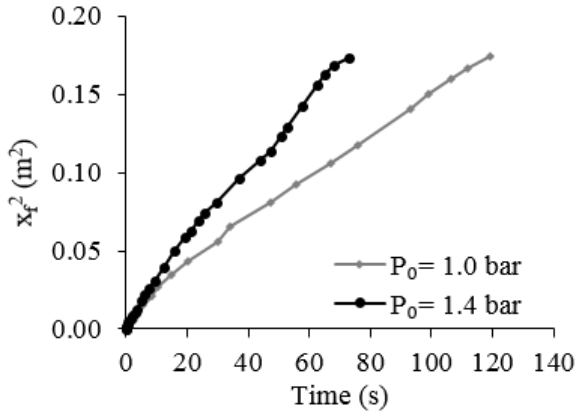

FIGURE IV.11: Evolution of squared flow front with time at different injection pressures

Figure IV.12 A plots of concentration evolution at different C_0 and P_0 values. Figure IV.12 B shows that higher content of suspended particles is attained with the higher pressure value (less filtration). That could have resulted from the direct connection between injection pressure and flow velocity. Faster flow induces higher particle velocity, which reduces the probability of their retention by the fibrous medium. Another reason could be the slight compaction of the yarns induced by the resin pressure and the subsequent increase of the macropore sizes [93].

IV.5.3 Viscosity of neat fluid

The influence of neat fluid viscosity on particle deposit is tested with two values: 0.035 Pa.s and 0.175 Pa.s. These values were selected to represent the viscosities of some of the commonly used resins for composites manufacturing. For the profiles of the flow front advancement (Figure IV.13), a pronounced deviation from linearity was noticed with the highest viscosity. Figure IV.14 plots the spatial evolution of C at two η_0 values with the grade W-210. Both viscosity values exhibited similar filtration trends along the part length. Similar concentration values in the range of the experimental error are observed (0.11-0.13%). These results agree with the ones obtained by Louis et al. [36], for two values of viscosity with a difference of factor 3 versus a factor of 5 for the current study.

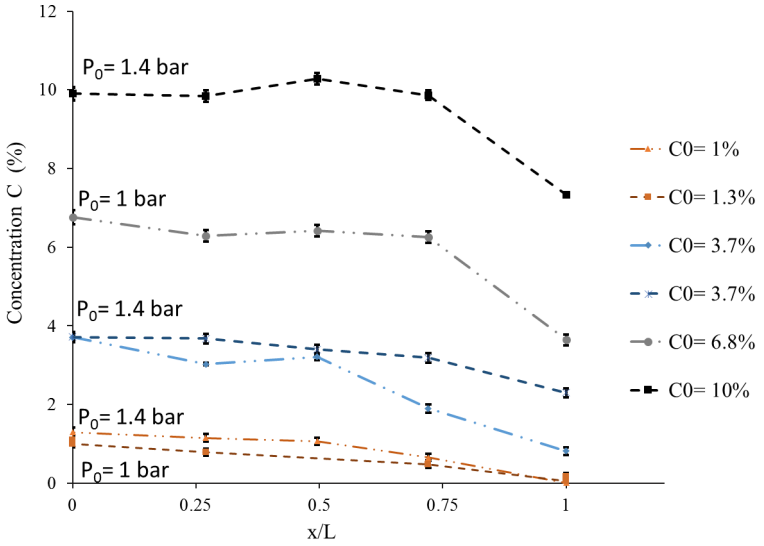

(A)

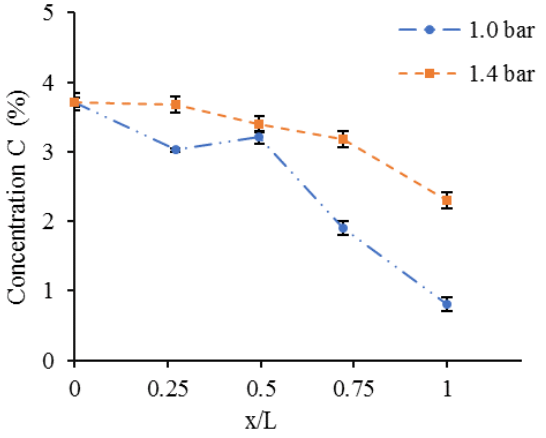

(B)

FIGURE IV.12: Spatial evolution of concentration as a function of the injection pressure for (A) C_0 from 1.3% to 10% at P_0= 1 and 1.4 bar, and (B) a comparison between the concentration profiles for C_0= 3.7% at P_0= 1 and 1.4 bar

IV.5.4 Fiber volume fraction

The fiber volume fraction is a crucial parameter in the LCM flow processes with functionalized or neat fabrics. In the present study, a V_f of 48% increased the impregnation time by a factor of 7 compared to a V_f of 38% at fixed initial concentration, injection pressure, particle size distribution and neat fluid viscosity (Figure IV.15).

Figure IV.16 presents the influence of fiber content of the filter (38%, 48% and 58%) on the concentration profiles. An increase of fiber content within a constant mold cavity volume induces a decrease in porosity and reduces the characteristic distances between individual fibers. This causes a decrease in the average inter-fiber distance compared to the average particle size, which increases the probability of the mechanical blockage of particles. All these consequences lead to increased filtration and steeper concentration

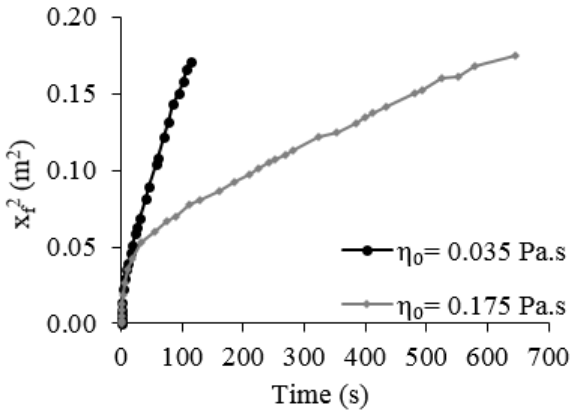

FIGURE IV.13: Evolution of squared flow front with time at variable fluid viscosities

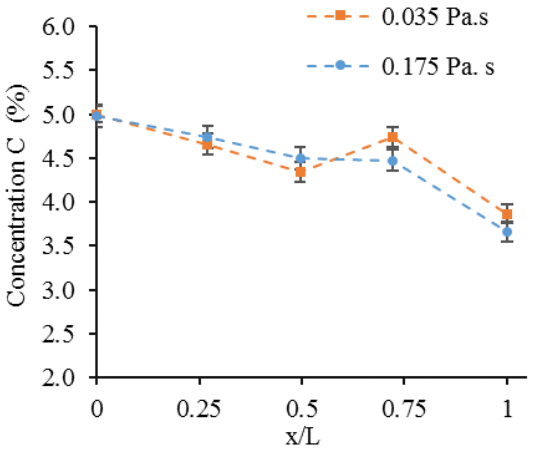

FIGURE IV.14: Spatial evolution of concentration as a function of the initial viscosity at η_0= 0.035 and 0.175 Pa.s for grade W-210

decrease. At V_f= 38%, a sudden rise in C is observed at x/L= 0.73. It could be caused by the sedimentation of large-sized particles. This effect is more pronounced at this specific experiment because of the relatively low fiber content (high porosity) that may facilitate the particle filtration transversely through the mold thickness and their migration towards the sampling tubes. A progressive retention was observed for V_f= 48%. At V_f= 58%, there was a difficulty in tube filling throughout the preform length. Only the inlet and outlet particle concentrations (C_0 and C_4) were obtained. The outlet fluid was almost pure, which means that most particles are blocked at the preform inlet at an early stage of impregnation. In their study for the filtration of nano-scale particles, Louis et al. [36] have drawn the same conclusions with a Kevlar woven fabric of V_f= 35%, 41%, and 50%. As presented in section II.2.2 of chapter II, for the same quasi-UD preform used for this study, a decrease in micro-pores and macro-pores as a function of V_f is reported (Figure II.2) by Bizet et al. [64, 94]. The surface fraction of macro-pores has started to drop right after the V_f value 52.7% to a ratio of 25.7% at V_f= 59.7%, to reach a ratio of 6.7% at V_f= 67.7%. This induces a reduction of the ratio

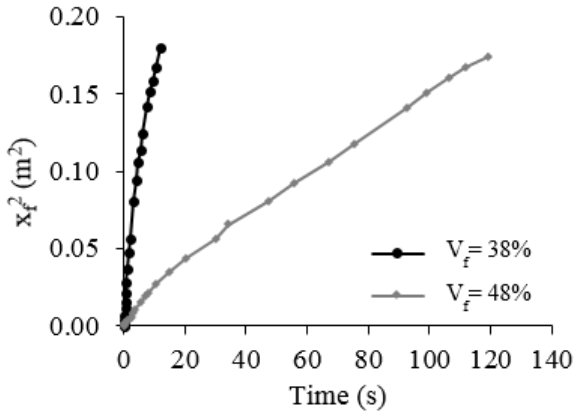

FIGURE IV.15: Evolution of squared flow front with time at variable fiber volume fractions

between the pores to particle size, which results in an increased filler deposit. Previous studies favored the use of low V_f fabrics whenever applicable for better filler distribution [25]. However, the effect of fiber content should be analyzed with multiple particle size distributions. The ratio between V_f and particle size is expected to have a tangible influence on filtration.

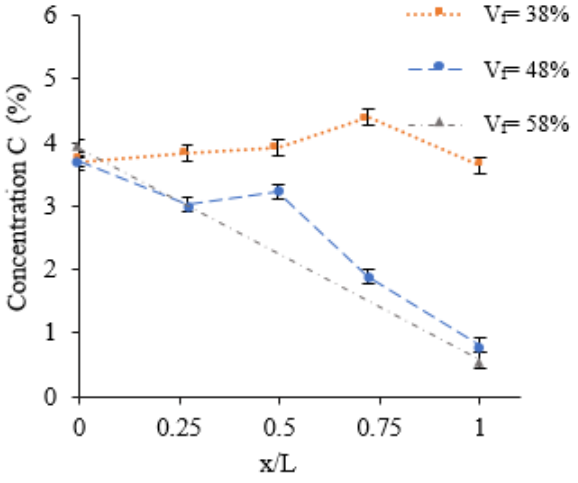

FIGURE IV.16: Spatial evolution of concentration as a function of the fiber volume fraction for V_f= 38%, 48% and 58% (grade W-610)

IV.5.5 Particle size distribution

Particle size is believed to play a major role in both the flow and filtration processes. It has been previously reported that an increase in particle size results in higher particle filtration [43]. However, the effect of particle size on the flow process has not been widely addressed. Figure IV.17 illustrates the squared flow front positions with time for suspensions of two different particle size distributions. Comparable filling times were observed with the two explored grades. However, the slope of x_f^2 vs time is only slightly

influenced by the variation in particle size distribution when the other experimental parameters are kept constant. Overall, these results show that particle size did not much affect the flow kinetics at fixed C_0. A zoom on the first instants of injection in Figure IV.17 reports that the non-linear zone of the curve increases with the particle size. The flow front curve is fit to a linear equation which took the form $x_f^2 = mt + a$, where m is the slope of the linear part of the curve of flow front advancement. m was constant for the two grades (0.0013 m^2/s). a is a parameter related to the high retention zone which increases with d_p (the value of a was respectively 0.0293 and 0.0354 m^2 for the grades W-210 and W-410). A set of experiments investigated the effect of particle

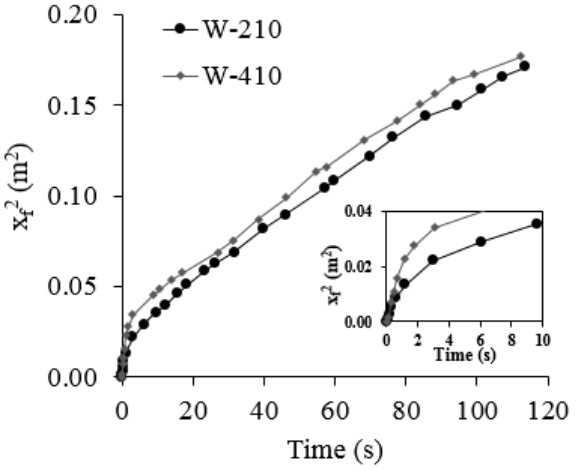

FIGURE IV.17: Evolution of squared flow front with time at variable particle size distributions

size on concentration with the three grades. Expectedly, and as shown by Fig. IV.18 A, for a medium of V_f= 38%, suspensions of the larger particles (W-410) marked higher retention than those of the smaller particles (W-210). The latter grade did not exhibit any filtration behavior. This is translated by higher concentration values with distance for the W-210 particle grade that remained constant along the preform, which means that the medium retains few or no particles. To assess the effect of the coupling between V_f and d_p, same experiments were repeated at V_f 48%. As illustrated by Fig. IV.18 B, lower concentration values were recorded for the larger particle size (more retention). Both grades have shown a progressive filtration behavior, except for the point at x/L=0.73, where the concentration increased. Figure IV.18 C compared the filtration behavior for W-610 particle grade at V_f= 38% and 48%. The normalized concentration C/C_0 reports that at the same particle size, the fiber content is the parameter that determines the particle deposit intensity. Hence, the influence of the d_p increase is substantiated by the V_f increase. Fernberg et al. recommended the use of small particle sizes for obtaining a better distribution. However, attention should be drawn to their influence on viscosity [25].

The presented results highlighted that the particle size distribution and the fiber content are the key parameters influencing filtration. The two parameters are coupled by the

ratio between the average pore size to the average particle size. The lower the ratio, the higher the retention of particles. The same effect was observed for nanoparticles that showed an agglomeration behavior, as filtration increased with the effective particle size [36]. Lefevre [6] defined the notion of critical particle diameter as the size beyond which the deposition is increased and the flow becomes difficult or impossible. For a given experiment, the calculation of this criterion is mainly based on the permeability of the reinforcement and the particle size.

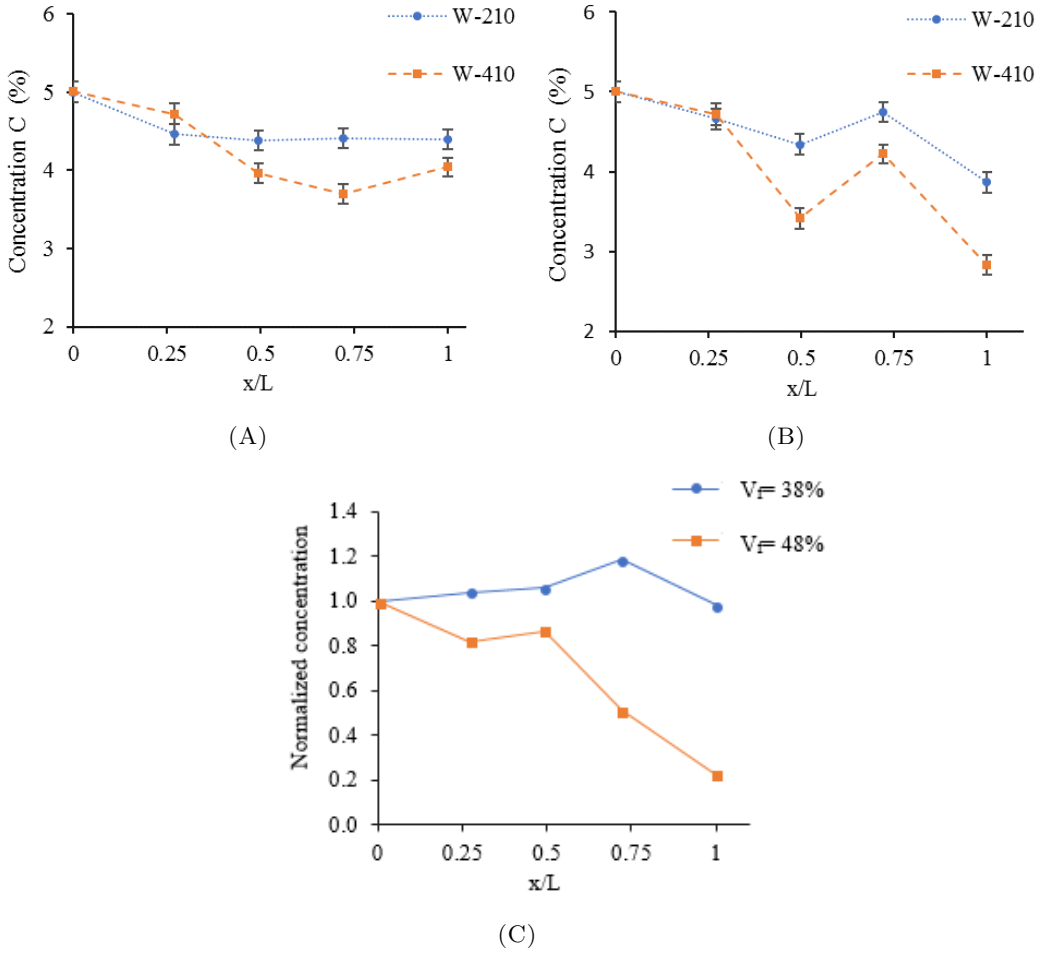

FIGURE IV.18: Spatial evolution of concentration as a function of size distribution for W-210 and W-410 for C_0= 3.7% at V_f of (A) 38%, (B) 48% and (C) 38% and 48% for W-610 at C_0= 5%

IV.5.6 Filling time

Fiber content, injection pressure and initial viscosity control the flow velocity and consequently the front advancement in the fibrous medium, which can be translated by the filling time. In the presence of particles, the flow becomes more sensitive to the change of any material or process variable. The progressive retention of particles results in a changing medium with a locally modified porosity. Figure IV.19 A shows that the

impregnation time increased by 20-40 s for a change of C_0 between 1.3% and 6.8%. An injection pressure of 1.4 bar reduced the filling time by half versus injection at 1 bar. Particle-filled experiments with C_0= 5% and a constant injection pressure and initial viscosity, the filling time marked a high rise from 27 s at V_f= 38% to 213 s at v_f= 48%, and 1560 s at 58% (Figure IV.19 B). The increase in particle size at a fixed concentration in suspensions did not seem to affect the impregnation time at low V_f (Figure IV.19 C). An increase of viscosity by a factor of 5 induced an increase of filling time by the same factor for two experiments at fixed d_p (5.2 μm) and C_0 (5%).

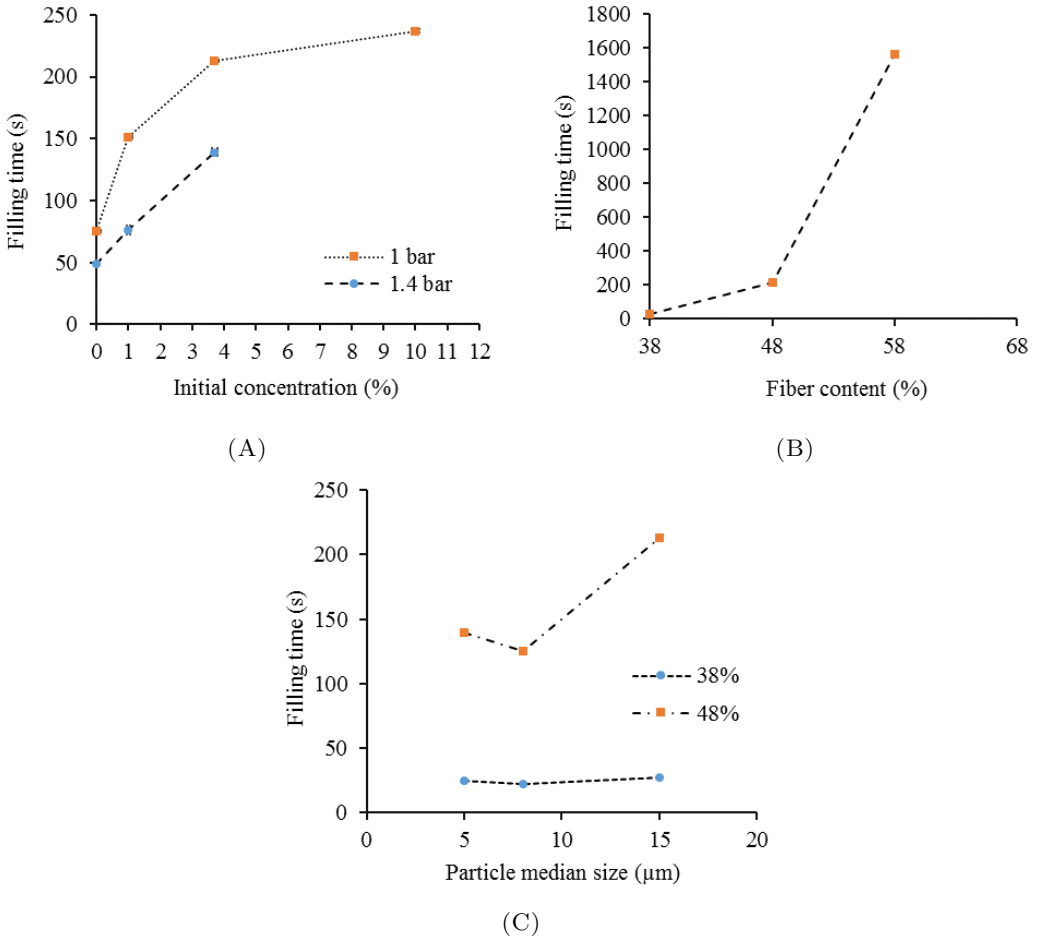

FIGURE IV.19: Filling time as a function of (a) pressure and initial concentration (b) fiber volume fraction and (c) particle median size and fiber content

IV.6 Discussion on flow and filtration behavior

In section IV.5, a sudden rise in concentration near the preform end (i.e x/L= 0.73) is observed for some of the cases. This could be explained by an increase in the number or the average size of suspended particles at this point (and hence the particle volume in the suspension). This point is further discussed in section IV.8.2 of this chapter.

For most squared flow front profiles, a non-linear part of the curve is noticed from the beginning of impregnation. A linear profile follows this zone till the end of injection. The non-linear zone corresponds to the first part of the preform where retention attains its maximum value, the zone at which the particles are increasingly accumulated. The decreased permeability of this part directly affects the front advancement, which results in the observed non-linearity. This is illustrated by Figure IV.20, for an experiment with a C_0 of 6.8% and V_f of 48%. The figure presents the zone of increased retention of approximately 0.15 m of the preform length, which is directly reflected by the non-linear part of the squared flow front curve. This density of the formed layer is a function of material and process parameters. The decrease of the slope of the linear curve fit $x_f^2 = f(t)$ reports a drop in the permeability value [13], for the reason that increased particle deposit hinders the flow at some locations. This is reported for the cases of the increase in C_0, V_f, and the decrease of P_0.

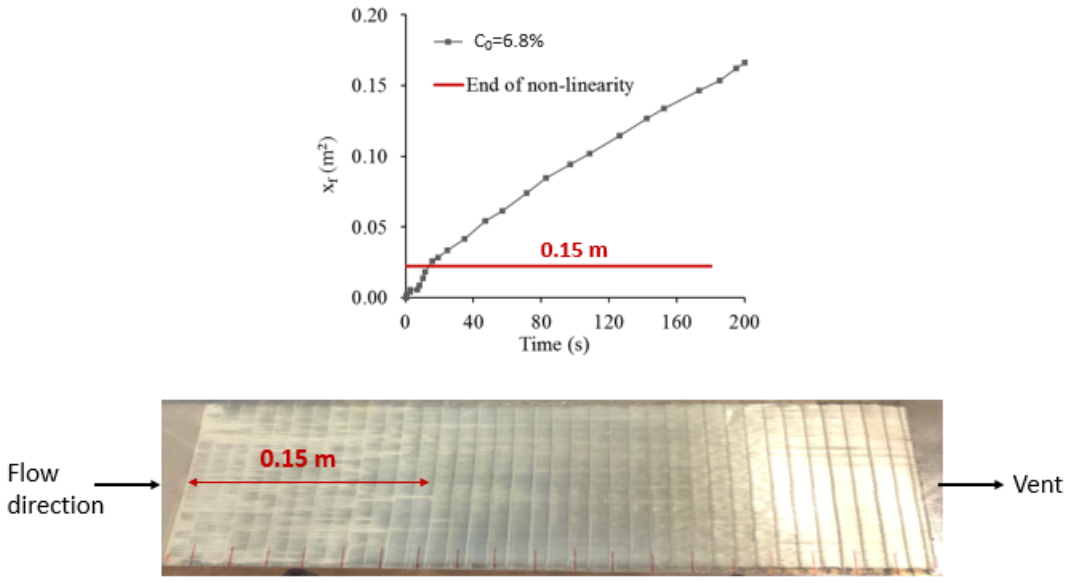

FIGURE IV.20: Illustration of the particle accumulation at the preform inlet for the experiment with C_0= 6.8% and V_f= 48% after the end of impregnation

In the range of the carried out tests, three key behaviors of flow and filtration were observed:

- normal suspension flow with no or slight filtration, like the tests with the grade W-210,
- normal suspension flow with progressive retention, as most of the realized experiments;
- partial clogging, like the case with P_0= 1.4 bar and C_0= 10%,
- complete clogging, long impregnation times like the case with V_f= 58% and C_0= 3.7%.

The observed phenomena underline an evident dependency of experiments' success on the combination of process and material variables. Therefore, further analysis should concentrate on the definition of a filtration parameter that defines the process window.

IV.6.1 Defects induced by particle deposition

This section highlights some experimental observations during filtration tests; besides the non-homogeneous particle distribution, the viscosity rise and permeability decrease. For an experiment at P_0= 1.4 bar and C_0= 10% and V_f= 48%, a strong deviation from linearity was noticed for x_f^2 with time. A particle layer was formed quickly by cake filtration at the inlet of the reinforcement. As a result, some zones at the inlet were blocked by a dense particle layer. Suspension entered the preform from the particle-free zones and advanced quickly at a part of the preform and slowly through others. This led to an uneven flow and caused some defects similar to the ones caused by the race-tracking phenomenon i.e., voids entrapment and dry spots [95]. Figure IV.21 illustrates some of the defects induced by the presence of particles for this experiment. In addition to that, a 4 mm zone of fiber wash-out was observed by the end of impregnation. At V_f= 58%, particles were subjected to cake filtration, which resulted in the blockage of flow channels. As a consequence, an enormous increase in filling time is registered. Significant defects could be caused by the increased filling time with curing resins. When the impregnation time increases, there is a risk of achieving resin gel time before the end of impregnation. This could lead to part rejection due to incomplete impregnation or high void content, hence the increase of the fabrication cost and time.

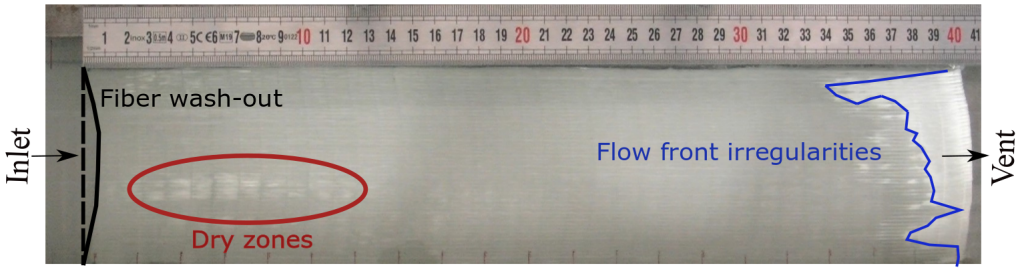

FIGURE IV.21: Filtration induced defects at P_0= 1.4 bar, C_0= 10% and V_f= 48%

IV.7 Evolution of particle granulometry

Each size distribution of the three used grades is constituted of a wide variety of particle sizes. Hence, a study of the evolution of particle granulometry is carried out for two main objectives:

- following the evolution of the particle size distribution from inlet to outlet along the preform length,

- extracting the size range of the particles retained inside the preform.

At the end of each experiment, samples of suspensions were extracted from the inlet, outlet and blocked particles. Throughout this section, the different categories of particles refer to the following: i) inlet for the initially injected particles extracted at C_0; ii) blocked for particles that are deposited at the preform inlet due to cake filtration (extracted from the formed cake layer after the end of the experiment); iii) outlet particles are those collected at C_4; iv) retained particles are the ones captured inside the fibrous medium (Figure IV.7). The particle size distribution of each sample (referred to herein as PSD) is measured with the help of the granulometer Mastersizer HYDRO 2000 SM, as described in section II.4.0.2. Figure IV.22 reports the results of these measurements for an experiment with P_0= 1 bar, V_f= 48%, C_0= 10%, η_0= 0.035 Pa.s and grade W-610. The distributions are presented in vol% (case study 1). Table IV.7 presents the evolution of the diameters from inlet to outlet for the three categories. It presents the diameters d(0.1), d(0.5), d(0.9) as well as the surface weighted means. For example, the size d(0.1) denotes that 10% of the particles (in volume%) have sizes smaller than 4.3 μm for inlet particles. The sizes d(0.5) of 15.2 μm, 13.6 μm and 10.4 μm for inlet, blocked and outlet particles respectively mean that these sizes divide the particle distribution into two equal populations. Results show a clear decrease in particle size from the inlet to the outlet. The larger particle sizes are within the blocked distribution at the preform inlet. This agrees with the previous findings from the literature, which states that the large particles are prone to cake filtration, while smaller ones pass through the reinforcement to the outlet [43].

TABLE IV.7: Particle size distribution for inlet, blocked and outlet particles (in Vol.%)

Particle size (μm)	**Inlet**	**Blocked**	**Outlet**
d(0.1)	4.3	6.7	4.3
d(0.5)	15.2	13.6	10.4
d(0.9)	33.6	24.9	21.7
Surface Weighted Mean D[3,2]	9.6	11.6	8.1

IV.7.1 Fitting data to the Lognormal distribution

Figure IV.22 represents particle distribution according to their volumes in the suspensions. Where larger particles occupy higher volumes prevail over smaller ones. Thus, the distribution in number will be determined. The number PSD is important for characterizing all the size categories of particles present in the suspension, regardless of the volume they occupy. The Vol.% PSDs are transformed to No.% PSDs using the following Equation:

$$No.\% = \frac{6\ Vol.\%}{d_p^3} \tag{IV.3}$$

The volume of one particle is considered as the volume of a sphere with a diameter d_p. The distribution in number (No.%) is obtained by dividing the volume distribution of each particle size present in the distribution by the volume of the corresponding size.

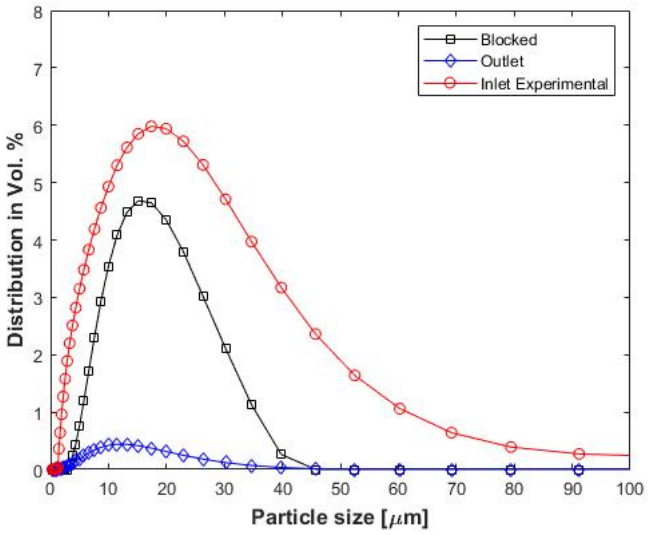

FIGURE IV.22: The particle size distribution in Vol.% for inlet, blocked and outlet particles at P_0= 1.0 bar and C_0= 10% for the first case study

To ease the results treatment and the analysis, the No.% distributions are fitted to the lognormal function. The lognormal distribution is one of the most used distributions for the representation of particle sizes. "It is a continuous probability distribution of a random variable whose algorithm is normally distributed. It is a typical example of positively skewed frequency curves" [96]. The lognormal function has two parameters μ and σ, respectively the mean and the standard deviation of the distribution (Equation IV.4). A Matlab optimization routine enabled the calculation of the parameters of each of the constituting distributions. Figure IV.23 presents the lognormal fit of the inlet (Figure IV.23 A), blocked (Figure IV.23 B), and the outlet (Figure IV.23 C) PSDs in No.% as well as the parameters μ and σ of each distribution. Similar to the Vol.% PSDs, No.% distributions show the blockage of substantial particle sizes while the small to medium ones pass through the preform to the outlet.

IV.7.2 Estimation of retained particle granulometry (first case study)

The measured distributions can be used to extract information about the retained PSDs [97]. The used concept is based on the hypothesis that the inlet particle distribution is constituted of the retained, blocked, and outlet particles with different fractions. Figure IV.24 and Equation IV.5 explain the principle of the drawn assumptions. The orange zones are the experimental data and the gray zone is the retained particle area with the unknown PSD.

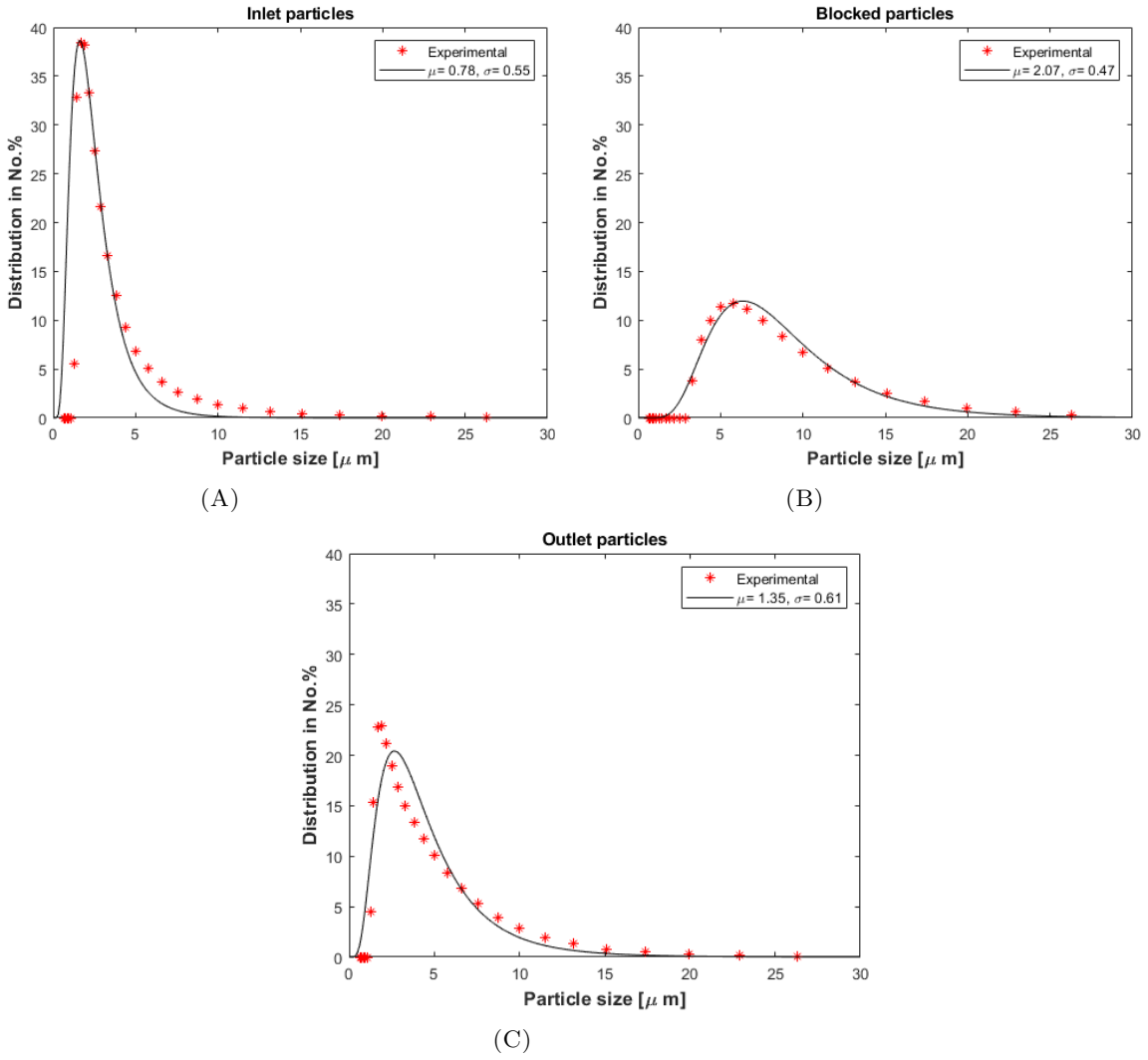

FIGURE IV.23: Lognormal fit of (a) inlet, (b) blocked and (c) outlet PSDs in No.%

The range of diameters retained by the fibrous medium are extrapolated from the measured inlet, outlet and blocked PSDs using two assumptions:

1. from mass conservation, the inlet PSD is considered as the sum of the retained, outlet, and blocked PSDs. Equations IV.5 and IV.6 presents this assumption, where the parameters $f^{exp}_{blocked}$ and f^{exp}_{outlet} are the discrete and experimental PSDs for blocked and outlet particles respectively; f^{exp}_{inlet} is the experimental inlet distribution. $w_{blocked}$, w_{outlet} and $w_{retained}$ are the fractions of each distribution.

2. retained PSD $f^{th}_{retained}$ is assumed to follow a lognormal distribution. Inlet, outlet, and blocked particles are described by their experimental distributions. The lognormal distribution is given by Equation IV.4 [98], where d_k represents the k^{th} particle size, μ and σ are the mean and standard deviation of the distribution respectively.

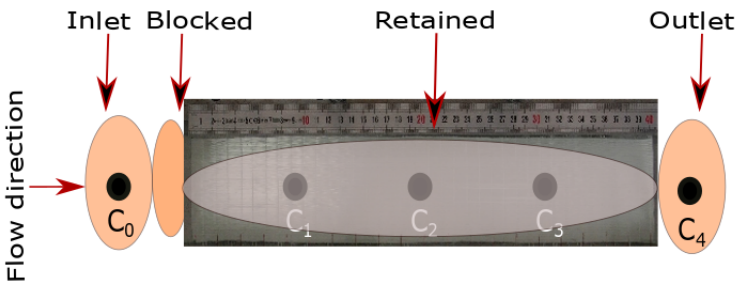

FIGURE IV.24: Illustration of the locations of the different PSD categories for the first case study

An optimization is carried out for the five parameters (μ, σ, $w_{blocked}$, w_{outlet} and $w_{retained}$) of the equation system (IV.4-IV.6) by minimizing the sum of squared errors between experimental and theoretical density functions for inlet particles. The optimization constraint states that the summation of the fractions of the outlet, retained and blocked PSDs is equal to 1, the fraction of the inlet distribution (Equation IV.6).

$$f^{th}_{retained}(d_k) = \frac{1}{\sqrt{2\pi} d_k \sigma} e^{\frac{-1}{2}\frac{(lnd_k-\mu)^2}{\sigma^2}} \tag{IV.4}$$

$$f^{exp}_{inlet}(d_k) = w_{blocked} f^{exp}_{blocked}(d_k) + w_{outlet} f^{exp}_{outlet}(d_k) + w_{retained} f^{th}_{retained}(d_k) \tag{IV.5}$$

$$w_{blocked} + w_{outlet} + w_{retained} = 1 \tag{IV.6}$$

Figure IV.25 presents the results of optimization. It plots the number PSDs of the inlet, blocked, and outlet particles, beside the extracted lognormal distribution for retained particles and the sum of the three categories (inlet fit).

Table IV.8 presents the values of the fractions w_i (obtained from optimization), the parameters μ and σ, as well as the median particle sizes of all the PSDs. The median sizes d_p presented in Table IV.8 confirms that the largest sizes are blocked, smaller particles pass through the preform and the small to medium-sized ones remain inside the preform.

Figure IV.26 illustrates the map of particle sizes for each category. Retained particles are in the range from 0.6 to 8 μm. Their amount decreases progressively around 4.5 μm where the sizes of the outlet particles become prevalent. Blocked particles are in the range from 4 μm to 40 μm. At this largest size, blocked particles represent more than 50% of the total number of particles. Three main conclusions merge from figure IV.26:

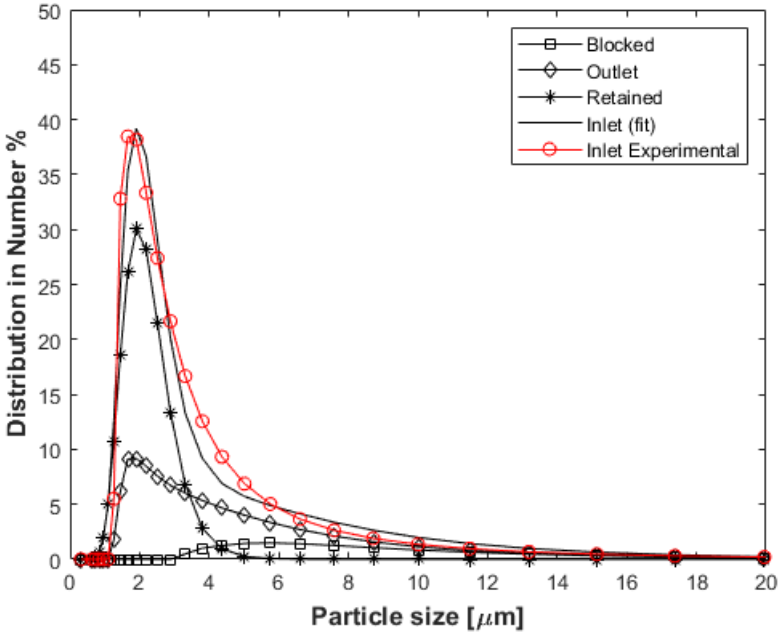

FIGURE IV.25: Optimization results on the retained PSD in No.% for case study 1

TABLE IV.8: Parameter values for inlet, blocked, retained and outlet PSDs (in No.%) for the first case study

Parameter	Inlet	Blocked	Outlet	Retained
w_i	1	0.13	0.40	0.47
μ (μm)	0.98	2.07	1.35	2.93
σ (μm)	0.45	0.47	0.61	1.05
d_p (μm)	2.66	7.93	3.86	2.10

- unexpectedly, particles with sizes around 5 μm could be blocked by the preform at the entrance, retained or could pass through the preform to the outlet,
- particles with sizes under 1.8 μm are mainly retained inside the preform,
- blocked particles is not only constituted of large-sized particles, but it also contains small to medium sizes.

These results indicate that particles with small sizes may be entrapped by the intra-tow zones, while large sizes are transported through the inter-tow spacing or blocked at the preform inlet.

IV.7.3 Evolution of particle granulometry (second case study)

The granulometry analysis is tested with a different particle grade in order to asses the influence of the initial size distribution. This second case is analyzed for an experiment with a suspension of grade W-210, with C_0= 5%, V_f= 48% and η_0= 0.175 Pa.s, injected

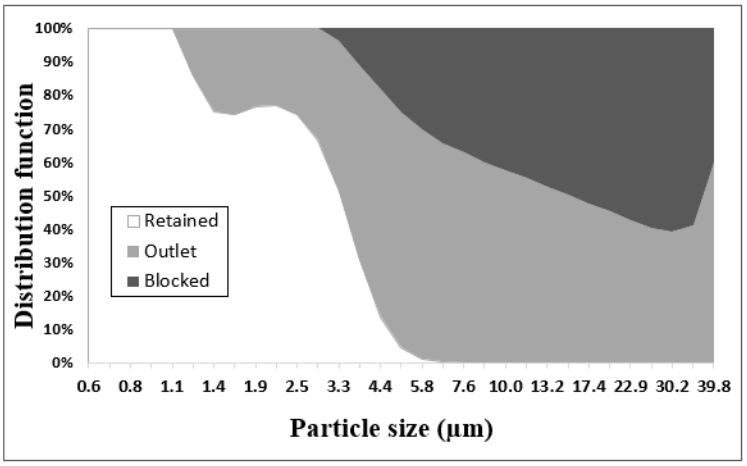

FIGURE IV.26: Distribution function repartition between retained, outlet and blocked particles as a function of particle size for the first case study

at P_0= 1 bar. For this specific experiment, the granulometry is measured for the all the sampling points, in addition to the blocked particles. For the following, the different PSD categories will include: inlet C_0, blocked, C_1, C_2, C_3, and outlet C_4. C_1, C_2, C_3 represent the suspension flowing through the fibrous medium. Figure IV.27 illustrates the sampling zones with an orange color.

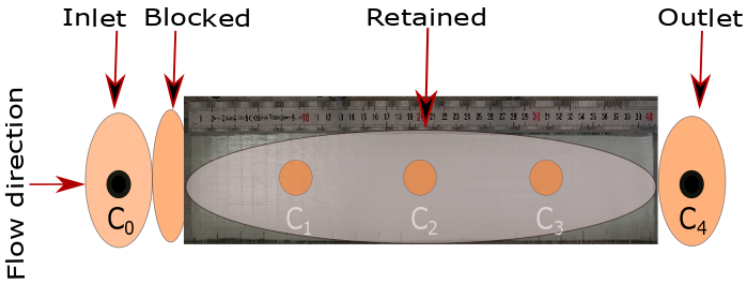

FIGURE IV.27: Illustration of the sampling of the different PSD categories for the second case study

From Table IV.9, the particle sizes d(0.1), d(0.5), d(0.9) and the surface weighted mean are presented for all the categories. The evolution of these sizes highlights that the blocked particles have the largest sizes. It is observed that a slight increase of the particle sizes with the flow distance takes place in the flow direction (from C_1 to C_3). This increase is more remarkable with d(0.9).

TABLE IV.9: The evolution of particle sizes through the preform length for the second case study (in Vol.%)

Particle size (μm)	**Inlet**	**Blocked**	**C1**	**C2**	**C3**	**Outlet**
d(0.1)	2.7	3.4	2.9	2.9	2.8	2.8
d(0.5)	6.0	7.2	6.3	6.4	6.5	5.9
d(0.9)	12.1	13.6	12.6	13.0	13.5	11.7
Surface weighted mean D[3,2]	5.0	6.0	5.2	5.3	5.3	5.0

An optimization routine is carried out to extract retained PSD for the second case study (the same routine applied for the first case study). Figure IV.28 plots the results of optimisation. It can be seen that the theoretical inlet PSD represents perfectly the experimental inlet PSD. Values of the parameters are detailed in Table IV.10.

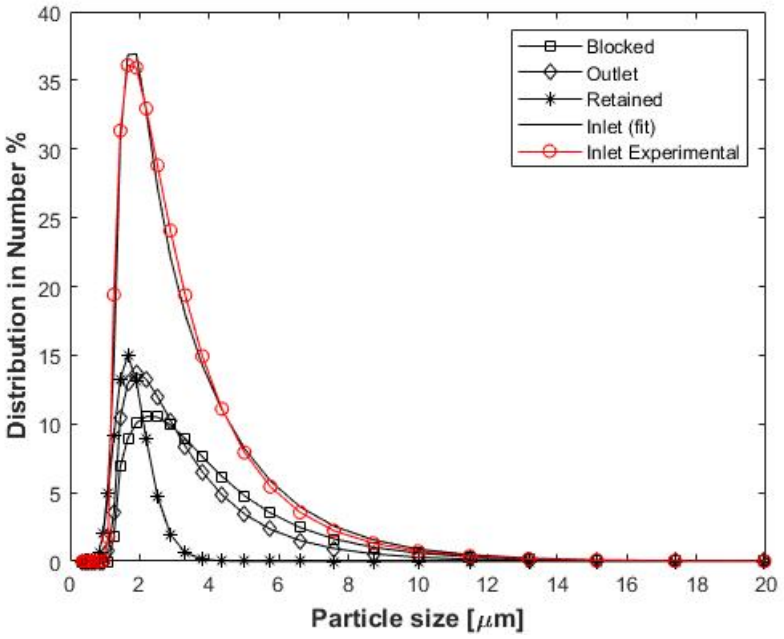

FIGURE IV.28: Optimization results on the retained PSD in No.% for the second case study

TABLE IV.10: Parameter values for inlet, blocked, retained and outlet PSDs (in No.%) for the second case study

Parameter	Inlet	Blocked	Outlet	Retained
w_i	1	0.42	0.40	0.18
μ (μm)	0.98	1.23	1.03	0.58
σ (μm)	0.46	0.51	0.45	0.28
d_p (μm)	0.88	3.41	2.81	1.78

The surface figure (IV.29) shows that, similarly to the first case, the blocked particles are constituted of the largest particle sizes. The blocked category also included medium-sized particles; they range from 1.3 μm to 20 μm. This could indicate that during cake filtration, large particles acted as a filter to smaller ones. The outlet particles had small and large sizes. The retained PSD included relatively large particle sizes (higher than the distribution median), unlike the first case.

The largest retained particle size was around 8 μm in the distribution of 15.2 μm median size, versus 8-9 μm with grade W-210 with a median of 5.2 μm. The maximum retained particle size is identical with different particle grades because the fiber volume fraction was the same for both experiments (48%). This means that the value inter-fiber distance is fixed for the two experiments. For the first case study, the largest particles in the

distribution may have hindered the flow channels, which inhibited smaller sizes from passing through the preform.

The analysis of the first and the second cases approximated the PSD evolution with respect to the initial median d_p of the distribution. The explored grades (W-610 with d_p= 15.2 μm and W-210 with d_p=5.2 μm) manifested similar trends. The blocked particles had large sizes and the outlet particles had a median higher than that of the inlet distribution. Whereas retained distributions had a lower median than the outlet particles.

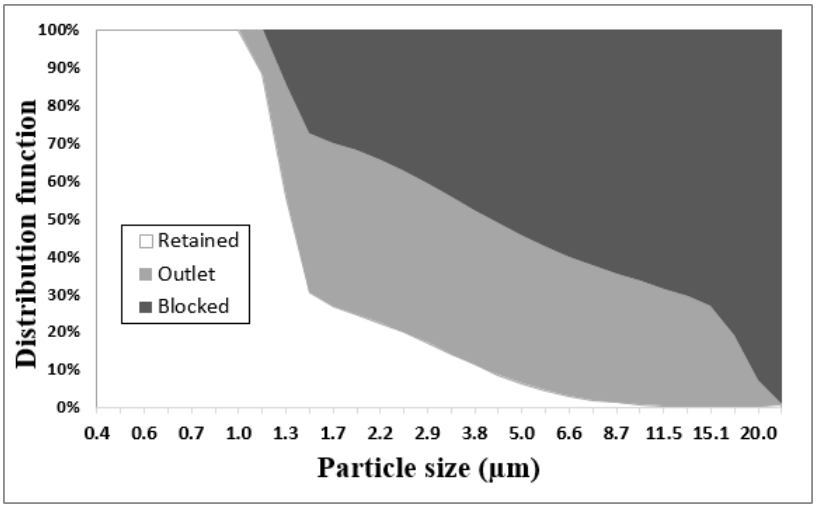

FIGURE IV.29: Distribution function repartition between retained, outlet and blocked particles as a function of particle size for the second study case

IV.8 Particle filtration mechanisms

The granulometry analysis of polydisperse particles successfully estimated the range of blocked particles and the PSD of the retained particles. However, it does not indicate the potential retention zones or the filtration mechanisms that took place. Part of the particles succeeds in passing to the outlet at the early stages of injection. The presence of large particles at the outlet shows that the macropores, i.e., the channels, may have served as pathways to the flow of particles, leading to 40% of small and large sizes recovered at the outlet [97].

IV.8.1 Cake filtration

Large-sized particles in the distribution exhibited a cake filtration behavior at the preform inlet. The formed particle layer can be observed in Figure IV.20 for a fibrous medium of a V_f= 48% injected with a suspension of a C_0= 6.8%. The two explored granulometry cases (sections IV.7.2 and IV.7.3) have shown a relatively high median

for the blocked particle category in comparison to the inlet median. For cake filtration, the large particle sizes in the blocked PSD show that they were filtered mechanically as they are larger than the inter-fiber distances. The formed layer acted as a filter for the suspended particles, including those with smaller sizes. This could explain the presence of small particles within the blocked PSD. Particles that succeed in entering the preform are prone to deep bed filtration. They are necessarily sized lower than the inter-fiber distances.

IV.8.2 Deep bed filtration

Important results from the granulometry analysis revealed that the fibrous medium mainly retains the smallest particle sizes. For the verification of these findings, the impregnated preforms from the first and the second case studies (section IV.7) are dried after the end of impregnation. Samples of tows are cut and observed using scanning electron microscopy (SEM). Results present the top surface of tows for the first case study (Figure IV.30) and the second case study (Figure IV.31). For deep bed filtration, several forces act on particles during their movement through the fibrous bed and filtration takes place through different mechanisms. During suspension flow through the medium, the moving particles often collide with the porous bed, giving rise to two possibilities: either stick to fibers/deposited particles by surface forces or move with the flow. In the latter case, these particles are prone to other types of filtration such as sedimentation [52, 99].

Surface forces and direct interception

From the figures IV.30 A and IV.30 B, it can be observed that small-sized particles are significantly deposited at the surface of fibers, with relatively high intensities. These results confirm the earlier findings that the smallest sizes of particles are retained within the preform. It is expected that surface forces between particles and fibers have caused Physico-chemical filtration. The range of the deposited particles is between 1 and 3 μm. Some authors assume that surface forces could be neglected for d_p>10 μm. Large-sized particles that pass through the preform could be filtered by a mechanical blockage between fibers whenever the inter-fiber spacing is less than the particle size. Figures IV.30 C and IV.30 D show the agglomeration of different sizes of particles at the fiber surface. The largest particles of the retained distribution (10-18 μm) may have acted as a filter for smaller ones (1-10 μm). The particle-particle interactions could have resulted in the formation of agglomerates of ceramic inclusions.

The second case study is explored through SEM analysis for three samples extracted from the suspension-impregnated preform after drying. The locations of samples were adjusted to the ones of the sampling tubes through the preform length (C_1, C_2 and C_3). Figure IV.31 shows a top view of the extracted tows at x/L= 0.27 (Figure IV.31), 0.5

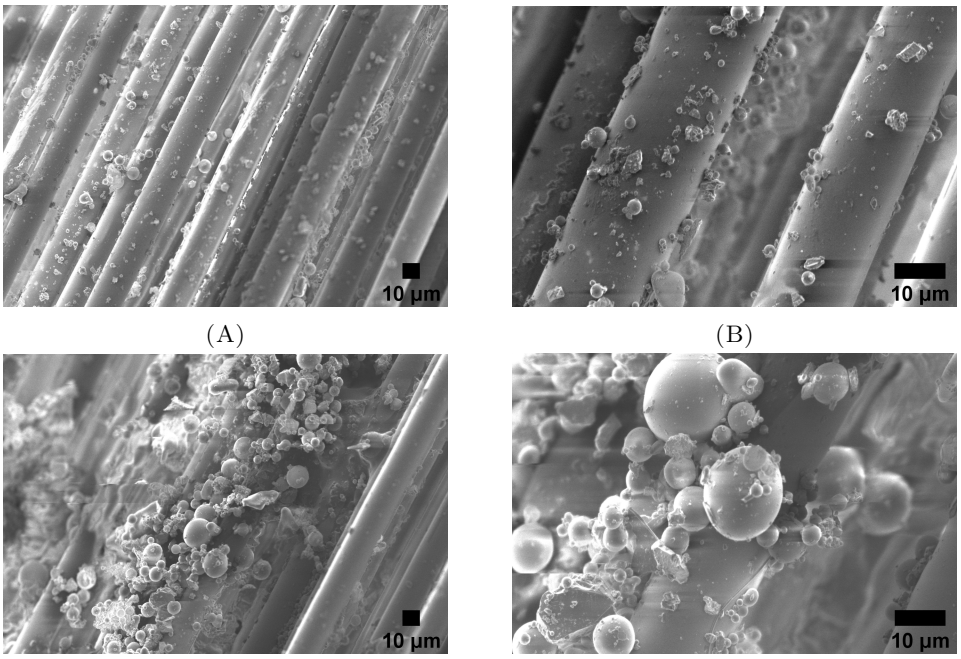

(A) (B)

(C) (D)

FIGURE IV.30: SEM images of yarns after impregnation with the particle-filled fluid on $x/L = 0.27$ at the magnifications (A) x500, (B) x500, (C) x500 and (D) x1500 (first case study)

(Figure IV.31) and 0.73 (Figure IV.31) of the preform length. These figures highlight increased retention at x/L= 0.27, which agrees with the fact that retention takes its maximum value at the preform inlet. The amount of retained particles decreased progressively for x/L= 0.5 and x/L= 0.73. Moreover, an increase of the top particle size with distance is observed.

Generally speaking (from Figure IV.31), the largest particles at the fiber surface, which constituted the agglomerate base ranged from 7 to 12 μm. Similar to the first case, small-sized particles ranging from 1 to 3 μm tended to settle at the surface of the fibers. Figure IV.32 illustrates the deposition of small particles at the surface of a fiber.

Transverse filtration/Filtration within tows

In dual-scale media, the flow has different velocities in micropores and macropores. As a result, two zones within tows are generated; a saturated region and a partially unsaturated region. The fluid in the macropores, which has higher velocity, impregnates tows transversely [100, 101, 102]. This effect is expected to influence the filtration behavior, as the study deals with a quasi-UD preform. Therefore, an important question is raised herein: do particles penetrate the fiber bundles transversely? To answer this question, selected tows from the second case study are divided into two symmetric parts longitudinally and the inner center of the tow is observed with SEM analysis.

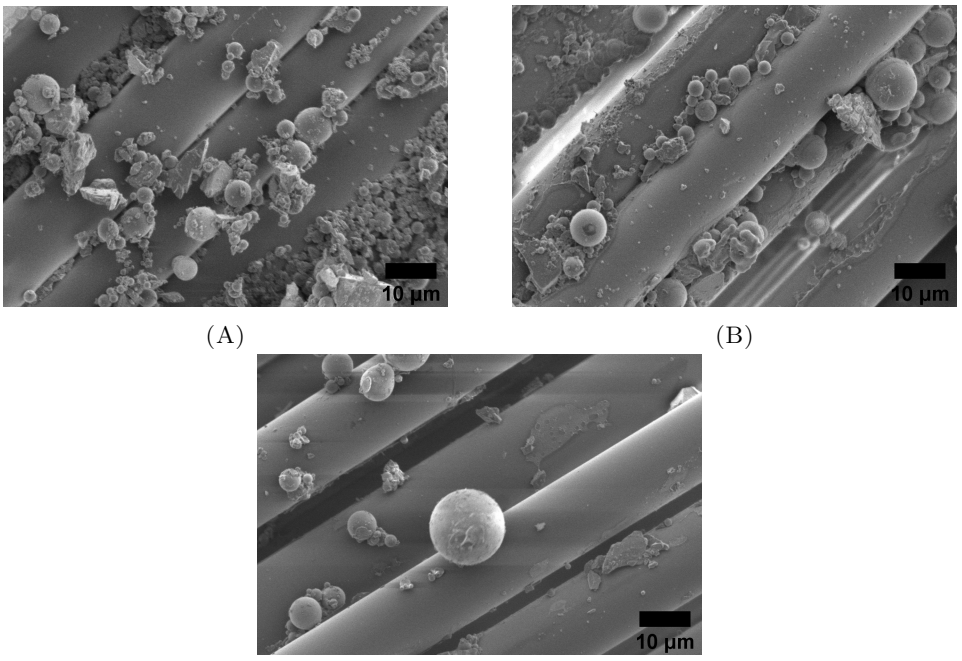

(A) (B)

(C)

FIGURE IV.31: SEM images of yarns after impregnation with the particle-filled resin at the magnification x1500 at x/L = (A) 0.27 (B) 0.5 and (C) 0.73 (second case study)

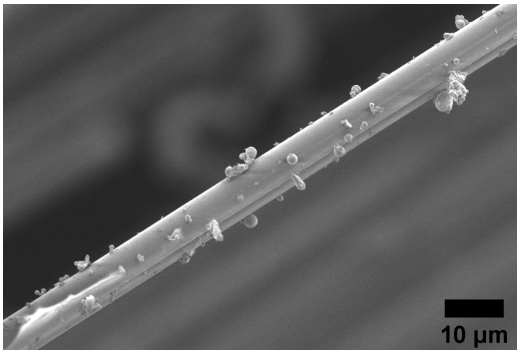

FIGURE IV.32: Illustration of particle deposition at the fiber surface

Figure IV.33 shows the tow interior zone at three locations; $x/L = 0.27$ (Figure IV.33 A), 0.5 (Figure IV.33 B) and 0.73 (Figure IV.33 C). It is observed that small-sized particles infiltrate through the bundle surface and a progressive decrease in particle content takes place in the flow direction. The figures highlight that particles are captured inside fiber bundles with the same mechanisms observed at the tow surface, i.e., mechanical blockage or surface forces. The diameters of 125 particles captured inside tows from the second case study were measured using ImageJ and the PSD is presented in Figure IV.34. The distribution has a median size of 1.8 μm. This value is comparable to the median size of the retained PSD obtained from the granulometry analysis (1.78 μm) presented in Table IV.10. This result further confirms the findings of the granulometry analysis. The maximum retained particle size was around 8 μm. This means that the inter-fiber spacing is necessarily higher than 8μm to permit the particle passage. The inter-fiber

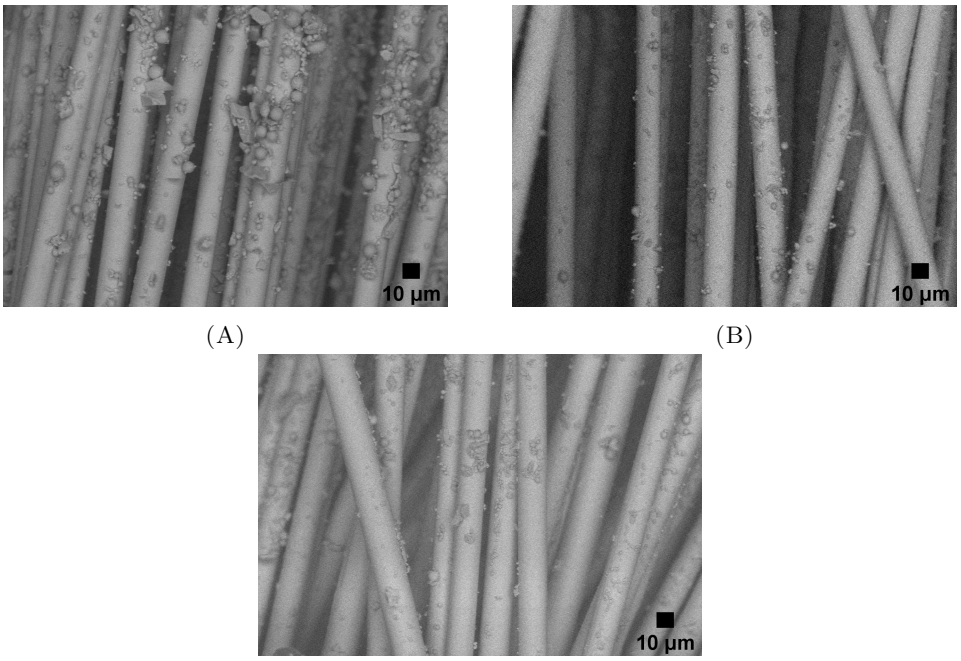

(A) (B)

(C)

FIGURE IV.33: SEM images inside fiber bundles at the magnification x100 at $x/L =$ (A) 0.27 (B) 0.5 and (C) 0.73 (second case study)

distances will be explored in section IV.9.

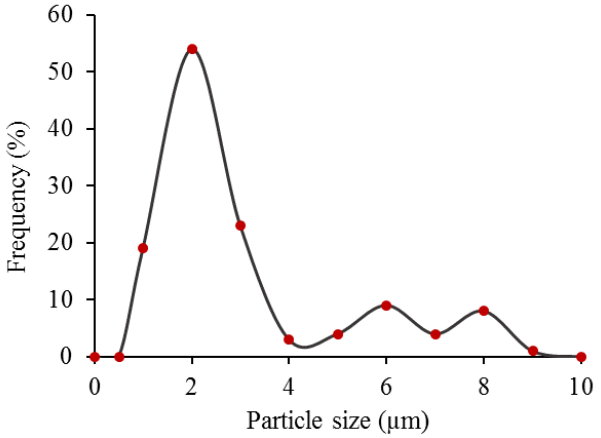

FIGURE IV.34: Particle size distribution inside fiber bundles

Sedimentation

The sudden rise in concentration at $x/L = 0.73$ could indicate that some of the large-sized particles are settled under the effect of gravitational forces. To evaluate the observed increase of the particle sizes through the preform, the C_1, C_2 and C_3 PSDs are plotted in Figure IV.35 separately of the other distributions. The most marked observation to emerge from this figure is that the three distributions are identical for the first

half of the curve and have the same mode (maximum value), while a slight shift to the right (>11μm) is noticed with increasing distance. This shift indicates an increase of the maximum particle size in the distribution, which is translated by the slight increase of d(0.5) and d(0.9) (refer to Table IV.9). It is expected that transverse filtration through the mold thickness led to particle migration towards the mold bottom; particles were then subjected to sedimentation that caused the concentration increase.

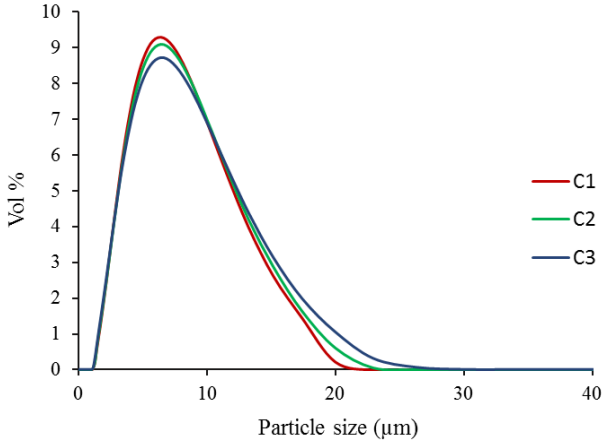

FIGURE IV.35: Vol.% PSDs for suspensions extracted at C_1, C_2 and C_3 for the second case study

The influence of gravity is enhanced with the distance due to the reduction in flow velocity towards the preform end. For the investigation of this phenomenon, the spatial evolution of concentration is plotted with the particle size. Figure IV.36 shows the slight increase of C at $x/L = 0.73$ with the increase of the particle size. The influence of gravity forces is enhanced with the decrease in flow velocity. As the preform is impregnated at constant pressure, the flow front velocity takes its maximum value at the beginning of injection. It then decreases following a power law to reach its minimum value at the end of impregnation.

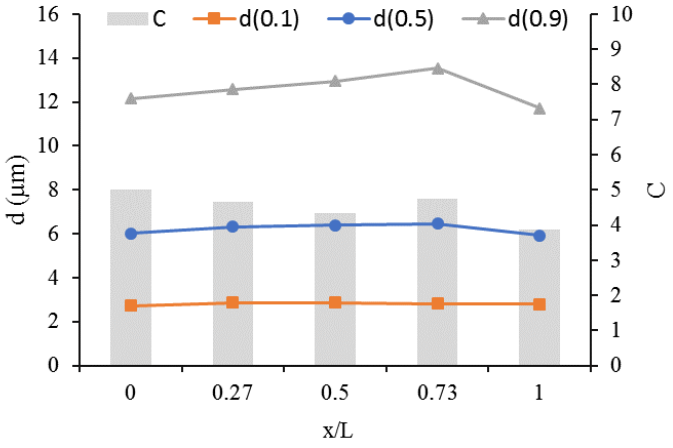

FIGURE IV.36: Particle sizes and concentrations from inlet to outlet (second study case)

Herzig [52] has shown that sedimentation should be taken into consideration for particles with $d_p > 1\mu$m. It could be negligible only if particles and liquid have comparable density values. The larger the particle size, the higher the effect of gravity forces F_g (Equation IV.7). The sedimentation velocity v_s is defined as the settlement velocity or the velocity of the vertical displacement of particles towards the bottom of the container. It is proportional to d_p^2 (Equation IV.8). The increase of v_s as a function d_p is shown in Figure IV.37 A. v_s is calculated and compared to the interstitial flow velocity v, which is related to the bulk flow velocity U by the relation $v = U/\epsilon$, where ϵ is the porosity of the fibrous medium. For $U = 10^{-3}$, 10^{-2} and 10^{-1} m/s, the ratio v_s/v is plotted in Figure IV.37 B as a function of particle size from 1 μm to 100 μm with a porosity ϵ= 0.52. The figure shows that the ratio between sedimentation to flow velocities increases with particle size. When the flow velocity decreases, the sedimentation velocity becomes dominant. I. e. the lower the flow velocity, the higher the sedimentation probability.

$$F_g = \frac{1}{6}\pi d_p^3(\rho_p - \rho_l)g \tag{IV.7}$$

$$v_s = \frac{d_p^2(\rho_p - \rho_l)g}{18\eta_0} \tag{IV.8}$$

For particles of sizes below 50 μm, the sedimentation velocity is lower than 10^{-2} m/s. The flow front velocity tangibly decreases at the end of the preform (in the order of 10^{-3} m/s for the present case). Hence, the difference between the sedimentation and flow velocity decreases, enhancing the effect of gravity forces on the large-sized particles. However, when particles and fluid have different densities, the velocity of the moving particles will be different from that of the carrying fluid [103].

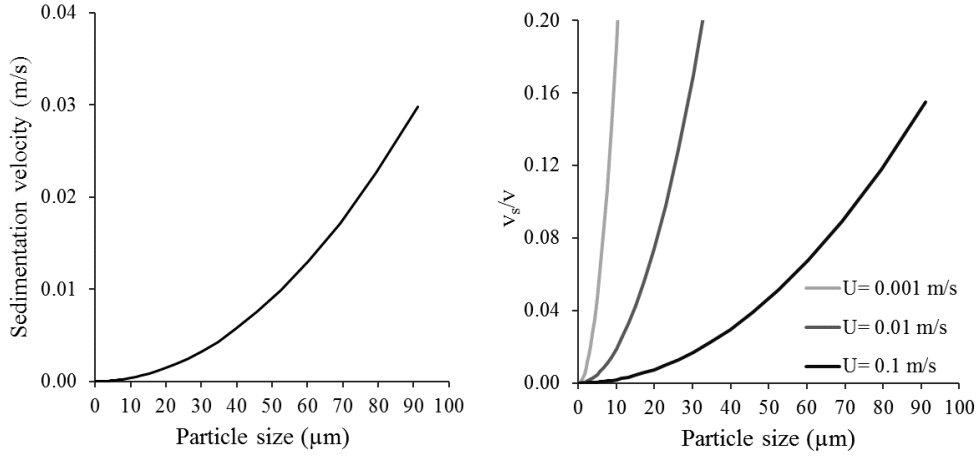

FIGURE IV.37: Illustration of (A) the dependency of the sedimentation velocity on particle size and (B) the evolution of the sedimentation velocity to the flow velocity v_s/v with particle size

The concentration of suspended particles is a superposition of two phenomena; the decrease of particle concentration due to particle retention on the one hand and the increase of the size of particles deposited in the sampling tubes toward the end of the preform on the other hand. With increased retention (e.g., due to high V_f), the drop in concentration is dominant and a decreasing concentration profile is obtained. In other cases, such as low V_f, the transverse filtration is enhanced with increased fiber inter-spacing and thus, the increase in concentration is dominant. Lefevre et al. [60] reported an increase in particle content at the end of the preform, which gives a U-shaped profile similar to the profiles observed in this study. The authors explained this phenomenon by the existence of liquid wells within the reinforcement during the flow, leading to a modification of the suspension concentration located at the flow front level.

IV.8.3 Filter efficiency

Analytical models for the determination of particle removal efficiency are presented in the literature for water filtration applications [52]. These models predicted the particle transport efficiencies according to their sizes. Authors found that smaller particles are transported by diffusion while larger ones were subjected to direct interception and settling. The following equations model the particle transport efficiency as a function of the suspended particle size. Submicrometric particles (with sizes $d_p < 1$ μm) are mainly transported by diffusion forces. The particle transport efficiency of this category is low as it is proportional to $d_p^{-2/3}$. Equation IV.9 calculates diffusion efficiency η_D which is developed by Levich [104].

$$\eta_D = 0.9 \left(\frac{k_B T}{\eta d_p v} \right)^{2/3} \tag{IV.9}$$

where k_B and T are respectively Boltzmann's constant and the absolute temperature.

Particles could also be blocked mechanically in constrictions and crevices by direct interception when their size exceeds the inter-fiber spacing [105, 106]. Equation IV.10 models the interception efficiency η_I.

$$\eta_I = \frac{3}{2} \left(\frac{dp}{D_{eq}} \right)^2 \tag{IV.10}$$

where D_{eq} is the equivalent diameter of the grains constituting the medium (presented in section IV.9 for fibrous media).

Sedimentation induced by gravity forces plays a major role in the deposition of this range of sizes and especially for agglomerates [107, 108]. The transport efficiency for large particles is proportional to d_p^2. Equation IV.11 determines the sedimentation efficiency

η_S which was proposed by Yao [106].

$$\eta_S = \frac{(\rho_p - \rho_f) g d_p^2}{18 \eta v} \tag{IV.11}$$

Figure IV.38 A plots the three collector efficiencies as a function of particle size. For small particle sizes, the diffusion forces are at their maximum; they decrease with the particle size increase. At around 0.1 μm, the collect efficiency by interception becomes predominant. At the same range, the sedimentation efficiency increases linearly with the particle size. The superposition of the three efficiencies presented in Figure IV.38 B shows that there exists a size limit for which the particle transport efficiency is minimum.

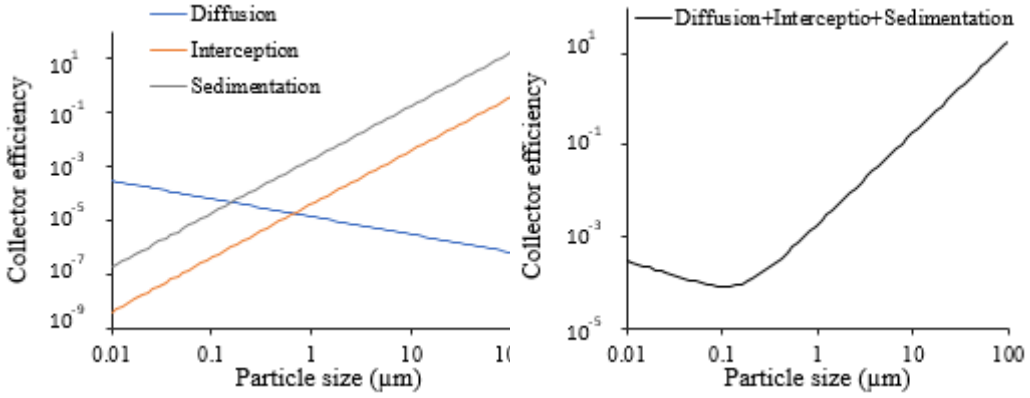

(A) (B)

FIGURE IV.38: The theoretical models for (A) single collector efficiencies and (B) the sum of the efficiencies of the acting forces as a function of particle size

Only a few particles in the studied PSDs have a size less than 1 μm. Hence, diffusion effects can be neglected. From d_p= 1 μm and above, particles are expected to be captured by direct interception or settled at the tow surface or the bottom of the mold by gravitational forces. The effect of sedimentation should be considered for the modeling of suspension flow through porous networks. It was observed experimentally that surface forces are enhanced for the particle sizes in the range 1-10 μm (section IV.8.2). Further research should be undertaken to propose a formula for predicting the filtration efficiency for particles of this category. This efficiency, which depends on the particle and preform characteristics, is expected to be high for this size range, raising the overall filtration efficiency.

IV.8.4 Classification of particle capture mechanisms

During the flow of suspensions of polydisperse particles through fibrous media, particles are expected to exhibit one of the following behaviors according to their size:

1. Part of the large-sized particles follows a surface filtration behavior and forms a cake filter at the preform inlet. The formed layer acts as a filter for the suspended

particles, including those with smaller sizes. This results in the presence of small and medium-sized particles within the blocked particle category.

2. Particles that succeed in entering the fibrous bed are prone to collide with the fibers. Then one of two possibilities takes place; either sticking to fibers/retained particles by surface forces and mechanical blockage or flowing with the suspension.

3. Part of the large particles is filtered transversely through the medium. As the flow velocity decreases by the end of the mold, gravitational forces are enhanced. As a result, those particles settle at the bottom of the mold under the effect of sedimentation.

4. Small particles with sizes less than the inter-fiber distances (for d_p <average micropore size) penetrate the intra-tow zones by transverse flow. They are captured inside tows by surface forces or direct interception.

Forces applied on particles cause their capture in different zones of the medium. In their research, Yao et al. [106] stated that the transmission efficiency of particles is highly dependent on their size d_p. Table IV.11 resumes the classification of filtration types and locations according to particle size.

TABLE IV.11: Filtration mechanisms and sites according to particle sizes

Filtration type	**Particle size (μm)**	**Capture mechanism**	**Retention zone**
Physico-chemical	$1<d_p<8$	Surface forces Interception	Fiber surface Intra-tow
Physico-chemical and Mechanical	$8<d_p<20$	Interception Surface forces Sedimentation	Fiber surface Intra-tow Constrictions
Mechanical	$d_p\geq 20$	Interception, Sedimentation	Constrictions Inter-fibers

IV.9 Inter-fiber distance and filtration criterion

The characteristics of the porous phase are generally accepted as being a major cause of filtration. The mechanical filtration could not be classified according to the particle size only; it should be accompanied by the average pore size of the medium; more precisely, the ratio between the particle size to the average pore size. In this section, different methods for determining the inter-fiber distances are presented and used to define a filtration criterion.

Inter-fiber distance

For the unidirectional non-crimp stitched fabric used in this study, it is possible to find a critical dimension above which the cake filtration occurs and the pores are blocked. This

quantity depends on the fiber content and the average fiber diameter. A characteristic length of pores δ_1 is defined as the mean free path of the fibrous medium calculated as a function of the average fiber radius $\overline{r_f}$ and the fiber volume fraction V_f [109]:

$$\delta_1 = \frac{\pi \overline{r_f}}{2} \frac{1 - V_f}{V_f} \tag{IV.12}$$

A simple formula based on the preform permeability K_f was proposed by Ward [110] to estimate the order of magnitude for the characteristic length of pores. Ward modeled this length (referred to herein as δ_2) as the square root of the medium permeability (Equation IV.13). This formula was verified experimentally with water-based suspensions flowing through granular media. In the present study, δ_2 is determined as $\sqrt{K_{Sat}}$, the saturated permeability of the neat fibrous bed.

$$\delta_2 = \sqrt{K_f} \tag{IV.13}$$

The inter-fiber distance is determined from a non-compact hexagonal stack. It is assumed that each fiber is separated from its neighbors by a distance δ_3. An elementary cell of an equilateral triangular is used as a base of calculations. The side of the triangle is $\delta_3 + 2r_f$. The distance δ_3 is calculated by:

$$\delta_3 = \overline{r_f} \left(\sqrt{\frac{2\pi}{\sqrt{3} V_f}} - 2 \right) \tag{IV.14}$$

For an average fiber radius for the quasi-UD preform $\overline{r_f}$= 8.7 μm, the three inter-fiber distances (δ_1, δ_2 and δ_3) are calculated are given by table IV.12 for the explored V_f values (38%, 48% and 58%). Figure IV.39 presents these distances for a wide range of fiber volume fractions (30%-65%). The curves represent the theoretical values and the points correspond to the percentages of fiber content used in the filtration experiments. It is observed that the difference between the three values is high at low volume fractions, this gap decreases considerably with the increase in V_f. However, δ_1 and δ_2 have close values at a significant part of the curve.

TABLE IV.12: characteristic pore length and inter-fiber distances

V_f	**38%**	**48%**	**58%**
δ_1	22.3	14.8	9.9
δ_2	28.2	12.6	5.7
δ_3	9.5	6.5	4.4

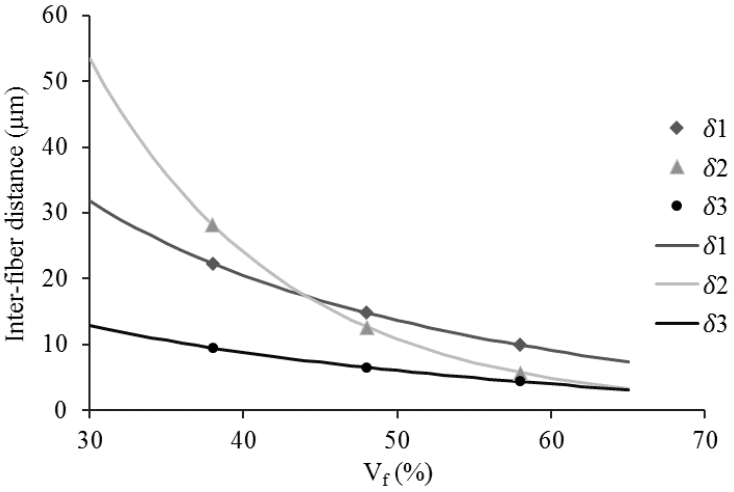

FIGURE IV.39: The evolution of the different inter-fiber distances with fiber content

Filtration criterion

The ratio $\lambda = D/d_p$ has been widely explored in the literature to define the filtration limits. Where D is the size of particles constituting the granular bed and d_p is the particle size. This ratio has been widely discussed for granular media for water treatment applications. Maroudas [111] has recognized two main retention behaviors: for $d_p/D > 0.15$, a cake filter of particles is formed; for $d_p/D < 0.065$, deep bed filtration takes place (depending on the characteristics of particles and the granular bed). For fibrous media, comparison between the two sizes is challenging and requires an adaptation of this quantity to fiber size as well as the medium properties [36]. A definition of an effective diameter is necessary to obtain a firm base of comparison with granular media. An equivalent diameter D_{eq} is introduced by Lefevre [6], it is given by the relation:

$$D_{eq} = \sqrt{\frac{36 h_k (1-\epsilon)^2 K_f}{\epsilon^3}} \tag{IV.15}$$

D_{eq} denotes the diameter of the grains constituting a granular medium having the same permeability as the fibrous one. The parameter λ is the ratio between the equivalent diameter to the particle size; it is given by:

$$\lambda = \frac{D_{eq}}{d_p} \tag{IV.16}$$

where λ is a non-dimensional constant. For the explored fiber volume fractions, the equivalent diameters are given by table IV.13. The value of D_{eq} increases with the V_f.

From literature, progressive retention was found to take place in the range $10 < \lambda < 20$, complete blockage happened at $\lambda < 10$ and no retention takes place at values >20 [52, 112, 113]. Failed experiments of this study (with full clogging) were found to be at

TABLE IV.13: Values of the equivalent diameter

V_f	38%	48%	58%
D_{eq} **(μm)**	261	195	146

values of λ of 9.73 and 12.84. However, other experiments were completed successfully with a normal flow at the same λ (12.84). Hence, the parameter λ is not enough to describe the filtration limit. This indicates that filtration is not only determined by the average size of the medium grains and suspended particles. For that reason, Lefevre et al. established another base for comparison between the different filtration behaviors. The parameter λ' (Equation IV.17) introduced the initial particle concentration C_0 to the evaluation procedure as follows:

$$\lambda' = \frac{D_{eq}}{d_p C_0} \tag{IV.17}$$

When determined for the performed experiments, λ' was found to be 128.4 and 194.5 for the failed experiments. All of the succeeded impregnations had higher λ' values, but the limit between flow and clogging experiments was unclear. Hence, a third parameter λ", which introduces the inter-fiber distance δ was defined by Lefevre (Equation IV.18). It permits to predict approximately whether the flow will be subjected to clogging or not for a given experiment, knowing the particle size, the initial concentration of the suspension and the fiber content in the preform.

$$\lambda'' = \frac{\delta}{d_p C_0} \tag{IV.18}$$

To plot the filtration limits, V_f was related to δ through Equations IV.12-IV.14. The term $\lambda'' d_p C_0$ represents the δ in Equation IV.18. The V_f was calculated using the three inter-fiber distances δ_1, δ_2 and δ_3 with the Equations IV.19, IV.20 and IV.21, respectively. In Equation IV.20, a and m represent the permeability parameters (as shown in Figure II.9 in section II.2.4.3). Figure IV.40 presents the V_f plotted as a function of $d_p C_0$, the red points denote the experiments at which clogging took place, the blue points are the experiments where normal flow and progressive retention were observed. The three curves represent the limits plotted with the three δ expressions.

$$V_f = \frac{\pi \overline{r_f}}{\pi \overline{r_f} + 2\lambda'' d_p C_0} \tag{IV.19}$$

$$V_f = \left(\frac{(\lambda'' d_p C_0)^2}{a} \right)^{\frac{1}{m}} \tag{IV.20}$$

$$V_f = \frac{2\pi}{\sqrt{3}} \left(\frac{\overline{r_f}}{2\overline{r_f} + \lambda'' d_p C_0} \right)^2 \tag{IV.21}$$

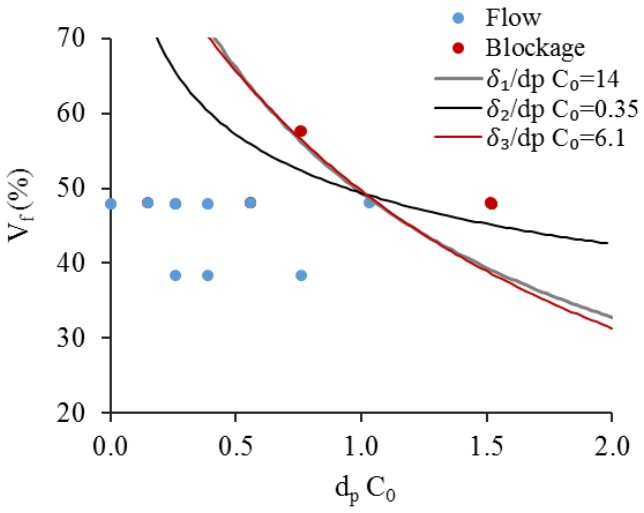

FIGURE IV.40: Theoretical limits and experimental points plotted with the filtration-parameter λ''

It was found from Figure IV.40 that the blockage limits plotted with δ_1 and δ_3 are almost identical with λ" of 14 and 6.1 respectively. Calculations with δ_2 resulted in a different curve shape with a limit at λ"= 0.35. Hence it is recommended to use the δ_1 and δ_3 for the future characterization of distances between fibers at a given V_f. The average value of δ_1 and δ_3 is taken to represent the inter-fiber spacing, which gives a value of 10.65 μm at V_f= 48%. This value is higher than the maximum size of particles retained inside fiber bundles (around 8 μm) of section IV.8.2. Although the two grades exhibited different PSDs, the maximum retained size was almost the same at fixed fiber volume fraction.

IV.10 Conclusion

This chapter addressed the effect of selected material and process parameters on the spatial evolution of particle concentration through fibrous media. Results have shown a continuous decrease in the concentration profiles except with a sudden rise of C near the preform outlet. The study has shown that the fiber content and the particle size are the most influencing parameters on particle filtration. As the studied particles have polydisperse distribution, a granulometry analysis was performed to extract the range of particle sizes retained inside the preform. It was found that the retained particles in the studied cases were constituted of the smallest sizes in the distribution. In contrast, the blocked category represented the largest sizes in the distribution. The analysis of particle granulometry along the preform length has shown that the increase in the particle concentration could be caused by the transverse filtration of particles and the sedimentation of large-sized particles near the preform outlet. Sedimentation is enhanced with the decrease in flow velocity, as the experiments are carried out under constant pressure injections.

The evidence from the SEM analysis confirms the entrapment of particles at the fiber surface and inside tows. In addition, the overall results demonstrated the key capture mechanisms of the retention of polydisperse particles according to their size and the corresponding capture sites. The scheme in Figure IV.41 illustrates the main filtration mechanisms encountered in this study, from the inlet to the outlet of the preform.

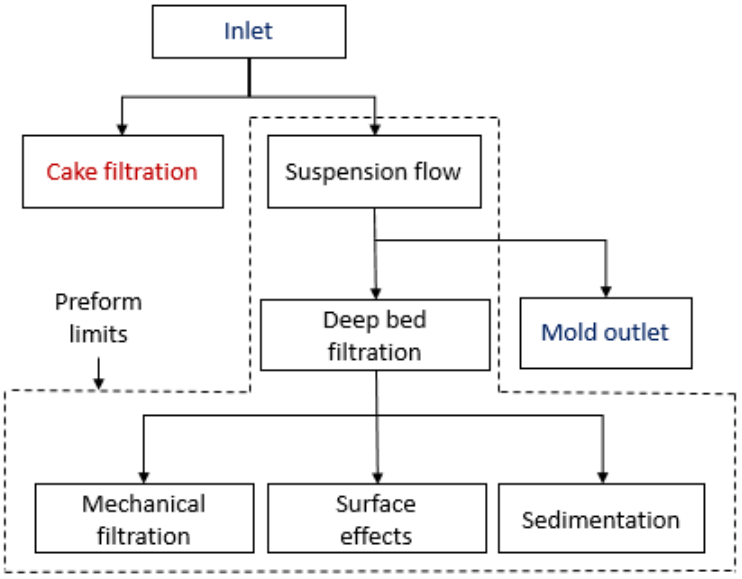

FIGURE IV.41: Illustration of the general filtration behavior of polydisperse particles in fibrous media

The developed methods presented in this study have succeeded in predicting the PSD of all the particle categories through the part length. The experimental results can be used for the determination of the main parameters that govern the filtration process. A comprehensive numerical simulation tool that couples flow and filtration models is required to model the studied experimental scenarios and estimate the filtration parameters. Once developed and validated, the numerical tool can predict filtration behavior with new cases not explored experimentally. The modeling and simulation of flow and filtration of suspensions are presented in chapter VI of this thesis.

The polydisperse nature of particles complicates the interpretation of results, especially in dual-scale media. This gives rise to the introduction of various capture mechanisms according to the particle size and retention site. Moreover, the decrease in flow velocity towards the end of the preform contributes to the enhancement of transverse filtration and sedimentation under gravity forces. Thus, further investigation is undertaken in the next chapter to mimic particle transport and capture in a single-scale media at the tow scale. To reduce the effect of polydispersity, the narrowest PSD will be used, then the evolution of particle volume content and count will be evaluated using different methods.

Chapter V

Filtration of micro-scale particle-loaded flow through unidirectional fibers

V.1 Introduction

Fibrous reinforcements used in LCM applications are often dual-scale porous media. The macro-scale is the scale of fiber preforms in which tow inter-distances are in the order of millimeters. The fiber inter-filament spacing inside tows are in the order of micrometers (micro-scale). The dual-scale nature of most LCM fabrics induces variabilities in the flow advancement in the inter and intra-tow zones [114]. Resin advances quickly in channels at high velocity, whereas at low flow velocity, it flows faster inside fiber bundles under the effect of capillary forces.

The characterization of flow at the micro-scale through fibers has been attracting widespread interest due to its effect on the general flow behavior and its direct influence on the global permeability and void formation behavior within dual-scale porous media. Microscopic structural parameters such as inter-fiber pore size, tortuosity, fiber size, shape and arrangement are responsible for the macroscopic permeability variations in porous media [115]. As highlighted by Kuentzer et al. [116], the permeability characterization of the dual-scale fabrics necessitates a versatile definition of both the bulk and micro-scale flow.

The vitality of the micro-flow subject led to important evolutions concerning the reproduction of single-scale fibrous media, both experimentally and numerically. To study the flow in single-scale media, researchers headed towards creating artificial fibrous media constituted of aligned fibers at different configurations. For most studies, assumptions of aligned fibers in ordered or random arrays have been made. Parallel fibers are randomly or uniformly distributed in a regular-shaped medium, e.g., of a rectangular or

circular cross-section (Figure V.1). Zarandi et al. [117] re-created rectangular media with fiber volume fractions of 40%, 45% and 50% for permeability testing purposes. For all the samples, fibers were distributed homogeneously between two Plexiglas sheets; fibers are hence forced to be parallel and straight between the two 20 cm long sheets. Screws are then used to adjust the required V_f (Figure V.1 A). The authors used a falling-head permeameter to measure the transverse and longitudinal permeability. In another study, Zarandi et al. [118] used the same method to characterize the permeability parallel and perpendicular to glass fiber wicks with random fiber arrangements and different V_f values (Figure V.1 B). The method is based on forcing the fluid to pass through a vertical graduated cylinder to the fiber-wick samples attached to the cylinder end under the gravity effect. The permeability is measured using the fluid levels in the cylinder at two instants of time. For transverse permeability measurements (not presented herein), the created fiber wick (Figure V.1 B) is constituted of glass fibers inserted inside a rectangular-section Plexiglas medium.

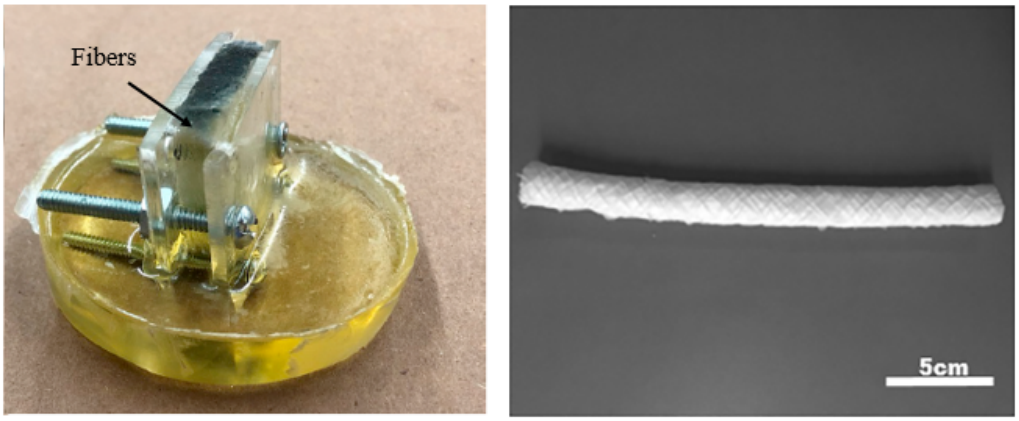

(A) (B)

FIGURE V.1: Examples for re-created fibrous media from the literature, with (A) sample parts are dipped in epoxy in order to lock the fibers in their places inside the sample[117] and (B) cylindrical wicks made of glass fibers [118]

Numerically, artificial porous structures are created using software such as GeoDict [117, 119], COMSOL [120] and real scanned structures by μCT (micro-Tomography) [121]. Yazdchi et al. [122] developed a micro-structural model using the finite element method (FEM) to predict the transverse permeability through unidirectional random arrays of fibers. The authors highlighted that the microstructure has a strong effect on the permeability of the fibrous medium.

In chapter IV, the filtration of particles was investigated for a unidirectional dual-scale fibrous medium macroscopically. The global filtration behavior was analyzed through integrated flow and filtration experiments. It was found that particles could be retained in both inter-tow and intra-tow regions through different filtration mechanisms depending on the particle size category. Nevertheless, no precise characterization of particle flow between fibers is provided. Hence, an experimental methodology is developed herein to

characterize the flow and filtration of suspensions through a single-scale medium constituted of aligned fibers. The process herein is different from the macro-scale flow through tows; as a single-scale inter-fiber spacing in the order of tens of microns governs the filtration mechanisms. As reported in chapter IV, process and material variables determine the final particle content and size distribution within composite parts. Therefore, identifying the key parameters and mechanisms that govern particle retention inside tows will help predict and control their distribution.

Although several studies have addressed the flow characterization in single-scale systems, the transport of particles through individual fibers has not yet been sufficiently investigated experimentally. Therefore, this chapter is a first contribution to understanding the filtration phenomena through random arrays of unidirectional fibers. A new experimental methodology is developed to inject suspension into the fibrous medium using a medical syringe driver. Characterization of flow and filtration will be assured using non-curing and curing fluids. For the characterization of particle content, two different methods are followed: thermal decomposition and image processing.

The three scales of the preform should be considered for characterizing and modeling filtration: the macro-scale, which describes the flow at the part level (cm-m), the meso-scale, which handles the flow at the level of fiber bundles (mm-cm) and the micro-scale, which describes the flow inside fiber bundles, between single fibers (μm). Figure V.2 illustrates the three scales of the used quasi-UD fabric.

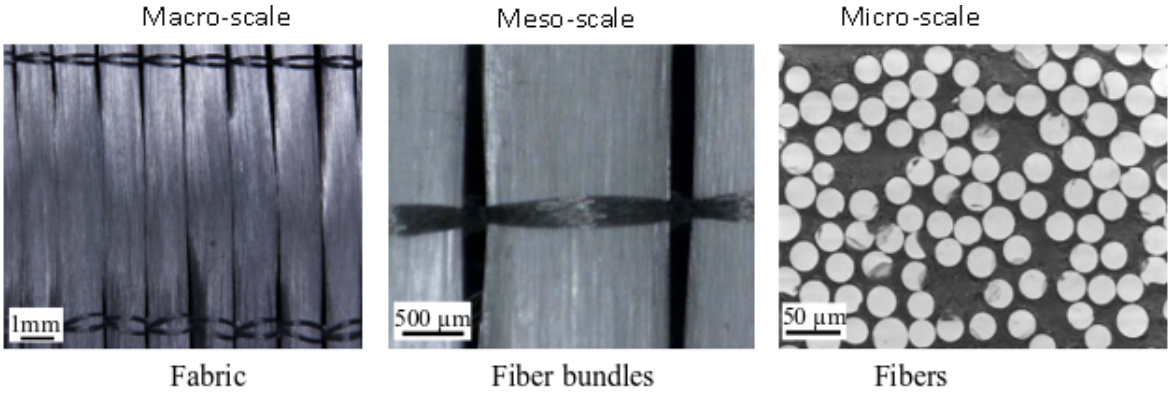

FIGURE V.2: Scales of the fibrous preform

The experiments performed in chapter IV enabled the characterization of flow and filtration of suspensions at the macro-scale and gave a qualitative analysis of the particle capture at the meso-scale. In this chapter, the level of experiments is down-scaled from the fabric to the tow level. The flow and filtration experiments are carried out with the following objectives:

- questioning the general filtration behavior in single-scale media,
- studying the spatial evolution of particle count and granulometry through unidirectional fibrous media.

V.2 Experimental methodology

The fibrous medium is constituted of parallel aligned fibers inserted in a cylindrical open-ended tube with a circular cross-section. A series of constant flow rate experiments are carried out with the help of a medical syringe. The suspension is injected in the direction axial to parallel fibers. The suspension passes from the device to the medium through a transparent injection tube. The flow front advancement and the pressure evolution are observed and registered at fixed distances. The experiments are performed with the model fluid for flow characterization and curing resin to quantify particle content and count.

V.2.1 Materials

Experiments were designated to study both flow and filtration behaviors of suspensions through aligned fibers. Ceramic particles dispersed in aqueous glycerol solutions or epoxy resin are used throughout the tests. Suspensions were prepared with variable particle concentrations.

Fibers

Fibers were pulled out from the tows of the quasi-UD fabric presented in II.2 and used in the chapters III and IV. The diameter of fibers is a crucial parameter in the flow characterization inside tows, as many permeability models depend on it. The fiber mean diameter obtained from optical microscopy images over 300 fibers is 17.4±0.2 μm. The size distribution of fibers ranges from 15.7 μm to 20.8 μm [64].

Model fluid and curing resin

For the study of suspension flow, glycerol/water mixtures (described in section II.3.2) were used with a 75/25% percentage (in wt.%). The mixture exhibits a density of 1.19±0.01 g/cm^3 and a viscosity of 0.035±0.002 Pa.s. Cured samples are fabricated for the study of the evolution of particle content and count. The resin SR GreenPoxy 56 with the catalyst SR 8100 is used as the carrying fluid (refer to section II.3.3 for more information).

Particles

3M Ceramic particles of grade W-210 are used for the experiments because they exhibited the narrowest distribution among the three explored grades (W-210, W-410 and W-610).

The distribution of this grade has a median particle size of 5.2 μm. More information about the particle characterization and size distribution are available in section II.4.0.2.

V.2.2 Experimental set-up

The injection system used in the previous chapter for macro-experiments is replaced by a new device to suit the change of scale from the preform to the fiber level. The experimental set-up consisted of an injection system and a tube to transport the suspensions from the injection port to the fibrous medium (Figure V.3).

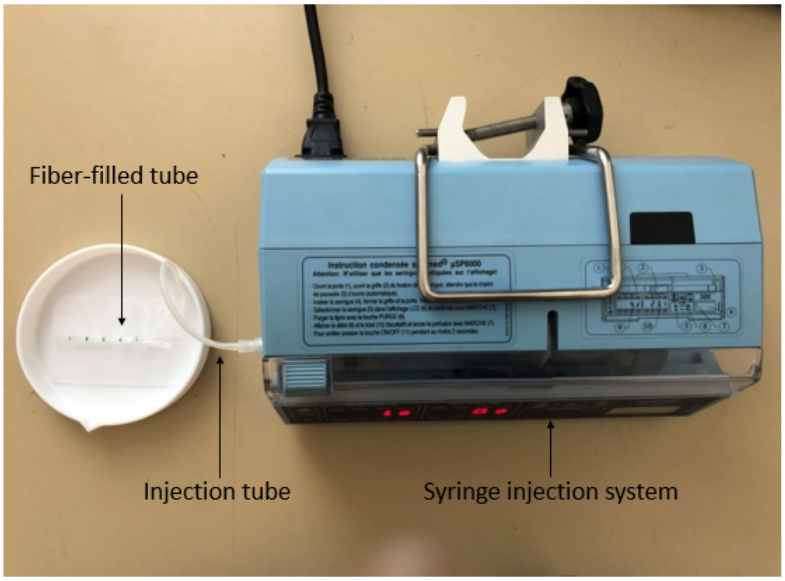

FIGURE V.3: Top view of the experimental set-up

Injection system

The injection is carried out by the syringe driver Syramed μSP6000 commonly used for medical purposes. It is a small, electricity-powered pump that delivers medication at constant flow rates. The Bescher burette syringe driver gives the possibility of measuring the pressure in the system. The monitor also permits the control of the total injected quantity and allows the adjustment of the injection flow rate in ml/hr. Figure V.4 illustrates the detailed parts of the injection device. For these experiments, suspensions are placed in the syringe (without a needle) of 60 ml capacity and then injected into the fibrous medium.

Injection tube

A silicone tube of an internal diameter of 1.15 mm is installed at the syringe end to transport the suspension to the fibrous medium. The walls of the tube are transparent

FIGURE V.4: Parts of the medical syringe used for the injection

to allow the visualization of the front advancement. The outlet of this tube is connected directly to the inlet of the fibrous medium.

Fiber placement inside the tube

The medium consisted of aligned glass fibers inserted in a parallel configuration inside a polymeric tube. The tube has an internal diameter of 0.8 mm, and a length of 40 mm (Figure V.5). The tube is weighed with a Sartorius scale with an accuracy of ±0.1 mg and a maximum capacity of 220 g. Fibers of the same length are extracted from the preform tows since the volume of a whole mesh exceeds the existing volume of the tube. Therefore, the fibers should be longer than double the tube length. Using a needle and thread, the fibers are attached from the middle and inserted into the tube. After insertion, fibers are cut to the tube limits with a cutter. The tube containing fibers is weighed again. The mass of fibers is calculated by subtracting the total mass from the tube mass.

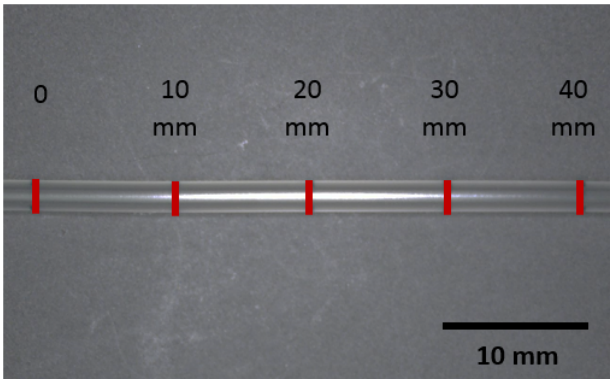

FIGURE V.5: Illustration of the graduated tube which envelops the fibrous medium

V.2.3 Characterization of the porous medium

The fiber-filled tube is built to constitute a single-scale medium with unidirectional fibers inserted parallel to each other. It is important to highlight that the real tows are different from the created medium in many aspects. First, real tows exhibit different forms according to their compaction in the preform. Second, they have stitches that change the cross-section of tows locally. Moreover, the main impregnation mechanism of the real tows in dual-scale media is usually the transverse flow [100, 102], where the built system is mainly injected longitudinally in the fiber direction.

The fiber volume fraction V_f of the medium is determined experimentally by dividing the fiber mass m_f by the product of its density ρ_f and the total volume in the tube V_{total}:

$$V_f = \frac{m_f}{\rho_f v_{total}} \tag{V.1}$$

The total volume of the tube is calculated as the volume of a cylinder with an internal radius r_t and a length L:

$$v_{total} = \pi r_t^2 L \tag{V.2}$$

Unfortunately, the fiber placement method exhibits a limitation; the manual insertion of fibers makes it challenging to adjust the fiber content in advance. Inevitably, this limitation affects the repeatability of experiments, as it is difficult to reproduce the same V_f several times. Therefore, the global porosity is considered herein as the ratio of the pore volume fraction to the total volume fraction of the tube ($\epsilon_0 = 1 - V_f$). When micrographs are used, the porosity is determined from the ratio between the pore area fraction to the total area, which is the tube cross-section. The area porosity, in this case, is equivalent to the volume porosity [117] and it is determined by [120]:

$$\epsilon_0 = 1 - \frac{\pi N \overline{d_f}^2}{4A_T} \tag{V.3}$$

with N the number of fibers, $\overline{d_f}$ the average fiber diameter and A_T the total cross-section area of the tube.
In the presence of particles, the medium porosity is altered as a function of the trapped particle fraction at a given position x and at a defined instant of time. In the case of samples prepared with particle-loaded resin, the porosity at a given cross-section is determined at the instant t=T as follows:

$$\epsilon = 1 - \frac{\pi}{4A_T}\left(N\overline{d_f}^2 - \sum_{i=1}^{M} d_{ap(i)}^2\right) \tag{V.4}$$

with M, the number of particles at a specific location at a given instant of time t. The diameter $d_{ap}(i)$ herein represent the apparent size of particles measured in one cross-section (inside the tube).

V.2.4 Parameters and protocol

Fibrous media are injected at low flow rates (Q= 2 ml/h) to avoid the fiber wash-out. Different V_f values are tested with pure and particle-loaded glycerol solutions. Curing resin is used for the preparation of particle-filled samples. A range of fiber volume fractions is explored at the given particle concentrations with glycerol/water mixtures and epoxy resin (V.1). Initially, the experimental plan included concentrations up to 5%. Tests revealed that suspensions with C_0 above 4% and more than 50% of fibers cause stagnation at the medium entrance. At this point, excessive cake filtration occurs, leading to obstruction of flow channels and a sudden rise in pressure. Therefore, flow and filtration are investigated for C_0 values up to 3%. The results will discuss the influence of initial particle and fiber content on flow and filtration, i.e., front advancement, particle content and pressure.

TABLE V.1: Experimental parameters: suspension concentration and fiber volume fractions of the fibrous media used with Glycerol solutions and curing resin

C_0 (%)	V_f (%)	
	Glycerol solutions	Curing resin
0	44.6 52.8	-
1	-	52.3
1.5	38.9	47.1
2	36.2	53.3
3	39.1	44.1 48.2 58.3

Experimental protocol

The realized impregnation experiments can be divided into two categories according to the used fluid:

1. Flow characterization
   Suspensions of aqueous glycerol solutions and ceramic particles are prepared and used at different concentrations for flow characterization.

2. Filtration study
   Curing resin is used for the characterization of particle content along the sample length.

The steps of the preparations and execution of experiments are detailed in Table V.2.

TABLE V.2: Experimental protocol

No.	Step	Details
1	Medium preparation	- Fibers are extracted from a quasi-UD reinforcement. - The group of fibers is inserted into the tube. - Fibers are cut to the length of the tube. - The tube is weighed before and after fiber insertion. - The fiber volume fraction is deduced.
2	Suspension preparation	- The glycerol and water are mixed with the required percentages. - The dispersing agent is added to the fluid or resin. - The required particle mass is determined, particles are then weighed and added to the mixture. - The suspension is dispersed with a magnetic stirrer for a minimum duration of 2 hours until a few minutes from the beginning of injection. - The syringe is filled with the suspension.
3	Experiment preparation	- The syringe is installed in the injection unit. - The apparatus is adjusted for the required injection flow rate.
4	Impregnation	- The device is set for pressure acquisition. - The impregnation is started.
5	Acquisition	The time and pressure are registered as soon as the flow front reaches the fibrous medium inlet at $t = 0s$ and at every 10 mm.

V.3 Flow characterization (model fluid)

Experiments are carried out with neat glycerol aqueous solutions to study the flow kinetics. In the following, the effect of fiber content on pressure evolution and front advancement is addressed for constant flow rate injections.

V.3.1 Flow front advancement

The arrival time of the flow front is registered at equal distances of 10 mm distributed through the total flow path (40 mm long) using a chronometer. Hence, the flow front

positions x_f are fixed to 0, 10 mm, 20 mm, 30 mm and 40 mm. Figure V.6 compares the experimental flow front positions with time at fiber volume fractions of 44.6% and 52.8%. The flow front exhibited linear evolution with time except for the last position for the two explored constant flow rate injections. This figure shows that the slope of the flow front profile versus time increased with the increase in fiber content. The impregnation time clearly decreased with the increase of V_f.

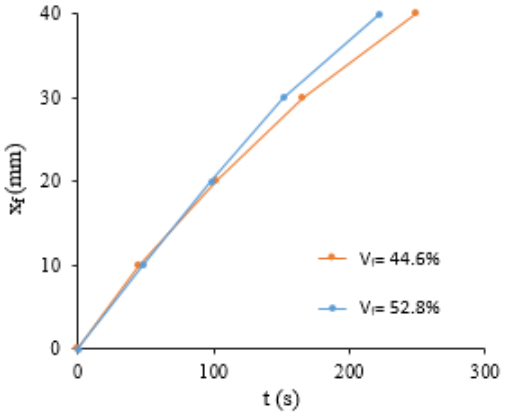

FIGURE V.6: Temporal evolution of flow front as a function of fiber content for V_f= 44.6% and 52.8% injected with neat glycerol solutions

Figure V.7 compares the flow front advancement with time at three different suspension concentrations (1.5%, 2% and 3%) for mediums having comparable V_f values (between 36.2 and 39.1%). In the range of suspensions explored, it was found that the flow front was qausi-linear with C_0= 2%, whilst it exhibited some non-linearities with time for two cases (C_0= 1.5% and 3%). The addition of particles caused a delay in front advancement at comparable V_f values. The slope of $x_f = f(t)$ has dropped with the increase of C_0. These results are consistent with the macroscopic effect of particle addition on the flow front for constant pressure injections (Figure IV.8 of chapter IV). The delay in front advancement could be a result of particle build-up at the tube inlet. It was shown in chapter IV that the filter density is proportional to the suspension concentration. Consequently, the obstructed flow inlet induced this effect on the flow front slope as a function of C_0.

The flow front profiles are expected to be disturbed by the gap between the tube wall and fibers, where the fluid can advance faster in these zones than in the fibrous medium, enhancing the transverse flow. This effect is decreased with the increase in fiber content inside the tube. The variations in flow front profiles could also arise from the high heterogeneity in the inter-fiber spacing at this scale.

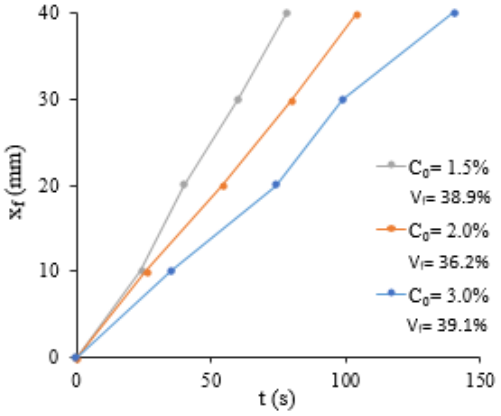

FIGURE V.7: Evolution of flow front position with time at comparable V_f values, injected with suspensions of C_0= 1.5%, 2% and 3%

V.3.2 Pressure evolution

The effect of V_f on the pressure spatial evolution is shown in Figure (V.8 A) for injections of pure test fluid (without particles). The pressure profiles exhibited increasing trends versus the flow front position x_f at V_f= 44.6% and 52.8%. Higher pressure was observed with the increase in fiber content (V_f= 44.6%).

Figure V.8 B shows the effect of particle addition on pressure profiles at comparable V_f values for the experiments presented in Figure V.7 (at C_0= 1.5%, 2% and 3% and V_f=36.2-39.1%). The pressure increased with the increase in particle concentration of the injected suspension. Non-linearities in pressure profiles are observed for those media impregnated using the syringe driver. This disturbance in pressure values could arise from the counter-pressure caused by the presence of the fibrous medium or the effect of capillary pressure.

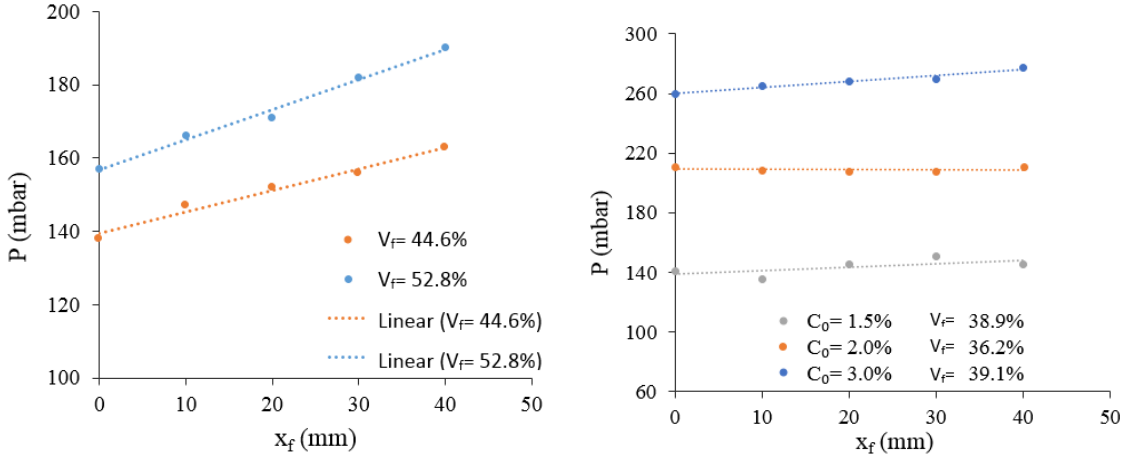

(A) (B)

FIGURE V.8: Evolution of pressure with flow front positions (A) at different fiber volume fractions (V_f= 44.6% and 52.8%) for neat fluid injections and (B) at comparable V_f values, injected with suspensions of C_0= 1.5%, 2% and 3%

V.4 Characterization of particle content (curing-resin)

After the study of suspension flow through the fiber-filled tube using a model fluid, the filtration of the same particle type is characterized using a curing resin. The same experimental protocol detailed in Table V.2 is applied for the suspension preparation and impregnation. Once the tube is filled, the sample is cured, cut, and prepared for characterization by calcination or image analysis of the composite cross-sections.

V.4.1 Thermal decomposition

Calcination (described in section I.4) is one of the most used methods for the characterization of particle content in composite samples [6, 36]. In this method, constituents must have different decomposition temperatures. For the meso-samples in question, degradation temperature is 450 $°C$ for the resin, 600°C for glass fibers and 1000$°C$for ceramic particles. Hence, the following steps are applied:

- fibers are inserted in the tube and weighed as described in V.3.1. The mass of fibers m_f is extracted before impregnation,
- the medium is impregnated with particle-loaded resin under constant flow rate as described in Table V.2,
- after curing, the tube surrounding the cured sample is removed and samples of the fibrous medium are cut into four equal parts,
- samples are placed in the oven in different containers at 450°C for 1 hour for resin degradation,
- samples are weighed after calcination, and the mass of each of the four parts is compared to the initial mass of neat fibers. The difference is assigned to the particle mass m_p.

Given that continuous fibers of the same length are inserted inside each tube, it is expected that the fiber content will not vary throughout the tube length. A test is carried out to calculate the experimental error in measuring the fiber mass for each sample quarter. A tube with 50% fibers in volume is impregnated with neat resin. The tube is removed, the sample is divided into four equal parts and heated in the oven. After calcination, each part is weighed separately. For a total fiber mass m_f of 29.9 mg, the theoretical mass of each quarter should be 7.4 mg. The measured experimental masses were respectively 6.8 mg, 7.1 mg, 6.8 mg and 7.4 mg with an average of 7.025 mg and a standard deviation of 0.25 mg. The difference could arise from the experimental errors related to the sample cutting.

Experiments are performed with particle-loaded resin to investigate the evolution of spatial particle content. Suspensions of C_0= 2% and 3% are injected into fibrous media of respectively 40.3% and 55.2% volume content. The total mass was measured three times: before the beginning of the experiment, after impregnation and after resin decomposition.

The particle weight percentage W_p is calculated as the ratio of particle mass to the total mass (particles and resin). The particle volume content is then determined from the W_p as follows [6]:

$$V_p\% = \frac{100}{\frac{\rho_p}{\rho_l}\left(\frac{100}{W_p\%} - 1\right) + 1} \tag{V.5}$$

This percentage represents the particles retained by the fibrous medium as well as the suspended particles at the end of injection (ψ).

Figure V.9 presents the results of particle content evolution in space for C_0= 2%, V_f= 55.2% (Figure V.9 A) and C_0= 3%, V_f= 40.3% (Figure V.9 B). The tube is cut to four equal segments, the particle content in the first, second, third and the fourth segments are respectively plotted at x=5, 15, 25 and 35 mm in Figure V.9. The particle content at x= 0 mm is considered as C_0. Similar particle content profiles were observed for the two experiments. It can be seen that the particle content is decreasing continuously with distance. Steeper decrease in particle content is observed for the highest V_p (3%) due to increased filtration at the medium inlet. The same trend was observed for most of the macroscopic experiments of chapter IV carried out at the preform scale.

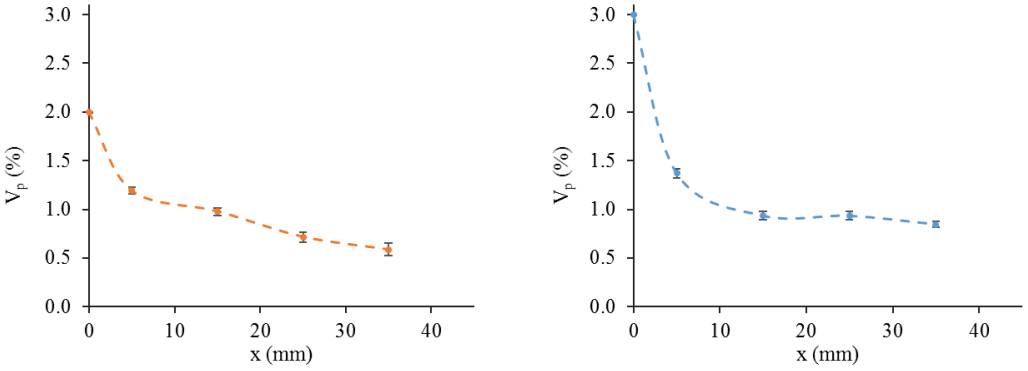

FIGURE V.9: Spatial evolution of particle content using thermal decomposition method for (A) C_0= 2%, V_f= 55.2% and (B) C_0= 3%, V_f= 40.3%

Limitations

Although its efficiency in predicting the filtration behavior, the calcination method exhibits several drawbacks, leading to the accumulation of errors. The small scale of the experiment imposes dealing with low fiber and particle masses. The low used particle concentrations do not allow for significant variations between the different measurements of the four sample parts, which makes it challenging to separate fiber mass from particle mass in the different quarters. With glass fibers, only the resin is decomposed with heating; hence, a very accurate measurement of the fiber mass before and after calcination is required to deduce a precise particle mass. As for this study, the same type of fibers used in the previous investigations is kept to avoid discrepancies that could arise from fiber size or type changes. Future investigations can replace glass fibers with degradable types such as Kevlar fibers for complete decomposition at relatively low temperatures. Moreover, this method only allows the extraction of particle content; further steps are needed to characterize particle count and size. For all the mentioned reasons, image processing will be tested for a more accurate characterization of particle and fiber contents at different locations.

V.4.2 Image processing

It has been widely agreed that image processing is one of the most effective methods for the determination of solid-phase fraction [123]. In this method, tubes are cut into four equal parts of 10 mm long after resin cure. Samples are then mounted to sample molds and surrounded then by an embedding resin (Figure V.10). Molds are placed in the oven for curing at 90°. After resin solidification, samples were polished as follows:

- 300 μm with SiC #120 grains and water,
- 1 min 20 s with SiC #320 grains and water,
- 1 min 20 s with SiC #1200 grains and water,
- 1 min with MD Largo with 9 μm Dp-blue,
- 1 min 30 s with MD-DP-DAC with 3 μm Dp-blue,
- 2 min 30 s with MD-Chem with 1 μm Dp-blue.

V.4.2.1 Characterization methodology

Three cuts were realized on the tube containing fibers to determine the spatial variation of particle content through the sample length. The tubes are cut at the red marks 1,2 and 3 indicated by Figure V.11. As a total, four cross-sections are observed with SEM

(A) (B)

FIGURE V.10: Sample preparation with (A) installation of tubes in the mold and (B) demolded and polished samples

after the sample cutting and polishing at the locations: 1- x= 10 mm, 2- x= 20 mm, 3- x= 30 mm and 4- x= 40 mm.

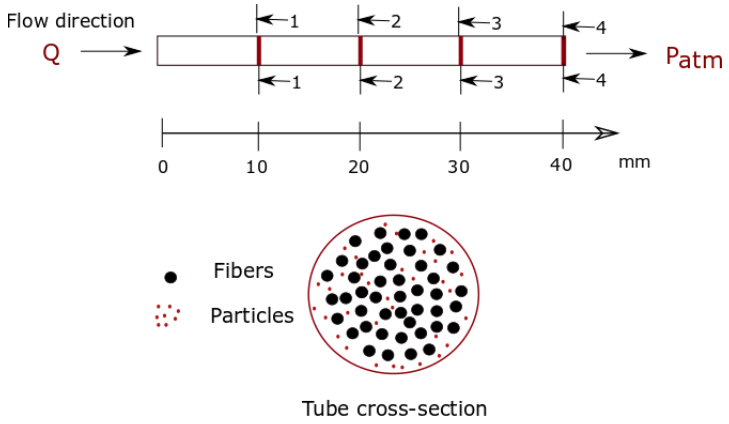

FIGURE V.11: Illustration of the sample preparation and the experiment principle for microscopic characterization

Figure V.13 shows a cross-section of a cured sample with uniquely fibers and resin at V_f= 46.6%. The white disks in these images are the fibers, the darker zones represent the resin areas and the black spot inside the tube is a void.

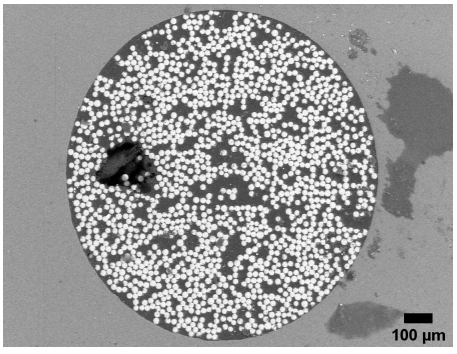

FIGURE V.12

FIGURE V.13: SEM images of a tube sample with uniquely glass fibers and curing resin with V_f= 46.6%, at magnifications of (A) x50 and (B) x75

The methodology presented in section V.2 is applied to fabricate composite samples with particle-loaded resin. Suspensions of resin and W-210 ceramic particles are injected through the fiber-filled tube. After impregnation, samples are cured overnight at room temperature. Tubes are cut and imaged by SEM for the following objectives:

- estimation of fiber volume fraction,
- characterization of the spatial evolution of particle percentage and number,
- identification of particle filtration trends inside the tube,
- qualitative analysis for voids distribution through the cross-section.

For filtration experiments, samples are injected with suspension concentrations of 1%, 1.5%, 2% and 3%. Figure V.14 shows SEM images of cured particle-filled suspensions with initial concentrations of 1% (Figure V.14 A) and 3% (Figure V.14 B), respectively. The white spots on these figures are the particles, whereas the dark gray color represents the resin. The figures show a clear increase in the number of particles with the initial concentration. Images also show good dispersion stability of the suspension. No agglomerate formation is observed in the cured resin samples. Images of particle-loaded resin are used to determine the actual area percentages of particles of the total area A_{p0} in a window of the dimensions 643μm x426 μm. Average values of C_0 were found to be 1.04%, 1.46%, 2.02% and 3.08% for suspensions prepared initially with respective C_0 values of 1%, 1.5%, 2% and 3%.

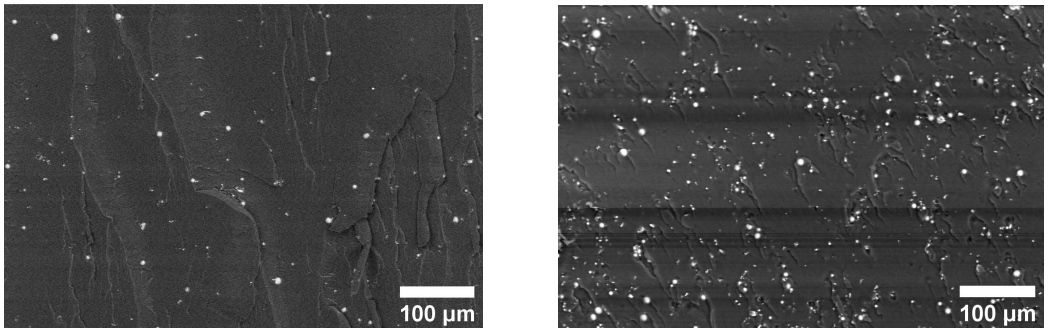

(A) (B)

FIGURE V.14: SEM images of a cured particle-loaded resin injected with (A) C_0= 1% and (B) C_0= 3%, at a magnification of x200

V.4.2.2 Experimental observations

The SEM images exhibited low contrast between glass fibers and ceramic particles. Figure V.15 shows a cross-section of particle-loaded sample with V_f= 47.1% and C_0= 1.5%. A better contrast was observed from this figure between voids and resin, and

fibers/particles and resin. However, qualitative analysis of the images has shown the following:

- particles are distributed in the dense fiber zones as well as in resin-rich areas,
- particles could be recognized from fibers with by the size difference,
- better distribution of fibers is observed inside the tube at relatively high fiber content.

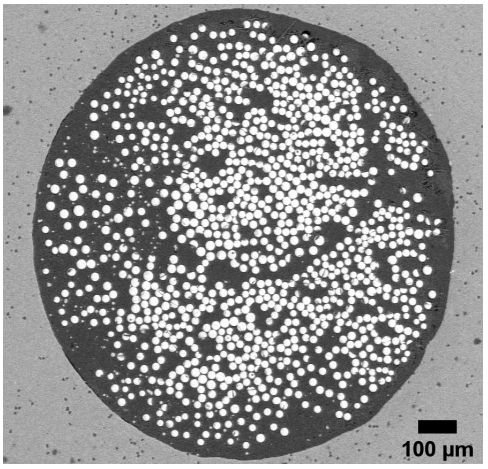

(A)

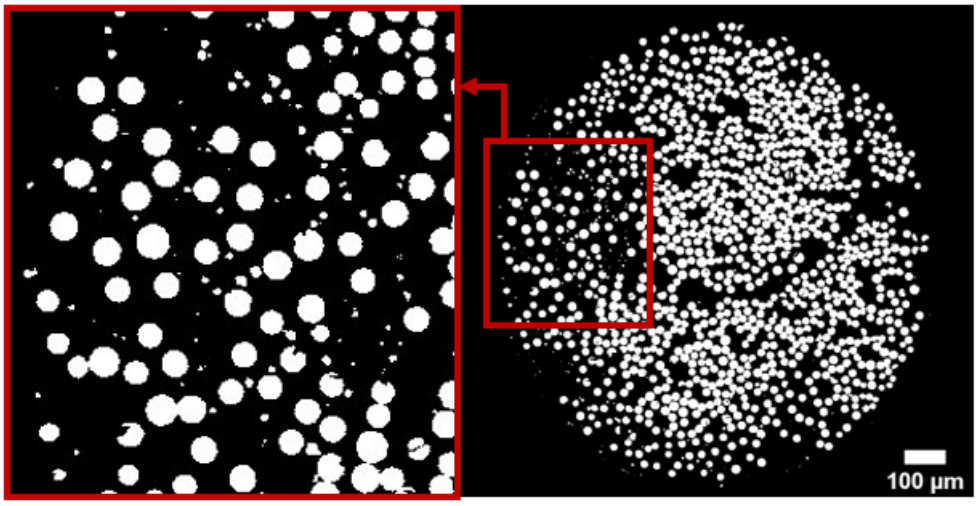

(B)

FIGURE V.15: SEM images of a particle-loaded sample with C_0= 1.5% and V_f= 47.1%, at a magnification of x75: (A) sample cross-section, (B) cross-section cropping and (C) sample after the threshold application

Particle and fiber known sizes are used as a base of comparison to distinguish ceramic particles from fibers. Image treatment is performed with the software ImageJ.

This analysis of each sample gives the fiber, particle and void area percentages, in addition to the number of particles at each cross-section. The area of each component

was divided by the total cross-section of the tube. One example is shown by Figure V.16 A below for an experiment with C_0= 1% and V_f= 52.3%. This figure shows the decrease in particle content with the flow path. From an initial concentration of 1%, the particle content drops to 0.58% at the medium exit. The filtration has shown a decreasing profile similar to the trend observed with calcination (section V.4.1). The number of particles present in the suspension follows a non-monotonous drop with the sampling distance (Figure V.16 B). A slight increase in particle count is observed at x= 20 mm (x/L=0.25); this increase may result from the accumulation of the large-sized particles that could not pass through fibers due to local variations of the inter-fiber spacing.

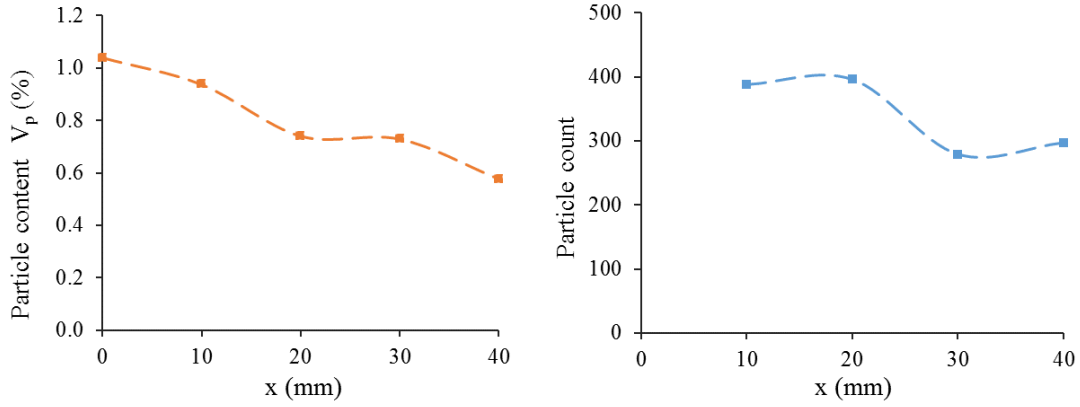

FIGURE V.16: Results of image processing of (A) particle content and (B) particle count versus distance for an experiment with C_0= 1% and V_f= 52.3%

V.4.2.3 Image decorrelation analysis

Image resolution plays a major role in the accuracy of the results. Hence, an image decorrelation analysis is performed for a series of images at the magnifications x50, x75, x200, x1000 and x3000. Figure V.18 plots the average resolution of SEM images as a function of their magnification. It can be clearly seen that the resolution in μm is improved with magnification. An image showing the overall cross-section of the tube including the fibers, resin and particles could be obtained at a magnification of x75. This magnification gives an average resolution of 3.2 μm, which falls in the range of particle sizes, and thus, it will increase the error percentage. The magnification x200 gives an acceptable resolution (around 1 μm); nevertheless, every cross-section has been divided into four equal quarters for every image characterization as this magnification does not cover the whole tube.

A sample of C_0= 1.5% and V_f= 47.1% (presented in Figure V.15) was analyzed twice for all the cross-sections at the magnifications x75 and x200. Results of the comparison are shown in Figure V.20. Results have shown a difference in the estimation of particle

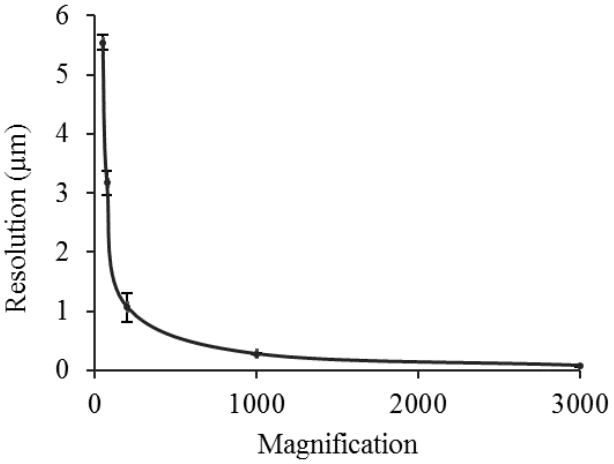

FIGURE V.17

FIGURE V.18: Image resolution as a function of magnification

content with the distance using two distinct magnifications. Images with x75 overestimated the particle area percentage considerably in comparison to those of x200. Thus, the evolution of particle content for the following cases will be calculated uniquely from SEM images with x200 magnification.

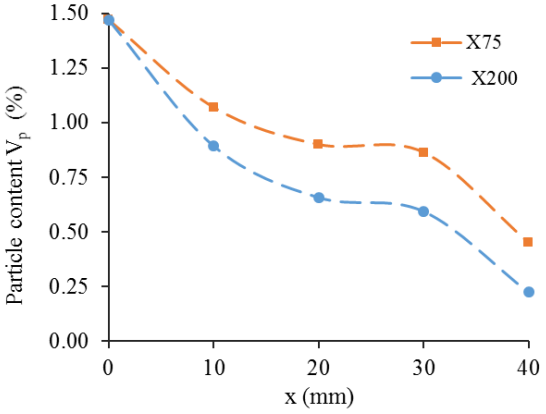

FIGURE V.19

FIGURE V.20: Comparison between the obtained results with the magnifications x75 and x200 for (A) particle content and (B) particle count versus distance

V.4.2.4 Limitations

Although the image treatment method has proven efficiency, several limitations could arise for the obtained results. The area percentages of particles depend largely on polishing and image quality. Moreover, debris of broken fibers from the polishing process could sometimes be considered as particles. Similarly, particle agglomerates could, in some cases, be dealt with as fibers.

V.5 Evolution of particle content

The macroscopic results highlighted the influence of material and process variables on the flow and filtration of the same suspensions (ceramic particles and glycerol mixtures). Results revealed that impregnation of fibrous media with suspensions is complicated and involves several variable interdependencies. Therefore, the variables for the impregnation of single-scale media are limited to the initial particle concentration and fiber content; to avoid complications that arise from the simultaneous characterization of multiple variables. The viscosity, flow rate and PSD were fixed throughout all the experiments. The effect of each variable is addressed separately hereafter.

V.5.1 Effect of fiber volume fraction

To evaluate the effect of fiber content on particle distribution, three different V_f values are compared at a C_0 fixed to 3%. The variations of particle content, count and void content are shown by figures V.21 A, V.21 B and V.21 C, respectively. A continuous decrease in particle content is observed with the filtration distance as the volume fraction of fiber increased. For the range of explored V_f values (44.1%, 48.2% and 58.3%), the particle content exhibited a decreasing trend. It has been shown in Figure IV.16 of Chapter IV that the reduction of pore space results in increased filtration. No clear void entrapment trend was observed, except for the second half of the tube, where the void percentage increases with V_f and with the filtration distance.

V.5.2 Effect of initial particle concentration

Figure V.22 shows the evolution of particle content (Figure V.22 A) and count (Figure V.22 B) for C_0= 1% and 2%. Figure V.22 C and Figure V.22 D plot respectively the evolution of particle content for C_0=1.5% at V_f= 47.1% and C_0= 3% at V_f= 58.3%. Similarly to the macroscopic experiments, the initial particle content does not seem to affect the filtration trend. A monotonous decrease of the percentage and the number of particles is noticed up to x =30 mm (x/L =0.75). After this point, the particle volume fraction follows a plateau or drops to lower values.

The difference in flow conditions for these tow-scale experiments is expected to alter the influence of some acting forces compared to the preform-scale experiments. One example is the gravity force which induced considerable particle sedimentation at the macro-scale (addressed in chapter IV), which was a consequence of macro-channels that allowed the free movement of large particles towards the mold bottom. Moreover, the flow velocity is fixed throughout the sample length, explaining the monotonous decrease in particle content in space. No sedimentation is observed in the examined samples; no sharp increase in particle content or accumulation of particles on the tube walls is

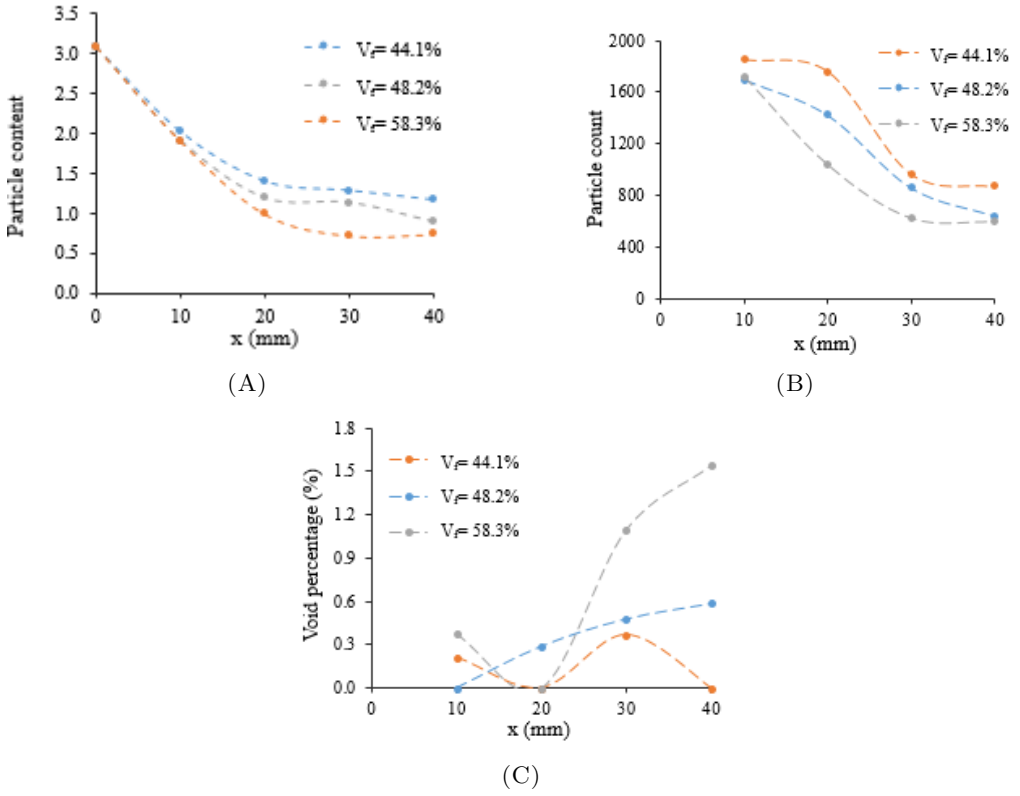

FIGURE V.21: Effect of fiber content on the spatial evolution of (A) particle content, (B) particle count and (C) void content versus distance for suspensions with C_0= 3% and V_f values: 44.1%, 48.2% and 58.3%

noticed towards the sample end for any of the explored cases. Good particle distribution is observed at the four cross-sections.

Because of the channel effect (the gap between fibers and tube wall), particles are expected to penetrate the fiber bundle transversely. Particle filtration is caused either by cake formation at the tube inlet or deep bed filtration (either the direct interception or the surface forces).

For three tests of different C_0, the evolution of particle volume fraction with the distance x is plotted at the end of impregnation for cured samples. Figure V.23 presents the experimental spatial particle content profiles for (A) C_0= 1% and V_f= 52.3%, (B) C_0= 1.5% and V_f= 47.1% and (C) C_0= 3% and V_f= 58.3%. The identified fitted equation of the experimental data is shown by the continuous line in Figure V.23 for each test. The particle volume fraction at a given position varies with the dimensionless distance x/L following the exponential relation:

$$V_p = C_0\, e^{-b\frac{x}{L}} \tag{V.6}$$

The values of the empirical parameter b are plotted in Figure V.24 for the three tests of Figure V.23. This parameter was found to show a logarithmic dependence on the initial

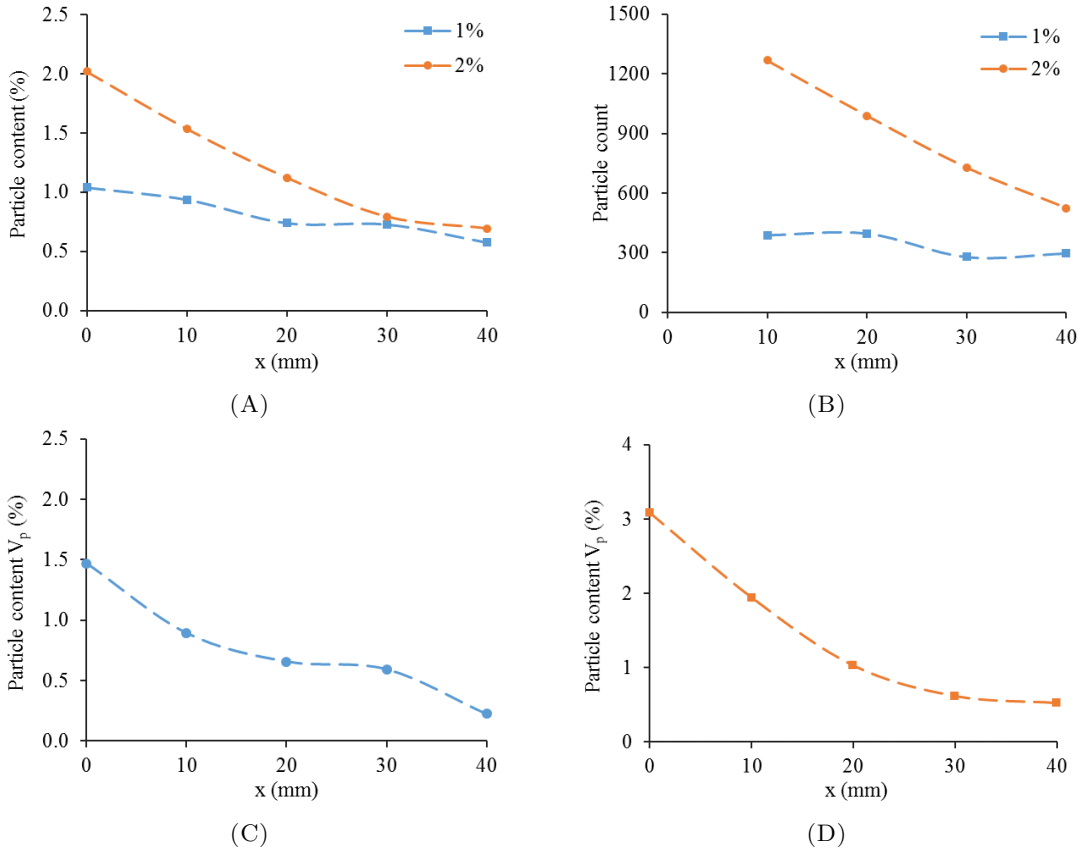

FIGURE V.22: Particle content versus distance as a function of suspension initial concentration for (A) C_0= 1% and 2% at V_f= 52.3% and 53.3% respectively, (B) particle count for the same experiments and (C) C_0= 1.5% at V_f= 47.1% and (D) C_0=3% at V_f= 58.3%

particle content C_0.

$$b = 0.8325 log C_0 + 4.2249 \tag{V.7}$$

V.5.3 Evolution of the particle size distribution

For an experiment with C_0= 3% and V_f= 59%, the diameters of 50-100 particles are measured at the sections x= 10 mm, 20 mm, 30 mm and 40 mm. Figure V.25 A presents the particle sizes for the sample particles. From this figure, it can be seen that the sizes of particles decrease slightly with distance. Larger sizes of particles ($\leq$7 μm) are present mainly at the beginning of the tube (x=10 mm and x= 20 mm). The largest particle size at x= 10 mm and x= 20 mm is around 8 μm, versus 7.5 μm and 6 μm at x= 30 mm and x= 40 mm, respectively. It is shown in Figure V.25 B that the average particle diameter changed from 3.1 μm (x= 10 mm), 3.7 μm (x= 20 mm) to 2.2 μm at x= 30 mm and 2.1 μm at 40 mm.

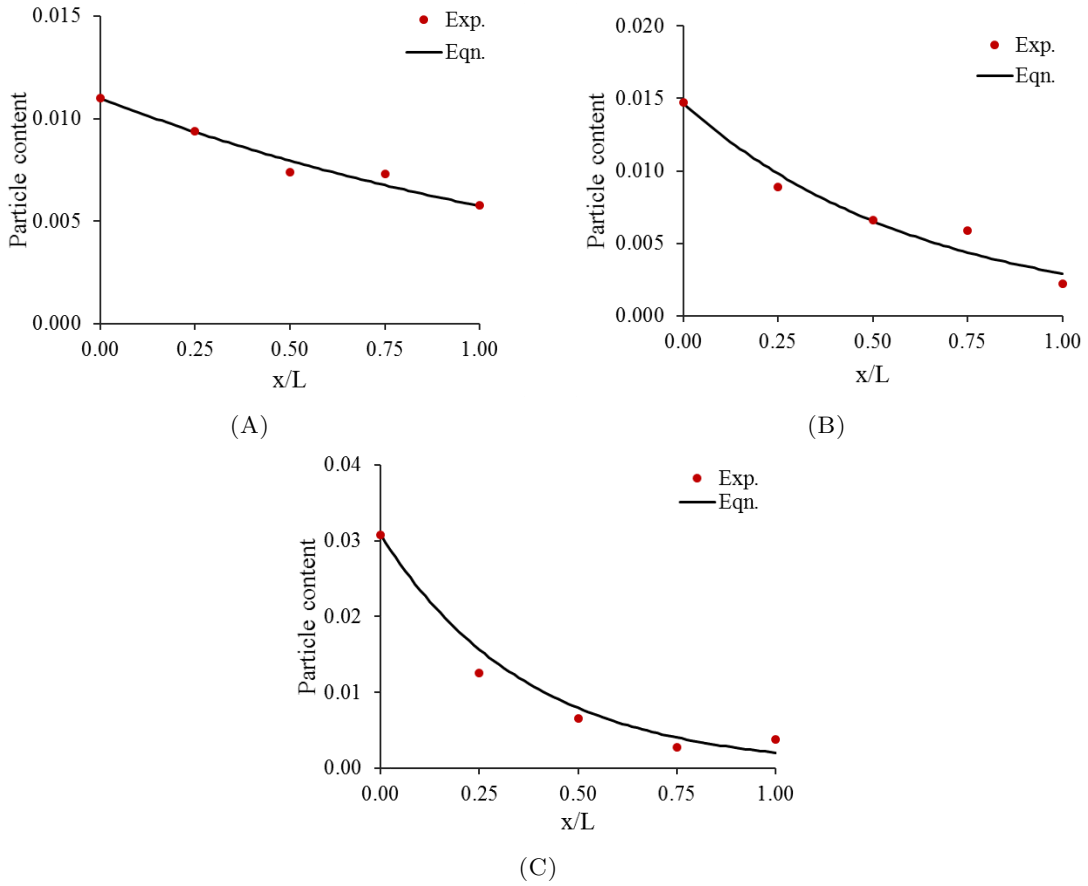

FIGURE V.23: Particle content versus distance as a function of suspension initial concentration for (A) C_0= 1% and 2% at V_f= 52.3% and 53.3% respectively, (B) particle count for the same experiments and (C) C_0= 1.5% at V_f= 47.1% and (D) C_0=3% at V_f= 58.3%

V.5.4 Inter-fiber distance and filtration criterion

The fibrous medium of the presented experiments contains aligned and randomly arranged fibers through the section length. Several types of fiber arrays exist in a cross-section of the same composite sample: triangular, quadratic, hexagonal and pentagonal. Which makes it challenging to define a specific pattern. Figure V.26 A illustrates these different fiber arrangements encountered in one cross-section of a sample at V_f of 48%. Because of the disordered distribution of fibers, defining one value for inter-fiber spacing δ is challenging to characterize at a fixed V_f. It can be observed in Figure V.26 B that in the same sample, there are zones of fiber aggregation and resin-rich areas. A low inter-fiber spacing is the image of local fiber agglomeration, whereas high δ values refer to resin-rich zones.

As an example, distances between fibers are measured for a sample of V_f= 48%. Results have shown a wide polydispersity in the measured values. For example, measurements of these distances ranged from 1 μm to 32 μm with an average measured value of 10.17 $\pm 7\mu$m. With such variability in δ, the characterization of the medium permeability

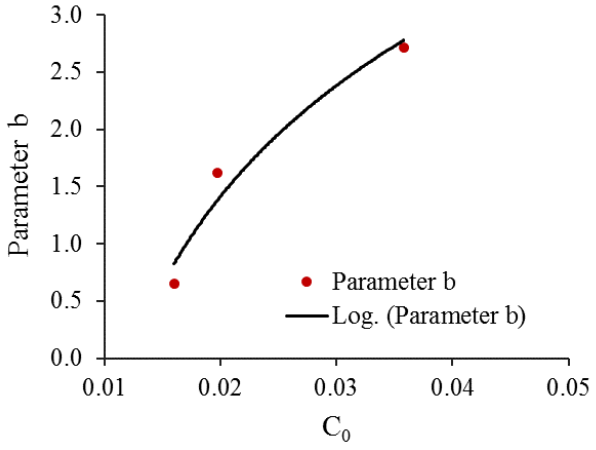

FIGURE V.24: Values of the parameter b for the test in Figure V.23 as a function of C_0

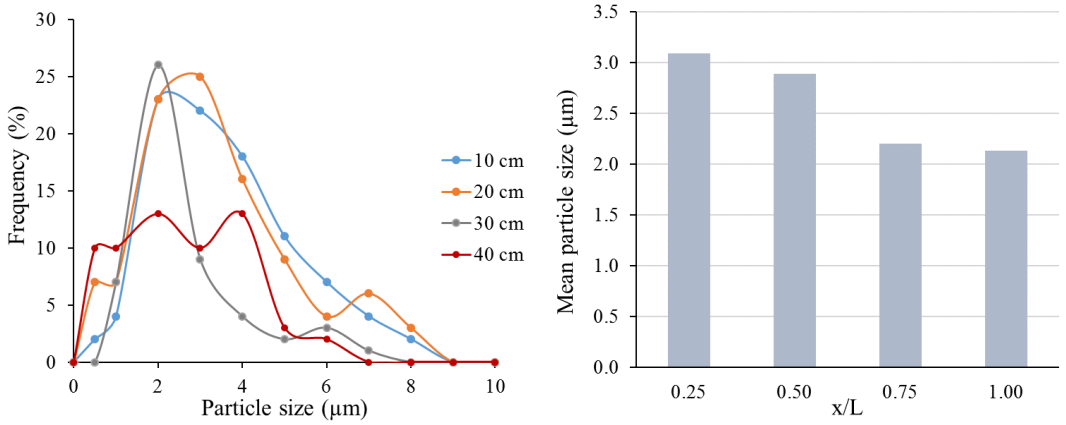

FIGURE V.25: The evolution of particle size distribution with (A) PSD at x= 10, 20, 30 and 40 mm, and (B) the evolution of the mean size at the same locations (x/L= 0, 0.25, 0.5, 0.75 and 1) for C_0= 3% and V_f= 58.3%

with models such as Happel [137] becomes challenging, as they consider the vertical and horizontal inter-fiber spacing. Another example is the model developed by Chen [138], which uses the mean value of δ in the determination of the axial permeability.

The average δ calculated by the models (Equations IV.12, IV.13 and IV.14) presented in section IV.9 have shown the following respective values: δ_1= 14.8 μ, δ_2= 12.6 μ, and δ_3= 6.5 μ. The average of the three values is 10.65 $\pm 2\mu$m. However, this average value does not reflect the polydispersity in the measurements of δ.

For the macroscopic particle-loaded experiments presented in chapter IV, filtration limits have been plotted using the inter-fiber spacing through the parameter λ'' introduced by Lefevre et al. [6]. This parameter is determined by Equation IV.18 ($\lambda''= \frac{\delta}{d_p C_0}$), for particles with a size d_p and initial concentrations C_0. It was recommended in section

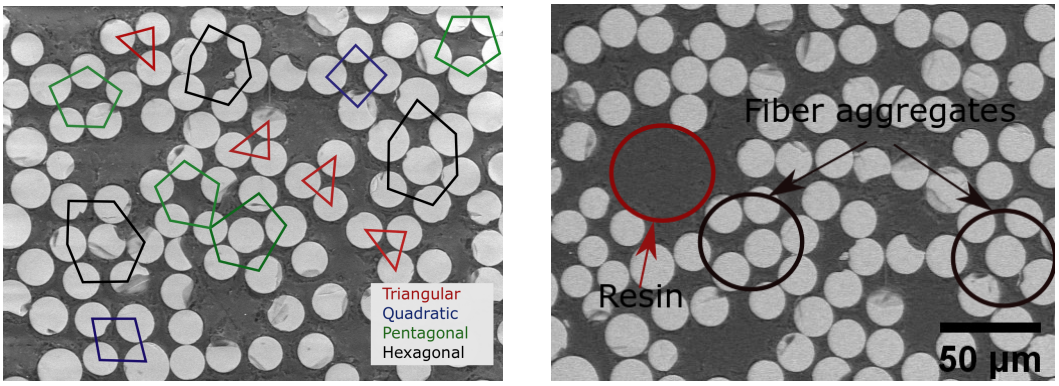

(A) (B)

FIGURE V.26: A sample with V_f= 48% showing (A) the potential fiber arrangements in a random fiber arrangement and (B) illustration of resin and fiber rich zones

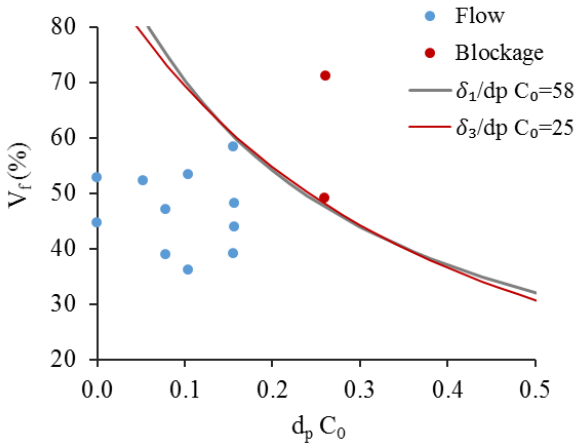

FIGURE V.27: Theoretical limits and experimental points plotted with the filtration-parameter λ'' (Equation IV.18)

IV.9 to use the distances δ_1 (Equation IV.12) and δ_3 (Equation IV.14) for the determination of λ", as they exhibit similar profiles. The filtration limits for the experiments realized at the tow scale are plotted in Figure V.27. The points in blue represent experiments with normal flow, whereas the red points denote experiments at which complete clogging took place and the injection syringe has stopped.
The values of λ" was found to be 58 and 25 respectively with δ_1 and δ_3. These values are almost four times higher than the ones of the macroscale experiments.

V.6 Conclusion

This work is a preliminary attempt to model suspension flow through unidirectional fibers experimentally. The presented work is a first step in the characterization of the filtration behavior in single-scale media through individual fibers. Using different

methods, the study has devised a procedure to investigate the flow and filtration in micron-scale fibrous media. Suspensions of test fluids were used for flow characterization at variable C_0 and V_f. Curing resin was employed to address the particle capture trends using two characterization methods; thermal decomposition and image analysis. The former method successfully estimated the particle volume fraction in the composite sample; nevertheless, it yielded several drawbacks. Only resin has been decomposed at the applied temperature with the selected combination of material. The tube cutting and the fiber mass measurement method increased the error percentage and decreased the accuracy of the results. Moreover, thermal decomposition does not provide information about particle count or sizes.

Thus, Scanning Electron Microscopy was adopted with image treatment for studying particle filtration. This method allowed to estimate the particle and fiber volume fractions at four cross-sections of each cured sample explored, in addition to the particle size distribution and count. However, caution must be taken in the interpretation of these results as image processing induces some errors in measurements because of the lack of contrast between particles and fibers. A scheme of the characterization methods applied is illustrated in Figure V.28 with the outputs and limitations of each method.

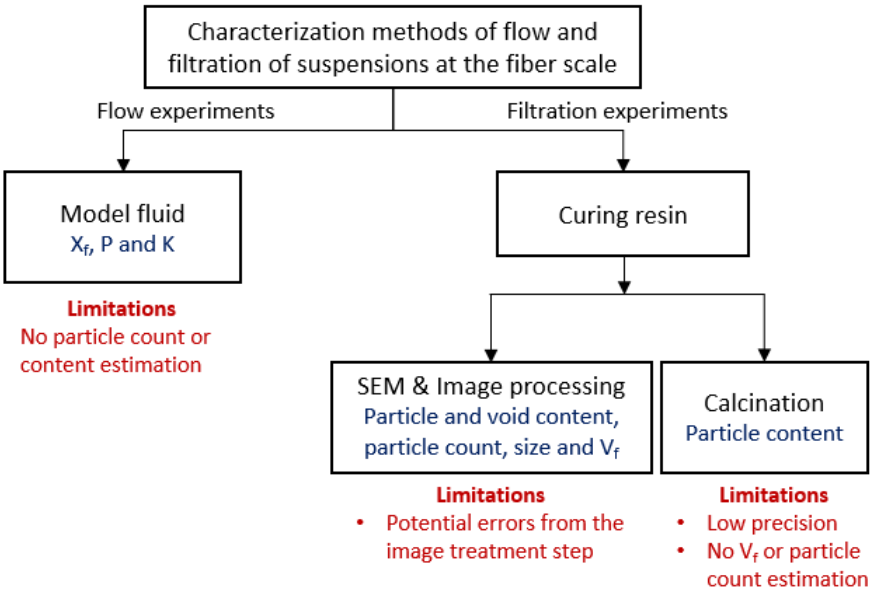

FIGURE V.28: Illustration of the methods followed in this work for the characterization of flow and filtration through tow-scale media

The system modeled herein is a reduced medium that can represent a down-scaled LCM injection. The characterization method is not specifically designed to address the suspension flow and filtration in the intra-tow regions as they exhibit different impregnation mechanisms. The initial concentration of suspension decreased continuously with the sampling distance. Particle count decreased non-monotonously along the length. The particle volume fraction varied as a function of the sample dimensionless length following an exponential relation. In the range of explored experiments, no sudden increase

in particle content is observed towards the end of the sample length, contrary to the macro-scale injections.

The applied methodology succeeded in addressing the spatial evolution of essential variables at the end of impregnation, such as the particle content and count, void percentage, pressure and flow front as well as the characterization of porosity. A relation was proposed to predict the particle content evolution as a function of the dimensionless part length. The filtration parameter λ" was higher than the one of the macro-scale tests for the range of the explored experiments. The system modeled herein is a reduced fibrous medium representing a down-scaled LCM injection with a single-scale porosity. The characterization method is not specifically designed to address the suspension flow and

filtration in the intra-tow regions as they are mainly impregnated transversely. Hence, it is challenging to draw conclusions concerning filtration inside fiber bundles from these experiments. Nevertheless, this experimental method can achieve transverse impregnation of tows by enlarging the gap between fibers and tube.

This work could present a basis for future studies of micron-scale filtration at the tow scale. However, further experimental investigations are needed to estimate the evolution of particle content through real fiber bundles, considering both transverse and axial impregnation and filtration through tows. As experiments are generally costly and time-consuming, future work should develop numerical approaches for determining the evolution of the variables investigated in this study inside fiber tows. This will enable the construction of solid parametric studies that reflect the influence of parameters as fiber size, configuration, and volume fraction through successive simulations with scanned or generated fibrous media.

Chapter VI

Numerical modeling of flow and filtration

VI.1 Introduction

The previous chapters presented experimental investigations for the influence of particle addition on composite processing in LCM processes. Throughout the literature and the performed experiments, controlling particle distribution was a key challenge in the fabrication of functional composites. Important results from chapter IV highlighted the dependency of particle filtration and distribution on several process and material parameters. However, the experimental results feature the profiles of suspension concentration at given injection conditions. Therefore, they do not predict the evolution of other filtration variables, such as the specific deposit of particles and material variables, such as porosity and permeability. Hence, a numerical tool is developed in this chapter to question the flow and filtration behaviors of particle-loaded flow through fibrous media.

For modeling filtration through fibrous preforms, the analogy has been made to wastewater treatment applications, where suspensions of polluted water are filtered through a granular medium commonly known as sand columns. Herzig et al. [52] presented comprehensive studies on the subject, with propositions of the main governing equations of filtration. Later, Lefevre et al. developed a model inspired by Herzig's model for the study of filtration of particles through fibrous media for composites processing [60]. Louis, Haji, Reia da Costa et al. [36, 61, 80] have used the model proposed by Lefevre with additional assumptions and/or simplifications.

Erdal et al. [35] derived a process model for the impregnation of ceramic composites with continuous fibers. The Authors have proposed a multidimensional transient model that couples the filtration equations and the flow model to predict the particle distribution

profiles during the process. This model was used later by Sas [63] and Shaker [8] to predict and compare the filtration behavior in RTM and CRTM processes.

In this chapter, the process of suspension injection into fibrous media is implemented into the simulation tool COMSOL Multiphysics through solid coupling between flow and filtration models. The models of Erdal and Lefevre, the most used filtration models in the literature for composite applications, will be detailed and used for the different simulations. The influence of selected variables will be investigated through several simulations in an extensive parametric study. Finally, the numerical results are compared to the experimental cases of chapter IV to identify the filtration parameters with each model.

The numerical simulation aims to contribute to the general understanding of process physics by predicting filtration variables and parameters. The main objectives of this chapter are summarized as follows:

- building a complete numerical tool to simulate the flow and filtration of suspensions during LCM processes,
- studying two of the most used filtration models,
- analyzing the influence of process and material variables numerically,
- addressing the interdependencies of variables,
- identifying the parameters of filtration models using experimental data.

VI.2 Flow and filtration modeling

This section presents the models and numerical methods used for computing the suspension flow inside a porous material. First, the simulations are performed for neat resin injections. Second, the medium constituted of fibers of an initial porosity ϵ_0 will be injected with particle-filled fluids, and the flow and filtration of suspensions will be simulated. The new filter will be constituted of fibers and retained particles and the porosity of the medium is modified as a function of the particle deposit.

VI.2.1 Flow modeling

The flow model presented herein is for non-reactive single-scale flow in a non-deformable fibrous medium. The mass balance equation governs the flow of the incompressible liquid as follows:

$$\nabla.(U) = 0 \tag{VI.1}$$

The superficial velocity U is the bulk flow velocity, i.e. the apparent flow velocity in the preform (U=ϵv). The interstitial velocity v is the suspension velocity through the fibrous material.
Darcy's law describes the flow of Newtonian fluids through porous media (e.g., fibrous and granular media). This empirical equation VI.2 was first determined from 1D experiments of water flow through sand columns [139]. It describes the unidirectional flow of a Newtonian fluid in a single-scale media.

$$Q = \frac{KA}{\eta}\frac{\triangle P}{\triangle x} \tag{VI.2}$$

Q is the volumetric flow rate, K the permeability of the porous medium, $\triangle P$ is the pressure variation between inlet and outlet, η is the dynamic viscosity of the fluid, A is the cross-section of the flow medium and $\triangle x$ is the length of the flow domain.

Darcy's equation can be obtained from the volume averaging of the Navier-Stokes equation for incompressible fluid flow with low Reynold's number, no slip-condition on the pore walls and negligible forces at the domain interfaces. The 3D form of Darcy's equation is:

$$\mathbf{U} = -\frac{[K]}{\eta}\nabla P \tag{VI.3}$$

where [K] here is the permeability tensor of the fibrous medium and $\mathbf{U}$ is the velocity vector.

Darcy's equation (VI.3) and the continuity equation (Equation VI.1) are combined in the following equation:

$$\nabla.(-\frac{K}{\eta}\nabla P) = 0 \tag{VI.4}$$

This equation is used for the determination of the macroscopic pressure field in the flow domain. The pressure field and Darcy's law are used for the computation of fluid velocity.

VI.2.2 Filtration modeling

Two filtration models from the literature will be presented and used in the filtration simulations; the model proposed by Erdal [35] and the model proposed by Lefevre [6].

VI.2.2.1 Erdal's model

The model is implemented in a boundary-fitted coordinate system for representing the evolving flow front, using numerical grid mapping to account for geometry irregularity. The discretization of governing equations at each time step is done by a finite differences scheme using a dynamic mesh generation. The flow and filtration models are coupled through the flow velocity, permeability and suspension viscosity.

Assumptions: Race-tracking effects are neglected. Suspension is considered as a continuum with averaged properties and agglomerate-free. The flow is isothermal and diffusion effects are neglected. Particles are assumed to have a narrow size distribution around 1 μm, which allows neglecting the gravity effects (the relative velocity between particles in suspension and the fluid is neglected).

The filtration model treats the constituents of the problem as three entities: the fluid, the filtered particles and the particles in suspension. In a control volume, the mass conservation of particles in a fluid necessitates that:

$$\dot{m}_{in} - \dot{m}_{out} + \dot{m}_{generated} = \dot{m}_{stored} \tag{VI.5}$$

where $\dot{m}_{in}$ and $\dot{m}_{out}$ are inlet and outlet mass flow rate of particles. The generation term $\dot{m}_{generated}$ denotes the effect of filtration on the particle conservation and $\dot{m}_{stored}$ reflects the retained particle content. By applying mass conservation on the three species (fluid, retained and suspended particles), the resulting mass balance equation becomes:

$$\frac{\partial(\epsilon C)}{\partial t} + \epsilon U \frac{\partial C}{\partial x} + \frac{\partial \sigma}{\partial t} = 0 \tag{VI.6}$$

where U is the unidirectional flow velocity through the preform length (x-direction).

A kinetic equation of filtration was proposed by Herzig [52] and used by Erdal [35] for modeling the evolution of particle deposit:

$$\frac{\partial \sigma}{\partial t} = kUC - k_r\sigma \tag{VI.7}$$

The equation supposes that the retention rate is proportional to the flux of suspended particles (UC), as presented by Ives [140] and Adin and Rebhun [141]. The proportionality constant is called the filtration coefficient k. Herzig has introduced this coefficient as the probability of particle capture; it depends on its initial value and the specific deposit σ with the relation $k = k_0 f(\sigma)$ [142]. During impregnation, retention and pore clogging increase the shearing action resulting from increased local velocities. Particles are then expected to be detached from the deposited ones and re-introduced to the suspension.

The equation accounts for particle re-suspension in the second term of the right-hand side of Equation VI.32 ($k_r\sigma$), where k_r is the detachment coefficient. The re-suspension constant k_r depends on C [80]. It is an empirical constant identified according to the porous material type.
σ_u is the ultimate particle deposit at which the clogging of the fibrous medium occurs. It is the value of σ at which the retention rate $\frac{\partial\sigma}{\partial t}$ becomes zero. By applying this condition, the detachment coefficient can be obtained by the equation:

$$k_r = \frac{kUC}{\sigma_u} \tag{VI.8}$$

By replacing k_r of Equation VI.33 in Equation VI.32, the kinetic equation becomes:

$$\frac{\partial\sigma}{\partial t} = kUC\left(1 - \frac{\sigma}{\sigma_u}\right) \tag{VI.9}$$

$$\frac{k}{k_0} = \frac{S}{S_0} \tag{VI.10}$$

where k_0 is the initial filtration rate, S and S_0 are the specific surface and its initial value respectively.

The following equation represents the change in porosity:

$$\epsilon = \epsilon_0 - \sigma \tag{VI.11}$$

According to the architecture of the constituting medium, the permeability of the flow domain K is related to the specific surface of the medium by the Kozeny–Carman relation as follows:

$$K \propto \frac{1}{S^2}\frac{\epsilon^3}{(1-\epsilon_0)^2} \tag{VI.12}$$

Combining the filtration coefficient k equation VI.35 and Kozeny-Carman's equation VI.37 gives the variations of k throughout the process:

$$k = k_0\left[\left(\frac{K}{K_f}\right)^{-\frac{1}{2}}\left(\frac{\epsilon}{\epsilon_0}\right)^{\frac{3}{2}}\left(\frac{1-\epsilon}{1-\epsilon_0}\right)^{-1}\right]^{a_1} \tag{VI.13}$$

where a_1 is a positive constant.

As the suspension impregnates the fibrous medium, particles are deposited at the surface of fibers, increasing the specific surface of the solid phase and decreasing the porosity. The variation in the specific surface changes the local permeability. Combining

Kozeny-Carman's relation with the specific surface expression results in the following permeability equation:

$$K = K_f \left[\frac{\epsilon}{\epsilon_0} \left(\frac{1-\epsilon}{1-\epsilon_0} \right)^{-4} \right]^{a_2} \tag{VI.14}$$

where a_2 is a positive parameter.

Erdal proposed a viscosity model that uniquely depends on the particle concentration. The presented empirical model is used for particles with a narrow particle distribution. The suspension is assumed to be Newtonian and that the change described by the formula occurs at a constant shear rate.

$$\eta = \eta_0 \left(1 - \frac{C}{A1} \right)^{-2} \tag{VI.15}$$

A1 is an empirical constant.

VI.2.2.2 Lefevre's model

In their work, Lefevre et al. [79] carried out an experimental and numerical study of filtration in fibrous media of a single-scale porosity. Lefevre et al. proposed a numerical model starting from Herzig's model created for wastewater treatment applications. The authors applied modifications and simplifications to Herzig's model as the porous media are different. It consists of a unidirectional flow through a fibrous medium at a constant pressure injection. All the study variables are functions of the time t and the position x. The simulation is based on a finite element method calculation with an iterative loop that performs a series of calculations for each element of the mesh.

Assumptions: Diffusion effects are neglected because particle size used in the study was higher than 10 μm. The addition of dispersing agent allowed neglecting the effect of particle sedimentation under the effect of gravity. The filtration coefficient k is assumed to be fixed to its initial value k_0.

Figure VI.4 illustrates an element of the filter with a length dx and a surface S. $C(x,t)$ the volume occupied by the particles in the total volume of suspension in motion is the volume concentration at position x and time t.

The conservation of particles in the volume Sdx during the time interval dt implies that:

$$entering\ particles - outlet\ particles = retained\ particles + suspended\ particles \tag{VI.16}$$

where:

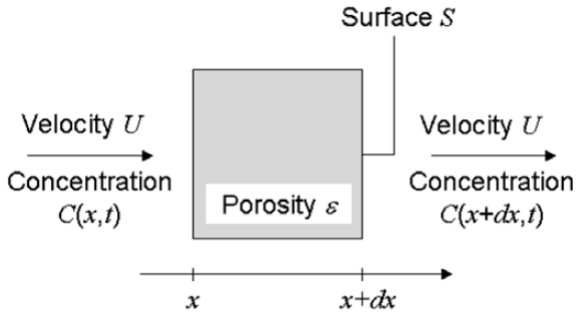

FIGURE VI.1: Filter element [143]

- entering particles= $C(x,t)USdt$
- outlet particles= $C(x+dx,t)USdt$
- retained particles= $(\sigma(x,t+dt)-\sigma(x,t))Sdx$
- suspended particles= $(\epsilon(x,t+dt)C(x,t+dt)-\epsilon(x,t)C(x,t))Sdx$

which gives the following continuity equation:

$$\frac{\partial(\sigma+\epsilon C)}{\partial t}+U\frac{\partial C}{\partial x}=0 \tag{VI.17}$$

By combining Equation VI.45 with Equation VI.42 the continuity equation becomes:

$$\epsilon\frac{\partial C}{\partial t}+U\frac{\partial C}{\partial x}=(\beta C-1)\frac{\partial \sigma}{\partial t} \tag{VI.18}$$

The kinetic equation proposed by Herzig VI.32 was used for modeling the particle deposit. For simplification, the filtration coefficient is considered constant throughout the process (k=k_0) and term of particle detachment ($k_r\sigma$) is neglected, as the applied pressure and the flow direction are kept constant throughout the injection. The kinetics equation finally becomes:

$$\frac{\partial \sigma}{\partial t}=k_0UC \tag{VI.19}$$

During the impregnation of the fibrous medium by the suspension, particles are captured by the filter, causing a reduction in porosity as a function of the total deposit: retained particles σ and entrapped liquid β. The following equation represents the change in porosity:

$$\epsilon=\epsilon_0-\beta\sigma \tag{VI.20}$$

An equation was added to the model to consider the change in entrapped fluid as a function of the retained particles:

$$\beta = \beta_0 - r\sigma \tag{VI.21}$$

The equation introduced the numerical constant of adjustment r.

The flow model is coupled with filtration model for a complete simulation of the process. The system of particle and fibrous medium is considered as a superposition of two systems; of which the overall permeability is calculated using the electrical analogy as follows:

$$\frac{1}{K} = \frac{1}{K_f} + \frac{1}{K_p} \tag{VI.22}$$

where K_f and K_p are the permeability of the fibrous and the particle media respectively. K_f is calculated using an empirical equation depending on the characteristics of the used reinforcement (check section II.2.4 of chapter II). K_p is calculated with Kozeny-Carman's law as follows:

$$K_p = \frac{d_p^2 \epsilon_d^3}{36 h_k (1-\epsilon_p)^2} \tag{VI.23}$$

where h_k is the Kozeny constant and ϵ_p is the porosity of the particle medium which is obtained by:

$$\epsilon_p = 1 - \sigma \tag{VI.24}$$

It is assumed that the suspension viscosity depends on the shear rate $\dot{\gamma}$ according to a power law of the type:

$$\eta = \mu_v \dot{\gamma}^{m_v - 1} \tag{VI.25}$$

where μ_v and m_v are constants identified experimentally. The local shear rate is estimated as a function of the Darcy's velocity U:

$$\dot{\gamma} = \frac{4U}{\delta\, \epsilon} \tag{VI.26}$$

δ is the inter-fiber spacing. The authors have stated that the viscosity values determined by Equation VI.50 are overestimated because of the approximate method used for the shear rate estimation. Therefore, an improvement of the model requires replacing the viscosity calculation approach with a new one that considers the influence of filler concentration on the viscosity. After the experimental characterization of suspension viscosity performed in section II.5.2, Eilers model [33] (Equation VI.52) will be used to predict the viscosity of the suspension as a function of particle concentration in the filtration simulation with Lefevre's model within this study.

$$\eta = \eta_0 \left(1 + \frac{[\eta]C}{2(1 - \frac{C}{C_{max}})}\right)^2 \tag{VI.27}$$

It is essential to highlight that the suspensions in question Newtonian for concentrations up to 20% according to the realized experimental characterization. Higher than this percentage, this model will no longer be valid, and the variations of viscosity with shear rate should be considered.

The flow and filtration models proposed by Erdal and Lefevre are listed in Table VI.3. These two models are used in the different simulations in the coming sections as presented in this table, except for the viscosity equation of Lefevre's model, which is replaced by Equation VI.52.

TABLE VI.1: Summary of the models of Erdal and Lefevre

Model	**Erdal**	**Lefevre**
Flow	$\nabla.(U) = 0$ $U = -\frac{K}{\eta}\nabla P$	
Filtration		
Mass conservation	$\frac{\partial(\epsilon C)}{\partial t} + \epsilon U\frac{\partial C}{\partial x} + \frac{\partial \sigma}{\partial t} = 0$	$\epsilon\frac{\partial C}{\partial t} + U\frac{\partial C}{\partial x} = (\beta C - 1)\frac{\partial \sigma}{\partial t}$
Filtration kinetics	$\frac{\partial \sigma}{\partial t} = kUC\left(1 - \frac{\sigma}{\sigma_u}\right)$ $k = k_0\left[\left(\frac{K}{K_f}\right)^{-\frac{1}{2}}\left(\frac{\epsilon}{\epsilon_0}\right)^{\frac{3}{2}}\left(\frac{1-\epsilon}{1-\epsilon_0}\right)^{-1}\right]^{a_1}$	$\frac{\partial \sigma}{\partial t} = k_0 UC$ $k = k_0$
Porosity	$\epsilon = \epsilon_0 - \sigma$	$\epsilon = \epsilon_0 - \beta\sigma$ $\beta = \beta_0 - r\sigma$
Permeability	$K = K_f\left[\frac{\epsilon}{\epsilon_0}\left(\frac{1-\epsilon}{1-\epsilon_0}\right)^{-4}\right]^{a_2}$	$\frac{1}{K} = \frac{1}{K_f} + \frac{1}{K_p}$ $K_p = \frac{d_p^2\epsilon_d^3}{36h_k(1-\epsilon_p)^2}$ $\epsilon_p = 1 - \sigma$
Viscosity	$\eta = \eta_0\left(1 - \frac{C}{A1}\right)^{-2}$	$\eta = \mu_v\dot{\gamma}^{m_v - 1}$ $\dot{\gamma} = \frac{4U}{\delta\,\epsilon}$

VI.3 Presentation of the simulation tool

The flow and filtration models are implemented in COMSOL Multiphysics software (v5.4). This software is designed to solve partial differential equations numerically while simultaneously integrating several coupled equations. It is based on the finite element method (FEM), which consists of discretizing the partial differential equations on a spatial grid to reduce them to a system of non-linear algebraic and differential non-linear equations [144]. A model for viscous, incompressible, isothermal flow through porous media is employed to simulate the RTM process in a 2D geometry. The software solves built-in as well as user-defined equations. It also allows defining constants or variables through equations and logical expressions to describe the different material and process parameters. The geometry of the problem can be drawn directly in the interface or imported from another tool [145].

VI.4 Numerical implementation

The mutual effects of the transport of suspension and particle capture on the different variables lead to a strong coupling between the linear and non-linear equations presented in sections VI.4.4.1 and VI.4.4.2. Therefore, the resolution of these equations was conducted in COMSOL Multiphysics software [146]. Darcy's law (VI.2) along with the continuity equation (VI.1) are implemented to compute the flow of suspensions. In addition, two user-defined partial differential equations (PDEs) are defined to model the filtration kinetics and the concentration conservation equations.

A time-dependent study with Phase initialization is introduced to solve the problem. The user-defined PDE (Partial Differential Equation) has the general form of Equation VI.53. The variable in question (σ or C) is noted as u. The coefficients as well are their values for the two studied models are detailed in Table VI.4.

$$e_a \frac{\partial^2 u}{\partial t^2} + d_a \frac{\partial u}{\partial t} + \nabla.(-c\nabla u - \alpha u + \gamma) + \beta_c.\nabla u + au = f \tag{VI.28}$$

VI.4.1 Geometry and meshing technique

The mold cavity is represented by a 2D geometry, with identical dimensions as the experimental preform (100 mm x 420 mm). The flow domain is divided into small cells (meshes) where the flow and filtration equations are solved at each iteration. The software gives the possibility of generating the meshes of the domain of different forms and sizes. For the simulations of this study, a quadrilateral mesh type is used, with fine to coarse sizes.

TABLE VI.2: Coefficients of the PDE (Equation VI.53) for filtration kinetics and concentration equations for the models of Erdal and Lefevre

Coefficient	Filtration kinetics		Concentration	
u	σ		C	
Coefficient	Erdal	Lefevre	Erdal	Lefevre
Diffusion coefficient (c)	0	0	0	0
Absorption coefficient (a)	$\frac{kUC}{\sigma_u}$	0	$\frac{\partial \epsilon}{\partial t}$	$-\beta \frac{\partial \sigma}{\partial t}$
Source term (f)	kUC	k_0UC	$-\frac{\partial \sigma}{\partial t}$	$-\frac{\partial \sigma}{\partial t}$
Mass coefficient (e_a)	0	0	0	0
Damping coefficient (d_a)	1	1	ϵ	ϵ
Conservative flux convection coefficient (α)	0	0	0	0
Convection coefficient (β_c)	0	0	U	U
Conservative flux source (γ)	0	0	0	0

VI.4.2 Flow front tracking

The simulation of the LCM processes necessitates the accurate tracking of the flow front during mold filling [147]. The level set (ls) method is one of the widely used for following the advancement of the resin front [83]. The built-in ls package is used an implicit method to describe the movement of an interface between two different fluids: resin and air. The level set function phils (referred to herein as ϕ) divides the flow domain into two sub-domains: the saturated domain with resin as the fluid, and the dry fabric, with air. The LS function is a scalar that assigns a value from 0 to 1 for every point in the flow domain. The value of ϕ changes progressively through the interface thickness from 1 to 0. It has a value of 0.5 at the interface between resin and air, 1 in the saturated regions and 0 in the dry zones. It relates the location of the interface with the fluid properties to be used in the whole domain [148]. Figure VI.5 illustrates the principle of the level set method application in the simulation tool. A transport equation governs the level set function (Equation VI.54), based on the advection of the function by the velocity field v.

$$\frac{\partial \phi}{\partial t} + v.\nabla\phi = \gamma_l s \nabla.(\epsilon_{ls}\nabla\phi - \phi(1 - \phi\frac{\nabla\phi}{\mid \nabla\phi \mid})) \tag{VI.29}$$

The left-hand side of the equation gives the exact interface motion, where the right-hand side is for numerical stability. ϵ_{ls} is the parameter controlling the interface thickness, and γ_{ls} is the re-initialization parameter; it is responsible for the stabilization of the level set function.

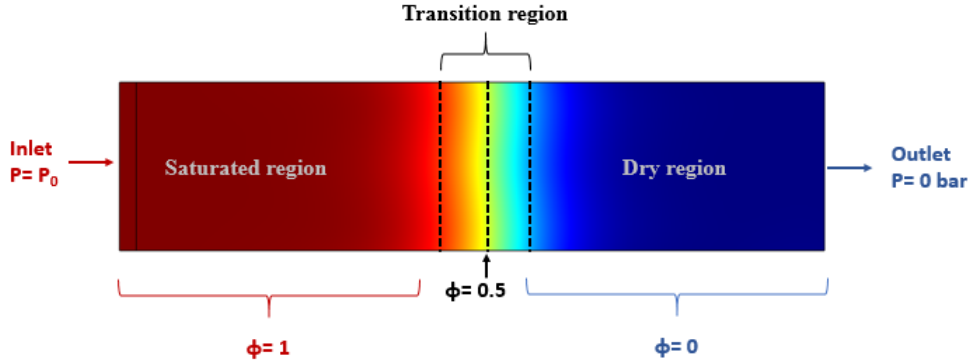

FIGURE VI.2: The distribution of the level set function (phils) throughout the flow domain

VI.4.3 Boundary and initial conditions

The left side of the rectangular mold is prescribed as the flow inlet (line injection), with a constant pressure injection $P = P_0$. The right-hand side is designated as the flow outlet, with a pressure $P = 0$ bar. All the pressure values presented in this study are relative pressures (i.e. the absolute pressure - the atmospheric pressure). The no-slip boundary condition is applied to the other two sides of the mold. The initial concentration C_0 is prescribed at the inlet, which gives the boundary condition $C(x = 0, t) = C_0$. The problem consists of two initial conditions; at $t = 0$, the suspension hasn't entered the mold cavity yet, hence the value of $C(x, t = 0) = 0$. Similarly, no retention takes place at the instant $t = 0$, therefore, $\sigma(x, t = 0) = 0$. Figure VI.6 illustrates the assigned boundary and initial conditions applied for all the simulations.

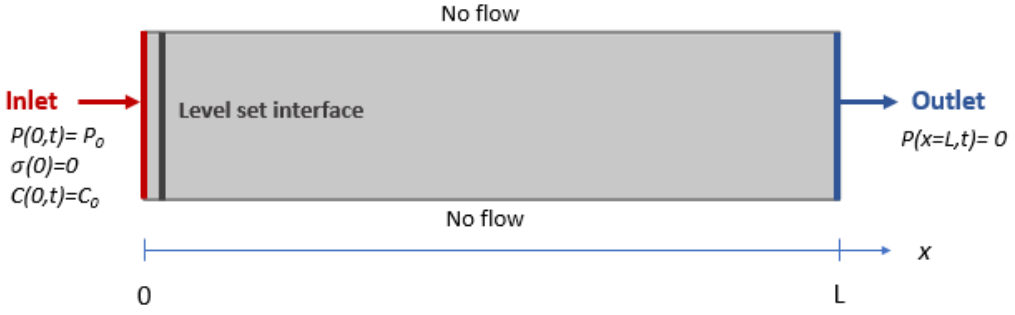

FIGURE VI.3: Boundary and initial conditions

VI.4.4 Filtration modeling

Two filtration models from the literature will be presented and used in the filtration simulations; the model proposed by Erdal [35] and the model proposed by Lefevre [6].

VI.4.4.1 Erdal's model

The model is implemented in a boundary-fitted coordinate system for representing the evolving flow front, using numerical grid mapping to account for geometry irregularity. The discretization of governing equations at each time step is done by a finite differences scheme using a dynamic mesh generation. The flow and filtration models are coupled through the flow velocity, permeability and suspension viscosity.

Assumptions: Race-tracking effects are neglected. Suspension is considered as a continuum with averaged properties and agglomerate-free. The flow is isothermal and diffusion effects are neglected. Particles are assumed to have a narrow size distribution around 1 μm, which allows neglecting the gravity effects (the relative velocity between particles in suspension and the fluid is neglected).

The filtration model treats the constituents of the problem as three entities: the fluid, the filtered particles and the particles in suspension. In a control volume, the mass conservation of particles in a fluid necessitates that:

$$\dot{m}_{in} - \dot{m}_{out} + \dot{m}_{generated} = \dot{m}_{stored} \tag{VI.30}$$

where $\dot{m}_{in}$ and $\dot{m}_{out}$ are inlet and outlet mass flow rate of particles. The generation term $\dot{m}_{generated}$ denotes the effect of filtration on the particle conservation and $\dot{m}_{stored}$ reflects the retained particle content. By applying mass conservation on the three species (fluid, retained and suspended particles), the resulting mass balance equation becomes:

$$\frac{\partial(\epsilon C)}{\partial t} + \epsilon U \frac{\partial C}{\partial x} + \frac{\partial \sigma}{\partial t} = 0 \tag{VI.31}$$

where U is the unidirectional flow velocity through the preform length (x-direction).

A kinetic equation of filtration was proposed by Herzig [52] and used by Erdal [35] for modeling the evolution of particle deposit:

$$\frac{\partial \sigma}{\partial t} = kUC - k_r\sigma \tag{VI.32}$$

The equation supposes that the retention rate is proportional to the flux of suspended particles (UC), as presented by Ives [140] and Adin and Rebhun [141]. The proportionality constant is called the filtration coefficient k. Herzig has introduced this coefficient as the probability of particle capture; it depends on its initial value and the specific deposit σ with the relation $k = k_0 f(\sigma)$ [142]. During impregnation, retention and pore clogging increase the shearing action resulting from increased local velocities. Particles are then expected to be detached from the deposited ones and re-introduced to the suspension.

The equation accounts for particle re-suspension in the second term of the right-hand side of Equation VI.32 ($k_r\sigma$), where k_r is the detachment coefficient. The re-suspension constant k_r depends on C [80]. It is an empirical constant identified according to the porous material type.
σ_u is the ultimate particle deposit at which the clogging of the fibrous medium occurs. It is the value of σ at which the retention rate $\frac{\partial\sigma}{\partial t}$ becomes zero. By applying this condition, the detachment coefficient can be obtained by the equation:

$$k_r = \frac{kUC}{\sigma_u} \tag{VI.33}$$

By replacing k_r of Equation VI.33 in Equation VI.32, the kinetic equation becomes:

$$\frac{\partial\sigma}{\partial t} = kUC\left(1 - \frac{\sigma}{\sigma_u}\right) \tag{VI.34}$$

$$\frac{k}{k_0} = \frac{S}{S_0} \tag{VI.35}$$

where k_0 is the initial filtration rate, S and S_0 are the specific surface and its initial value respectively.

The following equation represents the change in porosity:

$$\epsilon = \epsilon_0 - \sigma \tag{VI.36}$$

According to the architecture of the constituting medium, the permeability of the flow domain K is related to the specific surface of the medium by the Kozeny–Carman relation as follows:

$$K \propto \frac{1}{S^2}\frac{\epsilon^3}{(1-\epsilon_0)^2} \tag{VI.37}$$

Combining the filtration coefficient k equation VI.35 and Kozeny-Carman's equation VI.37 gives the variations of k throughout the process:

$$k = k_0\left[\left(\frac{K}{K_f}\right)^{-\frac{1}{2}}\left(\frac{\epsilon}{\epsilon_0}\right)^{\frac{3}{2}}\left(\frac{1-\epsilon}{1-\epsilon_0}\right)^{-1}\right]^{a_1} \tag{VI.38}$$

where a_1 is a positive constant.

As the suspension impregnates the fibrous medium, particles are deposited at the surface of fibers, increasing the specific surface of the solid phase and decreasing the porosity. The variation in the specific surface changes the local permeability. Combining

Kozeny-Carman's relation with the specific surface expression results in the following permeability equation:

$$K = K_f \left[\frac{\epsilon}{\epsilon_0} \left(\frac{1-\epsilon}{1-\epsilon_0} \right)^{-4} \right]^{a_2} \tag{VI.39}$$

where a_2 is a positive parameter.

Erdal proposed a viscosity model that uniquely depends on the particle concentration. The presented empirical model is used for particles with a narrow particle distribution. The suspension is assumed to be Newtonian and that the change described by the formula occurs at a constant shear rate.

$$\eta = \eta_0 \left(1 - \frac{C}{A1} \right)^{-2} \tag{VI.40}$$

A1 is an empirical constant.

VI.4.4.2 Lefevre's model

In their work, Lefevre et al. [79] carried out an experimental and numerical study of filtration in fibrous media of a single-scale porosity. Lefevre et al. proposed a numerical model starting from Herzig's model created for wastewater treatment applications. The authors applied modifications and simplifications to Herzig's model as the porous media are different. It consists of a unidirectional flow through a fibrous medium at a constant pressure injection. All the study variables are functions of the time t and the position x. The simulation is based on a finite element method calculation with an iterative loop that performs a series of calculations for each mesh element.

Assumptions: Diffusion effects are neglected because particle size used in the study was higher than 10 μm. The addition of dispersing agent allowed neglecting the effect of particle sedimentation under the effect of gravity. The filtration coefficient k is assumed to be fixed to its initial value k_0.

Figure VI.4 illustrates an element of the filter with a length dx and a surface S. $C(x,t)$ the volume occupied by the particles in the total volume of suspension in motion is the volume concentration at position x and time t.

The conservation of particles in the volume Sdx during the time interval dt implies that:

$$entering\ particles - outlet\ particles = retained\ particles + suspended\ particles \tag{VI.41}$$

where:

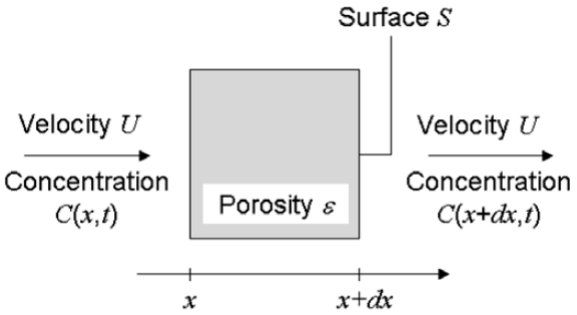

FIGURE VI.4: Filter element [143]

- entering particles= $C(x,t)USdt$
- outlet particles= $C(x+dx,t)USdt$
- retained particles= $(\sigma(x,t+dt)-\sigma(x,t))Sdx$
- suspended particles= $(\epsilon(x,t+dt)C(x,t+dt)-\epsilon(x,t)C(x,t))Sdx$

which gives the following continuity equation:

$$\frac{\partial(\sigma+\epsilon C)}{\partial t}+U\frac{\partial C}{\partial x}=0 \tag{VI.42}$$

By combining Equation VI.45 with Equation VI.42 the continuity equation becomes:

$$\epsilon\frac{\partial C}{\partial t}+U\frac{\partial C}{\partial x}=(\beta C-1)\frac{\partial \sigma}{\partial t} \tag{VI.43}$$

The kinetic equation proposed by Herzig VI.32 was used for modeling the particle deposit. For simplification, the filtration coefficient is considered constant throughout the process (k=k_0) and term of particle detachment ($k_r\sigma$) is neglected, as the applied pressure and the flow direction are kept constant throughout the injection. Thus, the kinetics equation finally becomes:

$$\frac{\partial \sigma}{\partial t}=k_0UC \tag{VI.44}$$

During the suspension flow, particles are captured by the filter, causing a reduction in porosity as a function of the total deposit: retained particles σ and entrapped liquid β. The following equation represents the change in porosity:

$$\epsilon=\epsilon_0-\beta\sigma \tag{VI.45}$$

An equation was added to the model to consider the change in entrapped fluid as a function of the retained particles:

$$\beta = \beta_0 - r\sigma \tag{VI.46}$$

The equation introduced the numerical constant of adjustment r.

The flow model is coupled with filtration model for a complete simulation of the process. The system of particle and fibrous medium is considered as a superposition of two systems; of which the overall permeability is calculated using the electrical analogy as follows:

$$\frac{1}{K} = \frac{1}{K_f} + \frac{1}{K_p} \tag{VI.47}$$

where K_f and K_p are the permeability of the fibrous and the particle media respectively. K_f is calculated using an empirical equation depending on the characteristics of the used reinforcement (check section II.2.4 of chapter II). K_p is calculated with Kozeny-Carman's law as follows:

$$K_p = \frac{d_p^2 \epsilon_d^3}{36 h_k (1-\epsilon_p)^2} \tag{VI.48}$$

where h_k is the Kozeny constant and ϵ_p is the porosity of the particle medium which is obtained by:

$$\epsilon_p = 1 - \sigma \tag{VI.49}$$

It is assumed that the suspension viscosity depends on the shear rate $\dot{\gamma}$ according to a power law of the type:

$$\eta = \mu_v \dot{\gamma}^{m_v - 1} \tag{VI.50}$$

where μ_v and m_v are constants identified experimentally. The local shear rate is estimated as a function of the Darcy's velocity U:

$$\dot{\gamma} = \frac{4U}{\delta\, \epsilon} \tag{VI.51}$$

δ is the inter-fiber spacing. The authors have stated that the viscosity values determined by Equation VI.50 are overestimated because of the approximate method used for the shear rate estimation. Therefore, an improvement of the model requires replacing the viscosity calculation approach with a new one that considers the influence of filler concentration on the viscosity. After the experimental characterization of suspension viscosity performed in section II.5.2, Eilers model [33] (Equation VI.52) will be used to predict the viscosity of the suspension as a function of particle concentration in the filtration simulation with Lefevre's model within this study.

$$\eta = \eta_0 \left(1 + \frac{[\eta]C}{2(1 - \frac{C}{C_{max}})}\right)^2 \tag{VI.52}$$

It is essential to highlight that the suspensions in question Newtonian for concentrations up to 20% according to the realized experimental characterization. Higher than this percentage, this model will no longer be valid, and the variations of viscosity with shear rate should be considered.

The flow and filtration models proposed by Erdal and Lefevre are listed in Table VI.3. These two models are used in the different simulations in the coming sections as presented in this table, except for the viscosity equation of Lefevre's model, which is replaced by Equation VI.52.

TABLE VI.3: Summary of the models of Erdal and Lefevre

Model	**Erdal**	**Lefevre**
Flow	$\nabla.(U) = 0$ $U = -\frac{K}{\eta}\nabla P$	
Filtration		
Mass conservation	$\frac{\partial(\epsilon C)}{\partial t} + \epsilon U\frac{\partial C}{\partial x} + \frac{\partial \sigma}{\partial t} = 0$	$\epsilon\frac{\partial C}{\partial t} + U\frac{\partial C}{\partial x} = (\beta C - 1)\frac{\partial \sigma}{\partial t}$
Filtration kinetics	$\frac{\partial \sigma}{\partial t} = kUC\left(1 - \frac{\sigma}{\sigma_u}\right)$ $k = k_0\left[\left(\frac{K}{K_f}\right)^{-\frac{1}{2}}\left(\frac{\epsilon}{\epsilon_0}\right)^{\frac{3}{2}}\left(\frac{1-\epsilon}{1-\epsilon_0}\right)^{-1}\right]^{a_1}$	$\frac{\partial \sigma}{\partial t} = k_0 UC$ $k = k_0$
Porosity	$\epsilon = \epsilon_0 - \sigma$	$\epsilon = \epsilon_0 - \beta\sigma$ $\beta = \beta_0 - r\sigma$
Permeability	$K = K_f\left[\frac{\epsilon}{\epsilon_0}\left(\frac{1-\epsilon}{1-\epsilon_0}\right)^{-4}\right]^{a_2}$	$\frac{1}{K} = \frac{1}{K_f} + \frac{1}{K_p}$ $K_p = \frac{d_p^2\epsilon_d^3}{36h_k(1-\epsilon_p)^2}$ $\epsilon_p = 1 - \sigma$
Viscosity	$\eta = \eta_0\left(1 - \frac{C}{A1}\right)^{-2}$	$\eta = \mu_v\dot{\gamma}^{m_v - 1}$ $\dot{\gamma} = \frac{4U}{\delta\,\epsilon}$

VI.5 Presentation of the simulation tool

The flow and filtration models are implemented in COMSOL Multiphysics software (v5.4). This software is designed to solve partial differential equations numerically while simultaneously integrating several coupled equations. It is based on the finite element method (FEM), which consists of discretizing the partial differential equations on a spatial grid to reduce them to a system of non-linear algebraic and differential non-linear equations [144]. A model for viscous, incompressible, isothermal flow through porous media is employed to simulate the RTM process in a 2D geometry. The software solves built-in as well as user-defined equations. It also allows defining constants or variables through equations and logical expressions to describe the different material and process parameters. The geometry of the problem can be drawn directly in the interface or imported from another tool [145].

VI.6 Numerical implementation

The mutual effects of the transport of suspension and particle capture on the different variables lead to a strong coupling between the linear and non-linear equations presented in sections VI.4.4.1 and VI.4.4.2. Therefore, the resolution of these equations was conducted in COMSOL Multiphysics software [146]. Darcy's law (VI.2) along with the continuity equation (VI.1) are implemented to compute the flow of suspensions. In addition, two user-defined partial differential equations (PDEs) are defined to model the filtration kinetics and the concentration conservation equations.

A time-dependent study with Phase initialization is introduced to solve the problem. The user-defined PDE (Partial Differential Equation) has the general form of Equation VI.53. The variable in question (σ or C) is noted as u. The coefficients as well are their values for the two studied models are detailed in Table VI.4.

$$e_a \frac{\partial^2 u}{\partial t^2} + d_a \frac{\partial u}{\partial t} + \nabla.(-c\nabla u - \alpha u + \gamma) + \beta_c.\nabla u + au = f \tag{VI.53}$$

VI.6.1 Geometry and meshing technique

The mold cavity is represented by a 2D geometry, with identical dimensions as the experimental preform (100 mm x 420 mm). The flow domain is divided into small cells (meshes) where the flow and filtration equations are solved at each iteration. The software gives the possibility of generating the meshes of the domain of different forms and sizes. For the simulations of this study, a quadrilateral mesh type is used, with fine to coarse sizes.

TABLE VI.4: Coefficients of the PDE (Equation VI.53) for filtration kinetics and concentration equations for the models of Erdal and Lefevre

Coefficient	Filtration kinetics		Concentration	
u	σ		C	
Coefficient	Erdal	Lefevre	Erdal	Lefevre
Diffusion coefficient (c)	0	0	0	0
Absorption coefficient (a)	$\frac{kUC}{\sigma_u}$	0	$\frac{\partial \epsilon}{\partial t}$	$-\beta\frac{\partial \sigma}{\partial t}$
Source term (f)	kUC	k_0UC	$-\frac{\partial \sigma}{\partial t}$	$-\frac{\partial \sigma}{\partial t}$
Mass coefficient (e_a)	0	0	0	0
Damping coefficient (d_a)	1	1	ϵ	ϵ
Conservative flux convection coefficient (α)	0	0	0	0
Convection coefficient (β_c)	0	0	U	U
Conservative flux source (γ)	0	0	0	0

VI.6.2 Flow front tracking

The simulation of the LCM processes necessitates the accurate tracking of the flow front during mold filling [147]. The level set (ls) method is one of the widely used for following the advancement of the resin front [83]. The built-in ls package is used an implicit method to describe the movement of an interface between two different fluids: resin and air. The level set function phils (referred to herein as ϕ) divides the flow domain into two sub-domains: the saturated domain with resin as the fluid, and the dry fabric, with air. The LS function is a scalar that assigns a value from 0 to 1 for every point in the flow domain. The value of ϕ changes progressively through the interface thickness from 1 to 0. It has a value of 0.5 at the interface between resin and air, 1 in the saturated regions and 0 in the dry zones. It relates the location of the interface with the fluid properties to be used in the whole domain [148]. Figure VI.5 illustrates the principle of the level set method application in the simulation tool. A transport equation governs the level set function (Equation VI.54), based on the advection of the function by the velocity field v.

$$\frac{\partial \phi}{\partial t} + v.\nabla\phi = \gamma_l s \nabla.(\epsilon_{ls}\nabla\phi - \phi(1 - \phi\frac{\nabla\phi}{\mid \nabla\phi \mid})) \tag{VI.54}$$

The left-hand side of the equation gives the exact interface motion, where the right-hand side is for numerical stability. ϵ_{ls} is the parameter controlling the interface thickness, and γ_{ls} is the re-initialization parameter; it is responsible for the stabilization of the level set function.

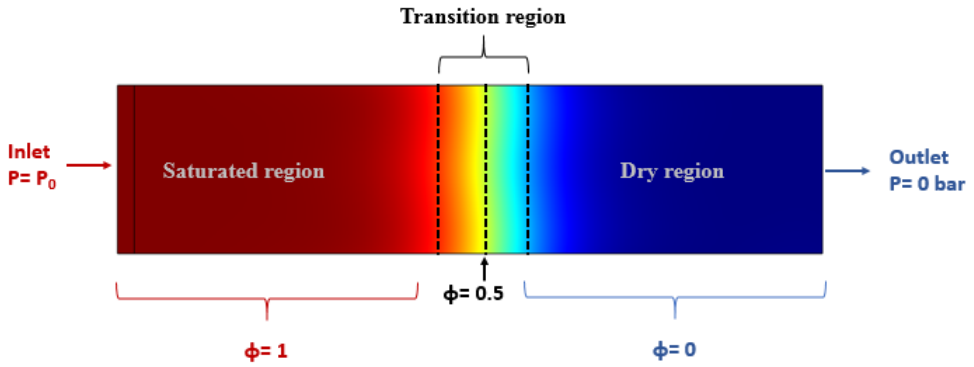

FIGURE VI.5: The distribution of the level set function (phils) throughout the flow domain

VI.6.3 Boundary and initial conditions

The left side of the rectangular mold is prescribed as the flow inlet (line injection), with a constant pressure injection $P = P_0$. The right-hand side is designated as the flow outlet, with a pressure $P = 0$ bar. All the pressure values presented in this study are relative pressures (i.e. the absolute pressure - the atmospheric pressure). The no-slip boundary condition is applied to the other two sides of the mold. The initial concentration C_0 is prescribed at the inlet, which gives the boundary condition $C(x = 0, t) = C_0$. The problem consists of two initial conditions; at $t = 0$, the suspension hasn't entered the mold cavity yet, hence the value of $C(x, t = 0) = 0$. Similarly, no retention takes place at the instant $t = 0$, therefore, $\sigma(x, t = 0) = 0$. Figure VI.6 illustrates the assigned boundary and initial conditions applied for all the simulations.

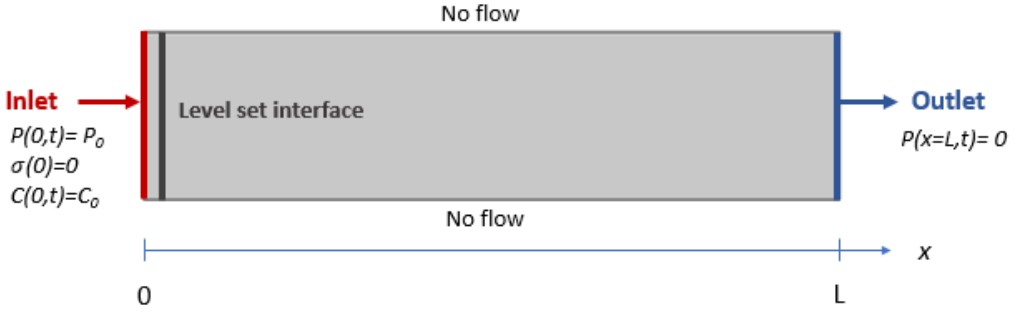

FIGURE VI.6: Boundary and initial conditions

VI.6.4 Input parameters

The input data needed for the problem resolution are: the injection pressure or flow rate of the suspension P_0 or Q_0, the initial preform porosity ϵ_0 or the fiber volume fraction V_f, the initial concentration of the suspension C_0, the viscosity of the neat fluid η_0,

the dimensions of the preform (length and width) and the initial filtration coefficient k_0. However, there is a need to introduce additional parameters according to the used filtration model: the viscosity constant A for Erdals model, the particle size d_p, the initial fraction of trapped liquid coefficient β_0 and the numerical constant r for Lefevre's model.

VI.6.5 General algorithm

The injection simulation is based on a finite element calculation, with an iteration loop performing a series of calculations for each mesh element at each time step. The solution to the problem requires a strong coupling between the flow and filtration models because the injection process exhibits high variable interdependencies (as seen in chapter IV). This coupling is realized inside the iteration loop. Each loop encompasses a flow solver, a filtration solver and an update of material parameters. The general algorithm is illustrated by Figure VI.7 [6]. The iteration loop is performed as in the following successive steps:

- Initially, the porous medium is of a macroscopic porosity ϵ_0 and an isotropic initial permeability of K_f. The suspension is injected into the medium with an initial viscosity of η at an injection pressure of P_0 (or flow rate Q_0). Darcy's law is used to calculate the velocity U of the suspension as a function of ϵ, K_f and η, using the mold dimensions, P_0, and V_f as inputs.
- The fractions of retained particles σ and liquid β are calculated at each time step in every element using the filtration kinetics equation and the concentration is estimated by the conservation equation accordingly. Inputs to the filtration model are the initial filtration coefficient k_0 and the initial suspension concentration C_0, in addition to the initially trapped liquid coefficient β_0 and the numerical parameter r with Lefevre's model.
- The material properties (the suspension viscosity η and the medium permeability K) are updated as a function of retained and suspended particles in each mesh element and at each iteration. The viscosity and the permeability are calculated by Equations VI.40 and VI.39 respectively with Erdal's model, and Equations VI.52 and VI.47 with Lefevre's model.

VI.6.6 Output data

The calculation loop is repeated until the last element of the mesh is filled. The simulation is stopped when the filling time is achieved (the part is completely injected $t = T$). The simulations allow the prediction of the timely and spatial evolutions of flow and filtration variables. The generated output data are: the particle deposit σ, the suspension

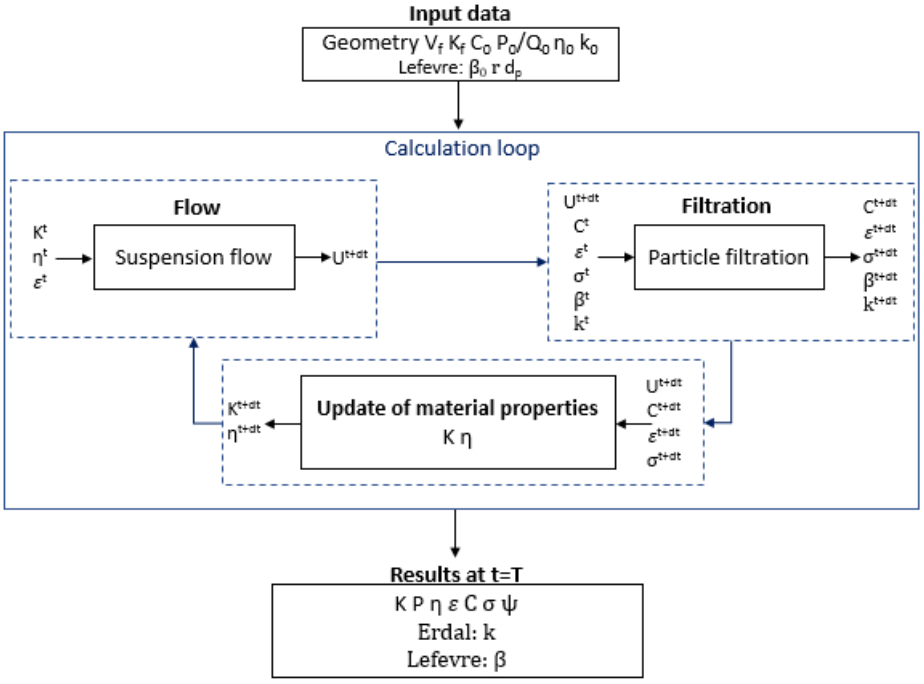

FIGURE VI.7: Coupling between flow and filtration during the injection of particle-filled resin into a fibrous reinforcement [6]

concentration C, the porosity ϵ, the permeability K, the particle content ψ, the pressure P, the viscosity η, the filtration coefficient k (Erdal's model) and the trapped liquid β (Lefevre's model).

VI.7 Numerical results

In this section, the results of the numerical simulations are presented and discussed. All the impregnations are performed with a line injection. First, the flow simulations for fluid injection into fibrous media are presented. Then a filtration model is added and the simulation results are presented respectively for the models of Erdal and Lefevre.

VI.7.1 Flow simulations

Before implementing the filtration equations, the flow model is firstly validated with the experimental and analytical data for neat resin injections to evaluate its accuracy. An experiment of chapter IV is used for validation. The study case is a constant pressure injection of P_0= 1 bar into a preform of a V_f= 48% (ϵ_0= 52%), with a neat fluid viscosity η= 0.035 Pa.s. The numerical flow front positions are compared to experimental ones at t = 0, 5 s, 10 s, 30 s, 45 s and 70 s. From Figure VI.8, it is observed that both results had almost identical flow positions at all the explored instants of time. Moreover, both numerical and experimental filling times were about 70 s.

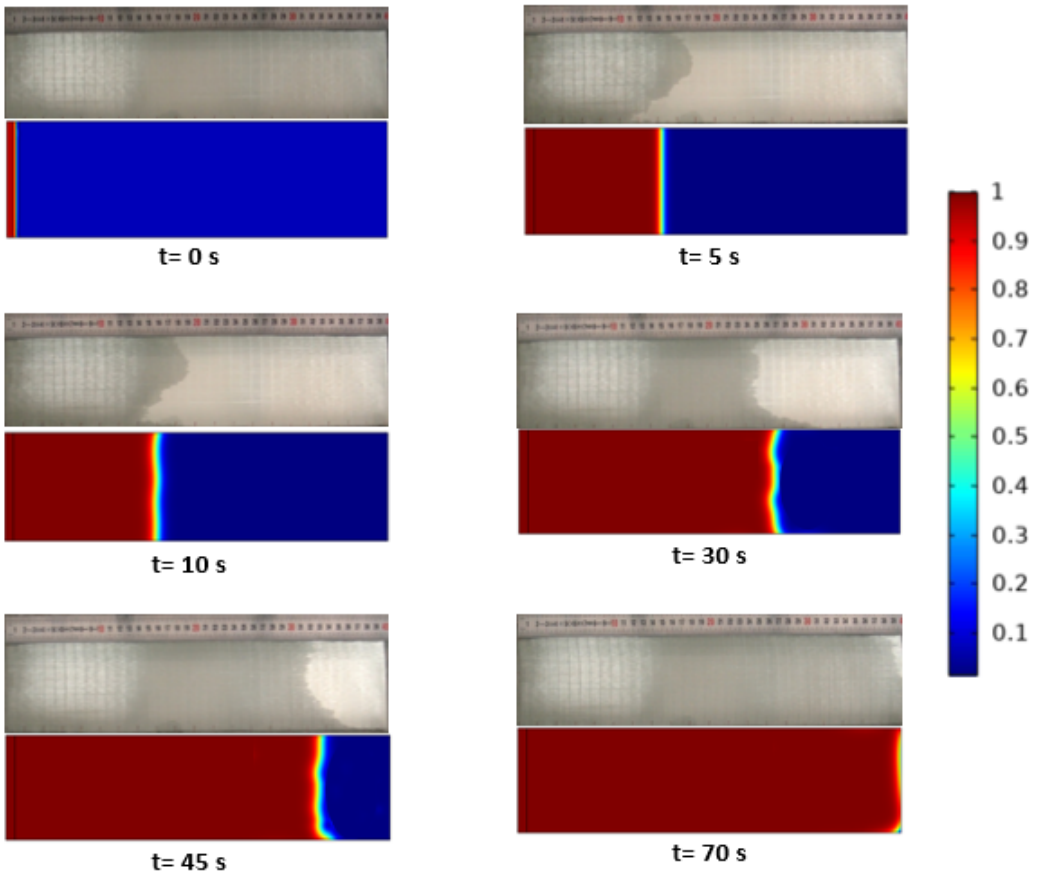

FIGURE VI.8: Experimental and numerical positions of flow front positions at different instants of time for a neat resin injection

A second experimental case is compared to analytical and numerical results for flow front positions and pressure profile. At this experiment (performed within the series of experiments of chapter IV), the preform had a V_f of 48% (ϵ_0= 52%), injected at P_0= 1.4 bar with a fluid viscosity η= 0.035 Pa.s. Results of this case are presented in Figure VI.9, which illustrates the spatial evolution of the analytical and numerical pressure at the end of mold filling (Figure VI.9 A), and the analytical, experimental and numerical flow front kinetics (Figure VI.9 B). The registered filling time was 42 s for analytical, experimental and numerical analyses. Numerical flow front presents good agreement with the experimental and analytical ones.

VI.7.2 Flow and filtration simulations

After validating the flow simulation by two experimental cases, the filtration kinetics and the concentration equations are implemented into the numerical tool in COMSOL Multiphysics to address the flow of suspensions through fibrous media. Indeed, the presence of particulate-fillers imposes a continuous variation of process parameters in time and space. The experiments presented in chapter IV have thoroughly explored the spatial evolution of concentration with several selected variables. The numerical

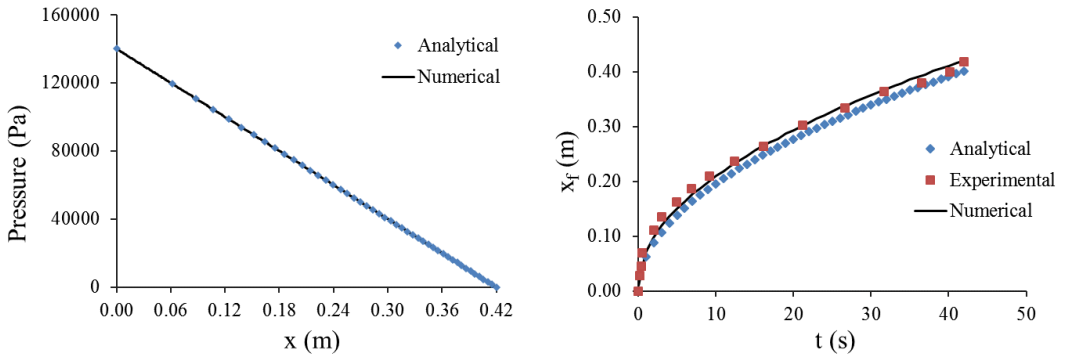

(A) (B)

FIGURE VI.9: Numerical, experimental and and analytical results showing (A) the spatial evolution of pressure and (B) the time evolution of flow front

simulations aim to give access to further flow-related variables such as the evolution of viscosity and pressure and filtration-related variables such as the particle deposit and the influence on the flow process, as well as the effect on material variables like permeability. For these simulations, diffusion and gravity effects are neglected. The suspension is assumed to be agglomerate-free. Particles and resin are assumed to have the same flow velocity (no relative velocity is considered). Finally, a parametric study is performed with each model to assess the influence of filtration parameters on flow and filtration behaviors. A parametric study is the first step toward the identification of the filtration model parameters. The experimental measurement method only allows obtaining the particle concentration profiles at the end of injection. Therefore, the parametric study will help to evaluate the reflection of filtration parameters on these concentration profiles.

VI.7.2.1 Erdal's model

A case study from experiments for a particle-filled injection is tested numerically to evaluate the spatial evolution of variables that are challenging to obtain experimentally. In this experiment, a suspension of C_0= 3.7% and η_0= 0.035 Pa.s is injected at P_0= 1 bar into a fibrous medium of V_f= 48%. The simulation results are presented in Figure VI.10. The numerical flow front and the squared flow position are compared to experimental data in the Figures VI.10 A and VI.10 B respectively. The numerical solution exhibited acceptable agreement with the experimental profile, with a good reproduction of the first non-linear zone of the flow front curve discussed in chapter IV.

To understand the effect of the different flow and filtration variables on the concentration profiles in the plate, the spatial evolution of each variable is presented at the end of injection as a function of distance in Figure VI.11. The figure presents the simulation profiles for ψ, C, σ, η, ϵ, K, k and P plotted against the flow distance x (ranged from 0 to L, the mold length) at the end of impregnation ($t = T$).

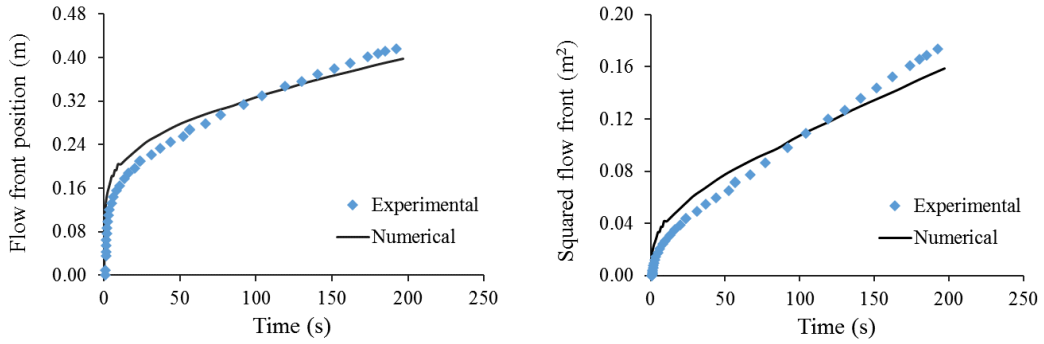

(A) (B)

FIGURE VI.10: Flow front kinetics obtained experimentally and numerically using COMSOL Multiphysics, with (A) flow front positions and (B) squared flow front positions during a particle-loaded impregnation

Retention (σ) As the suspension flows through the fibrous bed, a part of the suspended particles is subjected to bed and surface filtration. As a result, particles are captured by the fibrous medium. The specific deposit attains its maximum at the beginning of injection, then decreases monotonously with distance (Figure VI.11 A).

Particle content (ψ) Suspended and retained particles constitute the overall particle content ψ present in the composite part. The decreasing profile of ψ follows the same trend as C and σ (Figure VI.11 A).

Concentration (C) The concentration of suspension in movement C is C_0 at the preform inlet (x =0 m) because it is an imposed boundary condition. Particle loss leads to a progressive decrease in the effluent concentration because a part of the suspended particles is trapped within the preform. The Figure shows a clear drop in C with x along the preform (Figure VI.11 B).

Viscosity (η) The suspension viscosity marked a decreasing profile along the part length at $t = T$. The variation of the viscosity is governed by the concentration profile (Figure VI.11 B).

Porosity (ϵ) The spatial evolution of porosity is a reflection of the local particle deposit. An increasing trend is observed for ϵ with the flow path towards its initial value. When the retention is at its maximum value, the porosity takes its minimum value (Figure VI.11 C).

Permeability (K) The permeability is proportional to the system porosity and inversely proportional to the particle deposit. Thus, the lowest value of K is attained

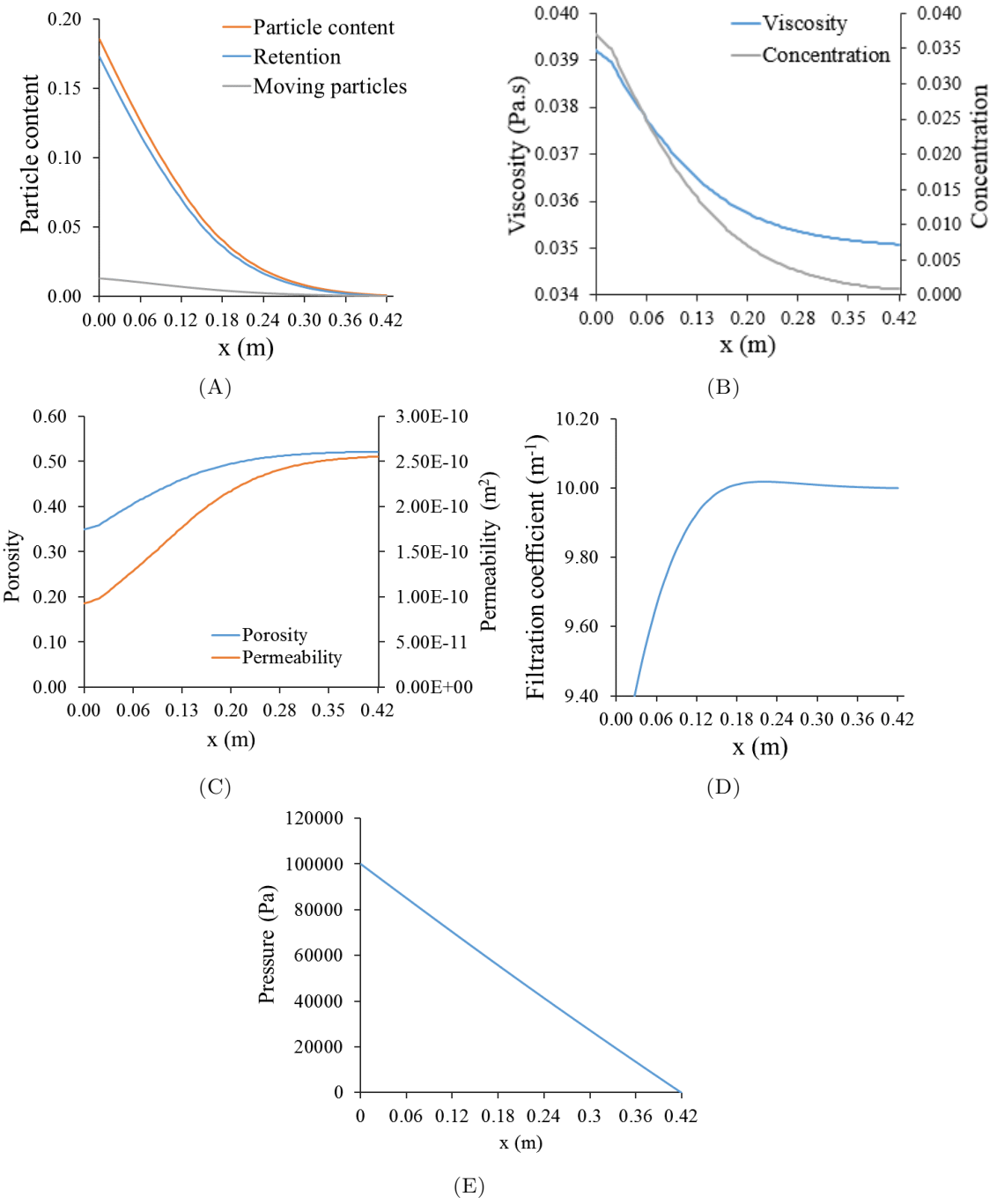

FIGURE VI.11: Evolution of different variables at the end of injection using Erdal's model for a case with C_0= 3.7%, η_0= 0.035 Pa.s, P_0= 1 bar and V_f of 48%, with (A) particle content, (B) viscosity and concentration, (C) porosity and permeability, (D) filtration coefficient and (E) pressure

at the beginning of the preform, then it increases continuously and converges to the permeability of the clean fibrous bed towards the end of the preform with minimum or no retention (Figure VI.11 C).

Filtration coefficient (k) The model of Erdal assumes that the filtration coefficient varies following Equation VI.38. The k profile features a continuous increase along the preform length because the retention occurs at the beginning of the process and the medium evolves continuously. Afterward, k converges to its initial value k_0 and almost exhibits a plateau till the end of the preform as the system tends to stabilize (Figure VI.11 D).

Pressure (P) A continuous decrease in pressure with the flow path takes place from the injection pressure P_0 at $x = 0$ m to the outlet pressure $P = 0$ at $x = L$ (Figure VI.11 E). Parabolic pressure profiles were obtained at higher initial particle concentrations (10-30%) using Erdal's model with constant flow rate injections [35].

Figure VI.11 also highlights the interdependencies of some process and material variables. The overall particle content is the sum of the moving and retained particles. Suspended particles had a lower contribution to the overall content in comparison to the deposited ones (Figure VI.11 A). It may be a result of using a relatively high filtration coefficient in this simulation (k_0=10 m^{-1}). However, only a comparison with experimental results will enable the estimation of the exact value of k_0. The viscosity follows the concentration trend along the preform length (Figure VI.11 B), as it is related to the local C value quadratically through the viscosity model (Equation VI.40)[149]. Figure VI.11 C shows the spatial change in the domain permeability with respect to porosity. The two quantities which are governed by the specific deposit increase continuously and tend to their initial values as the retention drops to zero at the end of the part.

Figure VI.12 presents the evolution of the permeability normalized to the permeability of the neat fibrous bed and plotted against the retention. Figure VI.12 A shows that the permeability decreases monotonously with the rise in particle deposit. Figure VI.12 B plots the variation of k normalized to its initial value with respect to σ. Erdal considers k as a geometrical variable that reflects the evolving medium porosity. k is directly related to σ through the specific surface of the solid phase of the filter, i.e., the fibers and the retained particles (Equation VI.35). At the beginning of injection no retention takes place ($\sigma(x, t = 0) = 0$) and the filter initially has a porosity of ϵ_0. When particle deposition starts, the filtrate amount in the fibrous bed begins to increase and the system porosity is modified accordingly. The specific surface starts to increase slightly at low specific deposits because of the availability of large pore volume. As the particle deposition continues, fibers and particles start forming networks and the specific surface decreases as particles are deposited between fibers. Hence, the filtration coefficient continuously decreases with particle deposit. This relation is dependent on the fiber content in question; a different behavior could be obtained at higher/lower fiber volume fractions. The value of k converges to zero only if 100% of the pores are filled with particles, which is a non-realistic situation. The retention is restricted by the maximum

deposit term σ_u, which ensures that the filtration term tends to zero before the specific deposit reaches the initial porosity.

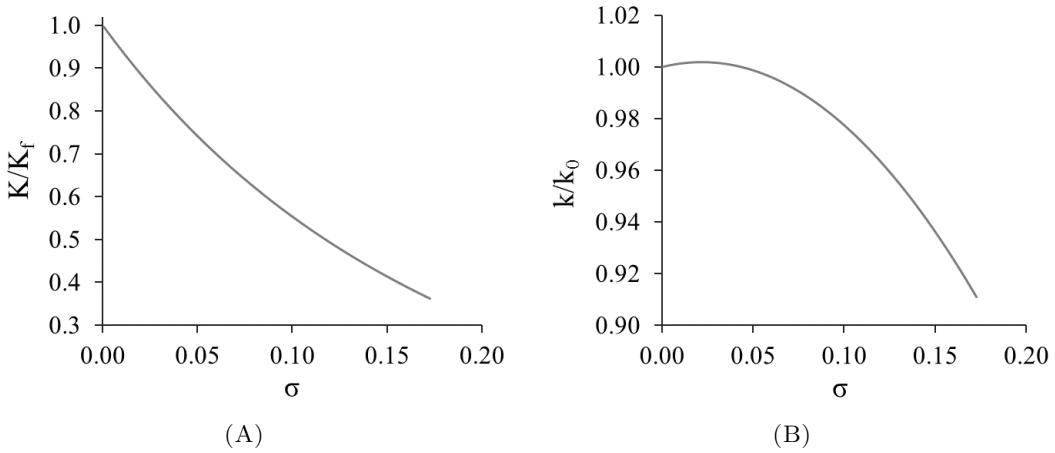

FIGURE VI.12: The evolution of the normalized (A) permeability and (B) filtration coefficient with specific particle deposit

Parametric study

This step evaluates the reflection of the filtration model parameters on the process variables to help draw a clear image of the effect of these parameters on the filtration variables, e.g., retention, which directly influences the concentration profile investigated experimentally. Only one parameter is changed per simulation to eliminate the effect of other variables. The model of Erdal contains two filtration parameters: the initial filtration coefficient k_0 and the ultimate particle deposit σ_u.

Initial filtration coefficient

The influence of k_0 on the flow and filtration processes is analyzed at the end of injection (at $t = T$). Figure VI.13 shows the mutual evolution of permeability and retention with the distance x at different k_0 values: 1 m^{-1} (Figure VI.13 A), 5 m^{-1} (Figure VI.13 B) and 10 m^{-1}(Figure VI.13 C). The particle deposition rate governs the permeability as it controls the medium porosity and the specific surface area S of the medium. K is inversely proportional to S in the Kozeny-Carman's equation VI.37, from which the permeability formula is derived. Hence, the permeability is inversely proportional to the specific particle deposit. K exhibits its minimum value at the preform inlet when σ is at its maximum value. Then σ decreases progressively and reaches its lowest value at the end of the preform. At the same time, K converges to the initial filter permeability at a minimum of zero specific deposit. Through the three figures, a steeper decrease in retention is remarked with the increase of k_0. Retention converges to zero at the end of injection for high k_0 values, while higher final σ is attained at the end of the preform with lower k_0 values. This is because high k_0 causes increased particle deposit

at the preform inlet, which enhances early cake formation. The blockage of flow channels reduces or completely prohibits the passage of particles to the preform outlet according to the formed cake density.

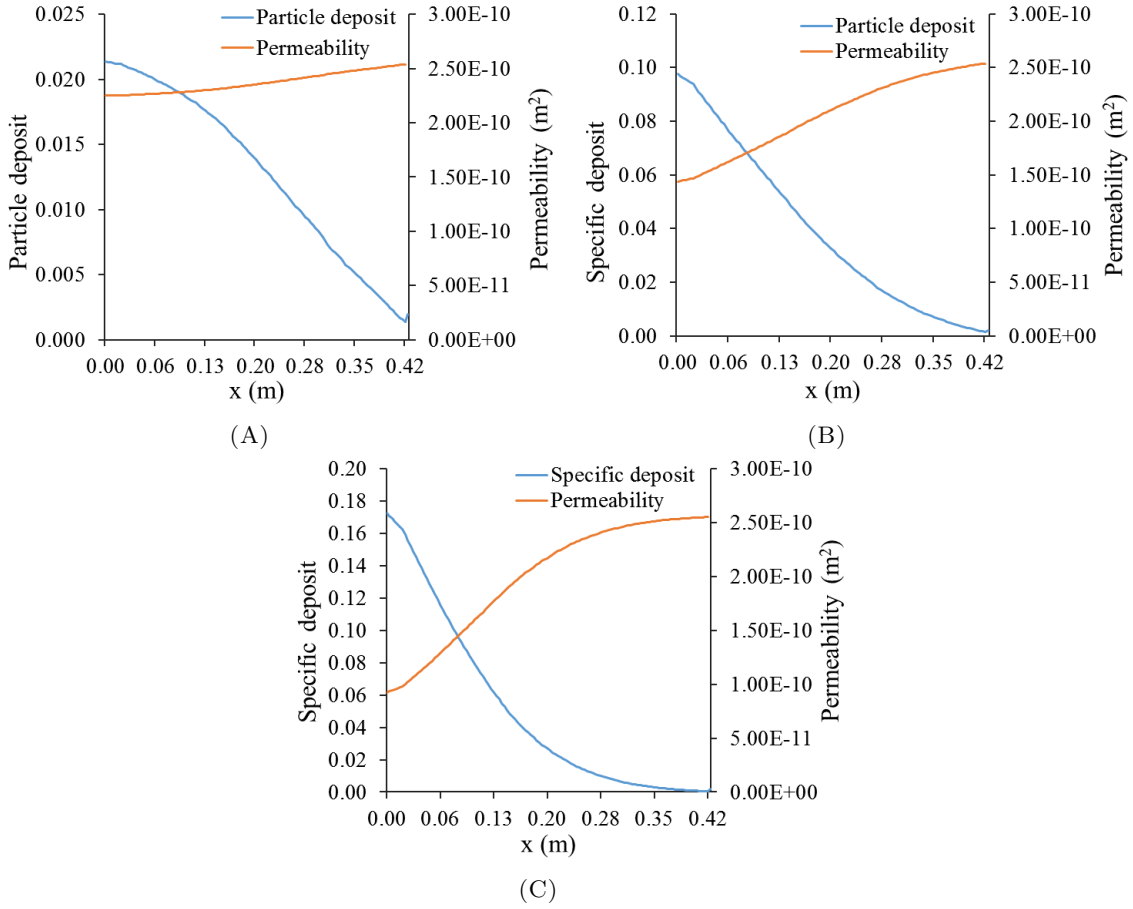

FIGURE VI.13: The influence of the initial filtration coefficient k_0 on the evolution of permeability and the specific particle deposit at (A) k_0= 1 m^{-1}, (B) k_0= 5 m^{-1} and (C) k_0= 10 m^{-1}

The filtration coefficient reflects the evolution of particle capture by the medium as k_0 is proportional to the specific particle deposit. From the literature, k_0 is found to be independent of particle concentration [52], but highly dependent on previously deposited particles [36, 142]. A higher value of k means that more filtration takes place and vise versa. The influence of this parameter on the particle content in the medium is presented in Figure VI.14. Results reveal the sensitivity of the retention behavior to the filtration coefficient (Figure VI.14 A). The filtration increases the loss of particles from the suspension; hence, the higher the k, the steeper the decrease in particle concentration (Figure VI.14 B). The overall particle content (Figure VI.14 C) is a superposition of that of retained σ and suspended particles ϵC, but deposited particles prevail. At low k_0, more homogeneous distribution is observed; however, a lower overall particle content is obtained at $t = T$. Steeper permeability rise is observed with the increase in k_0. However, for all k_0 values, K converges to the clean bed permeability K_f (Figure VI.14 D). These results compare well with the numerical results of Erdal [35].

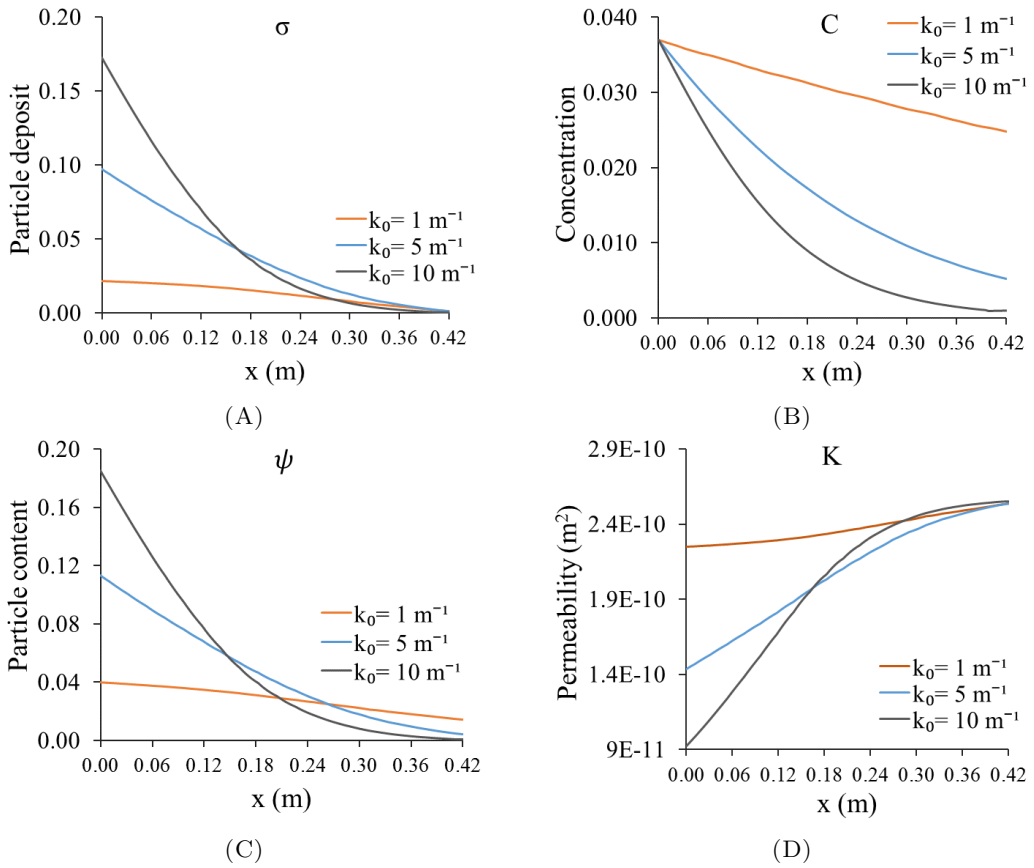

FIGURE VI.14: The influence of the initial filtration coefficient k_0 on (A) particle deposit, (B) concentration, (C) particle content and (D) permeability

Figure VI.15 A plots the permeability of the medium normalized to its initial value against the particle deposit. A monotonous decrease is noticed in K/K_0 with increased retention. Figure VI.15 B highlights the change of filtration coefficient with particle capture. Same profiles observed in Figure VI.12 B were obtained for all k_0 values (1, 5 and 10 m^{-1}). The value of the maximum specific deposit increased with the increase of k_0. An initial filtration coefficient higher by one order of magnitude (from 1 to 10 m^{-1}) resulted in a maximum particle deposit greater by a factor of 7. The evolution of the filtration coefficient depends on the fiber volume fraction of the medium [90], which explains obtaining the same profile for k/k_0 at fixed V_f.

Ultimate particle deposit σ_u

The ultimate filtration deposit σ_u is an empirical constant that depends on the characteristics of the porous medium. It is the particle deposit at full clogging. In Equation VI.34, when σ reaches σ_u in the right-hand side of this equation, the filtration coefficient k converges to its initial value k_0 and the equation reduces to the one used by Lefevre (Equation VI.44). The value of σ_u should not exceed the initial porosity of the medium ϵ_0.

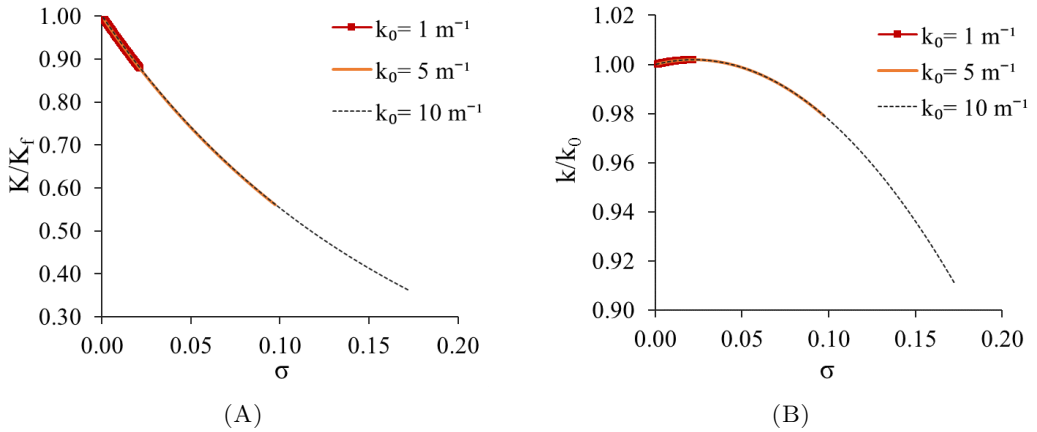

FIGURE VI.15: The influence of the initial filtration coefficient on the evolution of (A) the permeability and (B) the filtration coefficient

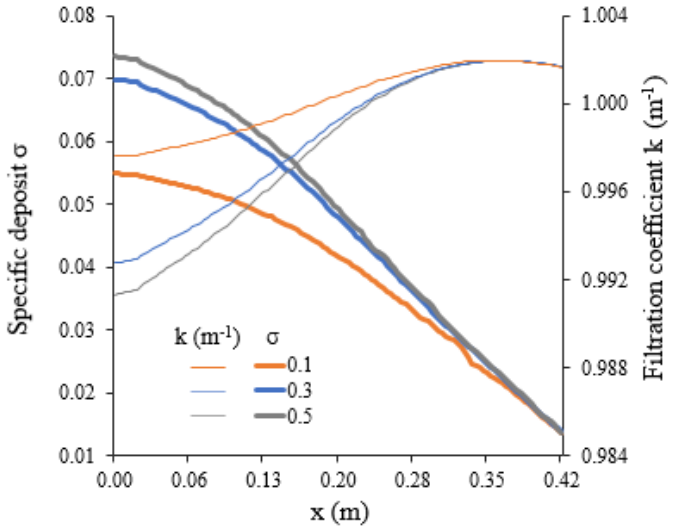

FIGURE VI.16: Effect of the ultimate particle deposit σ_u on retention and filtration coefficient, with values of 0.1, 0.3 and 0.5

Figure VI.16 plots the influence of σ_u on the evolution of k and σ for a case with V_f= 48%, C_0= 3.7%, η_0=0.035 Pa.s, P_0=1.4 bar and d_p=15.2 μm. The general behavior is that when the ultimate specific deposit increases, the filtration coefficient decreases and the particle retention increases especially at the preform inlet. The retention rate increases with the increase in σ_u as the right-hand side term of Equation VI.44 increases. Retention tends towards a fixed value 0.0138 with the all σ_u values. The filtration coefficient decreases with the increase of σ_u by an amount proportional to $(1-\frac{\sigma}{\sigma_u})$. The filtration coefficient converges to a constant value 1.002 m^{-1} slightly higher than its initial value 1 m^{-1} as σ approaches σ_u.

The choice of σ_u has a tangible effect on the retention behavior. In this study, σ_u is considered lower than the initial porosity of the fibrous medium because part of the pores is preserved for liquid entrapped between particles. When the ultimate filtration is attained, the filtration rate tends to zero.

VI.7.2.2 Lefevre's Model

In their study, Lefevre et al. recommended improving the rheology model to include the influence of the suspension concentration. Therefore, the model of viscosity is replaced by the Eilers model after the identifications of parameters experimentally for the same particle types used in the experimental part (refer to section II.5.2). Figure VI.17 presents the simulation results with Lefevre's model for the same case study explored with Erdal's model (Figure VI.11). For this simulation, the fraction of liquid entrapped between particles is neglected (β_0 is assumed to be 1).

In Figure VI.17 A, the total amount of particles is decomposed to suspended and moving particles. The retention decreases monotonously, whilst suspended particles decrease quasi-linearly and hence the overall particle content ψ, exhibited decreasing profile, which are the same trends observed with Erdal's model. Here, the retention at the end of the part is higher than zero, which gives higher overall particle content. The initial concentration C_0 imposed at the left side of the mold decreases progressively and reaches its minimum at $x = L$. The viscosity profile follows that of the concentration according to Eilers law (Figure VI.17 B). The permeability is inversely proportional to the local specific deposit as shown by Figure VI.17 C. The amount of filtered particles governs the spatial change in domain permeability because it controls the local porosity change. An increase in K and ϵ followed the decreasing filtration profiles. For this model, the filtration coefficient k is considered constant. Unlike the neat fluid injections, a parabolic pressure profile is noticed at the end of the preform (Figure VI.17 E).

Parametric study

The model presented by Lefevre contains several parameters that are not directly identifiable (i.e., k_0, β and r). Therefore, the influence of each parameter is studied separately with keeping all the other parameters fixed. Simulations are realized for a case with with C_0= 3.7%, V_f= 48%, P_0= 1 bar, β_0=1, r=1 and k_0=2 m^{-1}.

Initial filtration coefficient k_0

The influence of the initial filtration coefficient is presented in Figure VI.18. According to Equation VI.44, k_0 is the proportionality coefficient between the retention rate and the amount of suspended particles. The higher the k_0, the steeper the spatial decrease in retention and the higher the decrease in concentration (Figure VI.18 A) and the suspended particles (Figure VI.18 B). The porosity in Figure VI.18 C varies inversely to the particle content. However, all the porosity profiles converge toward ϵ_0.

The filtration behavior depends on the value of k_0; for low values, a slight and monotonous decrease in particle content is observed. For high k_0 values, a high retention gradient

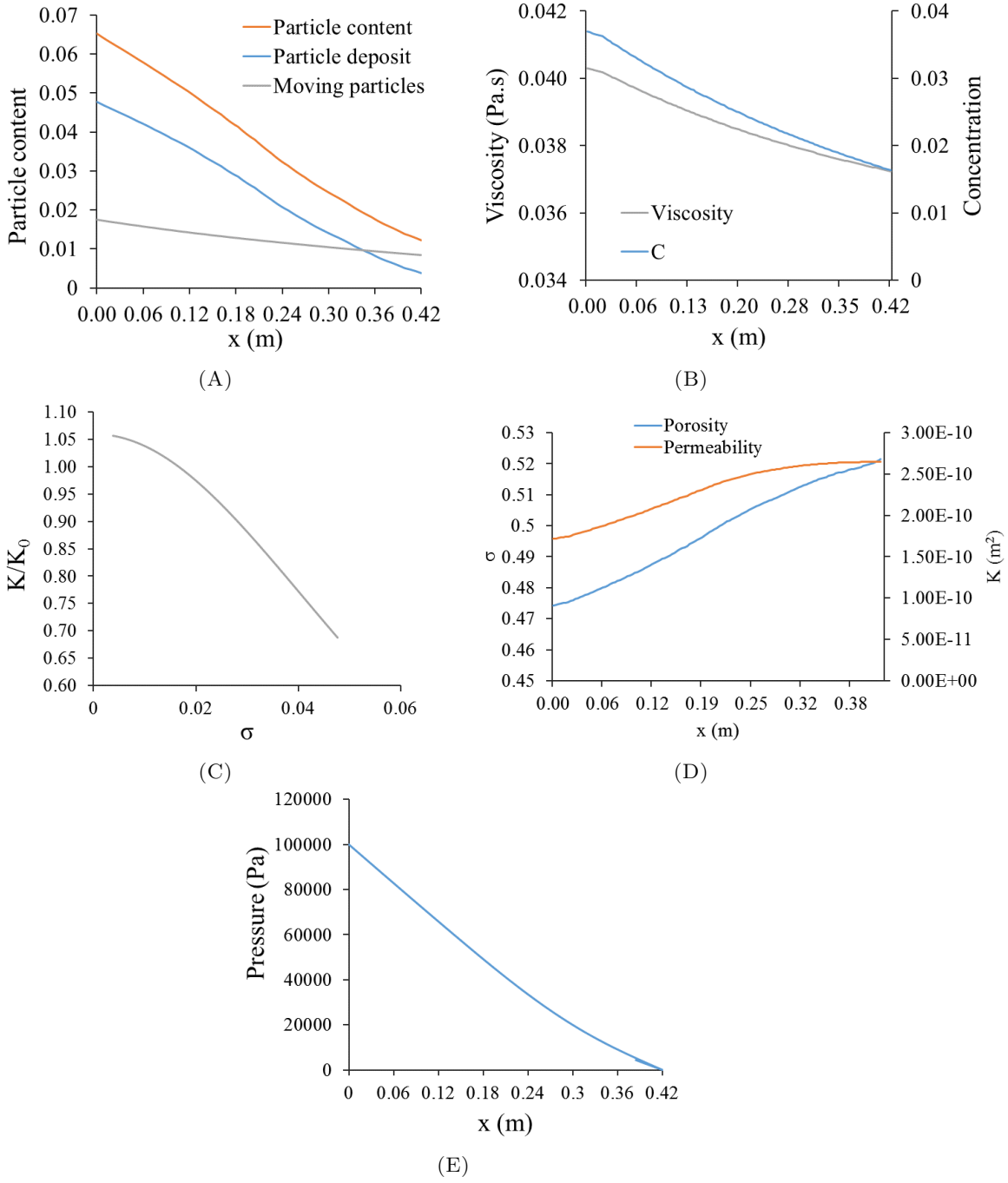

FIGURE VI.17: Simulation results of Lefevre model for a case with C_0= 3.7%, V_f= 48%, P_0= 1 bar, d_p= 5.2 μm, β_0=1 and k_0=2 m^{-1}

is noticed through the part length. The porosity profile follows an inverse trend of particle deposition. The surface plots in Figure VI.19 illustrates the evolution of particle deposit for k_0= 5 and 10 m^{-1} with flow path at the end of impregnation. The plots have marked elevated deposit ratio with increased k_0. The effect of k_0 on the particle deposit is remarkable. The percentage of retention increases with increasing filtration coefficient and the gradient of particle deposit steepens along the flow path.

The variation of pressure with the initial filtration coefficient k_0 is highlighted in Figure

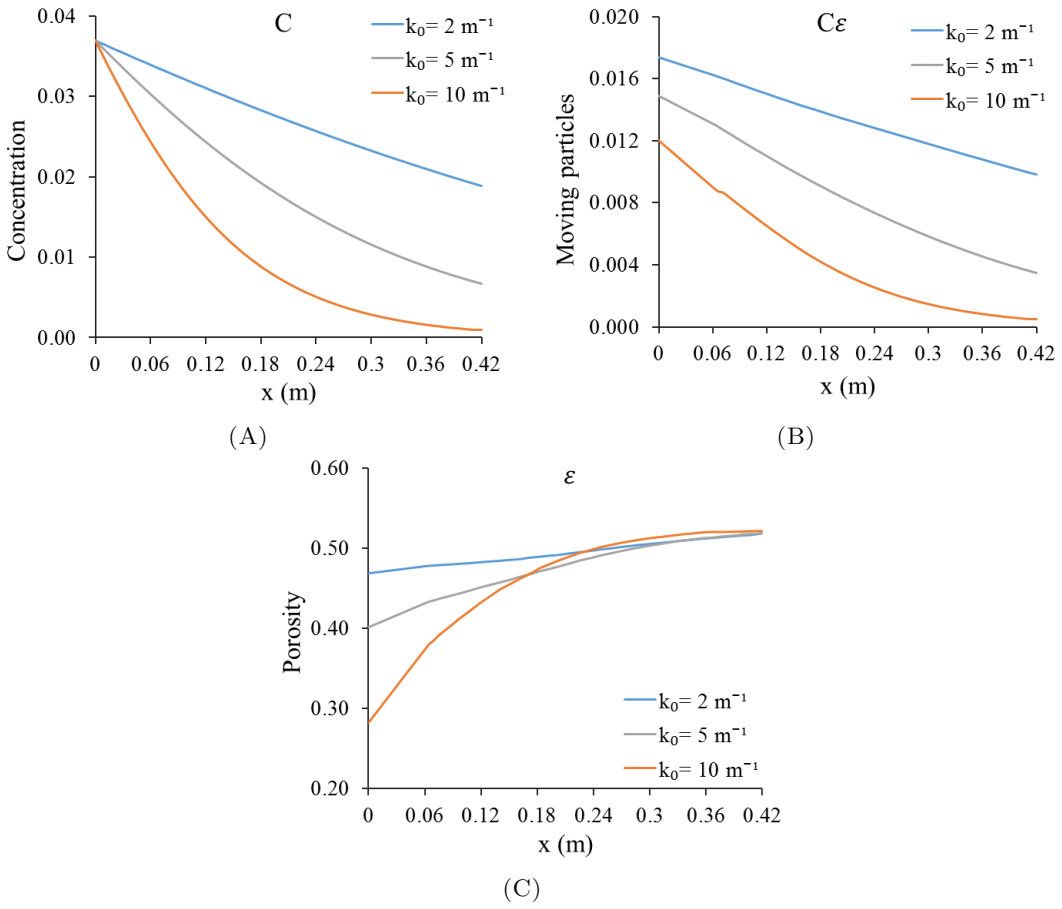

FIGURE VI.18: The influence of k_0 for a case with C_0= 3.7%, V_f= 48%, P_0= 1 bar, d_p= 15.2 μm, β_0=1, r=1 and k_0=2 m^{-1}, with (A) particle concentration, (B) suspended particles and (C) porosity

VI.20. The pressure varies only slightly by changing the filtration coefficient from 1 to 15 m^{-1}. However, the pressure gradient towards the end of the flow drops below the profiles of lower filtration coefficients.

Fraction of trapped liquid β_0

The physical parameter β denotes the liquid trapped between captured particles. The effect β is analyzed at $t = T$ for the initial value β_0 1, 2, 3 and 5. Figure VI.21 presents the influence of β on the porosity, concentration and the moving particles. The term $\beta\sigma$ is the total deposit, i. e. the trapped particles and liquid. When β=1 (no trapped liquid), this term is reduced to the retained particles ($\beta\sigma$=σ). It means that particle compactness is 1, which is not realistic. On the one hand, the higher the β, the higher the deposit volume, and the lower the ϵ (Figure VI.21 A). On the other hand, the concentration of particles in the suspension increases (Figure VI.21 B) as a result of suspension depriving of liquid. Figure VI.21 C illustrates the competition between these two effects. The lower β is the higher ϵC at the preform inlet, and the steeper the decrease in ϵC with space. The decrease in β_0 has an effect similar to the increase in

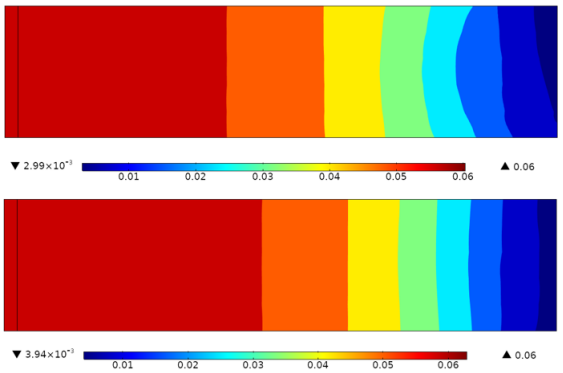

FIGURE VI.19: The evolution of particle content as a function of the filtration coefficient with k_0=5 m^{-1} (upper) and 10 m^{-1} (lower)

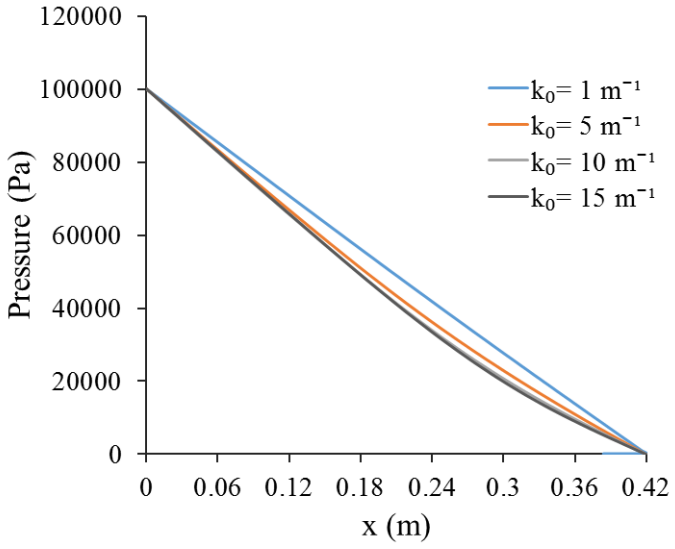

FIGURE VI.20: The evolution of pressure as a function of the filtration coefficient with k_0=1, 5, 10 and 15 m^{-1}

k_0; the lower the amount of trapped liquid, the steeper the decrease in the amount of particles in suspension. This means the higher the particle loss by retention with the distance.

The evolution of β is governed by σ as per Equation (VI.46). Figure VI.22 highlights the spatial evolution of β (Figure VI.22 A) and $\beta\sigma$ (Figure VI.22 B). As the retention attains the maximum value, β ia at its minimum value at x=0 and increases continuously until it converges to β_0 at the end of the preform, where the retention is minimum. The amount of the deposit $\beta\sigma$ is the product of two profiles, the decreasing σ and the increasing β.

The numerical parameter r

The effect of the numerical parameter r is tested through a series of simulations. Results are presented in Figure VI.23 for the spatial evolution of ψ and ϵC. It was found that

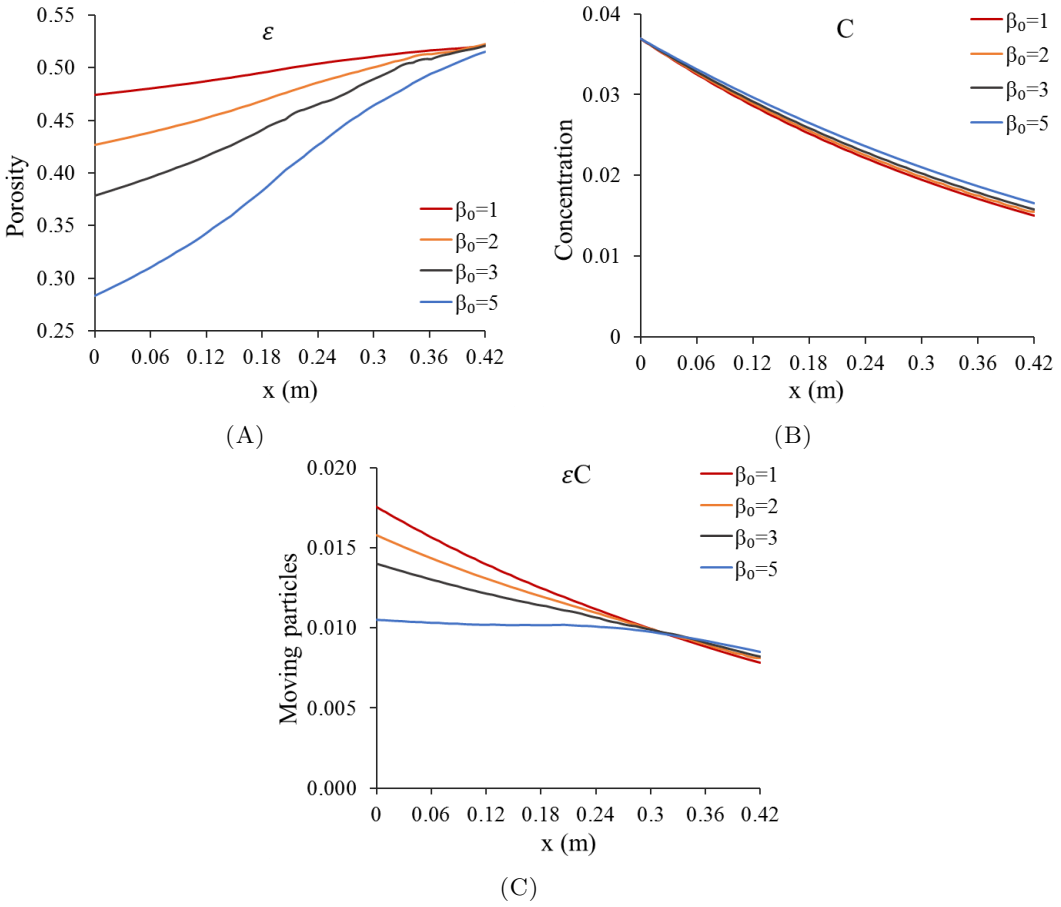

FIGURE VI.21: Simulation results showing the influence of β_0, with C_0= 3.7%, V_f= 48%, P_0= 1 bar, k_0=2 m^{-1}, r=1 and β_0=1, 2, 3 and 5, with (A) porosity, (B) concentration and (C) suspended particles

the amount of moving particles ϵC and the particle content are only slightly affected by the change in r in the range of the explored values (10, 40 and 100). From Equation VI.46, when r increases, β decreases more rapidly when σ is non-zero. Therefore, the porosity is higher at the beginning of the preform (Figure VI.23 A). This lowers the particle content at the beginning of the preform (Figure VI.23 B).

VI.8 Parameter identification

The presented models contain several parameters that need to be identified from experimental data. This step concerns parameters in the flow model (permeability of the fibrous medium and viscosity of the suspension) and parameters associated with the filtration models (of Erdal and Lefevre).

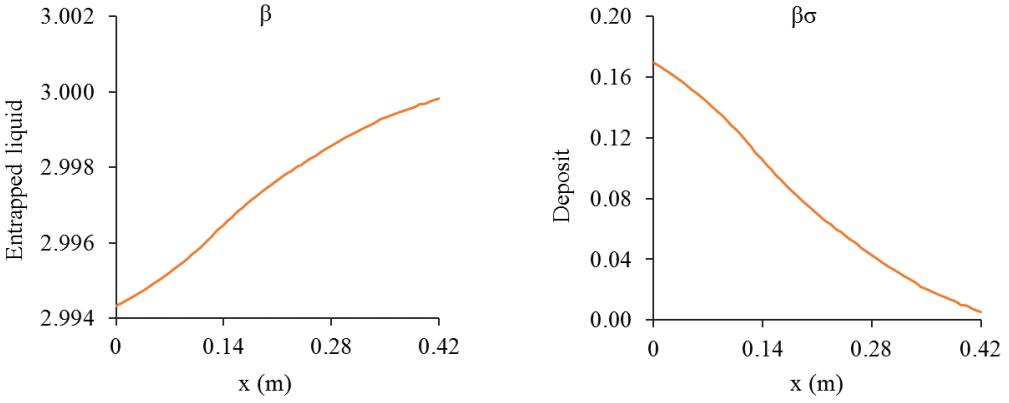

(A) (B)

FIGURE VI.22: Simulation results showing the spatial evolution of (A) β and (B) $\beta\sigma$, β_0=3 and r =0.1 m^{-1}, with (A) particle content, (B) viscosity and concentration

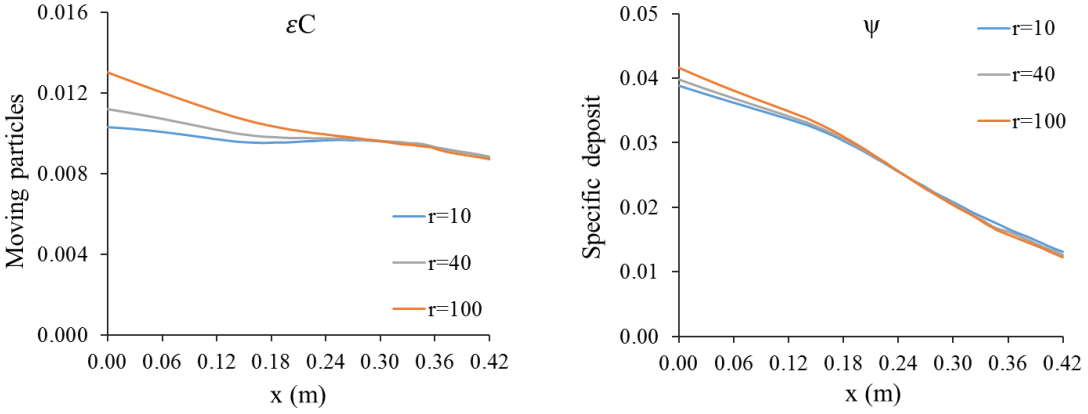

(A) (B)

FIGURE VI.23: The influence of the parameter r on the filtration behavior for a case with C_0= 3.7%, V_f= 48%, P_0= 1 bar, β_0=8.8, k_0=2 m^{-1} and r= 10, 40 and 100, with (A) particle content and (B) moving particles

First, the permeability of the fibrous bed is determined as a function of the fiber volume fraction with the empirical relation:

$$K_f = ae^{bV_f} \tag{VI.55}$$

The flow-related parameters a and b necessary for the determination of the preform permeability are determined with flow experiments detailed in section II.2.4.

The parameters of each viscosity and filtration model are detailed hereafter. A series of simulations of suspension flow through fibrous media are carried out at the same experimental conditions to extract the different parameters. The initial filtration coefficient is approximated by the inverse method, which consists of identifying the value of k_0 leading to the minimization of the least square error between numerical and experimental

data. The experiments of chapter IV allowed the extraction of the spatial concentration profiles. Therefore, the concentration evolution will be used as a base of comparison between experimental and numerical results.

VI.8.1 Erdal's model

In the model of Erdal, two parameters need to be identified; the viscosity parameter A and the initial filtration coefficient k_0. First, the viscosity parameter of Equation VI.40 was determined through the rheology study presented in section II.5.2.5 for the particle grades explored. A increases continuously with the particle size. The value of A depends on the particle size; it was found to be 0.65, 0.66 and 0.67, respectively, for the grades W-210, W-410 and W-610. The filtration parameter that needs to be identified using Erdal's model is the initial filtration coefficient.

Initial filtration coefficient k_0

The value of k_0 depends on the particle and medium pore size and the flow velocity [52]. Following Equation VI.38, k varies with porosity and permeability, which are governed by the amount of retained particles. Although the importance of this parameter, there is still ambiguity in determining its initial value k_0.
The results of chapter IV underlined the dependency of filtration on the fiber content V_f and the particle size distribution. Previous studies has identified k_0 as being independent of C_0 for dilute suspensions in wastewater treatment applications [142, 52]. Whereas Lefevre has reported very slight variations in k_0 as a function of initial concentration. Therefore, it is important to identify the evolution of k_0 as a function of these parameters for the experiments explored in chapter IV. Starting from the experimental concentration profiles, k_0 will be identified as a function of C_0, V_f and d_p.

The initial filtration coefficient is identified for experiments with variable C_0 while keeping the other parameters constant. The objective is to quantify the effect of C_0. Figure VI.24 shows the numerical results of concentration plotted against the experimental ones. The values of k_0 are detailed in Table VI.5 for all the experiments.

TABLE VI.5: Values of k_0 as a function of C_0

C_0	1.3	3.7	6.7
k_0	3	3	2.2
T_{exp}	151	213	237
T_{num}	170	220	228

It was found that the filtration coefficient remains constant with the change in C_0 at fixed process parameters with the lowest C_0 values 1.3% and 3.7%. This further confirms

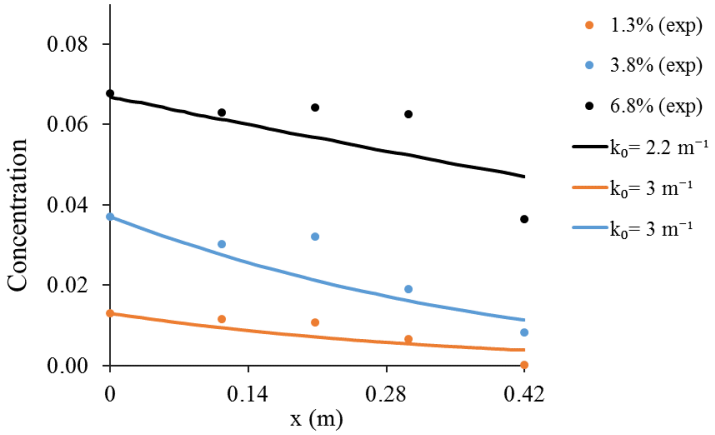

FIGURE VI.24: The experimental and numerical evolutions of concentration using Erdal's model at different C_0 values

previous findings from the literature, which has stated that the filtration coefficient is independent of the initial particle content C_0 [52]. However, k_0 marked a slight decrease with the increase in C_0 to 6.8%.These results agree with the findings of Lefevre for higher C_0 values, where k_0 decreased slightly with the increase in C_0 [6]. More precisely, an average k_0 of 1.8, 1.7 and 1.2 m^{-1} for C_0= 20%, 30% and 40%. Figure VI.25 shows the influence of C_0 on k_0 for the values of k_0 identified in this study (black circles) and the values identified in the study of Lefevre et al. [6]. This figure shows a continuous and non-monotonous decrease in k_0 with the increase in the initial concentration C_0.

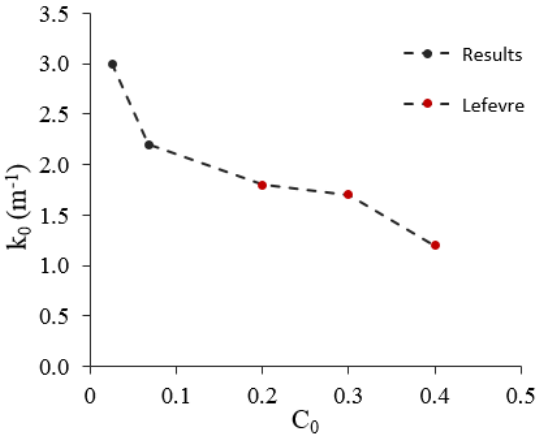

FIGURE VI.25: Influence of C_0 on the initial filtration coefficient. Black points are the k0 values identified within this study and the red ones are the values found by Lefevre et al. [6]

The results of chapter IV underlined the dependency of filtration on the fiber content V_f and the particle size distribution. For that purpose, k_0 is checked for the three tested fiber volume fractions: 38%, 48% and 58% at fixed process parameters. The comparison between numerical and experimental values is shown in Figure VI.26. The values of k_0 at variable V_f is depicted in Table VI.6.

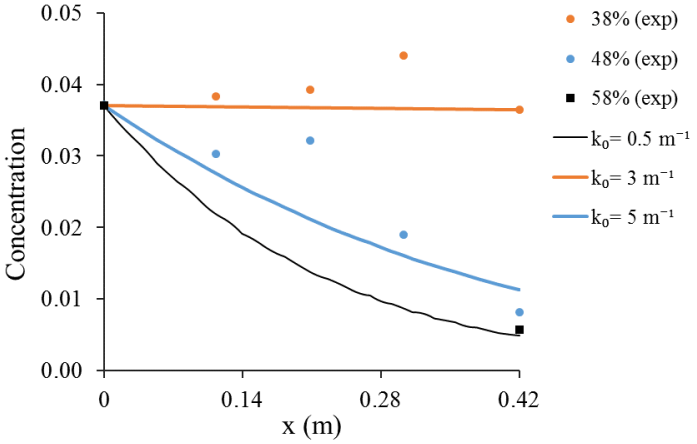

FIGURE VI.26: Effect of V_f on k_0 for an experiment with C_0= 3.7%, P_0= 1 bar, η_0= 0.035 Pa.s, particle grade W-610 and variable V_f

TABLE VI.6: Values of k_0 as a function of V_f

V_f	38%	48%	58%
k_0	0.5	3	5
T_{exp}	14	213	1560
T_{num}	15	220	1600

The same procedure was followed to identify k_0 as a function of particle size. The three particle distributions with medians sizes of 5.2 μm, 7.9 μm and 15.2 μm were tested for the used grades W-210, W-410 and W-610, respectively. Results are shown in Figure VI.27.

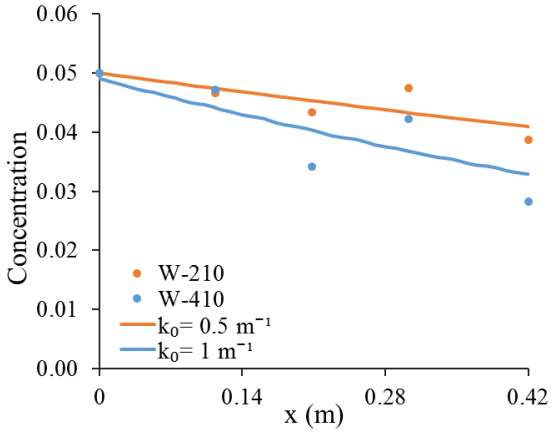

FIGURE VI.27: Effect of the median particle size d_p on k_0 for an experiment with C_0= 3.7%, V_f= 48%, P_0= 1 bar, η_0= 0.035 Pa.s and variable particle sizes d_p

Table VI.7 presents the values of k_0 at variable d_p as well as the experimental and numerical filling time. k_0 increased continuously with the particle size. A good reproduction of filling time is achieved with all the simulations.

The following trends have been identified from experimental results and modeling:

TABLE VI.7: Values of k_0 as a function of d_p

d_p (μm)	5.2	7.9	15.2
C_0	5%	5%	3.7%
k_0	0.5	1	3
T_{exp}	140	125	213
T_{num}	142	138	220

- k_0 decreased with the increase in the initial particle concentration C_0, however, all the values were of the same order of magnitude;
- k_0 increased continuously with V_f, d_p, P_0 and η_0.

The value of k_0 is found to be more sensitive to the change in V_f and d_p, which agrees with the experimental results of chapter IV.

VI.8.2 Lefevre's model

Three main parameters need to be identified with Lefevre's model: the initial filtration coefficient k_0, the fraction of trapped liquid β_0 and the numerical parameter r. The parameters of the viscosity model (Eilers model Equation VI.52) $[\eta]$ and C_{max} the intrinsic viscosity and the maximum packing fraction are characterized in section II.5.2. Their values depend mainly on the particle size distribution.

Initial filtration coefficient k_0

The value of k_0 was estimated as a function of the variables C_0, V_f and d_p using Erdal's model. However, the model of Lefevre considers the size of particles in the suspension through Kozeny-Carman's equation. Therefore, a new estimation for k_0 as a function of d_p will be carried out herein to check if there is a change in the preliminary estimated value. The same method in VI.8.1 was followed to identify k_0 for the experiments with d_p= 5.2 μm and 7.9 μm at V_f= 48%. The results are shown in Figure VI.28 and Table VI.8.

TABLE VI.8: Values of k_0 as a function of d_f with Lefevre's model

d_p (μm)	5.2	7.9
k_0	0.8	1.8
T_{exp}	140	125
T_{num}	160	133

Similarly to the trends found with Erdal's model, k_0 increased with the increase of the particle size. Higher k_0 values were registered with Lefevre's model. k_0 was respectively 0.5 and 0.8 m^{-1} for d_p= 5.2 μm with the models of Erdal and Lefevre. For d_p= 7.9 μm, k_0= 1 m^{-1} with Erdal's model versus 1.8 m^{-1} with Lefevre's model.

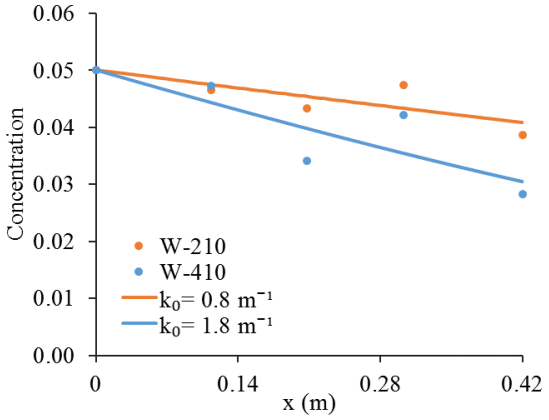

FIGURE VI.28: Effect of the median particle size d_p on k_0 for an experiment using Lefevre's model, with C_0= 3.7%, V_f= 48%, P_0= 1 bar, η_0= 0.035 Pa.s and variable particle sizes d_p

Fraction of trapped liquid β_0

β_0 decreases linearly as a function of the injected particle concentration C_0. The linear dependence law is identified by [6] as:

$$\beta_0 = -13.28C_0 + 9.3377 \tag{VI.56}$$

where C_0 ranges from 0 to 1.
According to the relation VI.56, the following β_0 values are used for the different simulations are: 9.2 for C_0=1%, 8.8 for C_0= 3.7%, 8.7 for C_0= 5%, 8.4 for C_0= 6.7% and 8 for C_0= 10%.

The numerical parameter r

As reported by Lefevre [6], r is constant and independent of the initial particle concentration. In their study, the value of r was found to be 30 for all the explored experiments.

VI.9 Discussion on the filtration models

The presented models are based on different assumptions and hypotheses. Both models use Darcy's law for flow simulation. However, Erdal proposed a model derived from Kozeny-Carman's model for permeability estimation, whilst Lefevre uses Kozeny-Carman's model. This enables Lefevre's model to consider the particle size as an inlet parameter, which was found in chapter IV to be one of the most influencing parameters in determining the retention behavior. In Erdal's model, the particle size is only considered implicitly through the parameter A, which reflects the evolution of viscosity

with d_p. The fraction of retained particles σ influences the filter efficiency and modifies the filtration coefficient k continuously. The change in k as a function of the evolving medium porosity is taken into account by Erdal's model, while it is considered constant in Lefevre's model. The latter model suggests that there is a fraction of liquid trapped between particles β with an initial value that changes inversely to the fraction of trapped particles. Erdal's model considers that β=1 for all initial concentrations. However, it takes into account the particle detachment possibility. Table VI.9 summarizes the comparison between the two models.

TABLE VI.9: Comparison between the filtration models of Erdal and Lefevre

Parameter	**Erdal**	**Lefevre**
Particle detachment	Considered	Neglected
Trapped liquid β	$\beta = 1$	Variable
Filtration coefficient k	Variable	$k = k_0$
Particle size d_p	Not considered	Inlet parameter

The differences between the assumptions in the two models explain the slight variations in profiles of the different quantities presented in this chapter at fixed flow and filtration variables. However, the slight variations in the identified parameter k_0 highlights that the parameters (i.e., particle size) are implicitly included in the concentration profiles controlled by σ.

VI.9.1 Domain of validity

Eilers model, implemented herein with the filtration model of Lefevre, predicts the evolution of viscosity as a function of particle concentration, independently of the shear rate. However, the rheology study of section II.5.2 has shown that suspensions of the used ceramic particles are Newtonian up to a concentration of 20%. Hence, the current model could not be applied beyond this particle percentage.
Otherwise, the model remains valid as long as the porosity is higher than zero, i.e., the particle deposit σ does not exceed ϵ. This value is restricted by σ_u in Erdal's model. In Lefevre's model, particle deposit is limited to $\epsilon_0 C_{max}$, where C_{max} is the maximum packing fraction of the used particles in a unit volume. The concentration varies in the range $[0, C_{max}]$, and β has a minimum value of $1/C_{max}$ [6].

VI.10 Model application and comparison

In this part, the flow and filtration parameters determined in the previous sections are applied to new experimental cases that were not used for parameter estimation. Figure VI.29 shows the results of the injection simulations for two experimental cases using Erdal's and Lefevre's models.

Simulations of suspension injection are performed with two new cases with different process parameters: **the first case** (Figure VI.29 A) with V_f= 48%, C_0= 3.7% and η_0=0.035 Pa.s, d_p=15.2 μm (particle grade W-610) injected at a pressure P_0= 1.4 bar. **The second case** (Figure VI.29 B) with V_f= 38%, C_0= 5% and η_0=0.035 Pa.s, P_0=1 bar with d_p=7.9 μm (particle grade W-410). **The third case** (Figure VI.29 C) consists of an experiment with V_f= 38%, C_0= 5% and η_0=0.175 Pa.s, P_0=1 bar with d_p=5.2 μm (particle grade W-210).

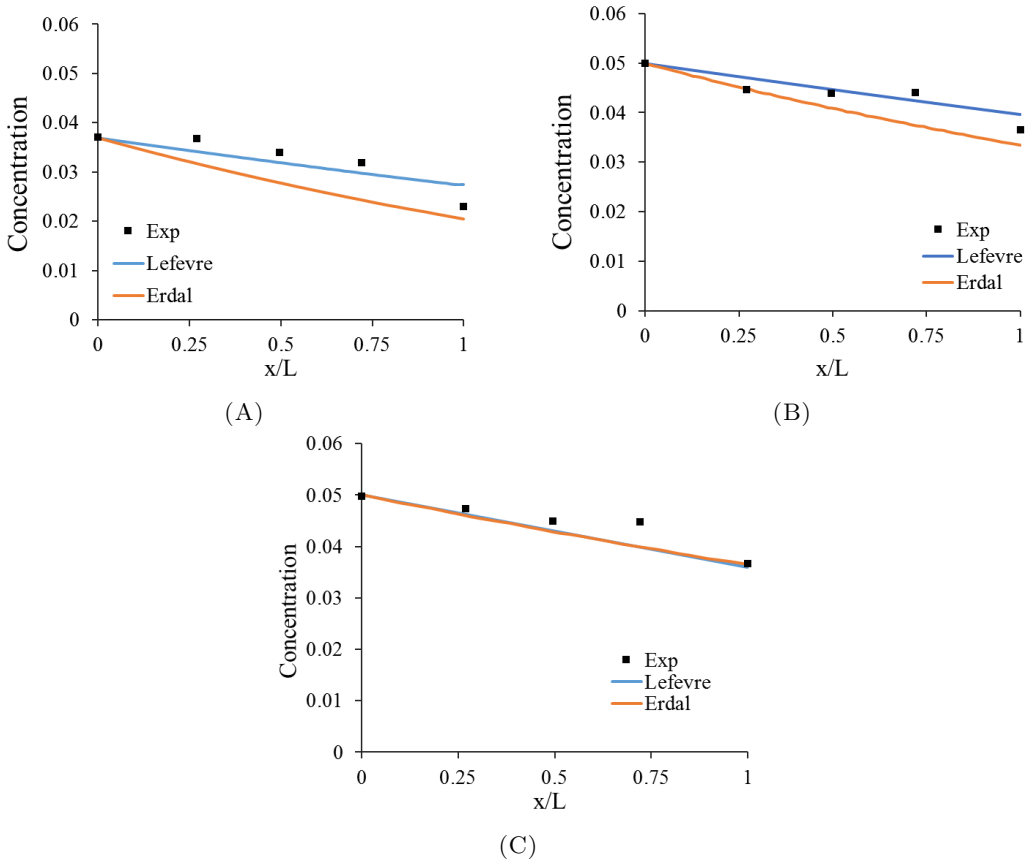

FIGURE VI.29: Evolution of experimental and numerical concentration obtained by the models of Lefevre and Erdal for (A) the first case, (B) the second case and (C) the third case

The choice of the different flow parameters has been made according to the identification carried out in chapter II. The value of β_0 for the model of Lefevre was determined according to Equation VI.56. A value of 30 was fixed for the numerical parameter r of Lefevre's model. The value of k_0 for the two models was selected according to the case in question from the identification step. It was reported earlier that this value is mostly influenced by the fiber volume fraction and the particle size. Hence, the first case is meant to validate the identified k_0 value (3 m^{-1}) at different injection pressure of 1.4 bar. For the second case, an average of k_0 values identified at V_f= 38% and d_p= 7.9 μm with the two models is used (1 m^{-1}). The third case tests the validity of the identified

k_0 value with a different neat fluid viscosity. This case was with a V_f= 38% and d_p= 5.2 μm, hence k_0 of 0.8 m^{-1} is used.

The two models predict the experimental concentration profiles for the explored cases successfully. Results show that the identified k_0 values remain valid even after changing the process variables such as injection pressure or material variables such as the neat fluid viscosity. Remarkably, the model of Lefevre was slightly closer to experimental data at fixed filtration coefficient for the first and the second cases compared to Erdal's model. At the same time, the two models have predicted identical concentration profiles for the third case at the same k_0 value.
To investigate the source of differences in the concentration estimation with the two models noticed with the first and the second cases, other variables are investigated and compared in Figure VI.30 with the two models, for the first case: i.e. porosity (Figure VI.30 A), particle content (Figure VI.30 B), specific deposit (Figure VI.30 C) and viscosity (Figure VI.30 D).

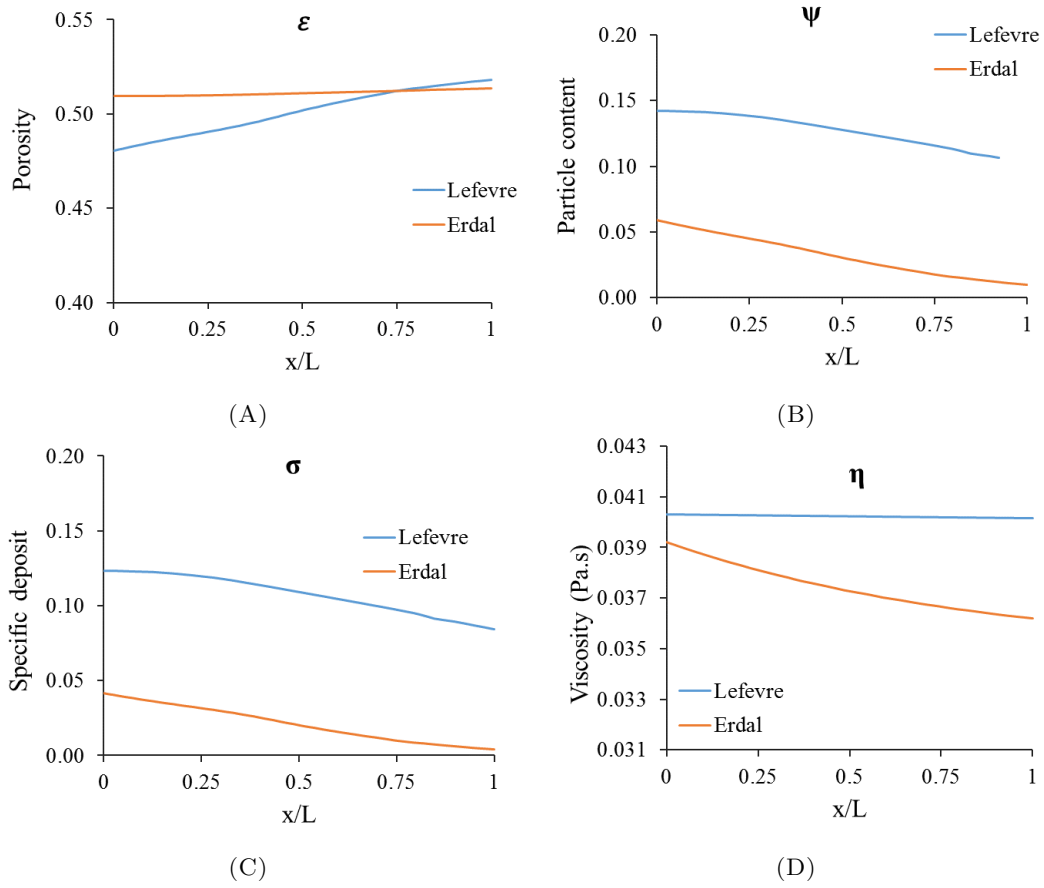

FIGURE VI.30: Simulation results showing a comparison of the filtration models of Erdal and Lefevre for the first case (Figure VI.29 A), with C_0= 3.7%, V_f= 38%, P_0= 1.4 bar, k_0=3 m^{-1}, η_0= 0.035 Pa.s, r= 30 and β_0=8.8, with (A) porosity, (B) particle content, (C) specific deposit and (D) viscosity

The comparison between the two filtration models of Lefevre and Erdal outlines different filtration profiles at the same simulation conditions and identical filtration coefficients.

Lefevre's model predicts higher variations in porosity. On the contrary, the Eilers model exhibit low less variations in viscosity compared to Erdal's model. However, higher retention is represented by Lefevre's model, which results in a higher overall particle content and lower porosity at the preform inlet with Lefevre's model. This explains the higher values of the initial filtration coefficients found using Erdal's model compared to Lefevre's model in section VI.8. However, the differences in the estimations of the two filtration models seem to depend on the process and material parameters in question.

VI.11 Conclusion

In this chapter, a numerical approach is developed to evaluate the influence of different variables on the macroscopic flow and filtration outputs, such as the particle deposit, porosity, pressure, permeability, and viscosity. Another objective targeted in this chapter is the parameter identification of filtration models without passing through the experimental part for future filtration studies. In the first place, the flow and filtration models proposed by Erdal [35] and Lefevre [79] were presented. The two models are implemented in COMSOL Multiphysics through strong numerical coupling between flow and filtration models to simulate the suspension flow process and the filtration of particles through the fibrous bed.

The numerical implementation is presented in detail, including the method of flow front tracking, the boundary conditions of the problem, the input and output data, and the calculation algorithm. The first numerical results compared the flow model results (without particles) with the experimental and analytical results. Then, a complete numerical study of the flow and filtration with the two models (Erdal and Lefevre) is carried out, which begins with the validation of the numerical model with experimental results (chapter IV) of flow front kinetics. The two validation tests (flow only and flow + filtration) show a good agreement between the numerical and the analytical and experimental results, which confirm the validity of the proposed numerical approach.

For each model, a parametric study is performed to investigate the effect of the physical parameters on the filtration behavior, such as the initial filtration coefficient, the ultimate particle deposit σ_u (in the case of Erdal's model), the trapped liquid fraction β and the numerical parameter r (in the case of Lefevre's model).

The parameters of flow models (permeability and viscosity) and filtration models are listed and the identification methods used are recalled. Those parameters associated with the flow have already been identified and discussed in chapter II. The filtration parameters were approximated using the inverse method by minimizing the least square error between experimental and numerical concentration profiles. The focus was drawn to the influence of the initial particle concentration, fiber volume fraction and particle size on the filtration behavior, especially on the value of k_0. Results have shown that for

a given macroscopic simulation, the spatial distribution of particles is highly impacted by the filtration coefficient. The value of the initial filtration coefficient decreased slightly with the increase in concentration. Inversely, it increases continuously with the increase of fiber volume fraction and particle size. However, k_0 was more influenced by the fiber volume fraction.

The robustness of the simulation tool is tested by comparing the numerical concentration profiles to the experimental ones for new cases which were not used to identify the parameters of the filtration model. In this step, the results of the two filtration models are compared. The parameters identified in section VI.8 were used for the new cases. The simulation tool successfully predicted the experimental concentration profile.

Conclusion and perspectives

Conclusion

Throughout this thesis work, extensive experimental and numerical investigations are provided at different stages to study the influence of particle addition to composites manufactured by LCM processes. After presenting a detailed literature review on the subject, materials used for the experimental study are characterized in detail (preform, test fluids and particles). Constitutive laws of the fibrous medium and the suspension are identified.

First, to avoid the complications that arise from non-homogeneous particle distributions, even particle distributions through the part length are assumed by sieving microscopic particles directly at the top surface of quasi-UD preforms. In this part, the influence of fabric functionalization on the flow process and compression behavior is explored at different particle volume fractions. Results have shown reductions in saturated and unsaturated permeability. However, the decrease in permeability ratio has shown that the unsaturated permeability is more sensible to particle addition than the saturated permeability. An increase in the overall stack thickness was noticed with fabric functionalization as a function of particle percentage. Higher fiber volume fractions were attained with compressible microspheres at the same applied pressure, giving lower permeability than the fabrics functionalized by rigid particles.

Next, a new level of complexity is added by experimentally exploring the filtration of polydisperse particles of different sizes and volume fractions through a quasi-unidirectional fibrous medium. Tests of suspension injection were carried out with three grades of ceramic micron-scale particle dispersed in aqueous glycerol solutions. The influence of process and material parameters was extensively studied through a series of experiments using variable initial concentrations, different injection pressures, a range of pure liquid viscosities, several fiber volume fractions and numerous particle size distributions. The method used has examined a key parameter in the RTM process: the spatial evolution of particulate-filler concentration and size distribution. Experimental results enabled the deduction of the main filtration mechanisms for each particle size category. The

capture mechanisms are identified according to the particle size and retention site; they are divided into cake filtration and deep bed capture mechanisms. Particles with sizes larger the inter-fiber distances exhibited cake filtration behavior. Particles that entered the preform followed surface filtration, mechanical blockage and sedimentation through the mold length.

Further investigations on particle filtration are performed to mimic particle transport and capture in tow-scale media injected axially to the fiber direction. For these tests, particles with the narrowest PSD are dispersed in glycerol/water blends and resin. Two characterization methods of particle content for cured composite samples are used, first, the thermal decomposition, which allowed the identification of particle volume fraction and SEM analysis, which succeeded to estimate the evolution of particle content, count, size and number through the length of cured samples at the end of injection, as well as the porosity of the fibrous medium. Results from these investigations showed that both cake and deep bed filtration take place in those single-scale media. Furthermore, contrary to the double scale media injected at constant pressure drop, no sedimentation is observed for these experiments.

A numerical simulation tool is developed using the commercial software COMSOL Multiphysics to simulate the suspension injection process. Two of the most used filtration models were implemented in the simulation tool. The numerical tool has been used to identify the filtration coefficient based on the experimental results of the concentration spatial evolution. The numerical tool is validated by comparing various experimental results of flow front dynamics and spatial concentration distribution. Finally, a complete simulation of suspension injection is performed using the identified parameters without resorting to the experimental method. The results of the simulation reproduced the experimental concentration profiles and filling time successfully.

This work has presented several experimental and numerical characterization methods and set-ups to study flow and filtration through porous media. The results of this study contribute to the comprehension of the physics of suspensions impregnation through fibrous media and, in particular, to help control LCM processes during the fabrication of functional composites by injection or infusion of particle-loaded resins. In addition, it provides information on the key parameters that govern the final distribution of particles within the preform.

Perspectives

The impregnation of preforms by particle-loaded resin is a complex process involving numerous process and material variables. The final particle distribution is of great importance because it can lead to non-homogeneous composite properties, adversely affecting the product quality. This work contributes to the comprehension of the filtration

physics and key parameters that control the injection of suspensions through porous media. Nevertheless, the studies presented open up several questions that need to be addressed and several perspectives that should be questioned:

- Part of the experimental characterization used model fluids to study flow and filtration and the simulation part assumed an isothermal flow. Further experimental and numerical investigations could use curing-resin to explore the influence of particulate-fillers on resin polymerization.
- More broadly, research is also needed to elucidate the effect of injection strategy on particle distribution, which can be realized through a series of experiments that compares single and multiple gate injections or linear and radial injections.
- Further research should study the filtration with LCM processes other than RTM and C-RTM processes, such as the vacuum infusion processes, which necessitates considering the thickness variation of the fibrous reinforcement during impregnation. Future investigations can also explore the effect of race-tracking on the final particle distribution within parts manufactured by LCM processes, both experimentally and numerically.
- The simulation tool could be extended to consider 3D and complex 2D geometries. The model could also be extended to consider the dual-scale of porosity by including a detailed description of the preform microstructure and microscopic particle dynamics.
- The modeling assumptions in the process simulations considered homogeneous particle and liquid velocities within the suspension. Further studies could consider the relative velocities between the particles and the resin at different particle/polymer densities. Moreover, the effects of gravity forces should be considered, as sedimentation is a dominant factor influencing particle filtration. Moreover, the influence of particle polydispersity needs to be explored thoroughly by considering the whole particle distribution in the flow and filtration models.
- Future studies should target the investigation of the influence of particle distribution and volume fraction on the evolution of mechanical properties in cured composite samples.

Nomenclature

The various notations used in this work are summarized in the following Table:

A	Surface area	K_{Unsat}	Unsaturated permeability
A1	Viscosity parameter	k_B	Boltzmann's constant
A_w	Areal weight	k_r	Particle detachment coefficient
b	Parameter of particle content	L	Preform/sample length
β	Coefficient of trapped liquid	λ	Dimensionless filtration parameter
C	Concentration	m	Slope
C_{max}	Maximum packing fraction	m_f	Mass of fibers
Ca	Capillary number	m_v	Parameter of viscosity power law
δ_i	Inter-fiber distance (i= 1, 2 and 3)	μ	Mean
d_p	Particle size	μ_v	Parameter of viscosity power law
D_{eq}	Equivalent diameter	n	Number of plies
e_f	Thickness of the fibrous structure	N	Number of fibers
η	Viscosity	P	Pressure
η_0	Neat fluid viscosity	P_n	Dimensionless pressure
η_r	Relative viscosity	ϕ	The level set function
$[\eta]$	Intrinsic viscosity	ψ	Total particle content
η_i	Filtration efficiency, i= S, I and D	Q	Flow rate
ϵ	Porosity	r	Numerical parameter
ϵ_{ls}	Interface thickness	ρ	Density
f	Particle size distribution function	r_f	Fiber radius
F_g	Gravity forces	R_s	Permeability ratio
ϕ	The level set function	S	Specific surface
g	Acceleration of gravity	σ	Specific deposit
γ	Surface tension	σ_u	Ultimate particle deposit
$\dot{\gamma}$	Shear rate	t	Time
γ_{ls}	Re-initialization parameter	T	Temperature
h_k	Kozeny's constant	u	Variable of the PDE
k	Filtration coefficient	U	Darcy's velocity
K	Permeability	v	velocity
K_{SFF}	Square flow front permeability	V	Volume
K_{ELE}	Elementary permeability	V_f	Fiber volume fraction

K_{INT}	Interpolated permeability	w_i	Fraction of distribution function
K_{SP}	Single point permeability	W_p	Mass of particles
K_{Sat}	Saturated permeability	x_f	Flow front position

The various subscripts used in this work are summarized in the following Table:

Subscripts and superscripts

0	Initial value	p	particles
ap	apparent	r	relative
D	Diffusion	S	Sedimentation
e	effective	T	Total
exp	experimental	th	theoretical
f	fiber	u	ultimate
I	Interception	w	weight
l	liquid	*	Normalized

List of Figures

List of Tables

Bibliography

[1] ASM Handbook. Volume 21: Composites. *USA: ASM International*, 2001.

[2] FT Wallenberger. Structural silicate and silica glass fibers. In *Advanced Inorganic Fibers*, pages 129–168. Springer, 2000.

[3] Suresh G Advani, E Murat Sozer, and L Mishnaevsky Jr. Process modeling in composites manufacturing. *Appl. Mech. Rev.*, 56(5):B69–B70, 2003.

[4] Glossaire des Matériaux Composites. », carma. *Actualisation décembre*, 2004.

[5] Stephen W Tsai. Daniel gay suong v. hoa. 2003.

[6] Delphine Lefevre. *Etude expérimentale, modélisation et simulation de la filtration lors de l'écoulement d'une résine chargée de particules à travers un renfort fibreux dans les technologies LCM.* PhD thesis, École des Mines de Douai, 2007.

[7] Mathieu Imbert. *High speed reactive RTM with on-line mixing in dualscale fibrous reinforcements, experimental and numerical developments and investigations.* PhD thesis, Ecole Centrale de Nantes, 2017.

[8] Khubab Shaker. *Study of particle loaded composites fabrication using liquid composite moulding technique.* PhD thesis, National Textile University, 2018.

[9] Roger N Rothon. *Particulate fillers for polymers*, volume 12. iSmithers Rapra Publishing, 2002.

[10] Long Jiang, Jinwen Zhang, and Michael P Wolcott. Comparison of polylactide/nano-sized calcium carbonate and polylactide/montmorillonite composites: reinforcing effects and toughening mechanisms. *Polymer*, 48(26):7632–7644, 2007.

[11] Roger Rothon. *Particulate-filled polymer composites.* iSmithers Rapra Publishing, 2003.

[12] Omar Restrepo, Kuang-Ting Hsiao, Alejandro Rodriguez, and Bob Minaie. Development of adaptive injection flow rate and pressure control algorithms for resin transfer molding. *Composites Part A: Applied Science and Manufacturing*, 38(6):1547–1568, 2007.

[13] E Manfredi and V Michaud. Packing and permeability properties of e-glass fibre reinforcements functionalised with capsules for self-healing applications. *Composites Part A: Applied Science and Manufacturing*, 66:94–102, 2014.

[14] A ZUPANCIC, ROMANO LAPASIN, and M ZUMER. Rheological characterisation of shear thickening tio2 suspensions in low molecular weight polymer solution. 1997.

[15] Mehdi Rahimian, Naser Ehsani, Nader Parvin, and Hamid reza Baharvandi. The effect of particle size, sintering temperature and sintering time on the properties of al–al2o3 composites, made by powder metallurgy. *Journal of Materials Processing Technology*, 209(14):5387–5393, 2009.

[16] Sun-Young Lee, In-Aeh Kang, Geum-Hyun Doh, Ho-Gyu Yoon, Byung-Dae Park, and Qinglin Wu. Thermal and mechanical properties of wood flour/talc-filled polylactic acid composites: Effect of filler content and coupling treatment. *Journal of Thermoplastic Composite Materials*, 21(3):209–223, 2008.

[17] RA Baker, LL Koller, PE Kummer, HS Katz, and JV Milevski. Handbook of fillers for plastics, 1987.

[18] K. C. Radford. The mechanical properties of an epoxy resin with a second phase dispersion. *Journal of Materials Science*, 6(10):1286–1291, Oct 1971.

[19] A. C. Moloney, H. H. Kausch, T. Kaiser, and H. R. Beer. Parameters determining the strength and toughness of particulate filled epoxide resins. *Journal of Materials Science*, 22(2):381–393, Feb 1987.

[20] Chun-Hway Hsueh. Effects of aspect ratios of ellipsoidal inclusions on elastic stress transfer of ceramic composites. *Journal of the American Ceramic Society*, 72(2):344–347, 1989.

[21] Effects of particle size, particle/matrix interface adhesion and particle loading on mechanical properties of particulate–polymer composites. *Composites Part B: Engineering*, 39(6):933 – 961, 2008.

[22] J Spanoudakis and RJ Young. Crack propagation in a glass particle-filled epoxy resin. *Journal of Materials Science*, 19(2):473–486, 1984.

[23] Baris Caglar, Laurent Orgéas, Sabine Rolland du Roscoat, E. Murat Sozer, and Véronique Michaud. Permeability of textile fabrics with spherical inclusions. *Composites Part A: Applied Science and Manufacturing*, 99:1 – 14, 2017.

[24] B Caglar, V Michaud, and EM Sozer. Experimental investigation of textile permeability in the presence of spherical inclusions.

[25] S. P. Fernberg, E. J. Sandlund, and T. S. Lundstrom. Mechanisms controlling particle distribution in infusion molded composites. *Journal of Reinforced Plastics and Composites*, 25(1):59–70, 2006.

[26] HA Barnes. Shear-thickening ("dilatancy") in suspensions of nonaggregating solid particles dispersed in newtonian liquids. *Journal of Rheology*, 33(2):329–366, 1989.

[27] Howard A Barnes, John Fletcher Hutton, and Kenneth Walters. *An introduction to rheology*, volume 3. Elsevier, 1989.

[28] R Deepak Selvakumar and S Dhinakaran. Effective viscosity of nanofluids—a modified krieger–dougherty model based on particle size distribution (psd) analysis. *Journal of molecular liquids*, 225:20–27, 2017.

[29] GK Batchelor. The effect of brownian motion on the bulk stress in a suspension of spherical particles. *Journal of fluid mechanics*, 83(1):97–117, 1977.

[30] Robin C Ball and Peter Richmond. Dynamics of colloidal dispersions. *Physics and Chemistry of Liquids*, 9(2):99–116, 1980.

[31] IM Krieger and TJ Dougherty. Concentration dependence of the viscosity of suspensions. *Trans. Soc. Rheol*, 3(1):137–152, 1959.

[32] Jan Mewis and Norman J Wagner. *Colloidal suspension rheology*. Cambridge University Press, 2012.

[33] von H Eilers. Die viskosität von emulsionen hochviskoser stoffe als funktion der konzentration. *Kolloid-Zeitschrift*, 97(3):313–321, 1941.

[34] Melvin Mooney. The viscosity of a concentrated suspension of spherical particles. *Journal of colloid science*, 6(2):162–170, 1951.

[35] Merve Erdal, Selçuk I. Güçeri, and Stephen C. Danforth. Impregnation molding of particle-filled preceramic polymers: Process modeling. *Journal of the American Ceramic Society*, 82(8):2017–2028.

[36] Bryan M Louis, Jesus Maldonado, Florian Klunker, and Paolo Ermanni. Particle distribution from in-plane resin flow in a resin transfer molding process. *Polymer Engineering & Science*, 59(1):22–34, 2019.

[37] Dilmurat Abliz, Benedikt Finke, David C. Berg, Carsten Schilde, and Gerhard Ziegmann. Flow of quasi-spherical nanoparticles in liquid composite molding processes. part i: Influence of particle size and fiber distance distribution. *Composites Part A: Applied Science and Manufacturing*, 125:105563, 2019.

[38] Stuart H McGee. Curing characteristics of particulate-filled thermosets. *Polymer Engineering & Science*, 22(8):484–491, 1982.

[39] M. Nordlund, S.P. Fernberg, and T.S. Lundström. Particle deposition mechanisms during processing of advanced composite materials. *Composites Part A: Applied Science and Manufacturing*, 38(10):2182 – 2193, 2007.

[40] Sang Hyuk Yum, Woo Il Lee, and Seung Mo Kim. Particle filtration and distribution during the liquid composite molding process for manufacturing particles containing composite materials. *Composites Part A: Applied Science and Manufacturing*, 90:330–339, 2016.

[41] Sang Hyuk Yum, Jeong U Roh, Joung Man Park, Jong Kyoo Park, Seung Mo Kim, and Woo Il Lee. Assessment of particle distribution in particle-containing composite materials using an electron probe microanalyzer. *Composites Science and Technology*, 82:38 – 46, 2013.

[42] JP Herzig and P Le Goff. Filtration dans les lits epais. i. résultats expérimentaux sur le colmatage et le décolmatage. *Powder Technology*, 5(3):195–200, 1972.

[43] Mourad Chohra, Suresh G. Advani, Ali Gokce, and Shridhar Yarlagadda. Modeling of filtration through multiple layers of dual scale fibrous porous media. *Polymer Composites*, 27(5):570–581.

[44] MR Kessler and SR White. Self-activated healing of delamination damage in woven composites. *Composites Part A: applied science and manufacturing*, 32(5):683–699, 2001.

[45] MR Kessler, Nancy R Sottos, and Scott R White. Self-healing structural composite materials. *Composites Part A: applied science and manufacturing*, 34(8):743–753, 2003.

[46] Amit J Patel, Nancy R Sottos, Eric D Wetzel, and Scott R White. Autonomic healing of low-velocity impact damage in fiber-reinforced composites. *Composites Part A: Applied Science and Manufacturing*, 41(3):360–368, 2010.

[47] Benjamin J Blaiszik, Marta Baginska, Scott R White, and Nancy R Sottos. Autonomic recovery of fiber/matrix interfacial bond strength in a model composite. *Advanced Functional Materials*, 20(20):3547–3554, 2010.

[48] AR Jones, BJ Blaiszik, Scott R White, and Nancy R Sottos. Full recovery of fiber/matrix interfacial bond strength using a microencapsulated solvent-based healing system. *Composites Science and Technology*, 79:1–7, 2013.

[49] Kazuaki SANADA, Noritoshi ITAYA, and Yasuhide SHINDO. 202 self-healing of interfacial debonding in fiber-reinforced polymers and effect of microstructure on strength recovery. In *The Proceedings of Conference of Hokuriku-Shinetsu Branch 2008.45*, pages 43–44. The Japan Society of Mechanical Engineers, 2008.

[50] Damiano Salvatori. *Strategies for faster impregnation in melt thermoplastic resin transfer molding process.* PhD thesis, École Polytechnique Fédérale De Lausanne, 2018.

[51] Damiano Salvatori, Baris Caglar, Helena Teixidó, and Véronique Michaud. Permeability and capillary effects in a channel-wise non-crimp fabric. *Composites Part A: Applied Science and Manufacturing*, 108:41–52, 2018.

[52] JP Herzig, DM Leclerc, and P Le Goff. Flow of suspensions through porous media—application to deep filtration. *Industrial & Engineering Chemistry*, 62(5):8–35, 1970.

[53] Choo Chang-upp and Tien Chi. Hydrosol deposition in fibrous beds. *Separations Technology*, 1(3):122–131, 1991.

[54] P Bedrikovetsky, D Marchesin, F Shecaira, AL Souza, PV Milanez, and E Rezende. Characterisation of deep bed filtration system from laboratory pressure drop measurements. *Journal of Petroleum Science and Engineering*, 32(2-4):167–177, 2001.

[55] Boumediene Benmezroua. *Etude numérique et expérimentale, à l'échelle microstructurelle, du transport granulaire dans les matériaux poreux saturés.* PhD thesis, INSA de Rennes, 2011.

[56] Suresh G Advani. *Processing and properties of nanocomposites.* World Scientific Publishing,, 2007.

[57] Pushpendra Singh, Sathish Gurupatham, Bhavin Dalal, M Hossain, Ian Fischer, and DD Joseph. Particles dispersion on fluid-liquid interfaces. *APS*, 63:GM–006, 2010.

[58] Farida Bensadoun, Nadir Kchit, Catherine Billotte, François Trochu, and Edu Ruiz. A comparative study of dispersion techniques for nanocomposite made with nanoclays and an unsaturated polyester resin. *Journal of Nanomaterials*, 2011, 2011.

[59] J.P. Herzig and P. Le Goff. Filtration dans les lits epais. i. résultats expérimentaux sur le colmatage et le décolmatage. *Powder Technology*, 5(3):195 – 200, 1972.

[60] David Lefevre, Sébastien Comas-Cardona, Christophe Binetruy, and Patricia Krawczak. Coupling filtration and flow during liquid composite molding: Experimental investigation and simulation. *Composites Science and Technology*, 69(13):2127–2134, 2009.

[61] Hind Haji, Abdelghani Saouab, and Yasir Nawab. Simulation of coupling filtration and flow in a dual scale fibrous media. *Composites Part A: Applied Science and Manufacturing*, 76:272 – 280, 2015.

[62] Wook Ryol Hwang, Suresh G. Advani, and Shawn Walsh. Direct simulations of particle deposition and filtration in dual-scale porous media. *Composites Part A: Applied Science and Manufacturing*, 42(10):1344 – 1352, 2011.

[63] Hatice Sinem Sas and Merve Erdal. Modeling of particle–resin suspension impregnation in compression resin transfer molding of particle-filled, continuous fiber reinforced composites. *Heat and Mass Transfer*, 50(3):397–414, 2014.

[64] Laurent Bizet. *Analyse d'un renfort a fibres pour materiau composite. microstructure et permeabilite.* PhD thesis, Université du Havre, 2004.

[65] S. Comas-Cardona, P. Le Grognec, C. Binetruy, and P. Krawczak. Unidirectional compression of fibre reinforcements. part 1: A non-linear elastic-plastic behaviour. *Composites Science and Technology*, 67(3):507 – 514, 2007.

[66] A. Hautefeuille, S. Comas-Cardona, and C. Binetruy. Mechanical signature and full-field measurement of flow-induced large in-plane deformation of fibrous reinforcements in composite processing. *Composites Part A: Applied Science and Manufacturing*, 118:213 – 222, 2019.

[67] N Vernet, E Ruiz, S Advani, JB Alms, M Aubert, M Barburski, B Barari, JM Beraud, DC Berg, N Correia, et al. Experimental determination of the permeability of engineering textiles: Benchmark ii part a applied science and manufacturing. 2014.

[68] Ferland Pierre, Guittard Dominique, and Trochu François. Concurrent methods for permeability measurement in resin transfer molding. *Polymer Composites*, 17(1):149–158.

[69] Krishna M Pillai. Modeling the unsaturated flow in liquid composite molding processes: a review and some thoughts. *Journal of Composite materials*, 38(23):2097–2118, 2004.

[70] CS Minier and NN Dalton. Physical properties of glycerine and it's solutions. *American Chemical Society Monograph*, 117:10, 1953.

[71] JF Richardson and RA Meikle. Sedimentation and fluidization-part iv; drag force on individual particles in an assemblage. *Trans. Inst. Chem. Eng*, 39:357–362, 1961.

[72] E Barnea and J Mizrahi. A generalized approach to the fluid dynamics of particulate systems: Part 1. general correlation for fluidization and sedimentation in solid multiparticle systems. *The Chemical Engineering Journal*, 5(2):171–189, 1973.

[73] Massimo Poletto and Daniel D. Joseph. Effective density and viscosity of a suspension. *Journal of Rheology*, 39(2):323–343, 1995.

[74] Jie Ding, Phillip J Tracey, Weihua Li, Gangrou Peng, Philip G Whitten, and Gordon G Wallace. Review on shear thickening fluids and applications. 2013.

[75] R. F. Probstein, M. Z. Sengun, and T-C. Tseng. Bimodal model of concentrated suspension viscosity for distributed particle sizes. *Journal of Rheology*, 38(4):811–829, 1994.

[76] Karen A Schulze, Abbas A Zaman, and Karl-Johan M Söderholm. Effect of filler fraction on strength, viscosity and porosity of experimental compomer materials. *Journal of dentistry*, 31(6):373–382, 2003.

[77] JS Chong, EB Christiansen, and AD Baer. Rheology of concentrated suspensions. *Journal of applied polymer science*, 15(8):2007–2021, 1971.

[78] RJ Farris. Prediction of the viscosity of multimodal suspensions from unimodal viscosity data. *Transactions of the Society of Rheology*, 12(2):281–301, 1968.

[79] Delphine Lefevre, Sébastien Comas-Cardona, Christophe Binétruy, and Patricia Krawczak. Modelling the flow of particle-filled resin through a fibrous preform in liquid composite molding technologies. *Composites Part A: Applied Science and Manufacturing*, 38(10):2154–2163, 2007.

[80] Elisabete F. Reia da Costa and Alexandros A. Skordos. Modelling flow and filtration in liquid composite moulding of nanoparticle loaded thermosets. *Composites Science and Technology*, 72(7):799 – 805, 2012.

[81] Gabriele Tagliavia, Maurizio Porfiri, and Nikhil Gupta. Analysis of flexural properties of hollow-particle filled composites. *Composites Part B: Engineering*, 41(1):86–93, 2010.

[82] Maurizio Porfiri and Nikhil Gupta. Effect of volume fraction and wall thickness on the elastic properties of hollow particle filled composites. *Composites Part B: Engineering*, 40(2):166–173, 2009.

[83] Fan Zhang. *Modélisation en contexte aléatoire des propriétés de transport des matériaux fibreux*. PhD thesis, Lille 1, 2011.

[84] Maximilian Tonejc, Martin Pletz, Ewald Fauster, and Ralf Schledjewski. Permeability customisation through preform manipulation utilising 3d-printing technology. *Polymers and Polymer Composites*, 25(9):651–660, 2017.

[85] Gábor Szebényi, Tibor Czigány, Balázs Magyar, and József Karger-Kocsis. 3d printing-assisted interphase engineering of polymer composites: Concept and feasibility. *Express Polymer Letters*, 11(7):525–530, 2017.

[86] Damiano Salvatori, Baris Caglar, and Véronique. 3d spacers enhance flow kinetics in resin transfer molding with woven fabrics. *Composites Part A: Applied Science and Manufacturing*, 119:206 – 216, 2019.

[87] Baris Caglar, Laurent Orgéas, Sabine Rolland Du Roscoat, E Murat Sozer, and Véronique Michaud. Permeability of textile fabrics with spherical inclusions. *Composites Part A: Applied Science and Manufacturing*, 99:1–14, 2017.

[88] Francois Robitaille and Raymond Gauvin. Compaction of textile reinforcements for composites manufacturing. i: Review of experimental results. *Polymer composites*, 19(2):198–216, 1998.

[89] Ana XH Yong, Alper Aktas, D May, Andreas Endruweit, SV Lomov, S Advani, P Hubert, SG Abaimov, D Abliz, I Akhatov, et al. Experimental characterisation of textile compaction response: A benchmark exercise. *Composites Part A: Applied Science and Manufacturing*, 142:106243, 2021.

[90] Merve. Erdal. *Impregnation molding of continuous fiber-reinforced ceramic-ceramic composites using preceramic polymers.* PhD thesis, University of Illinois at Chicago, 1998.

[91] S. Gueroult. *Analyse expérimentale de la saturation des milieux fibreux a double échelle de pores : application a la mise en œuvre des matériaux composites par procédé RTM.* PhD thesis, Université du Havre, 2012.

[92] Willem H Boersma, Jozua Laven, and Hans N Stein. Shear thickening (dilatancy) in concentrated dispersions. *AIChE journal*, 36(3):321–332, 1990.

[93] Joël Bréard, Yann Henzel, François Trochu, and Raymond Gauvin. Analysis of dynamic flows through porous media. part i: Comparison between saturated and unsaturated flows in fibrous reinforcements. *Polymer composites*, 24(3):391–408, 2003.

[94] Laurent Bizet, Joël Bréard, Guy Bouquet, Jean-Paul Jernot, and Moussa Gomina. Serial sections through a continuous fiber-reinforced polymer composite. *Image Analysis and Stereology*, 23(3):167–176, 2011.

[95] Nihad A Siddig, Christophe Binetruy, Elena Syerko, Pavel Simacek, and Suresh Advani. A new methodology for race-tracking detection and criticality in resin transfer molding process using pressure sensors. *Journal of Composite Materials*, 52(29):4087–4103, 2018.

[96] Edwin L Crow and Kunio Shimizu. *Lognormal distributions.* Marcel Dekker New York, 1987.

[97] Nihad A Siddig, Laurent Bizet, Ahmed El Moumen, and Abdelghani Saouab. Experimental characterization of polydisperse particle-loaded flow for linear resin transfer molding injections. *Polymer Composites.*

[98] JC Ferrari, F Castilhos, PHH Araújo, and C Sayer. Modeling particle size distribution in heterogeneous polymerization systems using multimodal lognormal function. *Brazilian Journal of Chemical Engineering*, 33(3):469–478, 2016.

[99] Jürgen Becker, Liping Cheng, Cornelia Kronsbein, and Andreas Wiegmann. Simulation of cake filtration for polydisperse particles. *Chemical Engineering & Technology*, 39(3):559–566, 2016.

[100] Christophe Binetruy, Bruno Hilaire, and José Pabiot. The interactions between flows occurring inside and outside fabric tows during rtm. *Composites Science and Technology*, 57(5):587–596, 1997.

[101] Christophe Binétruy. *Calcul et validation expérimentale de la perméabilité et prévision de l'imprégnation de tissus en moulage RTM*. PhD thesis, Lille 1, 1996.

[102] C Binetruy, B Hilaire, and J Pabiot. Tow impregnation model and void formation mechanisms during rtm. *Journal of composite Materials*, 32(3):223–245, 1998.

[103] MS Selim, AC Kothari, and RM Turian. Sedimentation of multisized particles in concentrated suspensions. *AIChE journal*, 29(6):1029–1038, 1983.

[104] Veniamin Grigorevich Levich. Physicochemical hydrodynamics. 1962.

[105] Lawrence H Sanford and Charles D Gates. Effects of synthetic detergents on rapid sand filter performance. *Journal (American Water Works Association)*, 48(1):45–54, 1956.

[106] Kuan-Mu Yao, Mohammad T Habibian, and Charles R O'Melia. Water and waste water filtration. concepts and applications. *Environmental science and technology*, 5(11):1105–1112, 1971.

[107] Ernest WJ Diaper and Kenneth J Ives. Filtration through size-graded media. *Journal of the Sanitary Engineering Division*, 91(3):89–116, 1965.

[108] RB Krone, GT Orlob, and Carl Hodgkinson. Movement of coliform bacteria through porous media. *Sewage and Industrial Wastes*, 30(1):1–13, 1958.

[109] Laurent Bizet, J Breard, G Bouquet, JP Jernot, and M Gomina. Interpretation of permeability in a unidirectional noncrimp stitched preform by geometrical description of the porosity. In *proceedings of the 7th International Conference on Flow Processes in Composite Materials*, 2004.

[110] JC Ward. Turbulent flow in porous media. *Journal of the hydraulics division*, 90(5):1–12, 1964.

[111] Alice Maroudas and Paul Eisenklam. Clarification of suspensions: a study of particle deposition in granular media: Part ii—a theory of clarification. *Chemical Engineering Science*, 20(10):875–888, 1965.

[112] Ramaswamy Sakthivadivel. *Clogging of a granular porous medium by sediment*. Hydraulic Engineering Laboratory, College of Engineering, University of . . . , 1969.

[113] James L Sherard, Lorn P Dunnigan, and James R Talbot. Basic properties of sand and gravel filters. *Journal of Geotechnical Engineering*, 110(6):684–700, 1984.

[114] Fuping Zhou, Nina Kuentzer, Pavel Simacek, Suresh G Advani, and Shawn Walsh. Analytic characterization of the permeability of dual-scale fibrous porous media. *Composites Science and Technology*, 66(15):2795–2803, 2006.

[115] M. Bodaghi, S.V. Lomov, P. Simacek, N.C. Correia, and S.G. Advani. On the variability of permeability induced by reinforcement distortions and dual scale flow in liquid composite moulding: A review. *Composites Part A: Applied Science and Manufacturing*, 120:188 – 210, 2019.

[116] Nina Kuentzer, Pavel Simacek, Suresh G. Advani, and Shawn Walsh. Permeability characterization of dual scale fibrous porous media. *Composites Part A: Applied Science and Manufacturing*, 37(11):2057 – 2068, 2006.

[117] M Amin F Zarandi, Salvador Arroyo, and Krishna M Pillai. Longitudinal and transverse flows in fiber tows: Evaluation of theoretical permeability models through numerical predictions and experimental measurements. *Composites Part A: Applied Science and Manufacturing*, 119:73–87, 2019.

[118] M. Amin F. Zarandi, Krishna M Pillai, and Bamdad Barari. Flow along and across glass-fiber wicks: Testing of permeability models through experiments and simulations. *AIChE Journal*, 64(9):3491–3501, 2018.

[119] Oliver Rimmel and David May. Modeling transverse micro flow in dry fiber placement preforms. *Journal of Composite Materials*, 54(13):1691–1703, 2020.

[120] Mohamad Karaki, Ali Hallal, Rafic Younes, Francois Trochu, Pascal Lafon, Amin Hayek, A Kobeissy, and Ahmad Fayad. A comparative analytical, numerical and experimental analysis of the microscopic permeability of fiber bundles in composite materials. *Int. J. Compos. Mater*, 7(3):82–102, 2017.

[121] Nishank Saxena, Ronny Hofmann, Faruk O Alpak, Steffen Berg, Jesse Dietderich, Umang Agarwal, Kunj Tandon, Sander Hunter, Justin Freeman, and Ove Bjorn Wilson. References and benchmarks for pore-scale flow simulated using micro-ct images of porous media and digital rocks. *Advances in Water Resources*, 109:211–235, 2017.

[122] K Yazdchi, S Srivastava, and Stefan Luding. Micro–macro relations for flow through random arrays of cylinders. *Composites Part A: Applied Science and Manufacturing*, 43(11):2007–2020, 2012.

[123] MK Um and WI Lee. A study on permeability of unidirectional fiber beds. *Journal of reinforced plastics and composites*, 16(17):1575–1590, 1997.

[124] A Tamayol and M Bahrami. Analytical determination of viscous permeability of fibrous porous media. *International Journal of Heat and Mass Transfer*, 52(9-10):2407–2414, 2009.

[125] JE Drummond and MI Tahir. Laminar viscous flow through regular arrays of parallel solid cylinders. *International Journal of Multiphase Flow*, 10(5):515–540, 1984.

[126] Alexander L Berdichevsky and Zhong Cai. Preform permeability predictions by self-consistent method and finite element simulation. *Polymer Composites*, 14(2):132–143, 1993.

[127] Z Cai and AL Berdichevsky. An improved self-consistent method for estimating the permeability of a fiber assembly. *Polymer composites*, 14(4):314–323, 1993.

[128] Josias Van der Westhuizen and J Prieur Du Plessis. An attempt to quantify fibre bed permeability utilizing the phase average navier-stokes equation. *Composites Part A: Applied Science and Manufacturing*, 27(4):263–269, 1996.

[129] B Rikard Gebart. Permeability of unidirectional reinforcements for rtm. *Journal of composite materials*, 26(8):1100–1133, 1992.

[130] Sinzi Kuwabara. The forces experienced by randomly distributed parallel circular cylinders or spheres in a viscous flow at small reynolds numbers. *Journal of the physical society of Japan*, 14(4):527–532, 1959.

[131] Manolis M. Tomadakis and Teri J. Robertson. Viscous permeability of random fiber structures: Comparison of electrical and diffusional estimates with experimental and analytical results. *Journal of Composite Materials*, 39(2):163–188, 2005.

[132] M V Bruschke and SG Advani. Flow of generalized newtonian fluids across a periodic array of cylinders. *Journal of Rheology*, 37(3):479–498, 1993.

[133] Ashok S Sangani and C Yao. Transport processes in random arrays of cylinders. ii. viscous flow. *The Physics of fluids*, 31(9):2435–2444, 1988.

[134] T G Gutowski, Z Cai, S Bauer, D Boucher, J Kingery, and S Wineman. Consolidation experiments for laminate composites. *Journal of Composite Materials*, 21(7):650–669, 1987.

[135] A Endruweit, F Gommer, and AC Long. Stochastic analysis of fibre volume fraction and permeability in fibre bundles with random filament arrangement. *Composites Part A: Applied Science and Manufacturing*, 49:109–118, 2013.

[136] Georg Bechtold and Lin Ye. Influence of fibre distribution on the transverse flow permeability in fibre bundles. *Composites Science and Technology*, 63(14):2069 –

2079, 2003. Polymer Composites: Design, Materials, Manufacturing, Dedicated to Professor M. Neitzel.

[137] John Happel. Viscous flow relative to arrays of cylinders. *AIChE Journal*, 5(2):174–177, 1959.

[138] Xiaoming Chen and TD Papathanasiou. Micro-scale modeling of axial flow through unidirectional disordered fiber arrays. *Composites Science and Technology*, 67(7-8):1286–1293, 2007.

[139] Henry Darcy. *Les fontaines publiques de la ville de Dijon: exposition et application...* Victor Dalmont, 1856.

[140] Kenneth James Ives. Simplified rational analysis of filter behaviour. *Proceedings of the Institution of Civil Engineers*, 25(3):345–364, 1963.

[141] A Adin and M Rebhun. Deep-bed filtration: accumulation-detachment model parameters. *Chemical engineering science*, 42(5):1213–1219, 1987.

[142] Tomihisa Iwasaki. Some notes on sand filtration. *Journal-American Water Works Association*, 29(10):1591–1597, 1937.

[143] Delphine Lefevre, Sébastien Comas-Cardona, Christophe Binétruy, and Patricia Krawczak. Modelling the flow of particle-filled resin through a fibrous preform in liquid composite molding technologies. *Composites Part A: Applied Science and Manufacturing*, 38(10):2154 – 2163, 2007.

[144] Darrell W Pepper and Juan C Heinrich. *The finite element method: basic concepts and applications with MATLAB, MAPLE, and COMSOL*. CRC press, 2017.

[145] COMSOL Multiphysics. Introduction to comsol multiphysics®. *COMSOL Multiphysics, Burlington, MA, accessed Feb*, 9:2018, 1998.

[146] Roger W Pryor. *Multiphysics modeling using COMSOL®: a first principles approach*. Jones & Bartlett Publishers, 2009.

[147] S Soukane and F Trochu. Application of the level set method to the simulation of resin transfer molding. *Composites Science and Technology*, 66(7-8):1067–1080, 2006.

[148] Jorick Naber. A runge-kutta discontinuous-galerkin level-set method for unsteady compressible two-fluid flow. *Modelling, Analysis and Simulation [MAS]*, (E0601), 2006.

[149] T Kitano, T Kataoka, and T Shirota. An empirical equation of the relative viscosity of polymer melts filled with various inorganic fillers. *Rheologica Acta*, 20(2):207–209, 1981.